Numerical investigation of compressibility effects in reacting subsonic flows

Thesis by
Guillaume Beardsell

In Partial Fulfillment of the Requirements for the
Degree of
Doctor of Philosophy

Caltech

CALIFORNIA INSTITUTE OF TECHNOLOGY
Pasadena, California

2020
Defended October 9, 2020

Guillaume Beardsell
ORCID: 0000-0001-7138-488X

ACKNOWLEDGEMENTS

First, I would like to thank my research advisor, Professor Guillaume Blanquart, for his passion, dedication, and mentorship. Whenever I saw a problem, he saw an opportunity. I would also like to thank my committee members, Professors Tim Colonius, Dale Pullin, and Melany Hunt, for providing valuable feedback. I also gratefully acknowledge financial support from the Natural Sciences and Engineering Research Council of Canada (NERSC Postgraduate Scholarship D).

I would like to thank the current and previous members of the FORCE, particularly Simon Lapointe, for helping me to get started when I first joined the group, and Joseph Ruan, for the numerous and fruitful discussions. Many other members of the FORCE were instrumental to my success during my PhD, providing useful feedback on manuscripts and oral presentations.

Next, I would like to thank my friends at Caltech, who enriched my PhD journey. Special thanks to Danilo Kusanovic, for the numerous coffee breaks during the day, and beers at night. I would also like to thank Joel Lawson and Florian Schaefer, for all the interesting discussions on topics ranging from science to politics. There are many more people who enriched my life at Caltech, and I would like to thank them for all the fun nights, barbecues, and hikes.

Lastly, I would like to thank my family. Specifically, I would like to thank my parents, who always encouraged me to pursue my dreams; my brother and sister, with whom a share a passion for learning; and my girlfriend, for her unwavering support as I was finishing my PhD.

ABSTRACT

Direct numerical simulations (DNS) of reacting flows are routinely performed either by solving the fully compressible Navier-Stokes equations or using the low Mach number approximation. The latter is obtained by performing a Mach number expansion of the Navier-Stokes equations for small Mach numbers. These two frameworks differ by their ability to capture compressibility effects, which can be broadly defined as phenomena that are not captured by the low Mach number approximation. These phenomena include acoustics, compressible turbulence, and shocks. In this thesis, we systematically isolate compressibility effects in subsonic flows by performing two sets of DNS: one using the fully compressible framework, and one using the low Mach number approximation. We are specifically interested in the interactions between turbulence, acoustics, and flames.

The addition of detailed chemistry in the compressible flow solver required the development of a novel time integration scheme. This scheme combines an iterative semi-implicit method for the integration of the species transport equations, and the classical Runge-Kutta method for the integration of the other flow quantities. It is found to perform well, yielding time steps limited by the acoustic CFL only. Furthermore, the computational cost per iteration of this hybrid scheme is low, being comparable to the one for the classical Runge-Kutta method.

After extensive validation, the first application is the investigation of flame-acoustics interactions in laminar premixed flames. The thermodynamic fluctuations that accompany the acoustic wave are shown to significantly impact the flame response. Using the Rayleigh criterion, the flame-acoustics system is found to be thermo-acoustically unstable for various fuels, flow conditions, and acoustic frequencies. As expected, the low Mach number approximation and the fully compressible framework are in good agreement at low frequencies, since the flame is very thin compared to the acoustic wavelength. The two frameworks differ for very large acoustic frequencies only. In the high frequency limit, the gain reaches a plateau using the low Mach number approximation, while it goes to zero using the fully compressible framework. This is related to the spatial variations in the acoustic pressure field, which are not present in the low Mach number approximation. However, for practically-relevant acoustic frequencies, the low Mach number framework is found to yield accurate results.

Next, a numerical methodology to simulate compressible flows in geometries that lack a natural turbulence generation mechanism is presented. It is found that, unlike in incompressible flows, special care must be taken regarding the energy equation and the presence of standing acoustic modes. When using periodic boundary conditions, forcing the dilatational velocity field promotes the growth of unstable modes. This is explained by extracting the eigenvalues of the linearized forced Navier-Stokes equations. Based on these observations, it is found necessary to force the solenoidal velocity field only. This methodology is applied first to simulations of subsonic homogeneous non-reacting turbulence. We present simulations results for turbulent Mach numbers varying from 0.02 to 0.65. The Mach number dependence of various quantities, such as the dilatational to solenoidal kinetic energy ratio, is extracted. The Mach number scaling of all quantities of interest is found to be readily explained by the low Mach number expansion, specifically the zeroth and first order sets of equations, for turbulent Mach numbers up to 0.1.

Finally, the interaction between subsonic compressible turbulence and premixed flames is investigated. Compressibility effects are isolated by comparing results obtained with the low Mach number approximation and the fully compressible framework, at the same flow conditions. Compressibility effects on chemistry are found to be limited for turbulent Mach numbers at least up to 0.4, especially when contrasted with the large impact of the Karlovitz number. Compressibility effects give rise to significant thermodynamic fluctuations away from the flame front, but these remain small compared to the large fluctuations due to the presence of the turbulent flame brush. The low Mach number approximation thus remains a valid framework for the Mach numbers considered, when the primary goal is to characterize the impact of turbulence on the chemical processes at play.

PUBLISHED CONTENT AND CONTRIBUTIONS

[1]   Beardsell, G. and Blanquart, G., "A cost-effective semi-implicit method for the time integration of fully compressible reacting flows with stiff chemistry," *Journal of Computational Physics*, 2020. DOI: `https://doi.org/10.1016/j.jcp.2020.109479`,
The author of this thesis developed the proposed time integration scheme, implemented it, performed all simulations, analyzed the data, made the figures, and wrote the mansucript.

[2]   Beardsell, G. and Blanquart, G., "Fully compressible simulations of the impact of acoustic waves on the dynamics of laminar premixed flames for engine-relevant conditions," *Proceedings of the Combustion Institute*, 2020. DOI: `https://doi.org/10.1016/j.proci.2020.06.003`,
The author of this thesis performed all simulations, analyzed the data, made the figures, and wrote the manuscript.

[3]   Beardsell, G. and Blanquart, G., "Impact of pressure fluctuations on the dynamics of laminar premixed flames," *Proceedings of the Combustion Institute*, vol. 37, no. 2, pp. 1895–1902, 2019. DOI: `https://doi.org/10.1016/j.proci.2018.07.125`,
The author of this thesis performed all simulations, analyzed the data, made the figures, and wrote the manuscript.

TABLE OF CONTENTS

LIST OF ILLUSTRATIONS

LIST OF TABLES

C h a p t e r   1

INTRODUCTION

Combustion is the main source of energy for power generation and transportation, and will remain so for decades to come. Currently, in the United States, combustion accounts for more than 80% of the total energy production, and is expected to still account for more than 75% of the total energy production in 2050 [4]. Liquid fuels, such as mixtures of large hydrocarbon molecules, are usually preferred due to their high energy density. Unfortunately, combustion of hydrocarbon fuels yields carbon dioxide, which contributes to global warming, and carbon monoxide, nitrous oxides, soot, and unburnt hydrocarbons, which have a detrimental impact on human health. Due to its central role in energy production, understanding combustion at a fundamental level is thus essential to increase efficiency and reduce pollutant emission.

A turbulent flow is often desired in combustion engines, as it increases mixing of the reactants, which enhances the combustion process, and yields increased power output. Hence, most combustion engines operate under turbulent conditions, e.g., in car engines where air and fuel are injected at great speed while being compressed by the quickly moving piston. On the other hand, acoustics are usually detrimental to engines, more specifically continuous-combustion engines such as gas turbines and rocket engines. The interaction of the acoustic field with the flame can cause large flow oscillations, resulting in vibrations leading to acoustic noise and mechanical fatigue. The interaction of turbulence, flames, and acoustics is therefore of great practical importance.

With the large increase in computational power over the past decades, numerical simulations have become an essential tool to further our understanding of these phenomena, by providing researchers with the full state of the flow at every point and time. In particular, Direct Numerical Simulations (DNS), in which all turbulent and chemical scales of the flow are resolved, yield high-fidelity results that can be used to 1) gain physical insight into the combustion dynamics, and 2) guide the development of reduced-order models.

1.1 Laminar premixed flames

In premixed flames, fuel and oxidizer (usually air) are mixed before combustion, at a temperature lower than the auto-ignition temperature of the mixture. We consider a hydrocarbon fuel C_xH_y mixed with O_2. In its most simple description, the system is described by a single-step, global reaction, i.e.,

$$C_xH_y + \nu_{O_2}O_2 \rightarrow \nu_{CO_2}CO_2 + \nu_{H_2}H_2O \,. \tag{1.1}$$
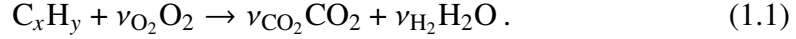
By doing a simple balance of the carbon and hydrogen atoms on Eq. (1.2), we find that the coefficient $\nu_{O_2,st} = (x + (y/4))$ leads to complete depletion of C_xH_y and O_2. In other words, we have a sthoichiometric mixture. The equivalence ratio is defined as

$$\phi \equiv \frac{X_F/X_O}{(X_F/X_O)_{st}} = \nu_{O_2,st}\,(X_F/X_O) \,, \tag{1.2}$$

where X_F and X_O are the mole fractions of fuel and oxidizer, and $(X_F/X_O)_{st}$ is the ratio of the fuel and oxidizer mole fractions at sthoichiometry. The equivalence ratio can also be expressed in terms of the mass fractions, i.e.,

$$\phi \equiv \frac{Y_F/Y_O}{(Y_F/Y_O)_{st}} = \frac{W_O\nu_{O_2,st}}{W_F}\frac{Y_F}{Y_O}, \tag{1.3}$$

where the relation

$$Y_s = X_s\frac{W_s}{W}, \tag{1.4}$$

is used, where W_s is the molecular weight of species s, and W is the mixture-averaged molecular weight.

Premixed flames are characterized by their unburnt conditions, i.e., their unburnt temperature T_u, pressure p_0, and ϕ. Mixtures with $\phi < 1$ are called lean, and mixtures with $\phi > 1$ are called rich. The laminar flame thickness is defined as

$$l_F = \frac{(T_b - T_u)}{|\Delta T|_{max}}, \tag{1.5}$$

where T is the temperature. The subscript $(\ )_u$ refers to quantities evaluated in the unburnt region, i.e., ahead of the flame front, and the subscript $(\ )_b$ refers to quantities evaluated in the burnt region, i.e., behind the flame front. Equation (1.5) is illustrated in Fig. 1.1 for a n-heptane/air flame at $\phi = 0.9$, $T_u = 800$ K, and $p_0 = 1$ atm. Note that Figure 1.1 only shows a small portion of the full flame, and T_b is achieved for $x \gg 3 \cdot 10^{-3}$ m, due to the slow conversion of carbon monoxide into

carbon dioxide. The laminar flame solution was obtained with the FlameMaster code [5], using a 35 species reduced chemical mechanism [6]. The propagation speed, or laminar flame speed, is computed as

$$S_L = \frac{\int_V \rho \dot{\omega}_F dV}{A_c \rho_u Y_{F,u}}, \tag{1.6}$$

where ρ_u and $Y_{F,u}$ are the density and fuel mass fraction in the unburnt region, respectively, and A_c is the cross-sectional area. The flame timescale is defined as $\tau_F = l_F / S_L$.
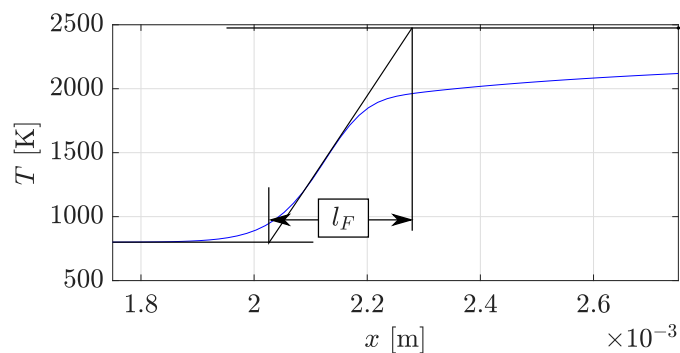
Figure 1.1: Extraction of the laminar flame thickness.

Figure 1.2 shows the normalized temperature, density, and kinematic viscosity profiles for the same flame. It can be seen that temperature increases while density decreases. Also, kinematic viscosity increases significantly due to its strong dependence on temperature. Figure 1.3 shows some species mass fraction profiles for that
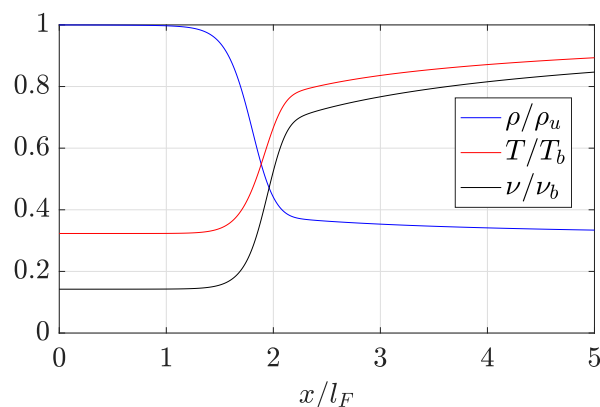
Figure 1.2: Normalized temperature, density, and kinematic viscosity profiles for a n-heptane/air flame at $\phi = 0.9$, $T_u = 800$ K, and $p_0 = 1$ atm .

same flame. It can be seen in Fig. 1.3a that as the fuel is consumed, intermediate

species are created, e.g., C_2H_4. The intermediate species eventually combine into final combustion products, i.e., CO_2 and H_2O. It can be seen in Fig. 1.3 that the conversion from carbon monoxide to carbon dioxide happens on a length scale much larger than the flame thickness. Hence, when performing simulations involving hydrocarbon fuels, we need to have a sufficiently long domain behind the flame front to capture this process.

(a)

(b)
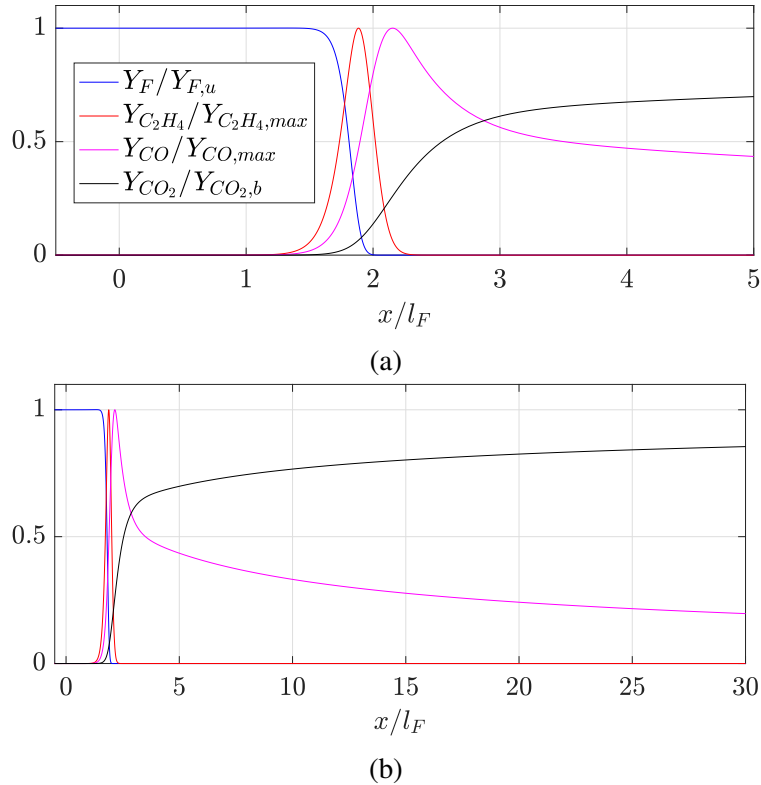
Figure 1.3: Normalized mass fraction profiles for some species in a *n*-heptane/air flame at $\phi = 0.9$, $T_u = 800$ K, and $p_0 = 1$ atm: zoom (a), and full flame (b). Figure (b) uses the same legend as Fig. (a).

Figure 1.4 shows the normalized fuel consumption rate $\dot{\omega}_F/\dot{\omega}_{F,max}$ and heat release $\dot{h}/\dot{h}_{max}$ for the same flame. It can be seen that heat release lags behind the fuel consumption, since the fuel needs to be broken down into small hydrocarbon molecules before being converted into combustion products. The long tail for the heat release is due to the slow conversion of CO into CO_2, which is an exothermic reaction.

Differential diffusion occurs when species and heat diffuse at different rates. It is characterized by the Lewis number

$$Le_s = \frac{\alpha}{D_s},$$

(1.7)
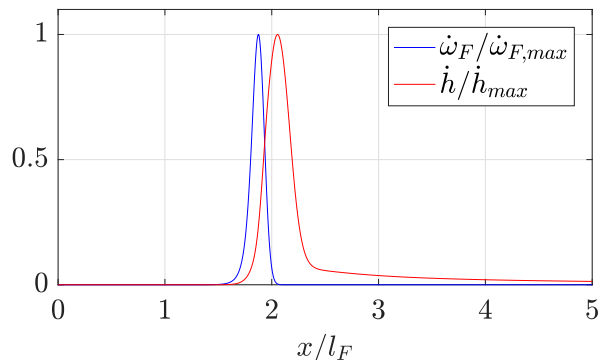
Figure 1.4: Normalized fuel consumption rate and heat release at $\phi = 0.9$, $T_u = 800$ K, and $p_0 = 1$ atm .

where α is the thermal diffusivity, and D_s is the mass diffusivity of species s. A common assumption in combustion modelling is to assume unity Lewis numbers, i.e., $Le_s = 1$. The simulation results presented in this section so far are obtained with non-unity Lewis numbers using a mixture-averaged formulation [7]. We now include results obtained with $Le_s = 1$. In Fig. 1.5, we show the species profiles of carbon dioxide and n-heptane in temperature space when differential diffusion is present ($Le_s \neq 1$), and absent ($Le_s = 1$). It can be seen that assuming unity Lewis numbers changes the flame structure significantly. This result is not surprising as premixed flames involve a balance between convection, diffusion, and chemistry. Figure 1.6 shows the magnitude of these different terms for the transport equation of the fuel. For $T < 1000$ K, convection is mostly balanced by diffusion. For $T > 1000$ K, convection, diffusion, and chemistry all play an active role, until the fuel is depleted at $T \approx 1700$ K. Finally, differential diffusion also impacts the laminar flame speed. For the simulation with unity Lewis numbers, $S_L = 1.73$ m/s, while $S_L = 2.25$ m/s when differential diffusion is present.

1.2 Flame-Acoustics Interactions

1.2.1 Overview

Thermo-acoustic instabilities have been studied extensively since Lord Rayleigh published his pioneering work on the topic in 1878 [8]. These instabilities arise in continuous-combustion systems, such as the "singing flame", and more problematically in the design of practical devices such as gas turbines, rocket engines, and ramjets [9]. They are characterized by large fluctuations of the flow field in the combustor. Low-frequency oscillations can cause significant mechanical vibrations in the system, which in turn increase fatigue and noise. In some cases, it can

(a) Carbon dioxide

(b) *n*-heptane
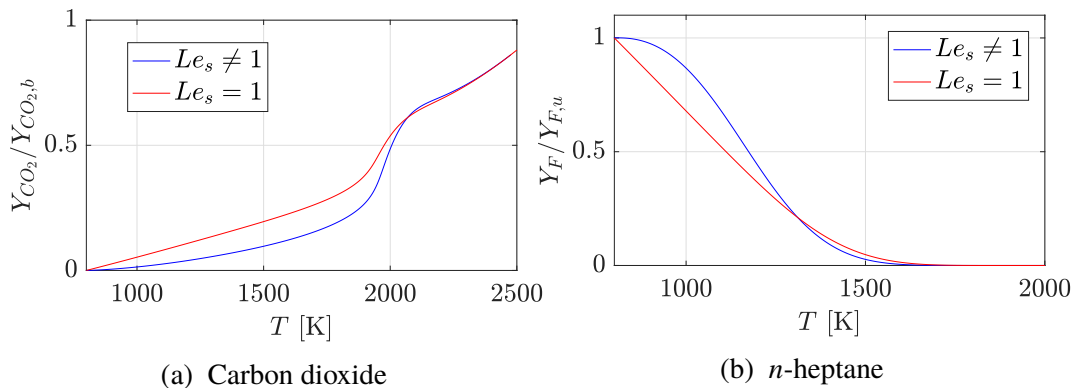
Figure 1.5: Normalized species mass fraction profiles in temperature space when differential diffusion is present (blue) or absent (red).
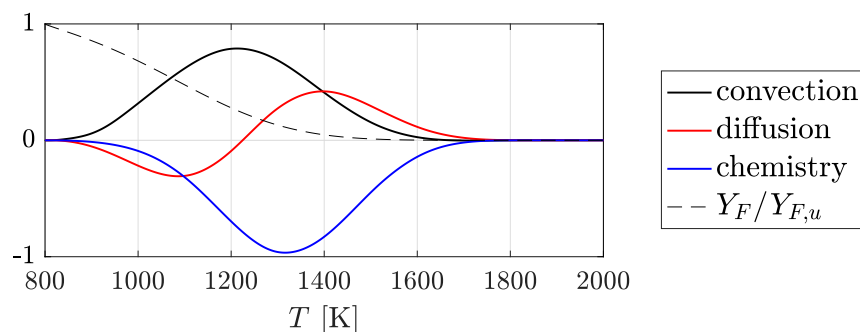
Figure 1.6: Magnitude of the convection, diffusion, and chemistry terms in the fuel transport equation at $\phi = 0.9$, $T_u = 800$ K, and $p_0 = 1$ atm.

even lead to catastrophic failure [10]. In other instances, the oscillations can cause flame blow-off. These instabilities result from the constructive interaction of heat release and acoustic pressure fluctuations. In the absence of acoustic damping, the combustion system is unstable when the Rayleigh criterion is satisfied, i.e.,

$$\iiint_V p_a \dot{h}' dV > 0 \,, \tag{1.8}$$

where p_a and $\dot{h}'$ are the acoustic pressure and fluctuating heat release rate, respectively, and V is the volume of the combustor.

The development of the Rocketdyne F-1 engine, used in the first stage of the Saturn V rocket which served as the main launch vehicle during the Apollo missions, is perhaps the most famous embodiment of the problematic nature of thermo-acoustic instabilities. Early in the development of the engine, pressure oscillations on the order of 400% of the mean chamber pressure (7757 kPa) were observed [11]. This led to the creation of "Project First" in 1962, which aimed to solve the combustion stability problems that plagued the engine. From 1962 to 1965, of approximately

3,200 full scale tests that were performed during the development of the F1 engine, about 2,000 were conducted as part of Project First [11]. A lot of progress has been made since then on understanding and addressing combustion instabilities. However, despite over half a century of research on combustion instabilities, they remain problematic during the design phase of new combustion systems [9].

1.2.2 Feedback mechanisms

A review of the different flame-acoustic interaction mechanisms in premixed combustion is given by Lieuwen *et al.* [9]. Figure 1.7 summarizes the main pathways that can lead to flame-acoustics interactions. Fluctuations in heat release can conceptually be divided into two broad categories: changes in the global geometry of the flame and changes in the local internal structure of the flame (local flame speed fluctuations). The former is usually associated with the velocity fluctuations induced by the acoustic wave. They can cause displacement of the mean flame front (flame location fluctuations) and changes in the total flame area, e.g., through Rayleigh-Taylor instabilities. Changes in the local internal structure of the flame can be due to the acoustic velocity field (e.g., through strain and curvature effects), and the thermodynamic fluctuations that accompany an incident acoustic wave (i.e., changes in density and temperature). The impact of the acoustic thermodynamic fluctuations on the flame response are sometimes referred to as direct pressure effects [12]. In a combustor, many or all of these pathways may play a role in the overall thermo-acoustic stability of the system.
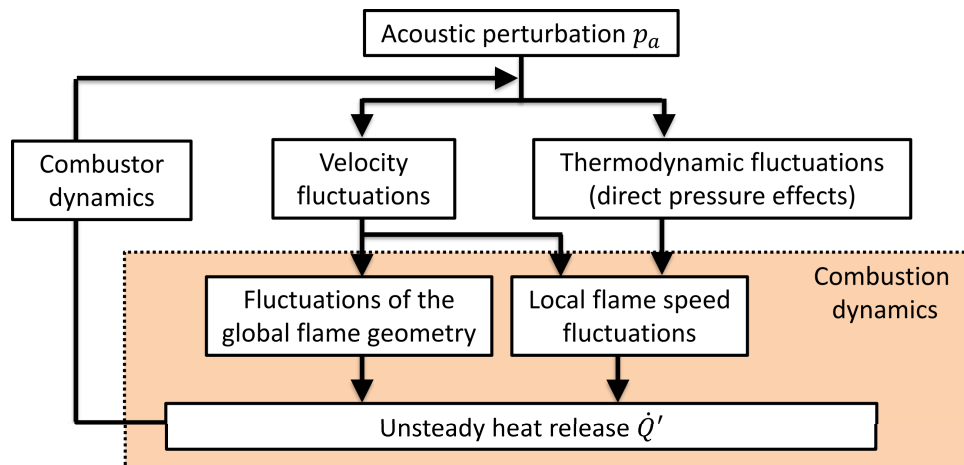
Figure 1.7: Diagram of the different pathways that can lead to interactions between flames and acoustic waves.

In the low frequency limit, simple scaling arguments indicate that the magnitude of

the unsteady heat release due to direct pressure effects is $O(M)$ smaller than the one due to the fluctuations induced by the velocity field, where $M \equiv S_L/c$ is the Mach number. Since $M \ll 1$ for most flames, this suggests that the impact of the thermodynamic fluctuations may be negligible for low frequencies [13]. However, although the steady-state response is fairly weak, the unsteady response can cause the local heat release to exceed its quasi-steady value by an order of magnitude [9]. Furthermore, the acoustic pressure and the unsteady heat release are expected to be in phase for a wide range of frequencies [2, 3, 12, 14]. The Rayleigh criterion [8] is thus satisfied and the flame-acoustics system is unstable when acoustic damping is neglected. It is thus unclear whether the thermodynamic-induced impact in practical combustion systems can be neglected, especially at high frequencies [9]. The aim of this thrust is to better characterize direct pressure effects, i.e., the flame response subjected to acoustic thermodynamic fluctuations.

1.2.3 Direct pressure effects

A significant amount of theoretical work has been performed on direct pressure effects using asymptotic analysis, either with a one-step model, e.g, [15–19] or a two-step model [20]. All of these studies have emphasized the role played by the relative time and length scales of the flame and pressure perturbation, i.e., $\omega \tau_F$ and l_F/λ. Here, $\omega = 2\pi f$ is the angular frequency of the acoustic perturbation, $\tau_F = l_F/S_L$ is the flame time scale, $l_F = (T_b - T_u)/\max |\partial T/\partial x|$ is the flame thickness, S_L is the laminar flame speed, and λ is the acoustic wavelength. While one-step chemical models are limited, the two-step model by Clavin and Searby [20] has been shown to agree well with numerical simulations of hydrogen/air flames using detailed chemistry [14]. Unfortunately, the analytical expressions obtained with a two-step model are significantly more complex than the ones obtained using a one-step model. Furthermore, for hydrocarbon fuels, a two-step model might not be sufficient to represent the flame dynamics. Hence, while these theoretical studies provide invaluable insight, numerical simulations are necessary to investigate the behavior of hydrocarbon fuels, especially larger molecules. The existing experimental [21] and numerical [12, 14] literature is scarce, and focuses on hydrogen and small hydrocarbons (methane and propane). The flame-acoustics interactions involving large hydrocarbon species, which are commonly used in many practical combustion devices, have not been explored before, and are the main focus of this research thrust.

1.3 Turbulence

1.3.1 Overview

Turbulent flows are omnipresent in both nature and human-made devices, and as a result have received a lot of attention throughout the last decades [22]. Turbulence is a vast subject, and we do not attempt to provide an extensive review of turbulence research in this section. Here, our aim is only to review some basic concepts, which will be useful later on in this thesis. Specifically, we discuss the different turbulent scales, and the different techniques used to obtain and sustain turbulence in simplified computational geometries such as periodic boxes.

Turbulence can be thought of as a random collection of coherent swirling structures of different sizes, often called eddies. The largest eddies can be created by different mechanisms, e.g., by the mean shear gradient in a jet. In a turbulent flow, the largest eddies are unstable, and break up into smaller eddies. The smaller eddies then break up into even smaller eddies, until the eddies are small enough that they are stable and dissipated by the action of molecular viscosity. This conceptual process, called the energy cascade, was proposed by Richardson in 1922 [23]. In 1941, Kolmogorov sought to answer fundamental questions such as: What are the characteristic velocity and time scale of the eddies, and what is the size of the smallest eddies? These questions, and more, are answered by Kolmogorov's three hypotheses [24] (in Russian, see [25] for the English translation).

The first Kolmogorov hypothesis is that the small-scale turbulent motions are statistically isotropic at sufficiently high turbulent Reynolds number

$$Re_t = \frac{u'l}{\nu},$$ (1.9)

where u' is the characteristic velocity, ν is the kinematic viscosity,

$$l = \frac{u'^3}{\epsilon}$$ (1.10)

is the integral length scale, and

$$\epsilon = \frac{\tau : \nabla u}{\rho}$$ (1.11)

is the dissipation rate [26]. Large scale motions are usually anisotropic, and their directionality depend heavily on the mechanism by which they are created, e.g., a turbulent jet. This hypothesis implies that as eddies break up into smaller ones,

they lose information about the directionality of the larger scales due to the chaotic nature of turbulence. In other words, the small scale turbulent motions are always isotropic at sufficiently high Reynolds numbers, and are thus universal.

The second Kolmogorov hypothesis, called Kolmogorov's first similarity hypothesis, states that at sufficiently high Reynolds numbers, the statistics of the small-scale turbulent motions are uniquely determined by ϵ, and ν. Applying dimensional analysis using these two quantities, the Kolmogorov microscales are constructed, i.e., the Kolmogorov length scale

$$\eta = \left(\frac{\nu^3}{\epsilon}\right)^{1/4} , \tag{1.12}$$

the Kolmogorov time scale

$$\tau_\eta = \left(\frac{\nu}{\epsilon}\right)^{1/2} , \tag{1.13}$$

and the Kolmogorov velocity scale

$$u_\eta = (\nu\epsilon)^{1/4} . \tag{1.14}$$

The Reynolds number associated with these scales is

$$Re_\eta = \frac{u_\eta \eta}{\nu} = 1 . \tag{1.15}$$

The Reynolds number being a measure of the ratio of the inertial forces to the viscous forces, Eq. (1.15) implies that viscous forces play an important role when eddies reach the size of the Kolmogorov length scale, and are thus dissipated at this scale.

The third Kolmogorov hypothesis, called Kolmogorov's second similarity hypothesis, states that at sufficiently high Reynolds number, the statistics of the turbulent motions in the *inertial subrange* have a universal form uniquely determined by their size l_i, and ϵ. The inertial subrange is defined as the intermediate range of scales $\eta \ll l_i \ll l$ in which turbulent motions are statistically isotropic but are still relatively unaffected by viscosity, i.e., they break up into smaller eddies, following the concept of energy cascade. The energy spectrum is defined as

$$k = \int_{\kappa=0}^{\infty} E(\kappa)d\kappa , \tag{1.16}$$

where k is the mean kinetic energy of the flow, $\kappa = 2\pi/l_i$ is the wavenumber, and $E(\kappa)$ represents the contribution to the kinetic energy of all the velocity Fourier modes in the range $\kappa < |\boldsymbol{\kappa}| < \kappa + d\kappa$. The expected form of the energy spectrum in the inertial subrange

$$E(\kappa) = C_\kappa \epsilon^{2/3} \kappa^{-5/3} \tag{1.17}$$

is obtained by applying dimensional analysis to Eq. (1.16) using Kolmogorov's second similarity hypothesis.

1.3.2 Compressible turbulence

A large portion of the literature on turbulent flows focuses on incompressible flows, i.e, in the limit when the turbulent Mach number

$$M_t = \sqrt{2k}/c\,, \tag{1.18}$$

goes to zero, where c is the sound speed. Note that some authors define the turbulent Mach number as $M_t = \sqrt{k}/c$ [26]. In this work, we use Eq. (1.18), as used by many authors [27–30]. Compressible turbulent flow, i.e., flows with $M_t > 0$, have received far less attention than their incompressible counterpart, and are not as well understood [29, 31, 32].

When studying compressible turbulent flows, it is useful to perform a Helmholtz decomposition of the velocity field into its solenoidal component

$$\boldsymbol{u}_s = \nabla \times \boldsymbol{A}\,, \tag{1.19}$$

where $\boldsymbol{A}$ is a vector potential, and dilatational component

$$\boldsymbol{u}_d = \nabla \phi\,, \tag{1.20}$$

where ϕ is a scalar potential, and

$$\boldsymbol{u} = \boldsymbol{u}_s + \boldsymbol{u}_d\,. \tag{1.21}$$

This decomposition is unique up to a constant. By definition, we have that

$$\nabla \cdot \boldsymbol{u}_s = 0\,, \tag{1.22}$$

and

$$\nabla \times \boldsymbol{u}_d = 0\,. \tag{1.23}$$

In practice, to obtain $\boldsymbol{u}_s$ and $\boldsymbol{u}_d$ from the full velocity field, one can take its divergence

$$\nabla \cdot \boldsymbol{u} = \nabla \cdot (\boldsymbol{u}_s + \boldsymbol{u}_d) = \nabla^2 \phi\,, \tag{1.24}$$

where the vector identity $\nabla \cdot (\nabla \times A) = 0$ has been used. Equation (1.24) is a Poisson equation that can be solved for ϕ, which can then be used to retrieve u_d using Eq. (1.20). Finally, u_s is obtained from Eq. (1.21).

In compressible turbulence without external heat addition, there are three main regimes [1] [26], depending on the impact of compressibility on the turbulence dynamics:

- The low-Mach number quasi-isentropic regime, in which M_t is small and interactions between the dilatational and solenoidal components of the velocity field are weak. The base flow is solenoidal, and the dilatational component obeys a quasi-linear acoustic dynamics. In the limit $M_t \to 0$, the flow field is purely solenoidal, i.e., incompressible;

- The nonlinear subsonic regime, in which $M_t < 1$, but non-linear phenomena arise due to the compressibility effects. In other words, the dilatational mode is not restricted to the linear acoustics only. In some cases, dilatational effects cause turbulence-induced very small shocks (referred to as eddy shocklets), which can impact the overall flow dynamics. A commonly accepted threshold for the onset of shocklets is $M_t > 0.4$ [26, 33];

- The supersonic regime, in which $M_t > 1$. In this regime, dilatational effects have a large impact on the flow field, and there are strong interactions between the dilatational and solenoidal modes.

In this work, we focus on moderate $M_t < 1$. In Chapter 5, we investigate compressible homogeneous non-reacting turbulence in the low-Mach number quasi-isentropic regime, and the nonlinear subsonic regime, through Direct Numerical Simulations (DNS). It is important to stress that even for $M_t < 1$, eddy shocklets (weak shocks) occur [26, 33]. However, the shocklet strength is proportional to M_t, hence they become weaker as M_t is decreased. Eddy shocklets are resolved when the Kolmogorov length scale is employed to determine to computational grid size, up to $M_t \approx 0.6$ [29]. Hence, a shock-capturing method is not required in this work, since all simulations are performed at $M_t \leq 0.6$.

---

[1]In his book, Sagaut [26] identifies four main regimes of compressible turbulence. In our description, we omit the low-Mach number thermal regime, in which external heat addition, e.g., through chemical reactions, causes the dilatational component of the velocity field not to be governed by acoustic phenomena only. For $M_t \to 0$, this regime is governed by the low Mach number approximation, detailed in Sec. 2.1.2. In the present section, we focus on compressible turbulent flows without external heat addition only. Hence, we omit this regime.

1.3.3 Direct numerical simulations of turbulent flows

DNS are a powerful tool to study turbulent flows. In this framework, the flow is resolved down to the Kolmogorov length scale. When constructing a computational grid, a commonly accepted criterion is that the cell spacing should be no more than twice the Kolmogorov length scale, i.e., $\Delta x < 2\eta$ [22]. Using $\epsilon = u'^3/l$, one gets from Eq. (1.12) that

$$\frac{\Delta x}{l} \sim Re_t^{-3/4}. \tag{1.25}$$

Furthermore, as Δx decreases, if an explicit time integration scheme is used, Δt has to be lowered to accommodate the convective Courant–Friedrichs–Lewy condition (CFL) condition, i.e,

$$.\Delta t \leq \frac{C_{max}\Delta x}{u'_{max}}, \tag{1.26}$$

where C_{max} depends on the integration method. To simulate one eddy turnover time

$$\tau = \frac{k}{\epsilon}, \tag{1.27}$$

the number of time steps $n_{\Delta t}$ scales like

$$n_{\Delta t} = \frac{\tau}{\Delta t} \sim Re_t^{3/4}. \tag{1.28}$$

Hence, for a 3D flow with $\Delta x = \Delta y = \Delta z$, the cost of a turbulent DNS scales like

$$\frac{n_{\Delta t}}{(\Delta x/l)^3} \sim Re_t^3. \tag{1.29}$$

It is apparent from Eq. (1.29) that simulating high Reynolds number turbulent flows using DNS is computationally challenging. The increase in computational power over the last decades has enabled researchers to conduct numerical simulations at ever increasing Reynolds numbers, e.g., in channel flows [34]. The goal of this research thrust is not to simulate yet another record-breaking Re_t. Instead, we aim to provide insight into compressible homogeneous non-reacting turbulence (Chapter 5), and compressible turbulent flames (Chapter 7) at moderate Re_t and M_t.

1.3.4 Turbulence forcing

Since DNS require all the scales to be resolved, simulations of complete geometries (e.g., turbulent jet) can be prohibitively costly. Hence, when performing a DNS, one often chooses to simulate a well-selected portion of the flow (e.g., the centerline of

the jet) [35]. However, by doing so, scales larger than the computational domain are removed. Shear from the large scales is responsible for kinetic energy injection at the small scales; their omission eliminates the mechanism by which turbulence can be sustained. In configurations lacking natural turbulent kinetic energy injection mechanisms such as triply periodic computational boxes, a statistically stationary turbulent state is usually achieved through the use of an additional forcing term in the momentum equations.

Most of the methods to sustain turbulence found in the literature have initially been developed in the context of DNS of homogeneous isotropic turbulence in triply-periodic domains. The most common method involves adding an external force in Fourier space, restricted to the lowest wavenumbers [31]. Other methods use stochastic forcing terms or ensure that the integrated kinetic energy remains constant. Another approach was proposed by Lundgren [36]. By considering the momentum equation for the fluctuating part of the velocity field, he suggested to add a term of the form $f_i = Au_i$ to the momentum equation in physical space, the so-called linear forcing method. A review of the different techniques used to sustain turbulence is given by Rosales *et al.* [37]. However, while all these techniques aim to mimic turbulence generation due to the large scales, none of them was derived directly from the Navier-Stokes equations.

Recently, Dhandapani *et al.*[38] derived a physics-based forcing term to simulate the fluctuating velocity field in a shear layer using a triply periodic box. Similarly, Rah *et al.*[35] derived the proper forcing term for the centerline of a jet from the Navier-Stokes equations. In both cases, they performed a Reynolds decomposition of the velocity field into a mean (large scale) component and fluctuating (small scale) component. Then, they considered the governing equations for the fluctuating velocity field. They found that the main contributions to the forcing term are due to the mean velocity gradients, and the normalization of the velocity field to enforce periodicity. The resulting forcing term was found to be linear in the velocity field, i.e., of the form

$$\boldsymbol{f} = \boldsymbol{A} \cdot \boldsymbol{u}, \tag{1.30}$$

where $\boldsymbol{A}$ is the so-called forcing matrix. This form of the forcing term is reminiscent of the approach proposed by Lundgren [36]. Lundgren's approach is a special case of Eq. (1.30), with $\boldsymbol{A}$ being a diagonal matrix.

In Chapter 5, we seek to extend the approach of Dhandapani *et al.*[38] and Rah *et al.*[35] to compressible flows, focusing on the centerline of a jet.

1.4 Turbulence-Flame Interactions

Most practical combustion devices operate under turbulent conditions, and hence, a lot of research has been devoted to understand turbulence-flame interactions [39]. The turbulent flame speed S_T is defined like the laminar flame speed S_L (Eq. 1.6), i.e.,

$$S_T = \frac{\int_V \rho \dot{\omega}_F dV}{A_c \rho_u Y_{F,u}}, \tag{1.31}$$

where A_c is the cross-sectional area. However, while S_L is usually constant, S_T fluctuates in time due to the stochastic nature of turbulence. The Karlovitz number is defined as the ratio of the flame time scale to the turbulent time scale, i.e.,

$$Ka = \frac{\tau_F}{\tau_\eta} = \frac{l_F}{S_L} \sqrt{\frac{u'^3}{l\nu}}. \tag{1.32}$$

Equation (1.32) can also be expressed in terms of the ratio of the relevant length scales

$$Ka = \frac{l_F^2}{\eta^2}, \tag{1.33}$$

where the relation

$$l_F \approx \frac{\nu}{S_L} \tag{1.34}$$

has been used. The Karlovitz number is typically evaluated using the viscosity in the unburnt region ν_u. When comparing results obtained with different unburnt conditions, it is more appropriate to evaluate viscosity at the reaction zone, since this is where turbulence has the biggest impact on the chemical processes at play [40, 41]. The reaction zone Karlovitz number is defined as

$$Ka_\delta = \frac{\delta_F^2}{\eta_\delta^2}, \tag{1.35}$$

where η_δ is the Kolmogorov length scale at the reaction zone, i.e., at the temperature corresponding to the peak fuel consumption rate in the turbulent flame. The laminar reaction zone thickness δ_F is defined as the region in which the fuel consumption rate $\dot{\omega}_F/\dot{\omega}_{F,max} > 0.05$ in the corresponding laminar flame, as shown in Fig. 1.8. For a n-heptane/air flame at $\phi = 0.9$, $T_u = 800$ K, and $p_0 = 1$ atm, $\delta_F \approx 0.3 l_F$.

The two ratios l/l_F and u'/S_L are related as

$$\frac{u'}{S_L} = Re_t \left(\frac{l}{l_F}\right)^{-1} = Ka^{2/3} \left(\frac{l}{l_F}\right)^{1/3} = Ka_\delta^{2/3} \left(\frac{l}{l_F}\right)^{1/3} \left(\frac{\delta_F}{l_F}\right)^{4/3} \left(\frac{\eta}{\eta_\delta}\right)^{4/3}, \tag{1.36}$$
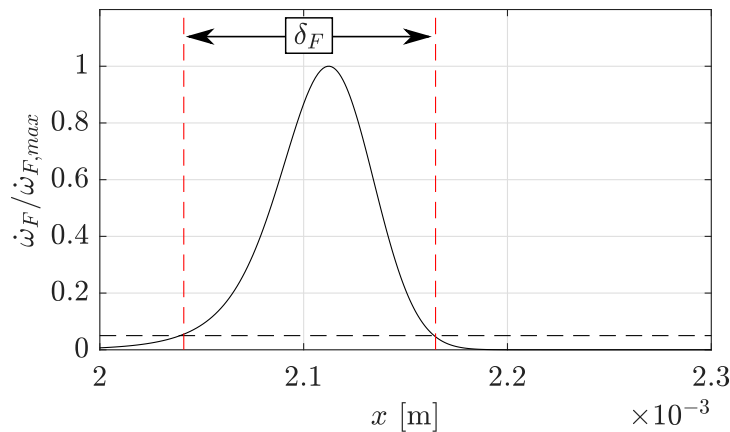
Figure 1.8: Extraction of the laminar reaction zone thickness δ_F, defined as the region in which $\dot{\omega}_F/\dot{\omega}_{F,max} > 0.05$.

where Eqs. (1.9), (1.32), (1.34), and (1.35) have been used. Turbulent combustion regimes are traditionally defined with the ratio of the turbulent velocity fluctuations to the laminar flame speed u'/S_L, and the ratio of the integral length scale to the laminar flame thickness l/l_F [39, 42]. The scalings given by Eq. (1.36) can be used to determine the different regimes of premixed turbulent combustion. Figure 1.9 shows the regime diagram proposed by Peters [39], also referred to as the Borghi diagram. The $Re_t = 1$ line separates laminar from turbulent flames. For $Ka < 1$, flames are either in the corrugated ($u' > S_L$) or wrinkled ($u' < S_L$) flamelet regimes. In the flamelet regime, turbulence is too weak to disrupt the flame front, and the turbulent flame can be viewed as a collection of locally one-dimensional laminar flames. For $Ka > 1$ and $Ka_\delta < 1$, the turbulent flame is in the thin reaction zone. In this regime, the Kolmogorov length scale is smaller than the flame thickness, and the preheat zone, i.e., the region ahead of the flame which is balanced by convection and diffusion, is expected to thicken. However, turbulence is still too weak to penetrate the reaction layer, which is much smaller than the flame thickness (see $\dot{\omega}_F/\dot{\omega}_{F,max}$ in Fig. 1.3a). For $Ka_\delta > 1$, the Kolmogorov length scale at the reaction zone is smaller than the laminar reaction zone thickness, and turbulence is expected to disrupt the chemical processes at play. It should be noted that the regime diagram only provides a qualitative picture of turbulent combustion. Turbulent flows involve a myriad of time and length scales that depend on the specific configuration considered. Hence, it is a simplification to consider single length and time sales to characterize turbulent combustion. Also, the regime diagram is inherently rooted in the low Mach number approximation, since the two non-dimensional numbers, i.e., u'/S_L, and l/l_F, do not involve the sound speed. The Mach number is another non-dimensional number

that might change the combustion characteristics, and can be thought of as a third axis not represented on the Borghi diagram.

In Fig. 1.9b, it should be noted that there exist few numerical studies of turbulent premixed combustion using detailed chemistry. Some of these simulation results were obtained using the fully compressible formulation of the Navier-Stokes equations (Sankaran *et al.*[47], Hawkes *et al.*[48], Wang *et al.*[49]), and some were obtained under the low Mach number approximation (Aspden *et al.*[45], Lapointe *et al.*[40, 46], Savard *et al.*[50, 51]), which will be presented in Sec. 2.1.2. Theoretically, this approximation is only exact for $M_t = 0$. For small M_t, it is expected to perform well under certain conditions, e.g., when the combustion system is not prone to thermo-acoustic instabilities. At larger M_t, compressibility effects may become important: turbulence is characterized by large density and temperature fluctuations, and transition from deflagration to detonation was observed [52]. Also, from Figs. 1.9a and 1.9b, it can be seen that there is almost no overlap between the conditions investigated through simulations and experiments. This is partly due to the prohibitively expensive computational resources needed to perform simulations with $l/l_F \gg 1$. The turbulent Mach number of many experiments is considerable, e.g., $0.3 < M_t < 1.0$ for the piloted premixed jet burner investigated by Dunn *et al.* [53].

In discussing possible compressibility effects, it is important to realize that the turbulent Mach number is related to the Karlovitz and Reynolds numbers as

$$M_t = \sqrt{3} K a^{2/3} \left(\frac{l}{l_F} \right)^{1/3} \frac{S_L}{c} = \sqrt{3} Re_t \left(\frac{l}{l_F} \right)^{-1} \frac{S_L}{c}. \tag{1.37}$$

Hence, for a fixed l/l_F and S_L/c, increasing the Karlovitz number leads to a larger turbulent Mach number. As computers become more powerful, researchers probe the high Karlovitz number limits to understand combustion in the broken reaction zone. In Fig. 1.9b, it can be seen that all simulations falling into this regime were performed under the low Mach number approximation. For the simulations by Lapointe *et al.*[40, 46], the largest turbulent Mach number is $M_t = 0.31$, which is when one might expect compressibility effects to become important. Hence, there is a need to verify that the low Mach number approximation remains valid at such high Karlovitz numbers, which are often accompanied by high M_t.

(a) Experiments

- ■ Aspden *et al.* (H$_2$, CH$_4$, C$_3$H$_8$)
- ○ Lapointe *et al.* (CH$_4$, n-C$_7$H$_{16}$, i-C$_8$H$_{18}$, ...)
- ▷ Sankaran *et al.* (CH$_4$)
- ◀ Hawkes *et al.* (H$_2$)
- ● Wang *et al.* (H$_2$)
- ◆ Savard *et al.* (n-C$_7$H$_{16}$)
- ✳ present work (n-C$_7$H$_{16}$)
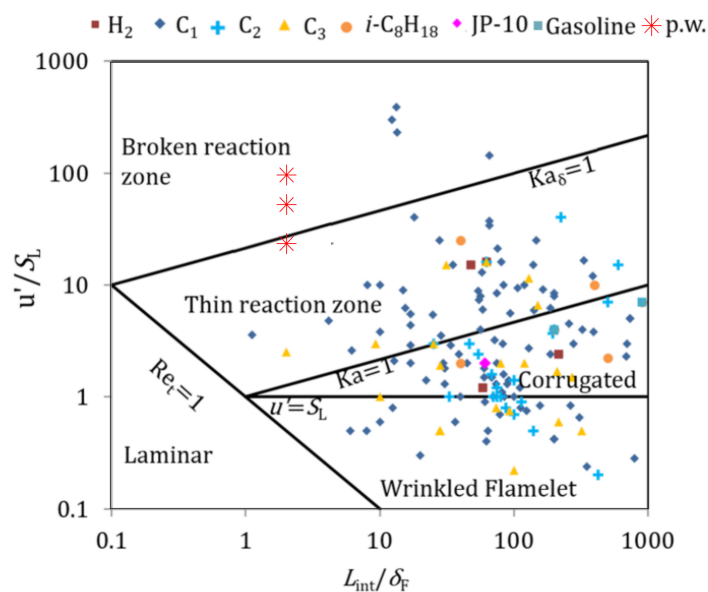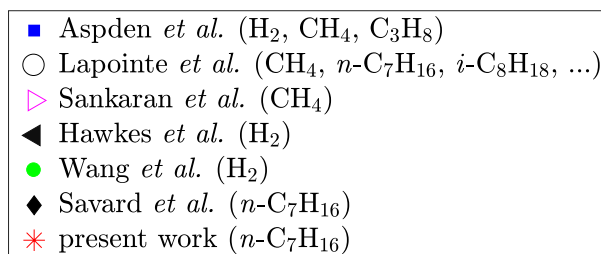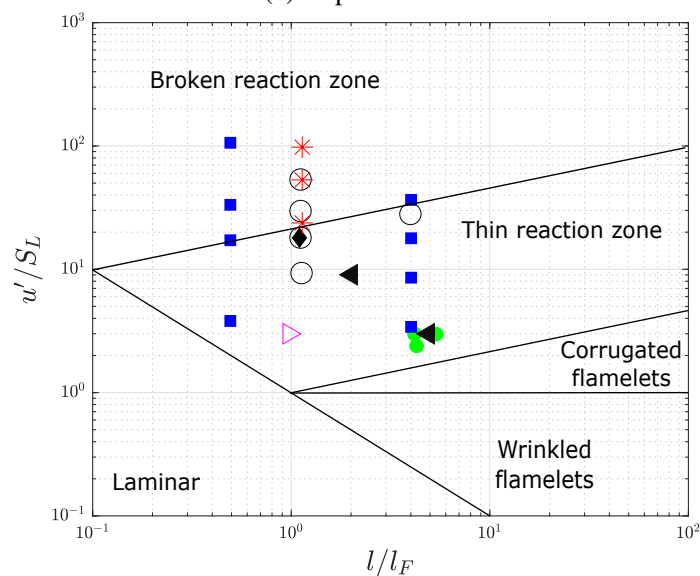
(b) Simulations

Figure 1.9: Regime diagrams showing fuels and flow conditions: (a) Survey of turbulent premixed flame experiments, adapted from Smolke *et al.*[43]; (b) Survey of turbulent premixed flame simulations using detailed chemistry, adapted from Savard [44]: Aspden *et al.*[45], Lapointe *et al.*[40, 46], Sankaran *et al.*[47], Hawkes *et al.*[48], Wang *et al.*[49], Savard *et al.*[50, 51].

1.5 Objectives and outline

In summary, the goal of this thesis is to perform numerical simulations to explore compressibility effects in subsonic flows by investigating interactions between **1**) flames, **2**) turbulence, and **3**) acoustics. This is achieved by using both the low Mach number approximation and the fully compressible framework. The specific objectives are as follows:

- Develop a time integration scheme for compressible flows with stiff chemistry;

- Investigate flame-acoustics interactions in laminar premixed flames (**1** and **3**);

- Design a forcing scheme for turbulent compressible flows in simplified geometries;

- Gain insight into compressible non-reacting subsonic homogeneous turbulence (**2** and **3**);

- Investigate compressibility effects in turbulent premixed flames (**1**, **2**, and **3**).

The two sets of governing equations, i.e., the fully compressible framework and the low Mach number approximation, are presented in Chapter 2. The numerical methodology for the fully compressible framework, including the novel time integration scheme for reacting flows using stiff chemistry, is presented in Chapter 3. In Chapter 4, we investigate flame-acoustics interactions in laminar premixed flames for various fuels and flow conditions. In Chapter 5, we design a forcing scheme for compressible flows in simplified geometries, i.e. in configurations that lack natural turbulent kinetic energy injection from the large scale shear. Using the forcing technique presented in Chapter 5, we investigate subsonic, non-reacting, compressible homogeneous turbulence in Chapter 6. Chapter 7 deals with compressibility effects in turbulent premixed flames. Finally, Chapter 8 summarizes the findings.

C h a p t e r 2

GOVERNING EQUATIONS

2.1 Governing equations

In the present thesis, simulations are performed using both the low Mach number approximation and the fully compressible Navier-Stokes equations. In this section, we provide a brief overview of the two frameworks.

2.1.1 Fully compressible framework

We consider the fully compressible Navier-Stokes equations for unsteady, chemically-reacting flows. The continuity, momentum, energy, and species transport equations are given by

$$\frac{\partial \rho}{\partial t} + \nabla \cdot (\rho \boldsymbol{u}) = 0, \tag{2.1}$$

$$\frac{\partial \rho \boldsymbol{u}}{\partial t} + \nabla \cdot (\rho \boldsymbol{u} \otimes \boldsymbol{u}) = -\nabla p + \nabla \cdot \boldsymbol{\tau}, \tag{2.2}$$

$$\frac{\partial \rho e_t}{\partial t} + \nabla \cdot (\boldsymbol{u} (\rho e_t + p)) = -\nabla \cdot \boldsymbol{q} + \nabla \cdot (\boldsymbol{\tau} \cdot \boldsymbol{u}), \tag{2.3}$$

$$\frac{\partial \rho Y_s}{\partial t} + \nabla \cdot (\rho \boldsymbol{u} Y_s) = -\nabla \cdot \boldsymbol{j}_s + \rho \dot{\omega}_s, \qquad s = 1, ..., n_s, \tag{2.4}$$

where ρ is the density, $\boldsymbol{u}$ is the velocity vector, p is the pressure, n_s is the number of species transported, and Y_s, $\boldsymbol{j}_s$, $\dot{\omega}_s$ are the mass fraction, diffusion flux, and chemical source term of species s, respectively. The total energy

$$e_t = e + \frac{|\boldsymbol{u}|^2}{2}, \tag{2.5}$$

is the sum of the internal energy e and the kinetic energy. The viscous stress tensor is given by

$$\boldsymbol{\tau} = \mu(\nabla \boldsymbol{u} + (\nabla \boldsymbol{u})^T - 2/3(\nabla \cdot \boldsymbol{u})\boldsymbol{I}), \tag{2.6}$$

where μ is the molecular viscosity of the mixture, and Stoke's hypothesis is assumed to be valid, i.e., we neglect the contribution of bulk viscosity. While the effects of bulk viscosity may not be negligible in the presence of shocks [54], they are often

neglected in subsonic flows [55]. [1] The species diffusion flux is given by

$$\boldsymbol{j}_s = -\frac{\rho D_s}{W} \nabla (WY_s) + \rho Y_s \boldsymbol{u}_c , \tag{2.7}$$

where D_s are the species diffusivities, and

$$\boldsymbol{u}_c = \sum_{s=1}^{n_s} \frac{D_s}{W} \nabla (WY_s) , \tag{2.8}$$

is the correction velocity to ensure conservation of mass. The molecular weight of the mixture W is given by

$$W = \left(\sum_{s=1}^{n_s} \frac{Y_s}{W_s} \right)^{-1} , \tag{2.9}$$

where W_s is the molecular weight of species s. The heat diffusion flux is given by

$$\boldsymbol{q} = -\lambda \nabla T + \sum_{s=1}^{n_s} h_s \boldsymbol{j}_s , \tag{2.10}$$

where λ is the thermal conductivity of the mixture, T is the temperature, and h_s is the enthalpy of species s. The system of governing equations Eqs. (2.1) to (2.4) is closed with the ideal gas law

$$p = \frac{\rho R T}{W} , \tag{2.11}$$

where R is the universal gas constant. The internal energy e can be computed from the enthalpy $h = e + p/\rho$, which is given by

$$h = \sum_{s=1}^{n_s} Y_s h_s , \tag{2.12}$$

where

$$h_s = h_{s,ref} + \int_{T_{ref}}^{T} c_{p,s}(T) dT , \tag{2.13}$$

where $c_{p,s}$ is the species heat capacity at constant pressure, and $h_{s,ref}$ is the species reference enthalpy, i.e., the species enthalpy at T_{ref}.

2.1.2 Low Mach number approximation

The low Mach number approximation is widely used for the simulation of reacting flows [12, 14, 39, 40, 45, 46, 50, 56–64]. Since this thesis involves comparisons of results obtained using the fully compressible framework and the low Mach number approximation, we briefly summarize how the low Mach number approximation is obtained, to emphasize how the two frameworks are related.

---

[1]The effects of bulk viscosity are negligible because, at low Mach numbers, the dilatational component of the velocity field is orders of magnitude smaller than the solenoidal component.

2.1.2.1 Derivation

We follow the derivation by Majda & Sethian [65]. First, we perform the nondimensionalization of the flow variables, i.e., we set

$$
\rho^* = \frac{\rho}{\rho_r} \qquad \boldsymbol{u}^* = \frac{\boldsymbol{u}}{u_r} \qquad t^* = \frac{t}{L_r/u_r} \qquad x^* = \frac{x}{L_r} \qquad e^* = \frac{e}{p_r/\rho_r},
$$
$$
p^* = \frac{p}{p_r} \qquad \mu^* = \frac{\mu}{\mu_r} \qquad \lambda^* = \frac{\lambda}{\lambda_r}
$$

(2.14)

where the starred quantities are nondimensional, and $p_r, T_r, \rho_r, u_r, \mu_r, \lambda_r, L_r$ are the reference pressure, temperature, density, velocity, dynamic viscosity, thermal conductivity, and length scales, respectively, chosen such that the nondimensional quantities are $O(1)$ for any low reference Mach number

$$
M_r = \frac{u_r}{\sqrt{\gamma p_r/\rho_r}},
$$

(2.15)

where $\gamma = c_{p,r}/c_{v,r}$ is the heat capacity ratio, $c_{p,r}$ and $c_{v,r}$ being the reference specific heats at constant pressure and volume, respectively. We shall not consider the species transport equation since its low Mach number counterpart is the same as Eq. (2.4). Inserting the quantities defined in Eq. (2.14) into Eqs. (2.1) to (2.3), we obtain

$$
\frac{\partial \rho^*}{\partial t^*} + \nabla^* \cdot (\rho^* \boldsymbol{u}^*) = 0 ,
$$

(2.16)

$$
\frac{\partial \rho^* \boldsymbol{u}^*}{\partial t^*} + \nabla^* \cdot (\rho^* \boldsymbol{u}^* \otimes \boldsymbol{u}^*) = -\frac{1}{\gamma M_r^2} \nabla^* p^* + \frac{1}{Re_r} \nabla^* \cdot \boldsymbol{\tau}^* ,
$$

(2.17)

$$
\frac{\partial \rho^* e^*}{\partial t^*} + \gamma M_r^2 \frac{\partial \rho^* |\boldsymbol{u}^*|^2/2}{\partial t^*} + \nabla^* \cdot (\boldsymbol{u}^* (\rho^* e^* + p^*))
$$
$$
+ \gamma M_r^2 \nabla^* \cdot (\boldsymbol{u}^* \rho^* |\boldsymbol{u}^*|^2/2) = -\frac{\gamma}{\gamma - 1} \frac{1}{Re_r Pr_r} \nabla^* \cdot \boldsymbol{q}^* + \frac{\gamma M_r^2}{Re_r} \nabla^* \cdot (\boldsymbol{\tau}^* \cdot \boldsymbol{u}^*) ,
$$

(2.18)

where $Re_r = \rho_r u_r L_r/\mu_r$ and $Pr_r = \nu_r/\alpha_r$ are the reference Reynolds and Prandtl numbers, respectively, $\nu_r = \mu_r/\rho_r$ is the reference kinematic viscosity, and $\alpha_r = \lambda_r/(\rho_r c_{p,r})$ is the reference thermal diffusivity. Note that Eq. (2.15) inherently assumes that the reference pressure and density are representative of the thermodynamic state of the flow, i.e., $p^*, \rho^* = O(1)$. One can choose different reference quantities, e.g., for pressure [66], leading to a different set of non-dimensional equations. The different choices and implications for p_r are briefly reviewed in Appendix

A. In Eqs.(2.17) – (2.18), we note a dependence in γM_r^2. We now proceed to expand all flow variables in power series of $\epsilon \equiv \gamma M_r^2$, e.g.,

$$(\rho \boldsymbol{u})^* = (\rho \boldsymbol{u})_0^* + \epsilon (\rho \boldsymbol{u})_1^* + \epsilon^2 (\rho \boldsymbol{u})_2^* + O(M_r^3)\,, \tag{2.19}$$

$$\rho^* = \rho_0^* + \epsilon \rho_1^* + \epsilon^2 \rho_2^* + O(\epsilon^3)\,, \tag{2.20}$$

$$p^* = p_0^* + \epsilon p_1^* + \epsilon^2 p_2^* + O(\epsilon^3)\,, \tag{2.21}$$

$$e^* = e_0^* + \epsilon e_1^* + \epsilon^2 e_2^* + O(\epsilon^3)\,, \tag{2.22}$$

$$\boldsymbol{u}^* = \boldsymbol{u}_0^* + \epsilon \boldsymbol{u}_1^* + \epsilon^2 \boldsymbol{u}_2^* + O(\epsilon^3)\,, \tag{2.23}$$

etc. The product of Eq. (2.20) and (2.23) gives

$$\rho^* \boldsymbol{u}^* = \rho_0^* \boldsymbol{u}_0^* + \epsilon \left[\boldsymbol{u}_0^* \rho_1^* + \boldsymbol{u}_1^* \rho_0^* \right] + \epsilon^2 \left[\boldsymbol{u}_0^* \rho_2^* + \boldsymbol{u}_2^* \rho_0^* + \boldsymbol{u}_1^* \rho_1^* \right] + O(\epsilon^3)\,. \tag{2.24}$$

Since $\rho^* \boldsymbol{u}^* = (\rho \boldsymbol{u})^*$, we have from Eqs. (2.19) and (2.24) that

$$(\rho \boldsymbol{u})_0^* = \rho_0^* \boldsymbol{u}_0^*\,, \tag{2.25}$$

$$(\rho \boldsymbol{u})_1^* = \boldsymbol{u}_0^* \rho_1^* + \boldsymbol{u}_1^* \rho_0^*\,, \tag{2.26}$$

$$(\rho \boldsymbol{u})_2^* = \boldsymbol{u}_0^* \rho_2^* + \boldsymbol{u}_2^* \rho_0^* + \boldsymbol{u}_1^* \rho_1^*\,. \tag{2.27}$$

Continuity (Eq. (2.16)) becomes

$$\left[\frac{\partial \rho_0^*}{\partial t^*} + \nabla^* \cdot (\rho \boldsymbol{u})_0^* \right] + \epsilon \left[\frac{\partial \rho_1^*}{\partial t^*} + \nabla^* \cdot (\rho \boldsymbol{u})_1^* \right] + \epsilon^2 \left[\frac{\partial \rho_2^*}{\partial t^*} + \nabla^* \cdot (\rho \boldsymbol{u})_2^* \right] + O(\epsilon^3) = 0\,. \tag{2.28}$$

Since Eq. (2.28) is supposed to hold for arbitrary ϵ, the coefficients in the square brackets must vanish, i.e.,

$$\frac{\partial \rho_l^*}{\partial t^*} + \nabla^* \cdot (\rho \boldsymbol{u})_l^* = 0\,, \tag{2.29}$$

for $l = 0, 1, 2$. Specifically, the zeroth order continuity equation is given by

$$\frac{\partial \rho_0^*}{\partial t^*} + \nabla^* \cdot (\rho_0^* \boldsymbol{u}_0^*) = 0\,, \tag{2.30}$$

It should be noted that this expansion is singular owing to the pressure term being divided by $\epsilon \to 0$ in Eq. (2.17). Inserting Eqs. (2.19)–(2.23) in Eq. (2.17), we obtain the singular order

$$\nabla^* p_0^* = 0\,, \tag{2.31}$$

and zeroth order

$$\frac{\partial \rho_0^* \boldsymbol{u}_0^*}{\partial t^*} + \nabla^* \cdot (\rho_0^* \boldsymbol{u}_0^* \otimes \boldsymbol{u}_0^*) + \nabla^* p_1^* = \frac{1}{Re_r} \nabla^* \cdot \boldsymbol{\tau}_0^* , \qquad (2.32)$$

momentum equations. Following a similar procedure, the zeroth order energy equation is given by

$$\frac{\partial \rho_0^* e_0^*}{\partial t^*} + \nabla^* \cdot (\boldsymbol{u}_0^* (\rho_0^* e_0^* + p_0^*)) = -\frac{\gamma}{\gamma - 1} \frac{1}{Re_r Pr_r} \nabla^* \cdot \boldsymbol{q}_0^* . \qquad (2.33)$$

In dimensional form, the zeroth order continuity equation (Eq. (2.30)), zeroth order momentum equation (Eq. (2.32)), and zeroth order energy equation (Eq. (2.33)) are given by

$$\frac{\partial \rho}{\partial t} + \nabla \cdot (\rho \boldsymbol{u}) = 0 , \qquad (2.34)$$

$$\frac{\partial \rho \boldsymbol{u}}{\partial t} + \nabla \cdot (\rho \boldsymbol{u} \otimes \boldsymbol{u}) = -\nabla p_h + \nabla \cdot \boldsymbol{\tau} , \qquad (2.35)$$

$$\frac{\partial \rho e}{\partial t} + \nabla \cdot (\boldsymbol{u} (\rho e + p_t)) = -\nabla \cdot \boldsymbol{q} , \qquad (2.36)$$

where we have dropped the subscripts, except for pressure where we need to distinguish between the thermodynamic pressure ($p_t = p_0$), and the hydrodynamic pressure ($p_h = p_1$). This set of equation is closed with the zeroth order equation of state

$$p_t = \frac{\rho R T}{W} . \qquad (2.37)$$

In this work, we refer to Eqs. (2.34)–(2.37), i.e., the zeroth-order set of governing equations in the low Mach number expansion, as the low Mach number approximation, as it is commonly referred to in the literature, e.g., [40, 45, 46, 50, 56, 58–60, 62–64, 67–71]. It is also interchangeably referred to as the zero Mach number approximation [12, 14, 61, 65, 72, 73].

In the low Mach number simulations presented in this work, the energy equation is solved in its temperature form. To obtain it, we first rewrite Eq. (2.36) as

$$\rho \frac{\partial h}{\partial t} + \rho \boldsymbol{u} \cdot \nabla h = \frac{dp_t}{dt} - \nabla \cdot \boldsymbol{q} , \qquad (2.38)$$

where Eq. (2.34) has been used to write Eq. (2.38) in advection form. Differentiating Eq. (2.12), one obtains

$$dh = c_p dT + \sum_{s=1}^{n_s} h_s dY_s , \qquad (2.39)$$

where Eq. (2.13) has been used, along with the relation for the heat capacity at constant pressure of the mixture

$$c_p = \sum_{s=1}^{n_s} Y_i c_{p,s} \,. \tag{2.40}$$

Inserting Eq. (2.39) in Eq. (2.38), one obtains

$$
\rho c_p \frac{\partial T}{\partial t} + \rho c_p \boldsymbol{u} \cdot \nabla T = \frac{dp_t}{dt} + \nabla \cdot (\lambda \nabla T) - \sum_{s=1}^{n_s} c_{p,s} \boldsymbol{j}_s \cdot \nabla T
$$
$$
- \sum_{s=1}^{n_s} h_s \left[\rho \frac{\partial Y_i}{\partial t} + \rho \boldsymbol{u} \cdot \nabla Y_s + \nabla \cdot \boldsymbol{j}_s \right] . \tag{2.41}
$$

The term in the square brackets in Eq.(2.42) can be simplified using the species transport equation (Eq. (2.4)). One then obtains

$$
\rho c_p \frac{\partial T}{\partial t} + \rho c_p \boldsymbol{u} \cdot \nabla T = \frac{dp_t}{dt} + \nabla \cdot (\lambda \nabla T) - \sum_{s=1}^{n_s} c_{p,s} \boldsymbol{j}_s \cdot \nabla T - \sum_{s=1}^{n_s} h_s \rho \dot{\omega}_s \,. \tag{2.42}
$$

It is more convenient in the low Mach number approximation to solve the energy equation in temperature form (Eq. (2.42)) than solving Eq. (2.36). Hence, the full set of governing equations is given by Eqs. (2.34), (2.35), (2.42), (2.4), along with Eq. (2.37).

2.1.2.2 Incompressible limit

In this section, we seek to recover the incompressible limit, i.e., the necessary conditions under which the velocity field is divergence-free. Expanding Eq. (2.34), one obtains

$$\frac{D\rho}{Dt} = -\nabla \cdot \boldsymbol{u} = 0 \,, \tag{2.43}$$

where $D(\ )/Dt = \partial(\ )/\partial t + \boldsymbol{u} \cdot \nabla(\ )$ is the material derivative. Hence, if density is constant along a particle path, the flow is incompressible. Under the following conditions:

- Constant thermodynamic pressure p_t, such that the first term on the RHS of Eq. (2.42) vanishes;

- No conduction, such that the second term on the RHS of Eq. (2.42) is zero;

- No diffusion, such that the third term on the RHS of Eq. (2.42) and the first term on the RHS of Eq. (2.4) vanish;

- No chemical reaction, such that the fourth term on the RHS of Eq. (2.42) and the second term on the RHS of Eq. (2.4) are zero;

Eqs. (2.42) and (2.4) reduce to

$$\frac{DT}{Dt} = 0 \,, \tag{2.44}$$

and

$$\frac{DY_s}{Dt} = 0 \,, \qquad s = 1, ..., n_s \,, \tag{2.45}$$

which together with Eq. (2.37) yields

$$\frac{D\rho}{Dt} = \frac{\rho}{p_t} \frac{Dp_t}{Dt} - \sum_{s=1}^{n_s} \left(\frac{\rho W}{W_s} \frac{DY_s}{Dt} \right) - \frac{\rho}{T} \frac{DT}{Dt} = 0 \,. \tag{2.46}$$

Hence, the incompressible limit is recovered from the low Mach number approximation if there is no conduction, no diffusion, no chemical reaction, and the thermodynamic pressure is constant. In this limit, Eqs. (2.34) and (2.35) are self-contained, i.e., the energy equation and equation of state are unneeded.

2.1.2.3   Remarks

There are significant differences between the low Mach number approximation and the fully compressible framework. In the fully compressible formulation, there exists only a single pressure p. In the low Mach number approximation, there are two pressures: the (small) hydrodynamic pressure p_h, which appears in the momentum equation and ensures that continuity is observed, and the (large) thermodynamic pressure p_t, which appears in the energy equation and the equation of state and is spatially constant. This changes the character of the equations. Consider the compressible Euler equations for a single fluid, i.e., Eqs. (2.1)–(2.3) with $\boldsymbol{\tau} = 0$ and $\boldsymbol{q} = 0$. By taking the divergence of the momentum equation, one can get the following wave-like equation for pressure

$$\frac{\partial}{\partial t} \left(\frac{1}{\gamma p} \frac{Dp}{Dt} \right) = \nabla \cdot (\boldsymbol{u} \cdot \nabla \boldsymbol{u}) + \nabla \cdot \left(\frac{1}{\rho} \nabla p \right) \,, \tag{2.47}$$

where $D(\ )/Dt \equiv \partial(\ )/\partial t + \boldsymbol{u} \cdot \nabla(\ )$ is the material derivative. In the case of small perturbations with no mean flow, Eq. (2.47) simplifies to the wave equation

$$\frac{\partial^2 p'}{\partial t^2} = c^2 \nabla^2 p' , \tag{2.48}$$

where $p' \ll p$ is the fluctuating pressure, and $c = \sqrt{\gamma p / \rho}$ is the sound speed. Eq. (2.48) governs the transport of acoustic waves in a still medium. Now, consider the low Mach number number equations for a single fluid. For simplicity, we assume that the initial density field is uniform, i.e., $\rho(\boldsymbol{x}, t = 0) = \rho_0$, and that the conditions listed in Sec. 2.1.2.2 are satisfied, i.e., $\nabla \cdot \boldsymbol{u} = 0$. Taking the divergence of the momentum equation (Eq. (2.35)), one obtains

$$\nabla^2 p_h = -\rho_0 \nabla \cdot (\boldsymbol{u} \cdot \nabla \boldsymbol{u}) . \tag{2.49}$$

Equation (2.49) is the Poisson equation for pressure in the incompressible limit, which is elliptic. For the compressible case, Eq. (2.48) (and by extension Eq. (2.47)) has a hyperbolic character. If a disturbance is made in a compressible field, then not every point in space will feel the disturbance at once. Disturbances will travel at the sound speed in the case of Eq. (2.48). On the other hand, because of its elliptic character, disturbances made in a low Mach number field are felt at once essentially everywhere. One of the consequences is that acoustics are non-existent in this framework. The same goes for shocks, i.e., they require the governing equations to support the existence of acoustic waves, which is not the case in the low Mach number approximation. Another difference between the two frameworks is the existence of a viscous term in the compressible energy equation, which is not retained in the low Mach number approximation since it is $O(M^2)$. This mechanism accounts for the conversion of kinetic energy into internal energy due to viscous heating.

2.1.3 Chemical model

The species production rate in Eq. (2.4) is given by

$$\dot{\omega}_s = \frac{W_s}{\rho} \sum_{j=1}^{n_R} \nu_{j,s} \dot{R}_j , \tag{2.50}$$

where n_R is the number of reactions in the mechanism, and $\nu_{j,i}$ is the stoichiometric coefficient of the ith species in the jth reaction (negative for reactants and positive

for products). The reaction rate is given by a modified Arrhenius expression [74]

$$\dot{R}_j = A_j T^{n_j} \exp\left(-\frac{E_{a,j}}{RT}\right) \prod_{s=1}^{n_S} \left(\frac{\rho Y_s}{W_s}\right)^{\nu^r_{j,s}} ,$$
(2.51)

where A_j is the Arrhenius rate constant, $E_{a,j}$ is the activation energy, n_j is a constant, and $\nu^r_{j,i} \equiv -\min(\nu_{j,i}, 0)$.

C h a p t e r   3

NUMERICAL METHODOLOGY

[1]   Beardsell, G. and Blanquart, G., "A cost-effective semi-implicit method for the time integration of fully compressible reacting flows with stiff chemistry," *Journal of Computational Physics*, 2020. DOI: `https://doi.org/10.1016/j.jcp.2020.109479`,

In this chapter, the focus is on describing the compressible flow solver used in this work. This solver is based on the code developed by Boeck *et al.* [75], which is itself based on the low Mach number flow solver NGA [76]. Details about the original (low Mach) formulation can be found in Desjardins *et al.* [76], Savard *et al.* [77], and previous theses [44, 78, 79]. We propose a novel time integration scheme that 1) alleviates the stiffness introduced by detailed chemical mechanisms, and 2) is high-order for the non-reacting portions of the flow, e.g., for the transport of acoustic waves away from the flame [1]. This scheme, which blends the semi-implicit midpoint method for the species transport and the classical fourth-order Runge-Kutta scheme (RK4) for the transport of the other flow variables, is presented in Sec. 3.1. In Sec. 3.2, we describe the spatial discretization. Section 3.3 describes the conductivity, viscosity, diffusivity, and chemical kinetics models used in this work. In Sec. 3.4, we detail how the boundaries of the computational domain are treated when periodicity is precluded, e.g., in the direction perpendicular to a deflagration front. Specifically, we provide a description of the Navier-Stokes Characteristic Boundary Conditions (NSCBC). In Sec. 3.5, we apply the numerical framework to various test cases. Finally, in Sec. 3.6, the main findings are summarized.

3.1   Time integration

3.1.1   Motivation

When using explicit time integration schemes, the various physical processes at play impose a limit on the maximum stable time step that can be used. These processes include viscous diffusion, conduction, species diffusion, chemistry, convection, and acoustics. When detailed chemical models are employed, oftentimes the smallest timescales of the chemical system are smaller than the acoustic time scale. Also, especially when differential diffusion is present, the diffusive CFL for some of the

smaller species can be smaller than the acoustic CFL. In this thesis, we seek to develop a time integration scheme that is limited by the acoustic CFL only. We also considered going beyond, and perform an implicit correction for the acoustics. Appendix G presents the concept and preliminary work.

In Appendix C, we perform a stability analysis on the RK4 scheme and the iterative explicit midpoint method, which are the building blocks of the hybrid scheme presented in this section. From this analysis, we obtain estimates of the maximum time step for the convective/acoustic and viscous/diffusive terms. Note that we only consider uniform meshes, i.e., $\Delta x = \Delta y = \Delta z$, which are used throughout this thesis. For both the RK4 scheme and iterative explicit midpoint method with four sub-iterations, a necessary CFL condition for the acoustics is

$$\Delta t < \frac{\Delta x}{|\boldsymbol{u}| + c}.$$ (3.1)

Note that the acoustic CFL condition is always more stringent than the convective one, since acoustic waves travel at a speed $|\boldsymbol{u}| + c$, while convective waves travel at speed $|\boldsymbol{u}|$. For a three dimensional flow, the viscous CFL condition is

$$\Delta t < \frac{\Delta x^2}{12\nu},$$ (3.2)

and the diffusion CFL condition is

$$\Delta t < \frac{\Delta x^2}{12D_s}.$$ (3.3)

The maximum time step for the chemical source terms can be estimated from the chemical Jacobian. In Chapter 7, we perform DNS of two *n*-heptane/air turbulent flames using a 35 species detailed chemical model [6], which we refer to as Flame C* and Flame D*. The flow conditions for these flames are given in Table 3.1, and the associated maximum explicit time steps associated are listed in Table 3.2. It can be seen that for both flames, the viscous CFL condition is less restrictive than the one for the acoustics. However, the maximum stable explicit time steps associated with diffusion and chemistry are smaller than the one for the acoustics. Since we want to use time steps that are restricted by the acoustic CFL only, we therefore seek to treat these terms implicitly.

In Sec. 3.1.2, we first briefly describe the iterative explicit midpoint method. Then, in Sec. 3.1.3, we review the semi-implicit correction for the chemical source terms

Table 3.1: Flow conditions for the turbulent flame configurations.

	T_u [K]	p_0 [atm]	ϕ	Ka_u
Flame C*	800	1	0.9	300
Flame D*	800	1	0.9	1010

Table 3.2: Maximum explicit time steps associated with the different terms for the turbulent flame configurations.

	Acoustics	Viscous	Diffusion	Chemistry
Flame C*	$8 \cdot 10^{-9}$	$2 \cdot 10^{-8}$	$3 \cdot 10^{-9}$	$5 \cdot 10^{-10}$
Flame D*	$3 \cdot 10^{-9}$	$5 \cdot 10^{-9}$	$9 \cdot 10^{-10}$	$5 \cdot 10^{-10}$

proposed by Savard *et al.* [77]. In Sec. 3.1.4, we describe how to perform a semi-implicit correction for the diffusion terms. Finally, in Sec. 3.1.5. we describe the novel time integration method, in which the semi-implicit midpoint method is used to advance the species mass fractions in time, while the RK4 scheme is used for the integration of the other flow variables, i.e., mass, momentum, and energy.

3.1.2 Iterative explicit midpoint method

The iterative explicit midpoint scheme applied to Eq. (2.4) yields

$$(\rho Y)_{k+1}^{n+1} = (\rho Y)^n + \Delta t \left[C_k^* + D_k^* + \Omega_k^* \right] , \qquad s = 1, ..., n_s \qquad (3.4)$$

where C, D, and Ω are the discretized convection, diffusion, and chemical source terms, respectively. The superscripts refer to the timestep at which the quantities are evaluated, n being the current timestep, while starred quantities are evaluated at the half timestep, e.g., $\Omega_k^* = \Omega\left(Y_k^*\right)$, with $Y_k^* = \left(Y_k^{n+1} + Y^n\right)/2$. The subscripts refer to the sub-iteration number, k being the current sub-iteration.

3.1.3 Semi-implicit correction for the chemical source term

Chemistry being the most limiting phenomenon regarding the maximum stable timestep, we seek to perform an implicit correction on Ω, i.e., we want to compute Ω_{k+1}^* instead of Ω_k^* in Eq. (3.4). In practice, this can be done by evaluating

$$(\rho Y)_{k+1}^{n+1} = (\rho Y)^n +$$
$$\Delta t \left[C_k^* + D_k^* + \Omega_k^* + \frac{1}{2}\left(\frac{\partial \Omega}{\partial (\rho Y)}\right)_k^{n+1} \left((\rho Y)_{k+1}^{n+1} - (\rho Y)_k^{n+1}\right) \right] , \qquad (3.5)$$

where $(\partial\boldsymbol{\Omega}/\partial(\rho\boldsymbol{Y}))_k^{n+1}$ is the chemical Jacobian. We can rewrite Eq. (3.5) as

$$(\rho\boldsymbol{Y})_{k+1}^{n+1} = (\rho\boldsymbol{Y})_k^{n+1} - \left(\boldsymbol{I} - \frac{\Delta t}{2}\left(\frac{\partial\boldsymbol{\Omega}}{\partial\rho\boldsymbol{Y}}\right)_k^{n+1}\right)^{-1} \cdot \boldsymbol{\theta}_k = (\rho\boldsymbol{Y})_k^{n+1} - (\boldsymbol{J}_k)^{-1} \cdot \boldsymbol{\theta}_k , \quad (3.6)$$

where $\boldsymbol{J}_k$ acts as a preconditioner on the residual of Eq. (3.4) at the current sub-iteration

$$\boldsymbol{\theta}_k \equiv (\rho\boldsymbol{Y})_k^{n+1} - (\rho\boldsymbol{Y})^n - \Delta t \left[\boldsymbol{C}_k^* + \boldsymbol{D}_k^* + \boldsymbol{\Omega}_k^*\right] . \quad (3.7)$$

As discussed in more detail by Savard *et al.* [77], the choice of $\boldsymbol{J}_k$ is somewhat arbitrary and affects the convergence properties only, e.g., setting $\boldsymbol{J}_k = \boldsymbol{I}$ yields the iterative explicit method. One can compute $\boldsymbol{J}_k$ according to Eq.(3.6) [80], which yields a fully implicit formulation for the chemical source term. However, this can be computationally expensive, since the chemical Jacobian is a full matrix, and $\boldsymbol{J}_k$ needs to be computed and inverted at each sub-iteration. It is simpler and faster to use the idea proposed by Savard *et al.*[77], which is to approximate the chemical Jacobian by its diagonal, i.e., set

$$\boldsymbol{J}_k = \boldsymbol{I} + \frac{\Delta t}{2}\left(\frac{\dot{\omega}_s^-}{Y_s}\right)_k^{n+1} \equiv \boldsymbol{I} - \frac{\Delta t}{2}\boldsymbol{\Lambda}_k^{n+1} , \quad (3.8)$$

where $\dot{\omega}_s^-$ is the consumption rate of species s. The matrix $\boldsymbol{\Lambda}_k^{n+1}$ is a very good approximation of the diagonal of $[\partial\boldsymbol{\Omega}/\partial(\rho\boldsymbol{Y})]_k^{n+1}$ since the production rate of a species $\dot{\omega}_s^+$ is usually not a function of its own mass fraction, and $\dot{\omega}_s^-$ is usually linear in the species mass fraction, i.e.,

$$\frac{\partial\rho\dot{\omega}_s}{\partial(\rho Y)_s} = \frac{\partial\rho\dot{\omega}_s^+}{\partial(\rho Y)_s} - \frac{\partial\rho\dot{\omega}_s^-}{\partial(\rho Y)_s} \approx 0 - \frac{\dot{\omega}_s^-}{Y_s} . \quad (3.9)$$

Note that since one has to compute $\dot{\omega}_s^-$ to get Ω_s, this approach only amounts to one extra division applied to the residuals of the species transport equations. This approximation is expected to perform extremely well since the maximum timestep due to the acoustics is small, see Secs. 5.1 to 5.3 in [77].

3.1.4 Semi-implicit correction for the diffusion terms

We first review how to perform a semi-implicit correction on the diffusion term only, i.e., without a correction for the chemical source term. In Eq. (2.4), we want

to compute D^*_{k+1} instead of D^*_k. This is done by rewriting Eq. (2.4) as

$$(\rho Y)^{n+1}_{k+1} = (\rho Y)^n +$$

$$\Delta t \left[C^*_k + D^*_k + \Omega^*_k + \frac{1}{2} \left(\frac{\partial D}{\partial (\rho Y)} \right)^{n+1}_k \left((\rho Y)^{n+1}_{k+1} - (\rho Y)^{n+1}_k \right) \right], \tag{3.10}$$

where $\partial D / \partial (\rho Y)$ is the Jacobian matrix associated with the diffusion term. Similarly to what was done with the chemical source term in Sec. 3.1.3, we rewrite Eq. (3.10) as

$$(\rho Y)^{n+1}_{k+1} = (\rho Y)^{n+1}_k - (J_k)^{-1} \cdot \theta_k, \tag{3.11}$$

where

$$J_k = I - \frac{\Delta t}{2} \left(\frac{\partial D}{\partial \rho Y} \right)^{n+1}_k \tag{3.12}$$

acts as a preconditioner on the residual of Eq. (3.4) at the current sub-iteration

$$\theta_k \equiv (\rho Y)^{n+1}_k - (\rho Y)^n - \Delta t \left[C^*_k + D^*_k + \Omega^*_k \right]. \tag{3.13}$$

In multiple dimensions, inverting Eq. (3.12), which is required by Eq. (3.11), can be computationally expensive, despite the sparse nature of the linear system. We use the method of Approximate Factorization to convert the single, multi-dimensional problem into smaller, one-dimensional problems that can be solved efficiently using a tridiagonal solver. The Jacobian matrix associated with the diffusion term can be split exactly into directional transport operators F_x, F_y, F_z, leading to

$$J_k = I - \frac{\Delta t}{2} \left(F_x + F_y + F_z \right), \tag{3.14}$$

which we rewrite as

$$J_k = \left(I - \frac{\Delta t}{2} F_x \right) \left(I - \frac{\Delta t}{2} F_y \right) \left(I - \frac{\Delta t}{2} F_z \right) + O(\Delta t^2). \tag{3.15}$$

This procedure introduces a second-order temporal error term, which is the same order of accuracy as the midpoint method; hence, it does not negatively impact the order of accuracy of the scheme.

When both the semi-implicit correction for the chemical source term and the diffusion term are desired, we again use the method of Approximate Factorization to convert the preconditioner

$$J_k = I - \frac{\Delta t}{2} \left(\Lambda^{n+1}_k + F_x + F_y + F_z \right), \tag{3.16}$$

into the product of three tridiagonal matrices and one diagonal matrix, i.e.,

$$J_k = \left(I - \frac{\Delta t}{2}\Lambda_k^{n+1}\right)\left(I - \frac{\Delta t}{2}F_x\right)\left(I - \frac{\Delta t}{2}F_y\right)\left(I - \frac{\Delta t}{2}F_z\right) + O(\Delta t^2). \qquad (3.17)$$

3.1.5 Embedding of the semi-implicit midpoint method with the RK4 scheme

The RK4 scheme requires the evaluation of the time derivative at the half timestep (2nd and 3rd stages) and at the full timestep (4th stage). The iterative midpoint method yields both, hence we can embed the midpoint method within the RK4 scheme in a straightforward manner.

Equations (2.1) to (2.4) are rewritten as

$$\frac{\partial}{\partial t}\begin{bmatrix} Q \\ (\rho Y) \end{bmatrix} = \begin{bmatrix} f_Q \\ f_Y \end{bmatrix}, \qquad (3.18)$$

where $Q = [\rho, (\rho u), (\rho e_t)]^T$. The proposed method is detailed in Table 3.3, and is completed with $Q^{n+1} = Q^n + k_1/6 + k_2/3 + k_3/3 + k_4/6$, and $(\rho Y)^{n+1} = (\rho Y)_4^{n+1}$. In the absence of semi-implicit correction, the first three iterations of the iterative explicit midpoint method and the first three stages of the RK4 scheme are mathematically identical, which is what makes the embedding simple. Note that we still solve for the flow variables Q with the RK4 scheme.

As part of the evaluation of f, Y is obtained as $Y = (\rho Y)/\sum_{s=1}^{n_s}(\rho Y)_s$. This specification is important since discretely $\rho \neq \sum_{s=1}^{n_s}(\rho Y)_s$, as a result of using different time integrators for continuity and the species transport equations. The discrepancy between ρ and $\sum_{s=1}^{n_s}(\rho Y)_s$ is quantified in Sec. 3.5.1. Finally, in the absence of mixing and/or chemistry, this approach reverts to the RK4 scheme and is hence 4th order. This property is verified in Sec. 3.5.1.2.

3.2 Spatial discretization

3.2.1 Description

The compressible and low Mach number solvers used in this work share a lot in common, especially regarding the spatial discretization. We briefly review the discretization and point out the similarities between the low Mach and fully compressible discretizations. The reader is referred to Ref. [76] for more details.

To improve the accuracy of the divergence term in the continuity and species transport equations, the computational grid is staggered in space, i.e., the scalars are

Table 3.3: Proposed time integration scheme blending the semi-implicit midpoint method for the species transport, and the RK4 scheme for the transport of the other flow variables (ρ, (ρu), and (ρe_t)).

Step	Function evaluation	Flow (RK4)	Species (semi-implicit midpoint)
1	$f^n = f\left(Q^n, (\rho Y)^n\right)$	$k_1 = \Delta t f_Q^n$	$(\rho Y)_1^* = (\rho Y)^n + \left(I + (\Delta t/2)\,(\dot\omega^-/Y)^n\right)^{-1}(\Delta t/2)\,f_Y^n$
2	$f^{(1)} = f\left(Q^n + k_1/2, (\rho Y)_1^*\right)$	$k_2 = \Delta t f_Q^{(1)}$	$(\rho Y)_2^* = (\rho Y)_1^* +$ $\left(I + (\Delta t/2)\,(\dot\omega^-/Y)_1^*\right)^{-1}\left((\rho Y)^n - (\rho Y)_1^* + (\Delta t/2)\,f_Y^{(1)}\right)$
3	$f^{(2)} = f\left(Q^n + k_2/2, (\rho Y)_2^*\right)$	$k_3 = \Delta t f_Q^{(2)}$	$(\rho Y)_3^{n+1} = 2\,(\rho Y)_2^* - (\rho Y)^n +$ $\left(I + (\Delta t/2)\,(\dot\omega^-/Y)_2^*\right)^{-1}\left(2\left[(\rho Y)^n - (\rho Y)_2^*\right] + \Delta t f_Y^{(2)}\right)$
4	$f^{(3)} = f\left(Q^n + k_3, (\rho Y)_3^{n+1}\right)$	$k_4 = \Delta t f_Q^{(3)}$	$(\rho Y)_4^{n+1} = (\rho Y)_3^{n+1} + \left(I + (\Delta t/4)\left((\dot\omega^-/Y)^n + (\dot\omega^-/Y)_3^{n+1}\right)\right)^{-1}$ $\left((\rho Y)^n - (\rho Y)_3^{n+1} + (\Delta t/2)\left(f_Y^n + f_Y^{(3)}\right)\right)$
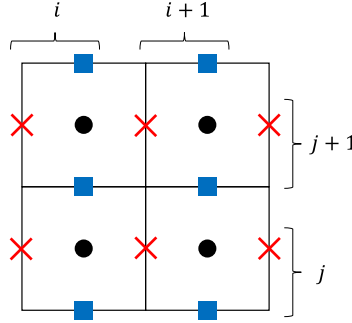
Figure 3.1: Staggered grid arrangement in 2D. The scalars are stored at the cell centers (black circles), the x-momentum on the vertical edges (red crosses), and the y-momentum on the horizontal edges (blue squares).

stored at the cell centers, while momentum is stored at the cell faces. This arrangement is depicted in Figure 3.1 for a two-dimensional uniform Cartesian mesh. We use second-order accurate interpolation and differentiation stencils. In the x_1 direction, they are given by

$$
\begin{aligned}
\overline{\psi}^{x_1} &= \frac{\psi(x_1 + \Delta x_1/2, x_2, x_3) + \psi(x_1 - \Delta x_1/2, x_2, x_3)}{2}, \\
\frac{\delta \psi}{\delta x_1} &= \frac{\psi(x_1 + \Delta x_1/2, x_2, x_3) - \psi(x_1 - \Delta x_1/2, x_2, x_3)}{\Delta x_1},
\end{aligned}
\tag{3.19}
$$

and are similarly defined in the x_2 and x_3 directions. Defining $g_i = (\rho u)_i$, the semi-discrete continuity equation is identical to its low Mach counterpart and is given by

$$
\frac{\partial \rho}{\partial t} + \sum_{i=1}^{3} \frac{\delta g_i}{\delta x_i} = 0.
\tag{3.20}
$$

The treatment of the momentum equation is identical to the one given in Desjardins *et al.*[76], i.e.,

$$
\frac{\partial g_i}{\partial t} + \sum_{j=1}^{3} \frac{\delta \left(\overline{g_j}^{x_i} \overline{u_i}^{x_j} \right)}{\delta x_j} + \frac{\delta p}{\delta x_i} = \sum_{j=1}^{3} \frac{\delta \tau_{ij}}{\delta x_j},
\tag{3.21}
$$

where

$$
\tau_{ij} = \overline{\mu}^{x_i x_j} \left(\frac{\delta u_i}{\delta x_j} + \frac{\delta u_j}{\delta x_i} - \delta_{ij} \frac{2}{3} \sum_{k=1}^{3} \frac{\delta u_k}{\delta x_k} \right).
\tag{3.22}
$$

In Eq. (3.22), δ_{ij} is the Kronecker delta, not to be confused with the differentiation operator $\delta(\ )/\delta x_i$. Unnecessary interpolations are avoided, e.g., $\overline{\mu}^{x_i x_j}$ is simply μ for $i = j$ in Eq. (3.22).

The third-order Bounded QUICK scheme [81] (BQUICK) is used for the convective term in the species transport equations. A bounded scheme such as BQUICK is ideally suited for the species transport since the physical bounds for the species mass fractions are obvious, i.e., $0 \leq Y_s \leq 1$. For the energy equation, the convective term is discretized using central differences. The full details of the discretization of the species transport and energy equations are given in Appendix B. Here, we focus on the discretization of the viscous transport term in Eq. (2.3).

Analytically, the viscous term in the total energy equation can be written as

$$\nabla \cdot (\boldsymbol{\tau} \cdot \boldsymbol{u}) = \boldsymbol{u} \cdot (\nabla \cdot \boldsymbol{\tau}) + \nabla \boldsymbol{u} : \boldsymbol{\tau}, \qquad (3.23)$$

where $\boldsymbol{u} \cdot (\nabla \cdot \boldsymbol{\tau})$ is the viscous term in the kinetic energy equation, and $\epsilon = \nabla \boldsymbol{u} : \boldsymbol{\tau}$ is the viscous term in the internal energy equation (viscous dissipation). We want Eq. (3.23) to be verified discretely. First, we consider the discrete form of $\boldsymbol{u} \cdot (\nabla \cdot \boldsymbol{\tau})$. Dotting Eq. (3.21) with $\boldsymbol{u}$, it is defined unambiguously as

$$\widetilde{\boldsymbol{u} \cdot (\nabla \cdot \boldsymbol{\tau})} = \sum_{i=1}^{3} u_i \overline{\sum_{j=1}^{3} \frac{\delta \tau_{ij}}{\delta x_j}}^{x_i}, \qquad (3.24)$$

where τ_{ij} is computed using Eq. (3.22) and the tilde $\widetilde{(\ )}$ denotes a discretized quantity. The interpolation $\overline{(\ )}^{x_i}$ in Eq. (3.24) brings the quantities from the cell faces to the cell center, where the summation over i is performed. To illustrate this in 2D, Fig. 3.2 shows where the quantities in Eq. (3.24) are located on the grid, for $\overline{u \delta \tau_{xx} / \delta x}^{x}$ (Fig. 3.2a), and $\overline{u \delta \tau_{xy} / \delta y}^{x}$ (Fig. 3.2b). Second, we look at the discrete form of the viscous term in the internal energy equation, i.e, the dissipation rate $\epsilon = \nabla \boldsymbol{u} : \boldsymbol{\tau}$. Performing products of quantities before interpolating them, the discrete form of ϵ can be written as

$$\widetilde{\nabla \boldsymbol{u} : \boldsymbol{\tau}} = \sum_{i=1}^{3} \sum_{j=1}^{3} \left(\delta_{ij} \tau_{ij} \frac{\delta u_i}{\delta x_j} + (1 - \delta_{ij}) \tau_{ij} \overline{\frac{\delta u_i}{\delta x_j}}^{x_i x_j} \right). \qquad (3.25)$$

Figure 3.3 shows where the quantities are located in 2D for $\tau_{xx} \delta u / \delta x$ (Fig. 3.3a), and $\overline{\tau_{xy} \delta u / \delta y}^{x y}$ (Fig. 3.3b).

Now, we seek to derive what should be the discrete form of the viscous term in the total energy equation $\widetilde{\nabla \cdot (\boldsymbol{\tau} \cdot \boldsymbol{u})}$, such that

$$\widetilde{\nabla \cdot (\boldsymbol{\tau} \cdot \boldsymbol{u})} = \sum_{i=1}^{3} u_i \overline{\sum_{j=1}^{3} \frac{\delta \tau_{ij}}{\delta x_j}}^{x_i} + \sum_{i=1}^{3} \sum_{j=1}^{3} \left(\delta_{ij} \tau_{ij} \frac{\delta u_i}{\delta x_j} + (1 - \delta_{ij}) \tau_{ij} \overline{\frac{\delta u_i}{\delta x_j}}^{x_i x_j} \right). \qquad (3.26)$$

(a) $\overline{u\delta\tau_{xx}/\delta x}^x$ (b) $\overline{u\delta\tau_{xy}/\delta y}^x$
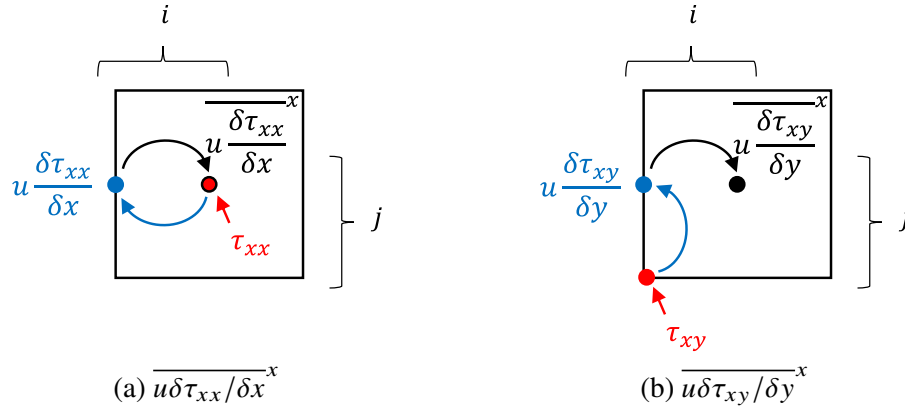
Figure 3.2: Discretization of the viscous term in the kinetic energy equation.

(a) $\tau_{xx}\delta u/\delta x$ (b) $\overline{\overline{\tau_{xy}\delta u/\delta y}^x}^y$
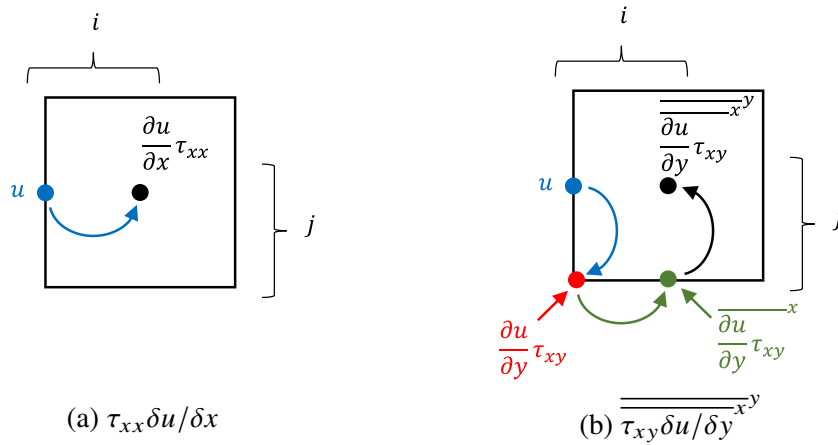
Figure 3.3: Discretization of the viscous term in the internal energy equation (dissipation rate).

We start by expanding Eq. (3.26) for $i = 1$, $j = 2$:

$$\widetilde{\frac{\partial(\tau_{xy}u)}{\partial y}} = u\overline{\frac{\delta\tau_{xy}}{\delta y}}^x + \tau_{xy}\overline{\overline{\frac{\delta u}{\delta y}}^x}^y$$

$$= \frac{1}{2\Delta x}\left(u_{m,n}(\tau_{xy,m,n+1} - \tau_{xy,m,n}) + u_{m+1,n}(\tau_{xy,m+1,n+1} - \tau_{xy,m+1,n})\right)$$

$$+ \frac{1}{4\Delta x}\left(\tau_{xy,m,n}(u_{m,n} - u_{m,n-1}) + \tau_{xy,m+1,n}(u_{m+1,n} - u_{m+1,n-1})\right) \qquad (3.27)$$

$$+ \frac{1}{4\Delta x}\left(\tau_{xy,m,n+1}(u_{m,n+1} - u_{m,n}) + \tau_{xy,m+1,n+1}(u_{m+1,n+1} - u_{m+1,n})\right)$$

$$= \frac{\delta}{\delta y}\left(\overline{\tau_{xy}\overline{u}^y}^x\right) .$$

Hence, generally, for the off-diagonal terms, we have

$$
u_i \overline{\frac{\delta \tau_{ij}}{\delta x_j}}^{x_i} + \tau_{ij} \overline{\frac{\delta u_i}{\delta x_j}}^{\overline{x_i}^{x_j}} = \frac{\delta}{\delta x_j} \left(\overline{\tau_{ij} \overline{u_i}^{x_j}}^{x_i} \right) .
\tag{3.28}
$$

We now consider the diagonal terms. We expand Eq. (3.26) for $i = 1$, $j = 1$:

$$
\begin{aligned}
\widetilde{\frac{\partial (\tau_{xx} u)}{\partial x}} &= u \overline{\frac{\delta \tau_{xx}}{\delta x}}^{x} + \tau_{xx} \frac{\delta u}{\delta x} \\
&= \frac{1}{2\Delta x} \left(u_{m,n} (\tau_{xx,m,n} - \tau_{xx,m-1,n}) + u_{m+1,n} (\tau_{xx,m+1,n} - \tau_{xx,m,n}) \right) \\
&\quad + \frac{1}{\Delta x} \left(\tau_{xx,m,n} (u_{m+1,n} - u_{m,n}) \right) \\
&= \frac{\delta}{\delta x} \left(u \overline{\tau_{xx}}^{x} \right) .
\end{aligned}
\tag{3.29}
$$

Hence, generally, for the diagonal terms, we have

$$
u_i \overline{\frac{\delta \tau_{ii}}{\delta x_i}}^{x_i} + \tau_{ii} \frac{\delta u_i}{\delta x_i} = \frac{\delta}{\delta x_i} \left(u_i \overline{\tau_{ii}}^{x_i} \right) .
\tag{3.30}
$$

It follows that the discrete form of the viscous term in the total energy should be

$$
\widetilde{\nabla \cdot (\tau \cdot u)} = \sum_{i=1}^{3} \sum_{j=1}^{3} \left(\delta_{ij} \frac{\delta}{\delta x_j} \left(u_i \overline{\tau_{ij}}^{x_i} \right) + (1 - \delta_{ij}) \frac{\delta}{\delta x_j} \left(\overline{\tau_{ij} \overline{u_i}^{x_j}}^{x_i} \right) \right) ,
\tag{3.31}
$$

which is the form that we implement in the solver.

3.2.2 Evaluation of primitive variables

The governing equations are in conservative form, i.e., we advance ρ, (ρu), (ρY), and (ρe_t) in time. However, many terms in Eqs. (2.1)–Eqs. (2.4) require the knowledge of the primitive variables u, T, p, and Y_s. At each sub-iteration, these quantities must therefore be computed. The velocities are computed as

$$
u_i = \frac{g_i}{\overline{\rho}^{x_i}} .
\tag{3.32}
$$

The species mass fractions are computed as

$$
Y_s = \frac{(\rho Y)_s}{\sum_{k=1}^{n_s} (\rho Y)_k} .
\tag{3.33}
$$

This ensures that $\sum_k^{n_s} Y_k = 1$. Temperature T is not known explicitly, and an implicit equation is solved using Newton's method

$$T_{m+1} = T_m + \left(\frac{\rho R T_m}{W} - \left(\rho \sum_{s=1}^{n_s} h_s(T_m) Y_s - \rho e_t + \frac{1}{2} \rho |\mathbf{u}|^2 \right) \right) \Big/ \left(\rho \sum_{s=1}^{n_s} c_{v,s}(T_m) Y_s \right),$$

(3.34)

where h_s and $c_{v,s}$ are the species enthalpies and heat capacities at constant volume, respectively, and m is the iteration number. Equation (3.34) is solved until the desired convergence is achieved (close to machine precision), and T_1 is taken to be the converged temperature at the previous sub-iteration/timestep. Pressure p is then obtained via the ideal gas law. The term $\rho |\mathbf{u}|^2$ in Eq. (3.34) is computed as $\sum_{i=1}^{3} \overline{g_i u_i}^{x_i}$ to be consistent with the low Mach formulation (see Eq. 22 in Ref. [76]).

3.3 Chemistry

3.3.1 Conductivity and viscosity models

The mixture thermal conductivity is computed as [82]

$$\lambda = \frac{1}{2} \left(\sum_{s=1}^{n_s} X_s \lambda_s + \left[\sum_{s=1}^{n_s} \frac{X_s}{\lambda_s} \right]^{-1} \right),$$

(3.35)

where X_s are the species mole fractions, and the species thermal conductivities λ_s are calculated using a modified version of Eucken's formula [83]. The mixture viscosity is obtained using the same form [40], i.e.,

$$\mu = \frac{1}{2} \left(\sum_{s=1}^{n_s} X_s \mu_s + \left[\sum_{s=1}^{n_s} \frac{X_s}{\mu_s} \right]^{-1} \right),$$

(3.36)

where the species viscosities μ_s are obtained using traditional kinetic theory [84].

3.3.2 Species diffusivity models

For the one-dimensional simulations presented in Chapter 4, a mixture-averaged formulation is used for the species diffusivities [7]. We also considered using multi-component diffusion, which is more precise than the mixture-averaged formulation, but it was found that the improvements were marginal [85]. To reduce the computational cost for the turbulent flame simulations presented in Chapter 7, we use constant non-unity Lewis numbers. The Lewis numbers are extracted from one-dimensional simulations using a mixture-averaged formulation. For each species, we extract the Lewis number at the location where the species mass fraction is maximum. It was

Table 3.4: Detailed chemical mechanisms used in the present work.

Mechanism	Fuel(s)	# species	# reactions
#1	CH_4	52	634
#2	H_2	9	54
#3	$n - C_7H_{16}$ / $n - C_{12}H_{26}$	107	1205
#4	C_7H_{16}	35	217
#5	C_7H_{16}	180	2168

shown by Burali *et al.* [86] and Savard [44] that, in turbulent *n*-heptane/air flames, differences in chemical source terms and species profiles are negligible whether the mixture-averaged model or the constant non-unity Lewis number approximation is used.

3.3.3 Chemical kinetics

In this work, different detailed chemical mechanisms are employed. These mechanisms contain a set of chemical reactions, along with the parameters required to evaluate the Arrhenius expressions described in Sec. 2.1.3. They also contain the thermodynamic data required to compute the species enthalpies h_s and heat capacities $c_{p,s}$. In Table 3.4, we provide the number of species and reactions for each chemical mechanism, along with the fuel(s) we use them for. Mechanism #1 is the well-established GRI-Mech 3.0 mechanism [87], which includes 52 species and 634 reactions. Mechanism #1 is used for the combustion of methane and air. Mechanism #2 is the 9 species, 54 reactions mechanism by Hong *et al.* [88], for which some of the rate constants have recently been updated [89, 90]. We use Mechanism #2 for the combustion of hydrogen and air. Mechanism #3 is CaltechMech 2.4 [91] , from which the aromatic species have been removed, which is justified by the slightly lean condition considered. We use Mechanism #3 for the combustion of *n*-heptane/air, as well as *n*-dodecane/air. It contains 107 species and 1205 reactions. Mechanism #4 is the reduced mechanism employed by Bisetti et al. [6], which we use for the combustion of *n*-heptane and air. In Mechanism #4, the aromatic species have also been removed, which yields a total of 35 species and 217 reactions. Finally, Mechanism #5 is JetSurF version 2.0 [92], from which the aromatic species and the molecules containing more than 7 carbon atoms have also been removed, again justified by the slightly lean conditions considered. Mechanism #5 contains 180 species and 2168 reactions, and we use it for the combustion of *n*-heptane and air.

A note on JetSurF version 2.0

The inverses of the eigenvalues of the chemical Jacobian $\tau_{\text{Jac, full}}$ correspond to the different chemical timescales of the system [77]. They are plotted in Fig. 3.4 for Mechanisms #4 and #5. The chemical Jacobians are evaluated in a one-dimensional premixed *n*-heptane/air flame at an equivalence ratio $\phi = 0.9$ and at standard conditions, at the location of maximum heat release. The species associated with each eigenvalue can be determined using the approximation of the diagonal of the chemical Jacobian detailed in Sec. 3.1. As shown in Fig. 3.4a, the two smallest timescales for Mechanism #4 are $O(10^{-9}s)$ and are associated with the pentyl and heptyl radicals. For Mechanism #5, the smallest timescale is $O(10^{-14}s)$ and is also associated with a pentyl radical. However, it is smaller than for Mechanism #4 by six orders of magnitude. After careful inspection of the thermodynamic properties of $2-C_5H_{11}$ (2-pentyl), we found out that its enthalpy of formation was erroneous. More precisely, it is about $115 kJ/mol$ higher than for 1-pentyl radicals, whereas the values for 2-alkyl radicals are commonly lower than for 1-alkyl radicals by about $10 kJ/mol$ [93].

A new chemical Jacobian was computed, using the thermodynamic properties of $3-C_5H_{11}$ instead of the original ones for $2-C_5H_{11}$. For this new chemical Jacobian, the timescale associated with $2-C_5H_{11}$ is significantly larger, and closer to the other pentyl radicals. It is is shown by the red dot in Fig. 3.4b. It is possible that JetSurF version 2.0 suffers from other issues that artificially increase its stiffness. However, one of the goals of this thesis is to show that the time integration scheme proposed in Sec. 3.1 can handle very stiff mechanisms well. That is why the unmodified JetSurF mechanism will be used for all simulations.

(a) Mechanism #4 (b) Mechanism #5
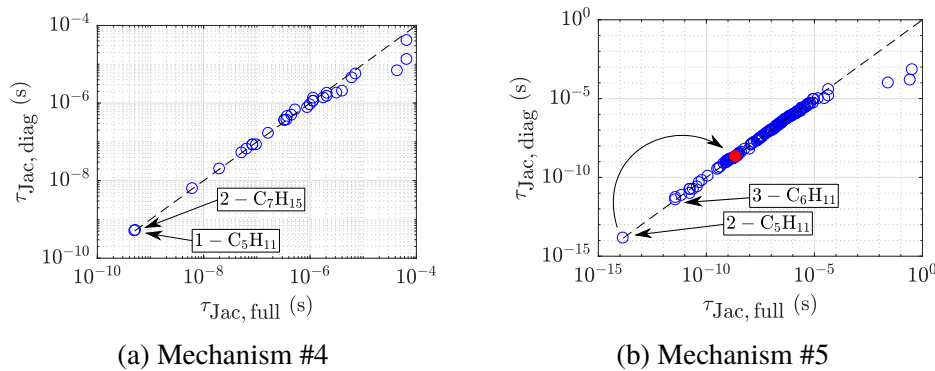
Figure 3.4: Comparison of the timescales for the full chemical Jacobian $\tau_{\text{Jac, full}}$ and its diagonal approximation $\tau_{\text{Jac, diag}}$.

3.4 Boundary conditions

In this section, we discuss how the boundaries are treated for flow configurations that are non-periodic in one direction.

3.4.1 Grid arrangement

The spatial arrangement at the inlet and outlet is the same for the low Mach number approximation and the fully compressible framework. The inlet spatial arrangement is shown in Fig. 3.5. In the $i = i_{min+1}$ cells, the second cells in x from the inflow, we have the regular grid arrangement detailed in Sec. 3.2. At i_{min}, the first cell of the computational grid, we have, in addition to the regular grid arrangement, the scalars at $i = i_{min-1}$ at the cell faces in x, and the y and z momentum at $i = i_{min-1}$ at the cell edges. The *inlet* quantities are the x momentum at $i = i_{min}$, the y and z momentum at $i = i_{min-1}$, and the scalars at $i = i_{min-1}$. The inlet quantities are thus all on the same plane, and are either imposed (Dirichlet boundary conditions), or treated with the Navier-Stokes Characteristics Boundary Conditions (NSCBC), detailed in Sec.3.4.2. The outlet grid arrangement is depicted in Fig. 3.6. At $i = i_{max}$, we have
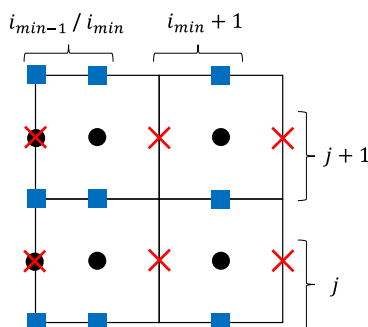
Figure 3.5: 2D grid arrangement at the inlet for configurations that are non-periodic in the x direction. The scalar locations are denoted by black circles, the x-momentum by red crosses, and the y-momentum by blue squares.

the regular staggered grid arrangement described in Sec. 3.2. The *outlet* quantities are the flow quantities at $i = i_{max+1}$, which all lie on the same plane. At the outlet, we either use Neumann boundary conditions or the NSCBC.

3.4.2 Navier-Stokes Characteristics Boundary Conditions

When simulating compressible flows, setting Dirichlet or Neumann boundary conditions yields reflecting boundaries for acoustic waves. This is often undesired, as one may want the acoustic waves generated inside the domain to be allowed to leave at the boundaries. To achieve this behavior, a widely-used set of boundary condi-
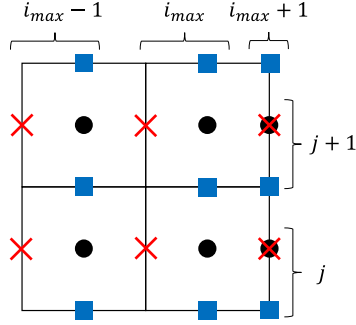
Figure 3.6: 2D grid arrangement at the outlet for configurations that are non-periodic in the x direction. The scalar locations are denoted by black circles, the x-momentum by red crosses, and the y-momentum by blue squares.

tions is the so-called Navier-Stokes Characteristics Boundary Conditions (NSCBC). Here, we shall consider that the non-homogeneous boundaries are planar and in the x-direction. Following Poinsot & Lele [94], one can use the characteristic analysis [95] to rewrite the hyperbolic terms corresponding to waves propagating in the x direction in Eqs. (2.1) – (2.3), i.e.,

$$\frac{\partial \rho}{\partial t} + d_1 + \frac{\partial (\rho v)}{\partial y} + \frac{\partial (\rho w)}{\partial z} = 0 , \tag{3.37}$$

$$\frac{\partial (\rho u)}{\partial t} + u d_1 + \rho d_3 + \frac{\partial (\rho u v)}{\partial y} + \frac{\partial (\rho u w)}{\partial z} = (\nabla \cdot \boldsymbol{\tau}) \cdot \boldsymbol{e}_x , \tag{3.38}$$

$$\frac{\partial (\rho v)}{\partial t} + v d_1 + \rho d_4 + \frac{\partial (\rho v^2)}{\partial y} + \frac{\partial (\rho v w)}{\partial z} + \frac{\partial p}{\partial y} = (\nabla \cdot \boldsymbol{\tau}) \cdot \boldsymbol{e}_y , \tag{3.39}$$

$$\frac{\partial (\rho w)}{\partial t} + w d_1 + \rho d_5 + \frac{\partial (\rho v w)}{\partial y} + \frac{\partial (\rho w^2)}{\partial z} + \frac{\partial p}{\partial z} = (\nabla \cdot \boldsymbol{\tau}) \cdot \boldsymbol{e}_z , \tag{3.40}$$

$$\frac{\partial (\rho e_t)}{\partial t} + (e_t - c_v T) \, d_1 + \frac{d_2}{\gamma - 1} + (\rho u) d_3 + (\rho v) d_4 + (\rho w) d_5$$
$$+ \frac{\partial v (\rho e_t + p)}{\partial y} + \frac{\partial w (\rho e_t + p)}{\partial z} = -\nabla \cdot \boldsymbol{q} + \nabla \cdot (\boldsymbol{\tau} \cdot \boldsymbol{u}) , \tag{3.41}$$

where

$$d_1 = \frac{\partial(\rho u)}{\partial x} = \mathcal{L}_2 + \frac{\mathcal{L}_1 + \mathcal{L}_5}{c^2}, \tag{3.42}$$

$$d_2 = u\frac{\partial p}{\partial x} + \rho c^2\frac{\partial u}{\partial x} = \mathcal{L}_1 + \mathcal{L}_5, \tag{3.43}$$

$$d_3 = u\frac{\partial u}{\partial x} + \frac{1}{\rho}\frac{\partial p}{\partial x} = \frac{\mathcal{L}_5 - \mathcal{L}_1}{\rho c}, \tag{3.44}$$

$$d_4 = u\frac{\partial v}{\partial x} = \mathcal{L}_3, \tag{3.45}$$

$$d_5 = u\frac{\partial w}{\partial x} = \mathcal{L}_4. \tag{3.46}$$

Finally, the amplitude variations for the characteristic waves are given by

$$\mathcal{L}_1 = \left(\frac{u - c}{2}\right)\left(\frac{\partial p}{\partial x} - \rho c\frac{\partial u}{\partial x}\right), \tag{3.47}$$

$$\mathcal{L}_2 = \frac{u}{c^2}\left(c^2\frac{\partial \rho}{\partial x} - \frac{\partial p}{\partial x}\right), \tag{3.48}$$

$$\mathcal{L}_3 = u\frac{\partial v}{\partial x}, \tag{3.49}$$

$$\mathcal{L}_4 = u\frac{\partial w}{\partial x}, \tag{3.50}$$

$$\mathcal{L}_5 = \left(\frac{u + c}{2}\right)\left(\frac{\partial p}{\partial x} + \rho c\frac{\partial u}{\partial x}\right). \tag{3.51}$$

In Poinsot & Lele [94], the d_1 term in Eq. (3.41) is multiplied by $|u|^2/2$. For flows with non-constant heat capacity, the d_1 term needs to be multiplied by $(e_t - c_v T)$ [96]. A schematic of the directions of the characteristic waves at the outlet is shown in Fig. 3.7. The directions of the waves are the same at the inlet.

Assuming that $u < c$ at the inlet, the amplitude variation for the characteristic wave $\mathcal{L}_1$ can be computed from the interior points. To do so, we use second-order frontward differentiation stencils. Taking into account the grid staggering, $\mathcal{L}_1$ can
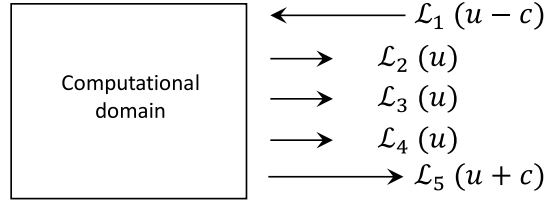
Figure 3.7: Schematic of the direction of the waves associated with the characteristic waves at the outlet.

be evaluated by computing

$$
\begin{aligned}
\left.\frac{\partial u}{\partial x}\right|_{i=imin} &= \frac{1}{2\Delta x}\left(-u_{min+2} + 4u_{imin+1} - +3u_{imin}\right), \\
\left.\frac{\partial p}{\partial x}\right|_{i=imin-1} &= \frac{1}{3\Delta x}\left(-p_{imin+1} + 9p_{imin} - 8p_{imin-1}\right).
\end{aligned}
\tag{3.52}
$$

We shall consider that $u > 0$ at the inlet, in which case $\mathcal{L}_1, \mathcal{L}_2, \mathcal{L}_3$, and $\mathcal{L}_4$ are incoming waves whose amplitude is unknown *a priori*. Their amplitude can be modulated to impose soft boundary conditions. Following Yoo & Im [97], we set

$$
\mathcal{L}_2 = \eta_2 \frac{\rho R}{2WcL_x}(T - T_{in}),
\tag{3.53}
$$

$$
\mathcal{L}_3 = \eta_3 \frac{c}{L_x}(v - v_{in}),
\tag{3.54}
$$

$$
\mathcal{L}_4 = \eta_4 \frac{c}{L_x}(w - w_{in}),
\tag{3.55}
$$

$$
\mathcal{L}_5 = \eta_5 \rho c^2 \frac{\left(1 - M^2\right)}{2L_x}(u - u_{in}),
\tag{3.56}
$$

where L_x is the domain length, the $(\ )_{in}$ quantities are the desired boundary values at the inlet, and η_i are relaxation coefficients. Rudy & Strikwerda [98] found $\eta_5 = 0.278$ to be the optimal value in theory, however their tests suggested that a larger value gives better results in practice. There is obviously a trade-off while choosing η. If η is too small, the flow quantities at the boundaries might drift significantly from the desired values. If η is too large, the boundary behaves as a "hard" wall and is no longer non-reflecting [97]. In the present work, $\eta_5 = 1$ was found to yield satisfactory results. The other relaxation coefficients are set as $\eta_2 = -\eta_5$, and $\eta_3 = \eta_4 = \eta_5$ [97].

At the outlet, we also assume that $0 < u < c$, in which case all wave amplitudes can be computed from interior data except $\mathcal{L}_1$, which is used to impose a soft boundary condition on pressure

$$\mathcal{L}_1 = \eta_1 c \frac{(1 - M^2)}{2L_x} (p - p_{out}) \; , \tag{3.57}$$

with $\eta_1 = \eta_5$, and where p_{out} is the desired pressure at the outlet. The other wave amplitudes, i.e., $\mathcal{L}_2, \mathcal{L}_3, \mathcal{L}_4$, and $\mathcal{L}_5$ are computed using second-order backward differentiation stencils.

To summarize, at the inlet/outlet, we solve Eqs. (3.37) – (3.41) by computing the $\mathcal{L}_i$ from interior data for the outgoing characteristic waves, and imposing soft boundary conditions according to Eqs. (3.53) – (3.57) for the incoming characteristic waves.

3.5 Results

In this section, we apply the numerical framework presented in the previous sections to various test cases. In Sec. 3.5.1, we assess the performance of the hybrid time integration scheme proposed in Sec. 3.1 for the simulation of reacting flows. In Sec. 3.5.2, we verify the spatial accuracy for the transport of acoustic and entropy waves. Finally, in Sec. 3.5.3, we test the NSCBC described in Sec. 3.4.

3.5.1 Time integration

The focus of this thesis is on flows in which both transport and chemistry are present. Hence, to evaluate the performance of the hybrid time integration scheme described in Sec. 3.1, we do not consider homogeneous reactors. Instead, we look at premixed flames as they are a perfect example of the tight coupling between chemistry and transport (see Sec. 1.1). We consider the combustion of a premixed n-heptane/air mixture under standard conditions and $\phi = 0.9$. The two flow configurations studied are a one-dimensional flat flame, and a statistically-stationary three-dimensional turbulent case. The focus of this section being placed on the performance of the hybrid RK4-midpoint time integration scheme described in Sec. 3.1 when stiff chemistry is present, the Lewis number of all species is set to unity.

3.5.1.1 Freely propagating one-dimensional flame

We now consider a one-dimensional flat n-heptane/air premixed flame at $\phi = 0.9$. The flame is freely propagating in a still unburnt mixture. We first show results obtained using Mechanism #4. Figure 3.8a shows the mass fraction of 1-pentyl

radical as a function of temperature, using the novel time integration scheme with $\Delta t = 2 \cdot 10^{-8}$ s (corresponding to an acoustic CFL of 0.9), and using the RK4 scheme for all flow variables with $\Delta t = 5 \cdot 10^{-10}$ s and $\Delta t = 2 \cdot 10^{-8}$ s. The 1-pentyl radical is chosen since it is associated with the largest eigenvalue (smallest timescale) of the chemical Jacobian. Clearly, the simulation using the RK4 scheme for the species with $\Delta t = 2 \cdot 10^{-8}$ s is unstable, and predicts negative pentyl mass fractions. In contrast, the results obtained with the proposed method and $\Delta t = 2 \cdot 10^{-8}$ s are in excellent agreement with the results obtained using the RK4 scheme for the species with $\Delta t = 5 \cdot 10^{-10}$ s. The accuracy plot shown in Fig. 3.8b confirms that the overall approach yields 2$^{\text{nd}}$ order accurate results in time, as expected. The normalized errors for the different species are evaluated in temperature space as

$$\sqrt{\int_T \left(Y_s - Y_{s,ref}\right)^2 dT \Big/ \int_T Y_{s,ref}^2 \, dT} \, ,$$

with a reference solution $Y_{s,ref}$ obtained with $\Delta t = 10^{-10}$ s.

The results obtained with Mechanism #5 are shown in Figure 3.9. Figure 3.9a shows the mass fraction of $2 - C_5H_{11}$ in temperature space, using the proposed framework with $\Delta t = 2 \cdot 10^{-8}$ s, and using the RK4 scheme with $\Delta t = 10^{-12}$ s and $\Delta t = 10^{-15}$ s. First, one observes that $\max(Y_{2\text{-}C_5H_{11}})$ is very small, as a result of the erroneously short consumption timescale predicted by the chemical Jacobian (Fig. 3.4b). Second, using the RK4 scheme for the species with $\Delta t = 10^{-12}$ s yields unphysical results, as the chemical timescale associated with $2 - C_5H_{11}$ is much smaller ($\tau_{2\text{-}C_5H_{11}} \sim 10^{-14}$ s). Third, the results obtained using the proposed approach with $\Delta t = 2 \cdot 10^{-8}$ s are in excellent agreement with the ones obtained employing the RK4 scheme for the species with $\Delta t = 10^{-15}$ s. Figure 3.9b shows the temporal accuracy for different species, which is found to be 2$^{\text{nd}}$ order accurate. For very small timesteps, the error for $2 - C_5H_{11}$ plateaus, which is likely due to its tiny mass fraction compared to the other species.

As briefly discussed in Sec. 3.1.5, blending two different time integrators introduces inconsistencies between the density field obtained from continuity and the one obtained from the species transport equations, i.e, $\rho \neq \sum_{s=1}^{n_s} (\rho Y)_s$. To quantify this error, we compute the normalized density error $\epsilon = |\rho - \sum_s (\rho Y)_s|/\rho$ for the two cases considered in this section. This quantity is found to be small, i.e., $\max(\epsilon) = 4 \cdot 10^{-6}$ when using Mechanism #4 and $\max(\epsilon) = 5 \cdot 10^{-5}$ when using Mechanism #5. In summary, the proposed time integration scheme stabilizes the

solution and yields 2nd order accurate results for the species mass fractions, while introducing minimal discrepancies between the two density fields.
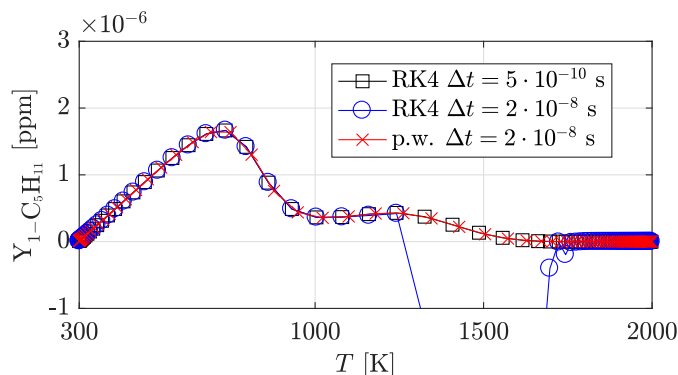
(a) Pentyl mass fraction
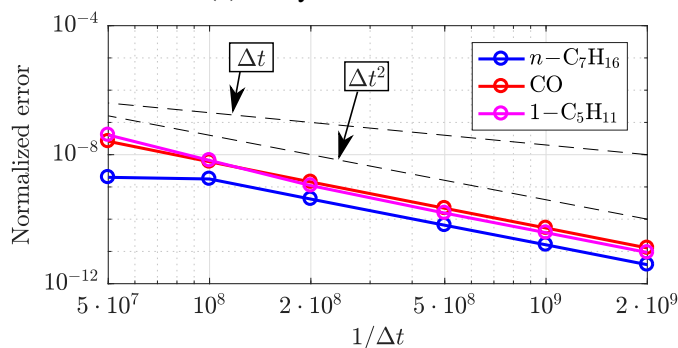
(b) Temporal accuracy

Figure 3.8: Performance of the proposed method for the laminar one-dimensional case using Mechanism #4.

3.5.1.2   Interaction of an acoustic wave with a one-dimensional flame

In this section, we consider an acoustic wave impinging on the one-dimensional flame considered in Sec. 3.5.1.1. The goal is to determine the accuracy of the proposed time integration scheme for the transport of acoustic waves. We employ Mechanism #4. A right-traveling acoustic wave is initially introduced ahead of the flame. Its pressure profile is shown by a solid black line labeled A in Fig. 3.10a. First, the wave travels from A→ B in the unburnt mixture. Then, from B→C, the wave is partially transmitted/reflected by the flame. To evaluate the temporal accuracy of the hybrid scheme, we extract (ρu) at the locations where $|p - p_0|$ is maximum, shown by the red stars in Fig. 3.10a. In Fig. 3.10b, we show the accuracy of the proposed method for each of the two segments ($\psi = (\rho u)$). The scheme is seen to be 4th order accurate for $A \rightarrow B$, where there is no chemistry or mixing.
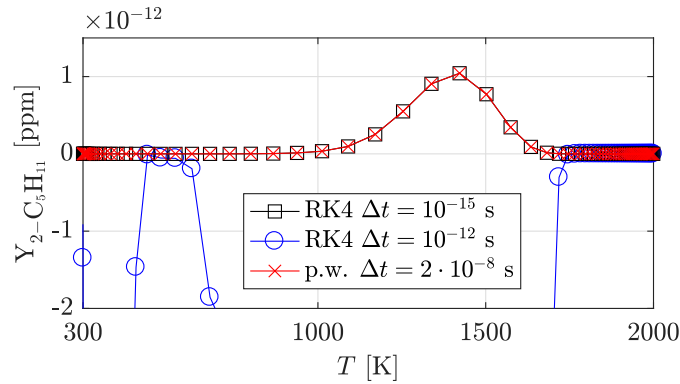
(a) Pentyl mass fraction
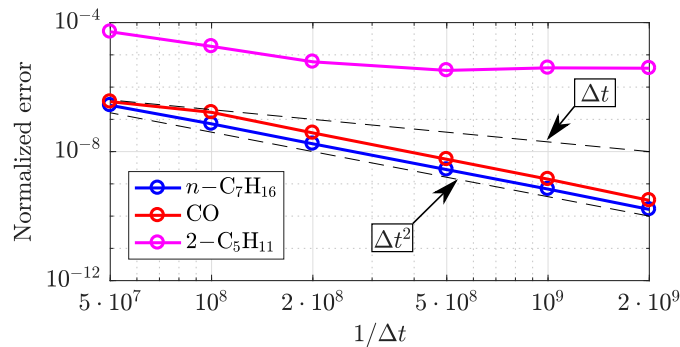
(b) Temporal accuracy

Figure 3.9: Performance of the proposed method for the laminar one-dimensional case using Mechanism #5.

From $B \rightarrow C$, as the acoustic wave goes through the flame, the scheme is 2nd order accurate, as expected.

3.5.1.3 Turbulent flame

We now examine the turbulent case, which corresponds to Flame C_1 in Lapointe *et al.* [40]. The unburnt temperature is $T_u = 800$ K, pressure is $p = 1$ atm, and Mechanism #4 is used. Two-dimensional slices showing temperature and pentyl mass fraction isocontours are shown in Fig. 3.11. These results are obtained with $\Delta t = 10^{-8}$ s, which corresponds to an acoustic CFL of 0.9. This configuration remains entirely subsonic, with local Mach numbers reaching 0.5. Figure 3.12 shows the joint probability density function of pentyl mass fraction and temperature for simulations performed using the original RK4 scheme for the species, and the proposed method. Again, negative mass fractions are predicted when using the RK4 scheme for the species transport with $\Delta t = 10^{-8}$ s, a problem which is solved by using the hybrid scheme presented in Sec. 3.1.5.
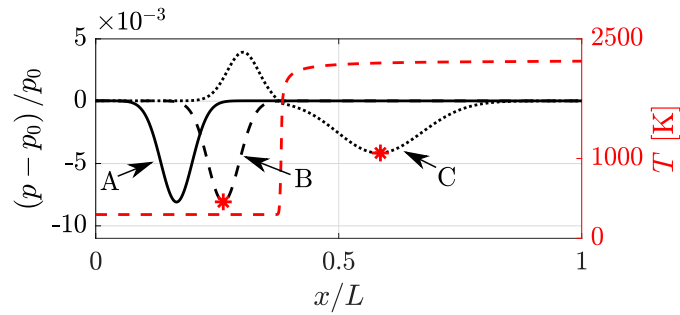
(a) Temperature and pressure profiles.
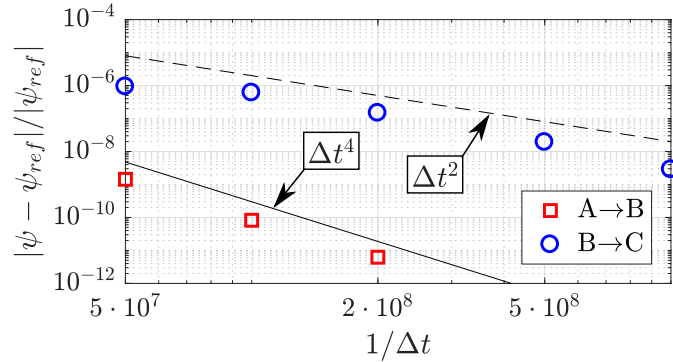
(b) Temporal accuracy.

Figure 3.10: Results for an acoustic wave impinging on a one-dimensional flame.

(a) Temperature T

(b) Pentyl mass fraction $Y_{1\text{-}C_5H_{11}}$

Figure 3.11: Two-dimensional slices showing isocontours for the turbulent case ($\Delta t = 10^{-8}$ s). Two temperature isolines are superimposed in white ($T = 1000$ K and $T = 1900$ K).

Figure 3.13 shows the spatial distribution of the normalized density error ϵ. This error is concentrated in the turbulent flame brush and disappears on the burnt side. In Fig. 3.14, we quantify this error as a function of time for three different timestep sizes. All simulations are such that $\rho = \sum_s (\rho Y)_s$ initially. Time is normalized with the eddy turnover time τ_0. In all cases, the errors remains bounded and almost constant over time at a value determined by the timestep size. Three phenomena contribute to ϵ: the different time integrators for continuity (RK4) and for the species transport (midpoint), the semi-implicit treatment of chemistry, and the use of a non-linear spatial transport scheme for the species mass fractions. The combined error due to the semi-implicit treatment of chemistry and the different time integrators

(a) RK4 for species, $\Delta t = 10^{-8}$ s

(b) RK4 for species, $\Delta t = 10^{-10}$ s

(c) Proposed method, $\Delta t = 10^{-8}$ s
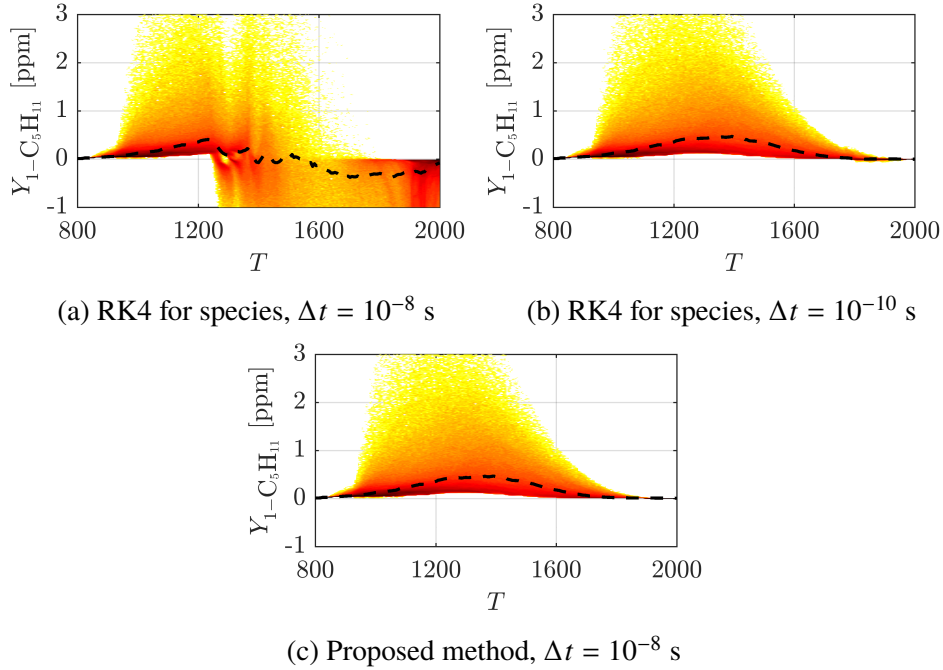
Figure 3.12: Joint probability density function of pentyl mass fraction and temperature for the turbulent case. The black dashed line represents the conditional mean.

is expected to decrease with the timestep size as Δt^2. To explore this further, we present in Figs. 3.14a and 3.14b results obtained with the linear transport scheme QUICK [99]. In this particular case, $\max(\epsilon) \sim \Delta t^2$, since the proposed method blends a 2nd midpoint method and the 4th order RK4 scheme. This is highlighted in Fig. 3.14b, where $\max(\epsilon)$ is rescaled by assuming a 2nd order convergence rate.

Figure 3.13: Two-dimensional slice showing isocontours of ϵ for the turbulent case ($\Delta t = 10^{-8}$ s). Two temperature isolines are superimposed in white ($T = 1000$ K and $T = 1900$ K).

The error due to the scalar transport scheme deserves more attention. The BQUICK scheme, along with other popular transport schemes such as WENO [100] and BCH [101], is non-linear. Non-linear schemes are desirable because they combine high accuracy, low dissipation, and boundedness. However, their non-linearity induces a discrepancy between the convective terms from the continuity equation (Eq. (2.1)) and the sum of the convective terms from the species transport equations

(Eq. (2.4)), i.e., $\sum_s \nabla \cdot (\rho u Y_s)) \neq \nabla \cdot (\rho u)$. Hence, as shown in Fig. 3.14c, $\max(\epsilon)$ decreases with the timestep size, but eventually reaches a plateau around $\max(\epsilon) \sim 10^{-4}$. It should be noted that this error is not due to the proposed time integration scheme, and will be present anytime a non-linear scheme is used for the species transport equations. In all cases, the discrepancy between the two density fields remains very small.

(a) QUICK scheme

(b) QUICK scheme (rescaled)

(c) BQUICK scheme
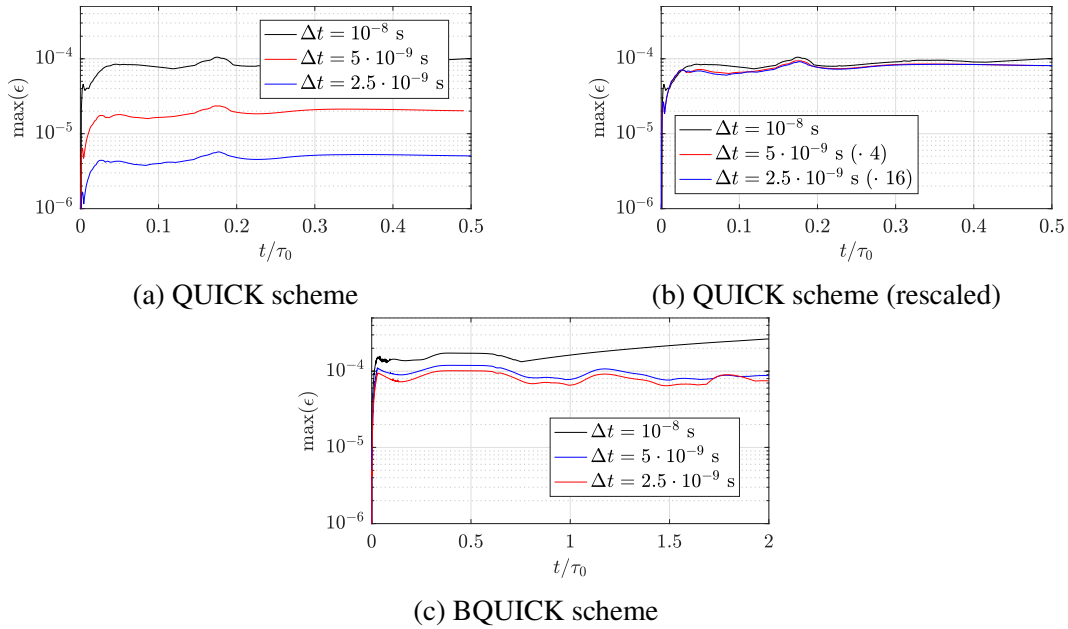
Figure 3.14: Maximum density error $\max(\epsilon)$ as a function of time for the turbulent case, using different schemes for the species transport.

3.5.2 Spatial discretization

To assess the spatial accuracy, we perform a series of inviscid one-dimensional simulations, including a traveling acoustic wave and an entropy wave in periodic domains. The first flow configuration is specific to the compressible formulation, whereas the second one assesses the ability of the solver to capture large density gradients typical of reacting flows.

3.5.2.1 Traveling Acoustic Wave

A one-dimensional traveling acoustic wave is the solution to the linearized Navier-Stokes equations with the following initial conditions:

$$p = p_\infty + A_p f(x), \qquad \rho = \rho_\infty + \frac{A_p}{c_\infty^2} f(x), \qquad u = \frac{A_p}{\rho_\infty c_\infty} f(x), \qquad (3.58)$$

where the subscript $(\ )_\infty$ denotes reference quantities, c_∞ is the reference sound speed, and A_p is the pressure amplitude of the acoustic wave. The computational domain is periodic with length L. We choose a sinusoidal initial pressure field $f(x) = \sin(kx)$, where $k = 2\pi/L$ is the wavenumber. Since the solution given by Eq. (3.58) is valid for $A_p \ll p_\infty$ only, we choose $A_p = 10^{-5} p_\infty$.

As discussed in Sec. 3.2.1, we use second-order central differentiation operators. These schemes are not diffusive, however they introduce dispersion errors. When solving a simple advection equation, i.e.,

$$\frac{\partial \phi}{\partial t} + a \frac{\partial \phi}{\partial x} = 0, \tag{3.59}$$

this causes waves $\phi_k(x) = \sin(kx)$ to move at a modified speed a' that depends on the wavenumber k. This behavior is traditionally characterized with a modified wavenumber diagram such as the one presented in Fig. 3.15. For the simple advection equation, the modified wavenumber k' is related to a' by

$$k' = \frac{ka'}{a}. \tag{3.60}$$

In the context of acoustics, dispersion errors cause waves to move at a modified sound speed $c'_\infty(k)$. In Fig. 3.15, the blue circles show the modified wavenumber relations extracted from the numerical simulations. We evaluate k' by using Eq. (3.60) with $a' = c'_\infty$. The latter is computed as $c'_\infty = L/t_{travel}$, where t_{travel} is the time it takes for the acoustic wave to travel the length of the domain, evaluated by fitting a sine wave to $p(x = 0, t)$. The thick dashed line shows the analytical modified wavenumber relation for a staggered grid arrangement using a second order differentiation stencil. The analytical and numerical results are in excellent agreement. To emphasize the improved accuracy obtained by using a staggered grid, the thin dashed line and thin solid line show the relation for a regular (i.e., collocated) grid using second order and fourth order stencils, respectively. It can be seen that using a second-order staggered stencil yields more accurate results than a collocated fourth-order stencil.

3.5.2.2 Entropy Wave

To further assess the spatial accuracy, we perform a series of inviscid simulations of entropy waves being convected at a uniform velocity u_∞ in a 1D periodic domain. The initial fields are

$$u = u_\infty, \qquad p = p_\infty, \qquad \rho = \rho_\infty \left(1 - \alpha g(r)\right), \tag{3.61}$$
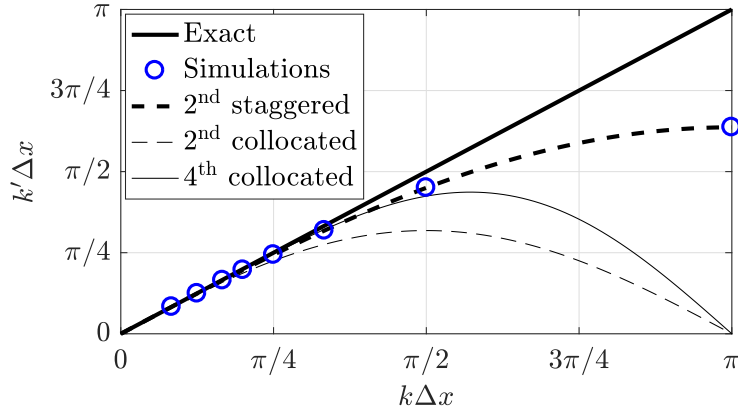
Figure 3.15: Modified wavenumber diagram. The numerical results are shown by blue circles. The thick dashed line show the analytical wavenumber relation for a staggered grid using a second order differentiation stencil. The thin dashed line and thin solid line show the relations for a collocated grid using second order and fourth order stencils, respectively. The thick solid line is the theoretical relation in absence of dispersion errors.

We choose $u_\infty = c_\infty/2$ and the following distribution

$$g(r) = \begin{cases} 1 - \exp\left(-R/r \exp\left(R/(r - R)\right)\right) & \text{if } r < R \\ 0 & \text{if } r \geq R \end{cases}, \qquad (3.62)$$

which is C^∞ and has compact support, and where $r = |x - x_0|$. We set $x_0 = L/2$, $\alpha = 0.5$, $\kappa = 1$, and $R = L/4$. We run the simulation for one flow-through time, i.e., $t_f = L/u_\infty$. The initial and final density field are shown in Fig. 3.16 for a simulation with $L/\Delta x = 256$. Small oscillations in the wake of the density profile can be observed and are characteristics of centered schemes.

The normalized error, computed as

$$\sqrt{\int_x \left(\rho(x, t_f) - \rho(x, 0)\right)^2 dx \Big/ \int_x \rho(x, 0)^2 dx}$$

is shown in Fig. 3.17 for different spatial resolutions. The expected order of convergence (namely second) is observed.

3.5.3 Boundary conditions

We provide a few test cases to verify the implementation of the NSCBC described in Sec. 3.4: a one-dimensional traveling acoustic wave, a one-dimensional entropy wave, and a two-dimensional vortex.
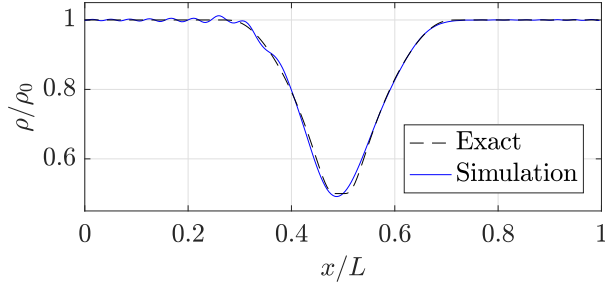
Figure 3.16: Comparison of the initial density field (dashed black line) with the numerical solution at $t_f = L/u_\infty$ for $L/\Delta x = 256$ (solid blue line).
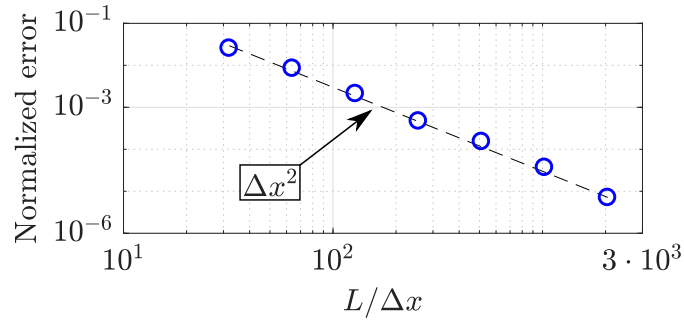
Figure 3.17: Normalized error of the numerical solution of Eq. (3.65) at $t_f = L/u_\infty$ for different spatial resolutions.

3.5.3.1 One-dimensional inviscid traveling acoustic wave

A one-dimensional traveling acoustic wave is the solution to the linearized Navier-Stokes equations with the following initial conditions

$$p = p_\infty + A_p g(r), \tag{3.63}$$

$$u = u_\infty \pm \frac{A_p}{\rho_\infty c_\infty} g(r), \tag{3.64}$$

completed with the isentropic relations $\rho = \rho_\infty (p/p_\infty)^{1/\gamma}$, and $T = T_\infty (p/p_\infty)^{(\gamma-1)/\gamma}$. The subscript $(\ )_\infty$ denotes reference flow quantities, and c_∞ is the reference sound speed. The $\pm$ sign in Eq. (3.64) determines if the wave is left or right-traveling. We use $g(r)$ given by Eq. (3.62), in which we set $r = |x - x_0|$, $x_0 = L/2$, $\kappa = 1$, and $R = L/10$. Since Eqs. (3.63) and (3.64) represent the solution for a traveling acoustic wave for $A_p \ll p_0$, we set $A_p/p_0 = 10^{-5}$. Figures 3.18 and 3.19 show the pressure field for a right and left-traveling wave, respectively. At time $t^* = t/(L/c_\infty) = 0.7$, the wave has interacted with the boundary. It can be seen in Figs. 3.18a and 3.19a that using Neumann boundary conditions at the outlet and Dirichlet boundary conditions at the inlet leads to a perfect reflection of the acoustic

wave. When using NSCBC (Figs. 3.18b and 3.19b), the amplitude of the reflected wave is strongly attenuated. The small amount of reflection is due to the relaxation terms given by Eqs. (3.53)–(3.56) (inlet) and Eq. (3.57) (outlet).

(a) Neumann boundary conditions

(b) NSCBC
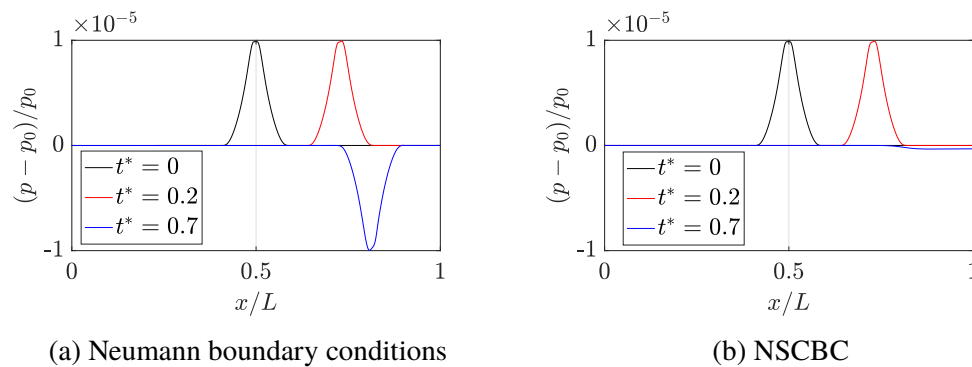
Figure 3.18: Pressure field for a right-traveling one-dimensional inviscid acoustic wave using different sets of boundary conditions.

(a) Neumann boundary conditions

(b) NSCBC
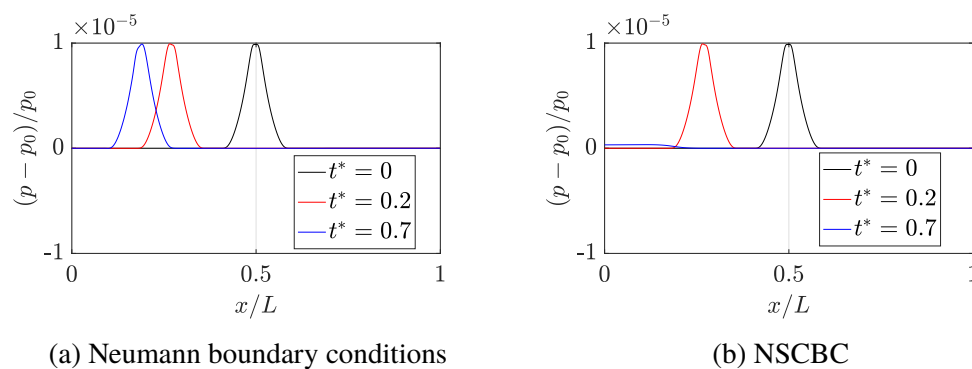
Figure 3.19: Pressure field for a left-traveling one-dimensional inviscid acoustic wave using different sets of boundary conditions.

3.5.3.2 One-dimensional inviscid entropy wave

To verify that entropy waves are correctly convected out of the domain at the outlet, we initialize a one-dimensional field with

$$u = u_\infty, \qquad p = p_\infty, \qquad \rho = \rho_\infty \left(1 - \alpha g(r)\right), \qquad (3.65)$$

where $g(r)$ is given by Eq. (3.62), with $r = |x - x_0|$. We set $\alpha = 0.5$, $\kappa = 1$, $x_0 = L/2$, $R = L/4$, and $u_\infty = c_\infty/2$. Fig. 3.20 shows the density field at different times. At $t^* = t/(L/u_\infty) = 0.8$, the wave has exited the domain, as desired, and the density field is constant.
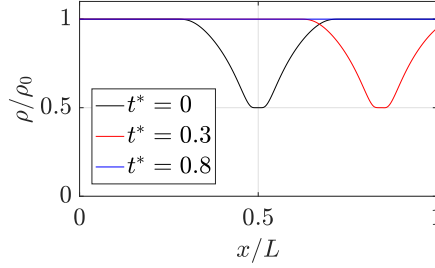
Figure 3.20: Density field for a 1D inviscid entropy wave using the NSCBC, with $t^* = t/(L/u_\infty)$.

3.5.3.3 Two-dimensional vortical flow

To further verify the implementation of the outlet boundary conditions, we examine the evolution of a two-dimensional vortex convected by a mean flow [94, 102]. To determine the initial conditions, we consider the following stream function

$$\psi(r) = C \exp\left(-\frac{r^2}{2R^2}\right), \tag{3.66}$$

where r is the distance from the vortex center, R is the vortex radius, and C determines the vortex strength. Next, neglecting viscous effects, we obtain the initial pressure profile by integrating the radial momentum equation, i.e.,

$$p(r) = p_\infty + \rho_\infty \int_{r' \to \infty}^{r} \frac{(\psi'(r'))^2}{r'} dr' = p_\infty - \frac{\rho_\infty C^2}{2R^2} \exp\left(-\frac{r^2}{R^2}\right). \tag{3.67}$$

In Cartesian coordinates, the initial velocity field is given by

$$\begin{pmatrix} u \\ v \end{pmatrix} = \begin{pmatrix} u_\infty \\ 0 \end{pmatrix} + \begin{pmatrix} \partial\psi/\partial y \\ -\partial\psi/\partial x \end{pmatrix}, \tag{3.68}$$

using $r = \sqrt{((x - x_0)^2 + (y - y_0)^2)}$, with $(x_0, y_0) = (L/2, L/2)$ being the vortex center. We set

$$Re_C \equiv \frac{C}{\nu} = 1000, \qquad R = \frac{L}{10}, \tag{3.69}$$

$$u_\infty = \frac{c_\infty}{20}, \qquad C = 6.25 \cdot 10^{-3} c_\infty L,$$

where Re_C is the Reynolds number based on the vortex strength. The initial density field is taken to be constant, i.e., $\rho = \rho_\infty$. The initial normalized y-velocity field is shown in Fig. 3.21a, with $v^* = v/(C/R)$ being the normalized velocity. The solid

(a) $t^* = 0$

(b) $t^* = 0.34$

(c) $t^* = 0.51$

(d) $t^* = 0.77$
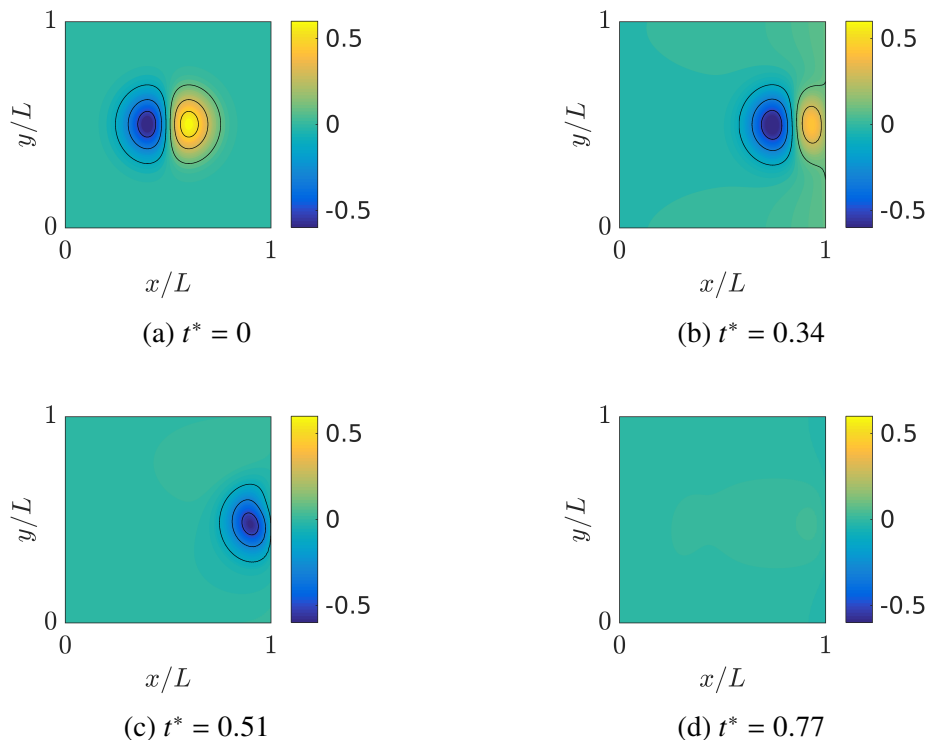
Figure 3.21: Normalized y-velocity fields at different times $t^* = t/(C/R)$ for an advected vortex using the NSCBC.

black lines denote $v^* = [-0.5, -0.3, -0.1, 0.1, 0.3, 0.5]$. The domain is periodic in the y direction, and the NSCBC are used in the x direction. We set $u_{in} = u_\infty$, $v_{in} = 0$, $T_{in} = T_\infty$, and $p_{out} = p_\infty$. The normalized y-velocity field is shown at later times in Figs. 3.21b – 3.21d. In Figs. 3.21b – 3.21c, the vortex is seen to be slightly distorted, which has previously been investigated [102]. At $t^* = 0.77$ (Fig. 3.21d), the vortex has exited the domain, and the maximum vertical velocity component is less than 5% that of the initial vortex.

3.6 Summary

We presented a novel time integration scheme that blends the semi-implicit midpoint method for the species transport and the RK4 scheme for the transport of the other flow variables. This scheme was tested by considering a freely-propagating one-dimensional flame, an acoustic wave impinging on a one-dimensional flame, and a turbulent flame. The novel time integration scheme was found to perform well. With this approach, the time step is limited by the acoustic CFL only, regardless of the chemical mechanism employed, while being accurate for the transport of acoustic waves. We also presented the spatial discretization, and performed verification

cases. The use of a staggered grid was found to be ideally suited for the transport of acoustic waves. Finally, we reviewed the NSCBC framework, and carried out various test cases to verify its implementation.

Chapter 4

FLAME-ACOUSTICS INTERACTIONS

[2] Beardsell, G. and Blanquart, G., "Fully compressible simulations of the impact of acoustic waves on the dynamics of laminar premixed flames for engine-relevant conditions," *Proceedings of the Combustion Institute*, 2020. DOI: `https://doi.org/10.1016/j.proci.2020.06.003`,

[3] Beardsell, G. and Blanquart, G., "Impact of pressure fluctuations on the dynamics of laminar premixed flames," *Proceedings of the Combustion Institute*, vol. 37, no. 2, pp. 1895–1902, 2019. DOI: `https://doi.org/10.1016/j.proci.2018.07.125`,

In this chapter, we focus on direct pressure effects as outlined in Sec. 1.2, i.e., we investigate the impact of acoustic thermodynamic fluctuations on the dynamics of one-dimensional premixed flames. The objective is to investigate the flame response for a wide range of fuels and acoustic frequencies, through DNS using detailed chemical models. The focus is placed on the combustion dynamics of hydrogen, methane, n-heptane and n-dodecane for they are of practical interest and behave very differently when subjected to acoustic waves. Hydrogen is considered as it is commonly used for propulsion, e.g. in the RS-25 engine. Similarly, many practical engine fuels contain large hydrocarbon molecules such as *n*-heptane, e.g., kerosene. Furthermore, the literature dealing with direct pressure effects involving large hydrocarbon fuels is lacking. We are specifically interested in extracting the phase and gain of the unsteady heat release response, which are directly related to the Rayleigh criterion (Eq. (1.8)), and thus the stability of the system.

This chapter is organized as follows. In Sec. 4.1, we describe the numerical methodology for the simulations using the low Mach number approximation and the fully compressible framework. We present the flow configuration, details of the spatial and temporal convergence, as well as the methodology used to compute the gain and phase responses. We provide a verification of the numerical framework by comparing our results with existing numerical data. Then, in Sec. 4.2, we analyze the results obtained under the low Mach number approximation. For the four fuels considered, we analyze the global flame response (heat release), as well as the response of key intermediate species, at standard temperature and atmospheric pres-

sure. This section is based on Beardsell & Blanquart [3]. In Sec. 4.3, the objective is to investigate the flame response under engine-relevant conditions using the fully compressible framework. The differences between results obtained using the fully compressible Navier-Stokes equations and the low Mach number approximation are investigated. This section is based on Beardsell & Blanquart [2]. Finally, the findings are summarized in Sec. 4.4.

4.1 Methodology

4.1.1 Flow configuration

We perform one-dimensional simulations to isolate the direct impact of the acoustic thermodynamic fluctuations on the flame response. This prevents potential multidimensional effects induced by the acoustic velocity field, e.g., Rayleigh-Taylor instabilities, from developing. Figure 4.1 shows the temperature and velocity profiles for Case 6 without acoustic perturbations. Fully premixed reactants enter the domain on the left with velocity u_{in}, and burnt products exit on the right. We impose $u_{in} = \overline{S}_L$, such that the mean flame position $\overline{x}_F$ remains constant. For the steady-state solution, the mass flux ρu is constant everywhere (see Eq. (2.1)). However, as the temperature increases through the flame, the density drops, and the velocity increases. The different flow configurations considered in this chapter are listed in Table 4.1. The chemical models (mechanisms) associated with each configuration are described in Sec. 3.3.3.
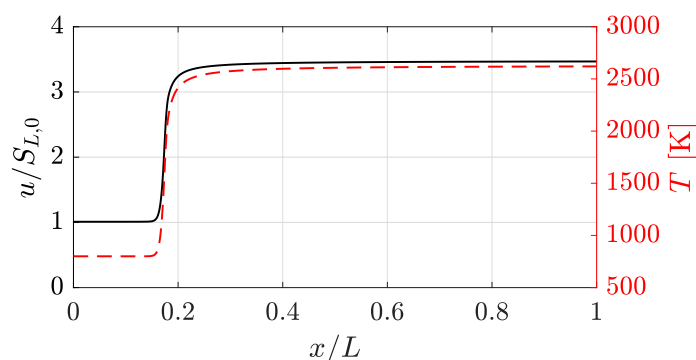
Figure 4.1: Velocity (solid black) and temperature (dashed red) profiles for Case 6 without perturbation.

4.1.1.1 Low Mach number simulations

For the simulations under the low Mach number framework, considered in Sec. 4.2, we consider Cases 1, 2, 3a, 3b, 3c, and 4, i.e., all the cases at standard thermodynamic

Table 4.1: Parameters of the simulations: ϕ is the equivalence ratio, $l_{F,0}$ is the laminar flame thickness, $S_{L,0}$ is the laminar flame speed, and $\tau_F = l_{F,0}/S_{L,0}$ is the flame time scale. The subscript $(\ )_0$ refers to quantities evaluated at the reference state (without perturbations).

Case	Fuel	Chemical mechanism	ϕ	p_0 [atm]	T_u [K]	$l_{F,0}$ [mm]	$S_{L,0}$ [m/s]	τ_F [ms]
1	H_2	#2	0.4	1	298	0.63	0.23	2.8
2	CH_4	#1	0.625	1	298	0.87	0.13	6.7
3a	n-C_7H_{16}	#4	0.9	1	298	0.39	0.35	1.1
3b	n-C_7H_{16}	#4	0.7	1	298	0.52	0.22	2.4
3c	n-C_7H_{16}	#4	1.3	1	298	0.37	0.34	1.1
4	n-$C_{12}H_{16}$	#3	0.9	1	298	0.36	0.37	0.97
5	H_2	#2	0.4	20	800	0.021	1.31	0.016
6	n-C_7H_{16}	#4	0.9	20	800	0.022	1.05	0.021

conditions. We set the acoustic pressure amplitude at 5% of the background pressure, i.e., $A_p = 5000$ Pa. The acoustic frequency f is varied from 50 Hz to 100 MHz.

4.1.1.2 Compressible framework

For the compressible simulations, investigated in Sec. 4.3, we consider Cases 1, 3a, 5, and 6. Cases 5 and 6 are designed to explore engine-relevant conditions, i.e., $T_{u,0} = 800$ K and $p_0 = 20$ atm. We also carry out low Mach number simulations for Cases 5 and 6 for comparison purposes. The acoustic frequencies range from 1 kHz to 50 MHz, and the normalized acoustic pressure amplitude is $A_p/p_0 = 2 \cdot 10^{-3}$ for all cases. Note that the chosen normalized pressure amplitude is smaller for the compressible simulations, to ensure that the velocity remains positive at the boundaries, as required by the NSCBC (see Sec. 3.4.2).

4.1.2 Numerical framework

4.1.2.1 Low Mach number approximation

It might seem counter-intuitive to explore flame-acoustics interactions using the low Mach number approximation, in which the acoustics are inherently removed from the system, as detailed in Sec. 2.1.2. However, for most of the acoustic frequencies considered in this work, the ratio of the laminar flame thickness to the acoustic wavelength is small, i.e., $l_F/\lambda_b \ll 1$, where λ_b is the acoustic wavelength evaluated using the sound speed in the burnt region. This allows us to use the same approach as the one presented and validated by Jiménez *et al.* [14], which is briefly summarized

here.

In this limit, the acoustic pressure gradients vanish in the vicinity of the flame and the flame only experiences a time-varying acoustic pressure $p_a(t)$. Because the Mach number of the flow is small ($M \sim 10^{-3}$), we can employ a low Mach number approach [103]. Recall that in the low Mach number approximation, the zeroth-order pressure (referred to as the background pressure) is a spatially uniform field (see Eq. (2.31)). This potentially time-varying quantity must be provided as an input to the simulation. We set the background pressure to

$$p_t(t) = p_0 + p_a(t) = p_0 + A_p \sin(\omega t), \tag{4.1}$$

where A_p is the acoustic pressure amplitude. Figure 4.2 shows a conceptual schematic of the flow configuration for the low Mach number simulations. A laminar planar flame is subjected to a standing acoustic wave. The flame is located at a velocity node, which also corresponds to a pressure anti-node. The ratio l_F/λ_b is small, and thus the flame does not feel the spatial variations in pressure.

Some of the simulation results that we present are obtained at frequencies for which $l_F/\lambda_b \lll 1$. We want to carry out simulations at such frequencies in order to get insight on the overall behavior of these dynamical systems. However, care must be taken when analyzing these results, as some compressibility effects may be missing. To aid the reader, the frequency at which $\lambda_b = 10\,l_F$ will be indicated by a vertical dashed line in all the plots. For the low Mach number simulations, the governing
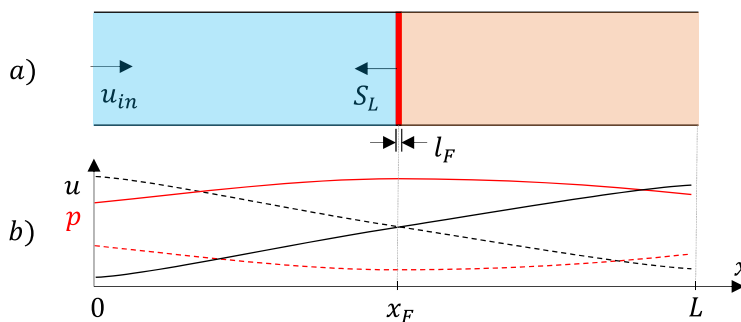
Figure 4.2: a) Conceptual schematic of the flow configuration for the low Mach number simulations. b) Examples of pressure (red) and velocity (black) profiles at different times (solid and dashed lines). The flame position x_F is at a velocity node.

equations are continuity (Eq. (2.34)), momentum (Eq. (2.35)), species transport (Eq. (2.4)), the equation of state (Eq. (2.37)), and the energy equation (Eq. (2.42)). To account for the varying thermodynamic pressure, the inlet temperature T_{in} is

continuously adjusted according to the isentropic relation

$$T_{in} = T_{u,0} \left(\frac{p_t}{p_0} \right)^{\frac{\gamma_u - 1}{\gamma_u}} . \tag{4.2}$$

4.1.2.2 Fully compressible framework

For the fully compressible simulations, we solve Eqs. (2.1)–(2.4), along with Eq. (2.11). We seek to generate acoustic waves at the outlet following

$$p(x = L, t) = p_0 + A_p \sin(\omega t) , \tag{4.3}$$

where $\omega = 2\pi f$ is the angular frequency. The NSCBC framework detailed in Sec. 3.4.2 is employed. At the outlet, acoustic waves are introduced in the domain by modulating the amplitude of the incoming characteristic wave. To do so, we slightly modify Eq. (3.57) by appending the imposed wave amplitude $\mathcal{L}_{1,imp}$, i.e.,

$$\mathcal{L}_1 = \mathcal{L}_{1,imp} + \eta_1 c_e \frac{(1 - M_e^2)}{2L_x} (p_e - p_{out}) . \tag{4.4}$$

The imposed characteristic wave amplitude $\mathcal{L}_{1,imp}$ is obtained by substituting the solution to the linearized one-dimensional Euler equations for a left-travelling acoustic wave

$$p = A_p \sin(\omega t + kx) \qquad u = -\frac{A_p}{\rho c} \sin(\omega t + kx) , \tag{4.5}$$

into Eq. (3.47), i.e.,

$$\mathcal{L}_{1,imp} = \left(\frac{u - c_e}{2} \right) \left(\frac{\partial p}{\partial x} - \rho c \frac{\partial u}{\partial x} \right) = A_p (u - c_e) \frac{\omega}{c_e} \cos(\omega t) . \tag{4.6}$$

In Eqs. (4.4)–(4.6), the subscript $(\ )_e$ refers to quantities evaluated at the outlet (exit). This generates incoming acoustic waves that follow Eq. (7.22), while allowing outgoing waves to leave the domain. This approach is similar to inlet wave modulation [104]. Also, since we want the outlet pressure to vary sinusoidally, we cannot set $p_e = p(x = L_x)$ in the second term on the RHS of Eq. (4.4). Doing so would result in the relaxation term in Eq. (4.4) dampening the desired outlet wave modulation. Instead, we replace p_e in Eq. (4.4) with a moving average

$$\tilde{p}_e = \frac{1}{\Delta t f} \int_{t' = t - \Delta t f}^{t} p_e dt' . \tag{4.7}$$

The desired temperature and velocity at the inflow are imposed using a set of relaxation terms (see Sec. 3.4.2).

4.1.3 Spatial and temporal convergence

For all simulations, we use 1200 uniformly spaced grid points with the domain length set to $L \approx 60 \, l_F$. This corresponds to about 20 points per flame thickness. To verify that the grid resolution was sufficient, additional simulations were performed for all cases at the highest frequency considered, with twice as many points per flame thickness. Small differences up to 1 % and 0.01 rad were observed for the heat release fluctuation gain and phase, respectively. The coarser grid was thus used for all subsequent simulations. The impact of the time step size (Δt) was assessed by repeating each simulation for all cases with a time step two times smaller. Differences in gain and phase remained within the tolerances used for the spatial convergence. Finally, it should be noted that the required time step becomes smaller as the frequency increases.

4.1.4 Evaluation of the gain and phase responses

As outlined in Sec. 1.2, the gain and phase of the heat release is important to determine if the flame is thermo-acoustically unstable through the Rayleigh criterion. From Eq. (2.42), we can obtain the temperature production term

$$\dot{\omega}_T = -\frac{1}{c_p} \sum_{s=1}^{n_s} h_s \dot{\omega}_s \,. \tag{4.8}$$

The total heat release is computed as

$$\dot{Q} = \int_{x=0}^{L} \rho c_p \, \dot{\omega}_T \, dx = \int_{x=0}^{L} \rho \dot{h} \, dx \,, \tag{4.9}$$

where $\dot{h}$ is the local heat release. In addition to the heat release, we also compute the gain and phase of the species mass fractions.

For a given quantity ψ, e.g., $\dot{Q}$, we assume that the oscillations reach a periodic steady-state with frequency f, which is what is observed in all cases. The amplitude of ψ is determined by using

$$A_\psi = \frac{1}{2} \left[\psi_{max,k} - \psi_{min,k} \right] \,, \tag{4.10}$$

where $\psi_{min,k}$ and $\psi_{max,k}$ are the extrema of ψ on the time interval $t \in [kT, (k+1) \, T]$, with $T = f^{-1}$ being the acoustic period. Here, k is the total number of cycles before a periodic steady state is reached. This state is deemed reached when the differences in amplitude between two subsequent cycles differs by less than 1%. For all cases,

a few cycles ($k \approx 3$) were found to be sufficient. The gain is then computed as

$$G_\psi \equiv \frac{A_\psi}{\overline{\psi}} \frac{p_0}{A_p},$$ (4.11)

where $\overline{\psi}$ denotes the time average of ψ. It was observed for all cases that $\overline{\psi} = \psi_0$, where ψ_0 is obtained from the unperturbed flame, thus confirming the linear response of the flame. In the following section, the gains are normalized by the gain when the frequency goes to zero, i.e., $G_\psi|_{\omega\to 0}$. The procedure by which the latter is computed is detailed in Sec. 4.2.2. To compute the phase angle (in radians), we use

$$\theta_\psi = \omega \left[t_{\psi_{max},k} - t_{p_{max},k} \right],$$ (4.12)

where $t_{\psi_{max},k}$ and $t_{p_{max},k}$ are the times at which ψ_{max} and p_{max} occur once the periodic steady state is achieved.

For the compressible simulations, the pressure field is not uniform in space. Then, we have to select where to evaluate p_{max}, which is required to compute the gain and phase. Fig. 4.3 shows the local heat release for Case 6 at an acoustic frequency $f = 10^7$ Hz. It can be seen that $\dot{h}$ is confined to a thin region. The most appropriate pressure to evaluate the impact on the heat release is then the pressure at the location of maximum local heat release, i.e., the location where $\dot{h}$ is maximum.
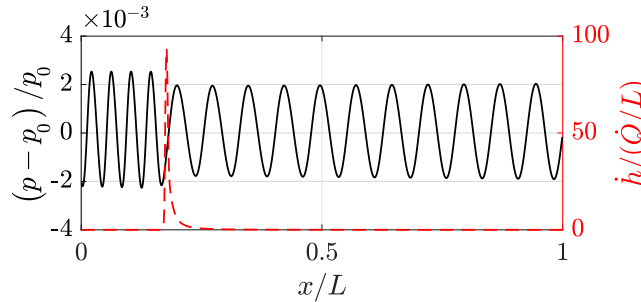
Figure 4.3: Normalized local heat release (dashed red) and oscillating pressure (solid black) profiles for Case 6 with $f = 10^7$ Hz, corresponding to $\omega\tau_{F,0} = 1.2 \cdot 10^3$.

4.1.5 Verification

We first verify our numerical implementation by comparing our low Mach number results for Case 1 (hydrogen) and Case 2 (methane) with the ones obtained by Jiménez *et al.* [14], for the same flow conditions (i.e., $T_{u,0}$, p_0, and ϕ). For methane, we use the same chemical model,i.e., GRI-Mech 3.0. In Figs. 4.4 and 4.5, the gain and phase of $\dot{Q}$ are shown. The acoustic angular velocity is normalized by the flame timescale $\tau_F = l_{F,0}/S_{L,0}$, which was found to be the adequate time scale in previous theoretical analyses [15–19]. The agreement is excellent.
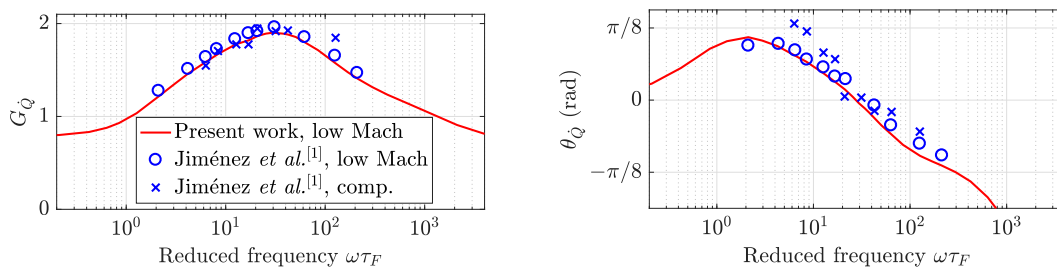
Figure 4.4: Gain (left) and phase (right) of the heat release fluctuations as a function of the reduced frequency, for Case 2 (methane). The lines are from the present study, and the blue circles and crosses are numerical results reported by Jiménez *et al.* [14].
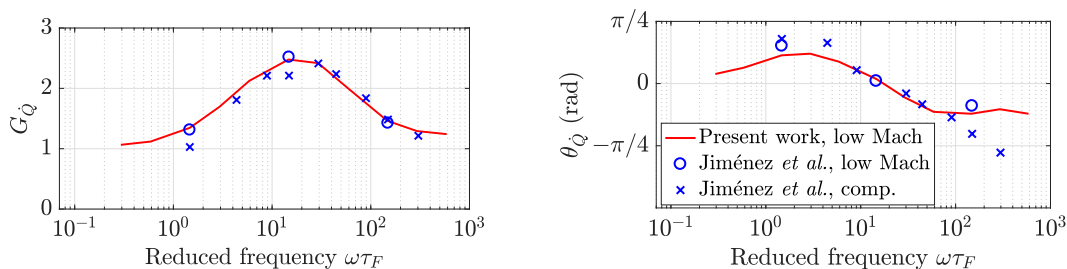
Figure 4.5: Gain (left) and phase (right) of the heat release fluctuations as a function of the reduced frequency, for Case 1 (hydrogen). The lines are from the present study, and the blue circles and crosses are numerical results reported by Jiménez *et al.* [14].

4.2 Low Mach number results

4.2.1 Overview

Figure 4.6 shows the heat release gain and phase response for Cases 1,2, 3a and 4. The gains are normalized by their respective values when $\omega \to 0$. The horizontal dashed lines show the theoretical gain estimated for the limit $\omega \to \infty$. The procedure by which the low-frequency limit is computed is discussed in Sec. 4.2.2, while the methodology used to compute the high-frequency limit is detailed in Sec. 4.2.5. For comparison purposes, Fig. 4.6 also shows the one-step and two-step results given by Clavin *et al.* [19] and Clavin & Searby [20], respectively. In Fig. 4.6a, the one-step model increases monotonically, unlike any of the cases considered. The two-step model reaches a local maximum before decreasing below its quasi-steady state value. However, neither models are sufficient to describe the evolution of heavy hydrocarbon fuels. Figure 4.7 shows the responses of $\dot{Q}$ and key intermediate species for Cases 1, 2, 3a, and 4. To compute the species gain (Eq. (4.10)) and phase (Eq. (4.12)), the quantity $Y_{s,max}$ is defined as the maximum value of Y_s in the domain at a given time. In Fig. 4.7, the gain of the radical species is seen to drop

(a) Gain
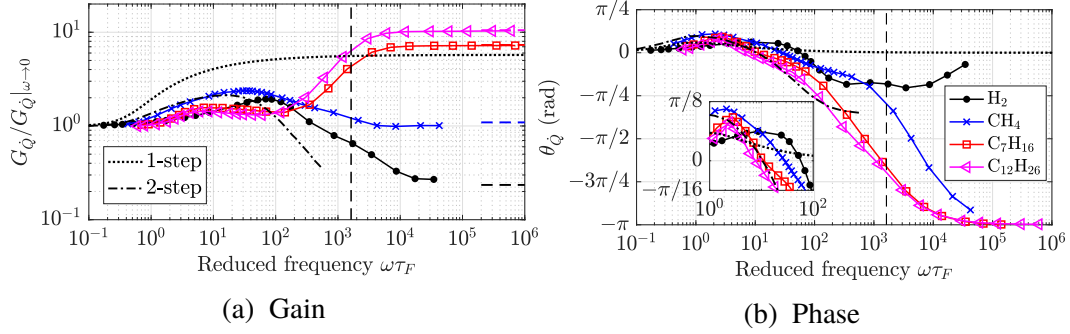
(b) Phase

Figure 4.6: Gain and phase of the fluctuating heat release for Cases 1, 2, 3a and 4. The vertical dashed line frequency at which $\lambda_b = 10 l_F$ for the most restrictive case. The horizontal lines denote the high-frequency solutions obtained using Eq. (4.18).

at high frequencies. More precisely, it decreases with ω^{-1}, which will be explored in Sec. 4.2.4. Note that the phases and gains of some intermediate species are not shown at very high frequencies, as their evaluation becomes difficult due to the small amplitude of the fluctuating response. Figure 4.8 shows the flame structure at different moments during the acoustic cycle, for Case 3a at $f = 1$ kHz (i.e. $\omega\tau_F = 6.9$). This frequency was chosen as it corresponds to a local maximum in $G_{\dot{Q}}$. One can see that, even when the gain is maximum, the species profiles change very little during an acoustic cycle. That is why, at very high frequencies, when fluctuations are even smaller, the extraction of the gain and phase becomes difficult. Fig. 4.9 shows the mean of various quantities for Case 3a (n-heptane), normalized by their value at steady state, i.e., when the flame is unperturbed. All quantities change by less than 2%, indicating that the flame response is linear for the pressure amplitude considered (i.e., $A_p = 5$ kPa). All present results are thus also valid for $A_p < 5$ kPa. This is confirmed in Fig. 4.10, in which the flame response for Case 1 at $A_p = 500$ Pa and 5 kPa is compared. The agreement is excellent, therefore confirming that we are in the linear regime. We also ran an additional simulation with all the diffusion coefficients (i.e., D_i, α, ν) multiplied by 10. Although l_F, S_L and $\dot{Q}$ all increase by a factor of $\sqrt{10}$, the gains and phases are identical once properly normalized.

Additionally, we investigated variations due to the equivalence ratio for n-heptane. Cases 3a, 3b, and 3c are at the same flow conditions, and only differ by their equivalence ratio ($\phi = 0.9$, 0.7 and 1.3, respectively). The response plots for Cases 3b and 3c are shown in Fig.4.11. Qualitatively, the heat release and species responses are identical. Quantitatively, they change slightly, as expected since the steady-state flame structures are different.

(a) Normalized gain for Case 1

(b) Phase angle for Case 1

(c) Normalized gain for Case 2

(d) Phase angle for Case 2

(e) Normalized gain for Case 3a

(f) Phase angle for Case 3a

(g) Normalized gain for Case 4

(h) Phase angle for Case 4
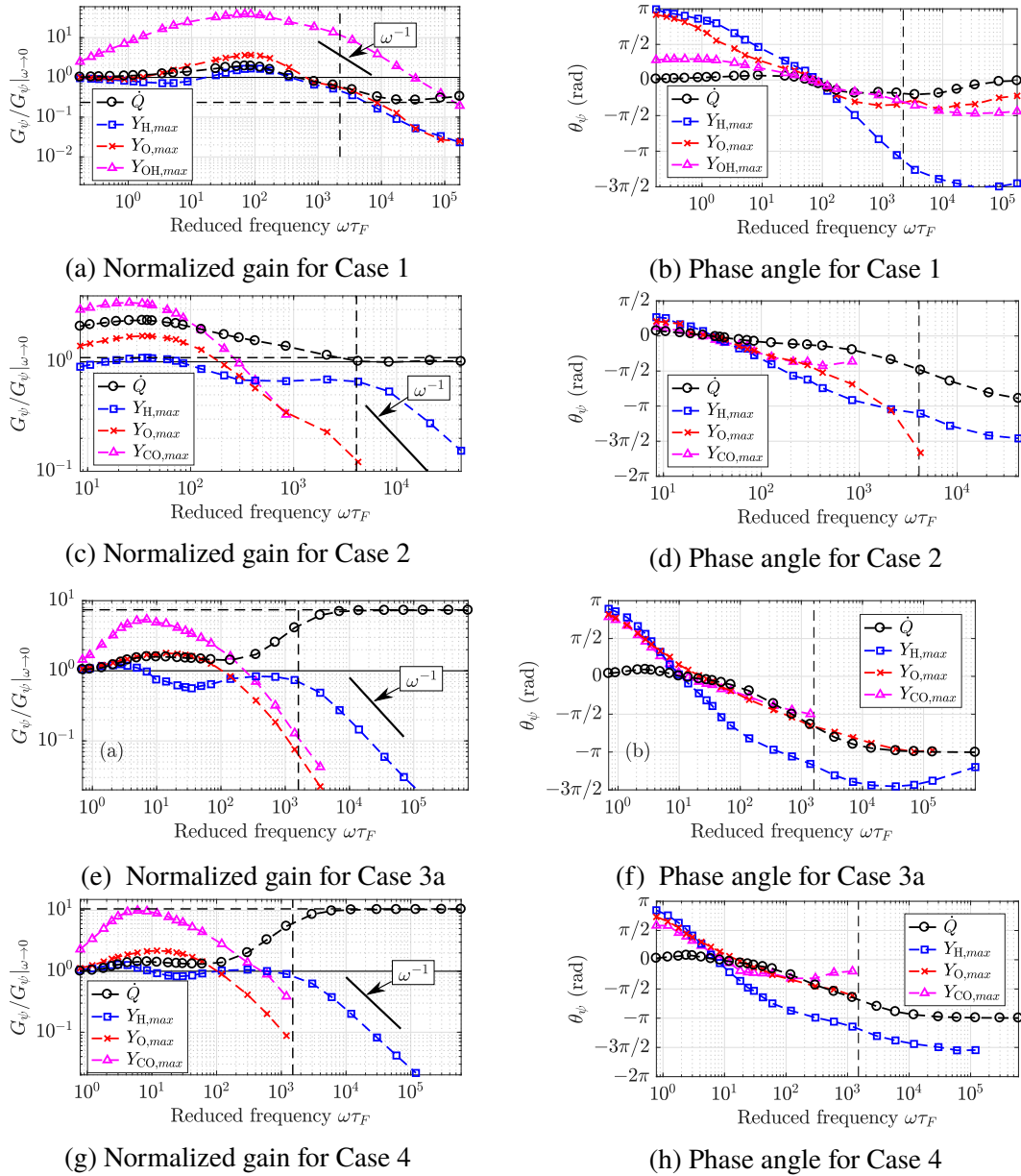
Figure 4.7: Gain (left) and phase (right) of heat release (black circles) and different intermediate species: hydrogen radical [blue squares], oxygen radical [red crosses], and carbon monoxide [pink triangles] for the hydrocarbon fuels (Case 2, 3a, and 4), and hydrogen radical [blue squares], oxygen radical [red crosses], and hydroxyl radical [pink triangles] for hydrogen (Case 1). The phases and gains of some intermediate species are not shown for certain frequencies, as their evaluation becomes difficult due to the small amplitude of the fluctuating response at high frequency.
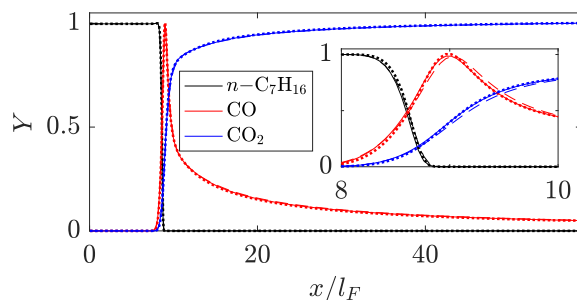
Figure 4.8: Flame structure for Case 3a at $f = 1$ kHz. The solid, dotted, and dashed lines correspond to the flame response at $p_t = p_0$, $p_t = p_0 + A_p$, and $p_t = p_0 - A_p$, respectively.
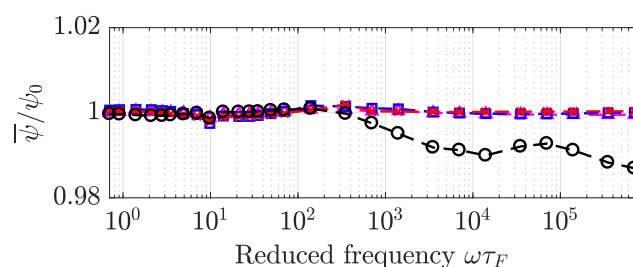
Figure 4.9: Normalized mean of the integrated heat release and the maximum of different intermediate species, for Case 3a (n-heptane). The means are normalized by their steady state value. The legend is the same as for Fig. 4.7f.

(a) Normalized gain

(b) Phase angle
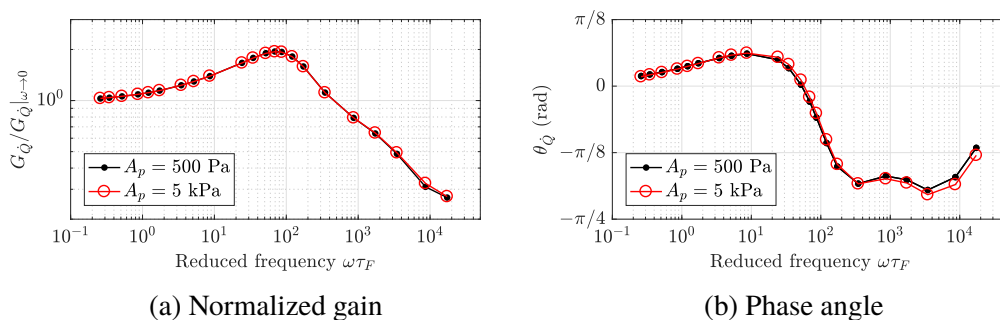
Figure 4.10: Comparison of the gain and phase of the heat release for Case 1 (hydrogen) for $A_p = 500$ Pa (black dots) and $A_p = 5$ kPa (open red circles).

Regarding $\dot{Q}$, one can see from Fig. 4.6 that the cases differ mainly by the magnitude of the gains (most notably $G_{\dot{Q}}$ at high frequency), the frequency for which the local peaks occur in the middle range, and the phase at high frequency. These variations in the flame responses are due to different chemical kinetics, which underscores the need for detailed chemistry when investigating direct pressure effects.

(a) Normalized gain for Case 3b

(b) Phase angle for Case 3b

(c) Normalized gain for Case 3c

(d) Phase angle for Case 3c
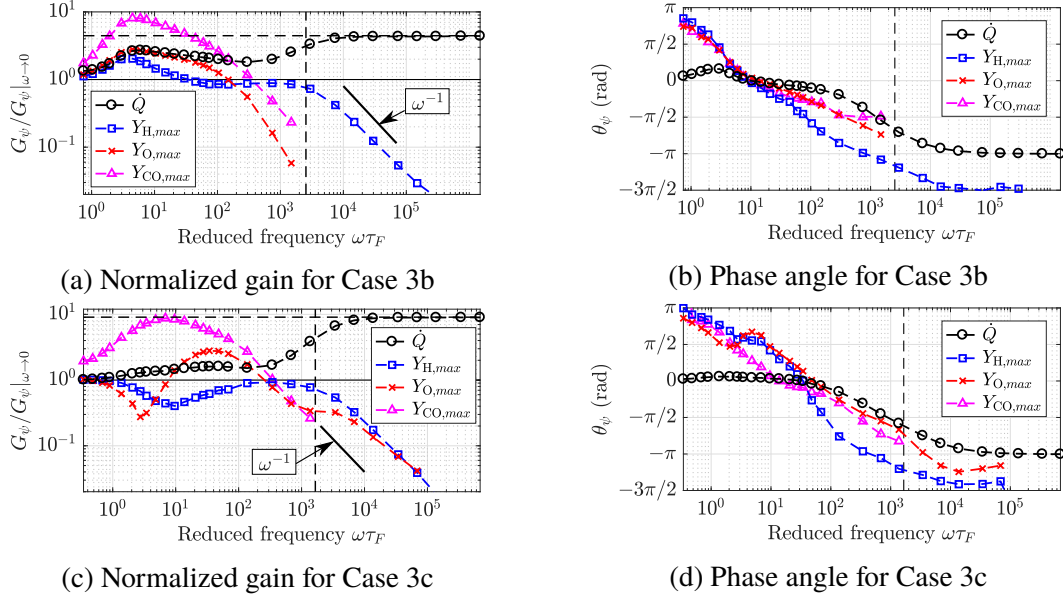
Figure 4.11: Gain and phase of heat release (black circles) and different intermediate species: hydrogen radical [blue squares], oxygen radical [red crosses], and carbon monoxide [pink triangles]. The phases and gains of some intermediate species are not shown for certain frequencies, as their evaluation becomes difficult due to the small amplitude of the fluctuating response at high frequency.

4.2.2 Low frequency limit

The acoustic wave impacts the flame response through the pressure time-derivative term in Eq. (2.42). This term scales like $A_p \omega$ and thus becomes negligible compared with the others when $\omega \to 0$. In this limit, the flame is in quasi-steady state. Therefore, the phase of all the flow variables has to be either 0 or π, and the gain of the fluctuating response $G_\psi|_{\omega \to 0}$ can be computed by carrying two steady-state simulations, one at the maximum pressure $p_t = p_0 + p_a$ and one at the minimum $p_t = p_0 - p_a$. In these two simulations, the inlet temperature is adjusted according to Eq. (4.2). The heat release gains in the low-frequency limit $G_{\dot{Q}}|_{\omega \to 0}$ are given in Table 4.2 for the different cases. In Figs. 4.7 and 4.11, at low frequencies, the normalized gains approach their predicted value and the phases go to 0 or π, as expected. The only exception is Case 2, for which the heat release and species gains are still far from $G_\psi/G_\psi|_{\omega \to 0} \to 1$ for $\omega \tau_F = 1$. It is likely that the GRI-Mech 3.0 mechanism contains large chemical timescales that would require one to perform simulations at even lower acoustic frequencies to recover the quasi-steady state behavior.

Table 4.2: Gain of the heat release fluctuations when $\omega \to 0$.

Case	1	2	3a	3b	3c	4
$G_{\dot{Q}}\vert_{\omega \to 0}$	1.01	0.78	0.94	0.72	0.91	0.91

4.2.3 Middle range frequencies

In Fig. 4.6, we first observe that the phase of the fluctuating heat release response $\theta_{\dot{Q}}$ becomes zero for $\omega \tau_F \sim 1 - 100$. The frequency for which $\dot{Q}$ is in phase with p_t roughly corresponds to a local maximum gain $G_{\dot{Q}}$. Taking the example of Case 3a (Figs. 4.7e and 4.7f), the frequency for which $\theta_{\dot{Q}} = 0$ also roughly corresponds to $\theta_{Y_H,max} = 0$, $\theta_{Y_O,max} = 0$, and $\theta_{Y_{CO},max} = 0$. Heat release increases the temperature locally, which in turn increases most reaction rates. Radical species being involved in many key reactions, a higher concentration will tend to speed up the combustion process. If $Y_{H,max}$, $Y_{O,max}$, and $\dot{Q}$ are all in phase with the acoustic signal, more heat release is thus expected. This might explain why the gain $(G_{\dot{Q}})$ reaches a local peak when the phase is almost zero. The response plots of three other radicals, i.e., hydroxyl radical (OH), methyl radical (CH$_3$) and formyl radical (HCO), are presented in Appendix D (Figs. D.1 and D.2) for all cases considered. Like for O and H, the species gains are seen to increase initially for $\omega \tau_F > 1$, and then go down as ω^{-1} at high frequencies. The frequency at which their phase is zero is also very close to the frequency at which $G_{\dot{Q}}$ is maximum.

4.2.4 High frequency limit - species

We now consider the flame response at high frequencies. It is important to remember that the present results were obtained using a low Mach number approximation, which breaks down when $\omega \to \infty$ (see Sec. 4.1.2.1). That being said, these results provide valuable insight into the dynamics of the chemical system, decoupled from compressibility effects.

By splitting Y_i into its mean $\overline{Y}_i$ and fluctuating Y_i' components, considering small fluctuations (relative to the mean), and leveraging the fact that the flame sits at a velocity node (i.e., $u = \overline{u}$), Eqs. (2.4) and (2.50) can be rearranged to obtain a transport equation for Y_i'

$$\frac{DY_i'}{Dt} = -\frac{1}{\overline{\rho}} \nabla \cdot \dot{j}_i' + \frac{W_i}{\overline{\rho}} \sum_{j=1}^{n_R} \nu_{j,i} \dot{R}_j', \tag{4.13}$$

where $D(\ )/Dt$ is the material derivative. From Eq. (2.50), we obtain the linearized

fluctuating production term

$$\frac{\dot{R}'_j}{\overline{\dot{R}_j}} = \left(n_j + \frac{E_a}{R\overline{T}}\right)\frac{T'}{\overline{T}} + \left(\sum_{i=1}^{n_S} v^r_{j,i}\right)\frac{\rho'}{\overline{\rho}} + \sum_{i=1}^{n_S} v^r_{j,i}\frac{Y'_i}{\overline{Y}_i}. \tag{4.14}$$

In the linearized approximation, A_ρ and A_T are a linear combination of A_p (i.e., acoustic forcing) and A_{Y_i} (i.e., unsteady chemistry). As a result, the Right-Hand Side (RHS) of Eq. (4.14) also scales linearly with A_p and A_{Y_i}. In Eq. (4.13), the diffusion term scales like A_{Y_i} (see Eq. (2.7)), and the material derivative scales like ωA_{Y_i}. Hence, A_{Y_i} has to decrease for ω sufficiently large, since A_p is imposed and A_{Y_i} is bounded by A_p. Once A_{Y_i} becomes small enough, the relevant scaling for the RHS of Eq. (4.14) becomes A_p only, such that $A_{Y_i} \sim \omega^{-1} A_p$. This is what was observed in Fig. 4.7, and this observation holds for all the species considered, as can be seen in Figs. D.1 and D.2.

4.2.5 High frequency limit - heat release

In this section, we detail how the high frequency behavior of the heat release gain $G_{\dot{Q}}|_{\omega\to\infty}$ can be obtained relatively simply from the steady-state solution at p_0.

Let c be some monotonically increasing progress variable that is not *directly* impacted by the pressure fluctuations. Temperature and density cannot be used as progress variables since they are related to p_t through the equation of state. A combination of the mass fractions of combustion products would be suitable. In the limit $\omega \to \infty$, the gains of all species mass fractions go to zero. Chemistry is thus "frozen" and the instantaneous species mass fractions are only functions of the progress variable. Under small pressure fluctuations and as shown in Sec. 4.2.1, the mean species profiles (as $\omega \to \infty$) are the same as the steady state profiles, i.e., $\overline{Y}_i(c) = Y_{i,0}(c)$.

The heat release rate may be rewritten as

$$\dot{Q} = -\sum_{j=1}^{n_R} \Delta h_{R,j} \int_{x=0}^{L} \dot{R}_j dx, \tag{4.15}$$

where $\Delta h_{R,j}$ is the enthalpy of reaction for reaction j. While $G_{Y_i} \to 0$, the flame still experiences the isentropic thermodynamic changes associated with the acoustic wave, i.e.,

$$T^* = T_0(c)\left(\frac{p_t(t)}{p_0}\right)^{\frac{\gamma-1}{\gamma}}, \quad \rho^* = \rho_0(c)\left(\frac{p_t(t)}{p_0}\right)^{\frac{1}{\gamma}}. \tag{4.16}$$

We can now evaluate $\dot{R}_j|_{\omega\to\infty}$ by using $\rho = \rho^*, T = T^*$ and $Y_i = Y_{i,0}$ in Eq. (2.51), which becomes

$$\dot{R}_j|_{\omega\to\infty} = A_j T_0^{n_j} \exp\left(-\frac{E_{a,j}}{RT_0}\left(\frac{p_0}{p_t}\right)^{\frac{\gamma-1}{\gamma}}\right) \prod_{i=1}^{n_S} \left(\frac{\rho_0 Y_{i,0}}{W_i}\right)^{v_{j,i}^r} \left(\frac{p_t}{p_0}\right)^{\frac{n_j(\gamma-1)+v_{j,i}^r}{\gamma}} . \tag{4.17}$$

An additional consideration must be taken since the flame is periodically compressed/expanded by the acoustic wave. Since the flame structure remains intact, $dx = (\rho_0/\rho)dx_0 = (p_t/p_0)^{-1/\gamma}dx_0$, with x_0 being the spatial coordinate in the steady-state solution at $p_t = p_0$. Putting everything together, Eq. (4.15) becomes

$$\dot{Q}|_{\omega\to\infty} = -\sum_{j=1}^{n_R} \Delta h_{R,j} \int_{x_0=0}^{L} \dot{R}_j|_{\omega\to\infty} \left(\frac{p_t}{p_0}\right)^{-\frac{1}{\gamma}} dx_0 . \tag{4.18}$$

To compute $G_{\dot{Q}}|_{\omega\to\infty}$, we use Eq. (4.11) with $A_{\dot{Q}}$ obtained by evaluating Eq. (4.18) at $p_t = p_0 \pm p_a$. In Fig. 4.6a, the horizontal dashed lines show the high frequency gains obtained using this procedure. The agreement with the unsteady simulations is excellent.

4.3 Compressible results and engine-relevant conditions

In this section, we perform fully compressible simulations using the outlet wave modulation framework detailed in Sec. 4.1.2.2 for hydrogen/air and n-heptane/air, at standard thermodynamic conditions (Cases 1 and 3a), and engine-relevant conditions (Cases 5 and 6). The focus is placed on comparing the compressible results with the ones obtained using the low Mach number approximation.

4.3.1 Heat release

Figure 4.12 shows the normalized gain and phase of the heat release for the four different cases considered. The blue open circles are obtained using the fully compressible framework, while the red dots are obtained using the low Mach number approximation. To aid the reader, the frequencies at which $\lambda_b = l_{F,0}$ and $\lambda_b = 10l_{F,0}$ are indicated by vertical dotted and dashed lines, respectively, where λ_b is the acoustic wavelength in the burnt region.

The results obtained using the low Mach number and the fully compressible frameworks are in excellent agreement at low frequencies, as expected. For all cases, as explored in Sec. 4.2.3, the gain peaks locally for $\omega\tau_{F,0} \sim 10^1 - 10^2$, and the corresponding phase is close to zero.

(a) Normalized gain for Case 3a

(b) Phase angle for Case 3a

(c) Normalized gain for Case 6

(d) Phase angle for Case 6

(e) Normalized gain for Case 1

(f) Phase angle for Case 1

(g) Normalized gain for Case 5

(h) Phase angle for Case 5
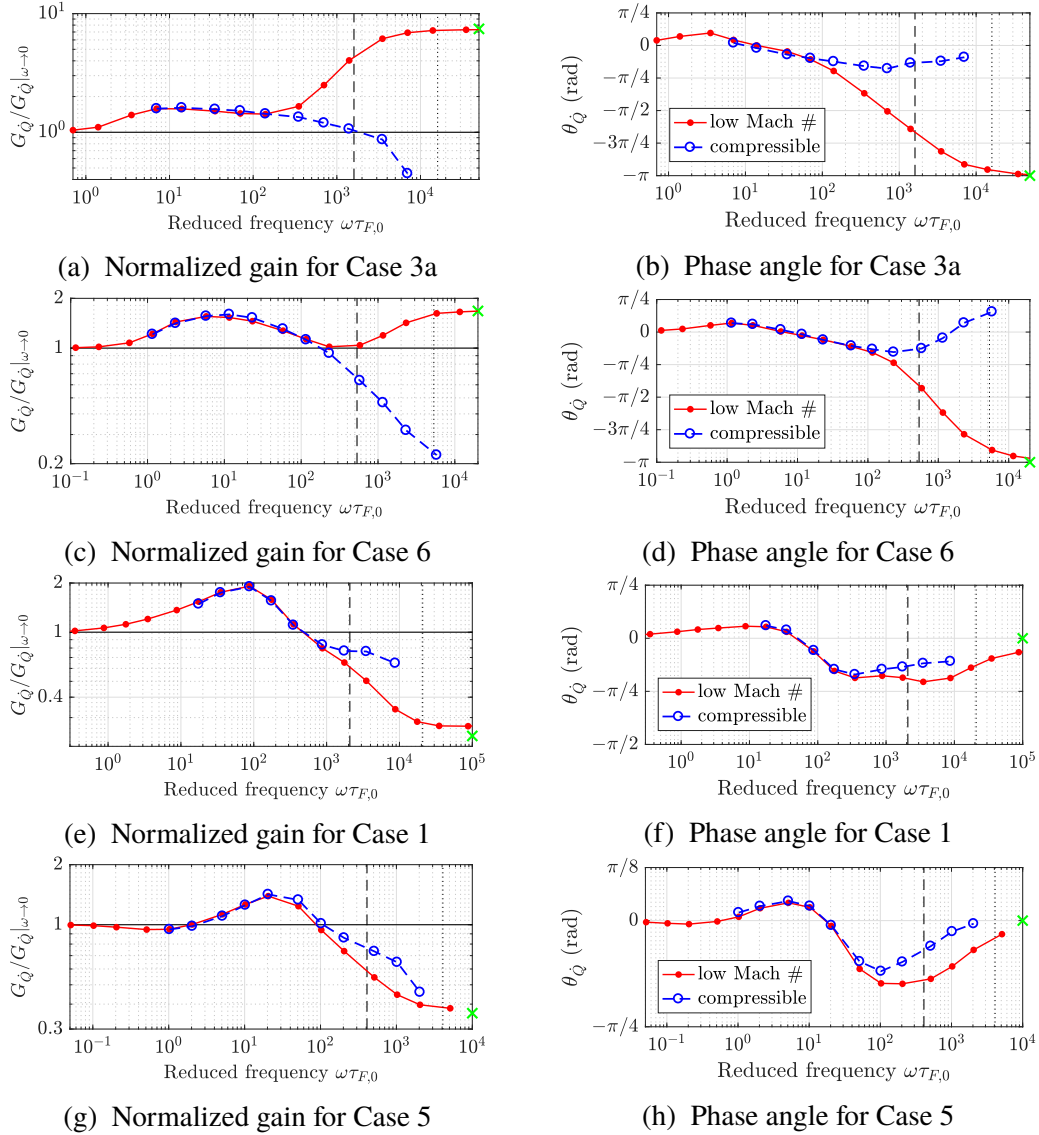
Figure 4.12: Normalized gain and phase angle of the fluctuating heat release $\dot{Q}$. The red dots were obtained by solving the low Mach number approximation equations, and the blue open circles were obtained using the fully compressible formulation. The vertical dotted and dashed lines are the frequency at which $\lambda_b = l_{F,0}$ and $\lambda_b = 10l_{F,0}$, respectively.

The two frameworks start yielding different results for $\lambda_b/l_{F,0} \lesssim 10^2$, which corresponds to $f \gtrsim 10^4$ Hz for the cases at standard thermodynamic conditions, and $f \gtrsim 10^6$ Hz for the ones at elevated pressure and temperature. For comparison purposes, typical frequencies at which thermo-acoustic instabilities occur in practical combustors are $f \sim 10^3 - 10^4$ Hz [105]. For $\lambda_b/l_{F,0} \lesssim 10^2$, the gain reaches a constant value at high frequencies for the simulations using the low Mach number approximation, which was investigated in Sec. 4.2.5. On the other hand, for the fully compressible simulations, the gain decreases sharply at high frequency for Cases 1 and 3a. One of the main assumptions in the low Mach number simulations is that the acoustic pressure is constant in space. Obviously, this assumption performs well at frequencies for which $l_{F,0} \ll \lambda_b$. However, for sufficiently high frequencies, the spatial variations in pressure impact the flame dynamics, and the results obtained with the low Mach number approximation are inaccurate. It is interesting to note that deviations between the two sets of simulation results occur for wavelengths significantly larger than the flame thickness.

4.3.2 Species response

Figure 4.13 shows the gain and phase of the response of key intermediate species (hydrogen radical and oxygen radial) for Case 5, corresponding to hydrogen/air at elevated temperature and pressure.

(a) Normalized gain   (b) Phase angle
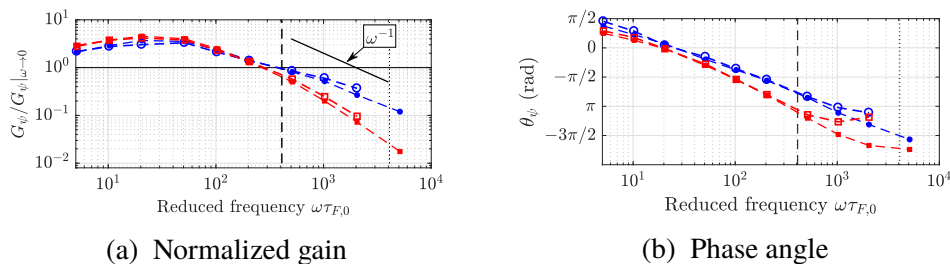
Figure 4.13: Response of different intermediate species (H radical [blue circles] and O radical [red squares]) for case 5 using the low Mach number approximation (closed symbols) and the fully compressible formulation (open symbols).

Two key observations should be made. First, the species responses are in very good agreement for the low Mach number approximation and the fully compressible formulation. In other words, the spatial fluctuations of the pressure field do not appear to impact the species profiles. Second, in the high frequency limit, i.e., $\omega \to \infty$, chemistry becomes "frozen". The acoustic timescale is much faster than any chemical timescale in the system, and the species don't have time to react to the thermodynamic changes.

This behavior was observed in Sec. 4.2.4 under the low Mach number approximation, and it was found that the species gain should decrease as ω^{-1}. This result was obtained by considering the scaling of the different terms in the transport equation for the fluctuating species mass fractions Y'_s. In the low Mach number case, the diffusion term scales like A_{Y_s}, while it scales like $\kappa^2 A_{Y_s}$ in the fully compressible case, where κ is the acoustic wavenumber. In the fully compressible simulations, the species gain should hence decrease as ω^{-2} instead of ω^{-1}, when the Péclet number $Pe = \omega/(D_s \kappa^2) < 1$. This corresponds to $\omega\tau_{F,0} > 10^6$, which is much greater than the frequencies considered in this work ($\omega\tau_{F,0} < 10^4$). Hence, the species responses are expected to be similar for the low Mach number and fully compressible cases, as can be observed in Fig. 4.13.

4.3.3 High frequency limit

The intent is to leverage the frozen nature of the chemistry to estimate the gain and phase response of the heat release at high frequencies.

Here, we follow a similar approach to the one employed in Sec. 4.2.5. At high frequency, the species profiles are the same as the ones of the unperturbed flame, i.e., $Y_s(c)|_{\omega \to \infty} = Y_{s,0}(c)$, where c is any monotonically increasing progress variable that is not *directly* impacted by the acoustic pressure fluctuations. Leveraging the fact that acoustic perturbations are isentropic, one can then predict the sensitivity of the local heat release $\dot{h}$ to pressure oscillations as $\omega \to \infty$, directly from the unperturbed solution. In this limit, chemistry is frozen, and the fluctuation in heat release rate $\dot{Q}'|_{\omega \to \infty}$ is only a function of the isentropic thermodynamic fluctuations. Linearizing Eq. (4.9), one obtains

$$\dot{Q}'|_{\omega \to \infty} = - \int_{x_0=0}^{L} \rho_0 \left.\frac{\partial \dot{h}}{\partial p}\right|_0 [p(x,t) - p_0] \; dx_0 \,, \tag{4.19}$$

where x_0 is the spatial coordinate in the steady-state solution without acoustic perturbations. To obtain Eq. (4.19), the relation $\rho dx = \rho_0 dx_0$ was used, which accounts for the expansion/contraction of the flame due to the acoustic wave. Figure 4.14 shows $(\partial \dot{h}/\partial p)|_0$ for Case 6. Several regions can be identified. In the close proximity of the maximum heat release rate ($x/L \approx 0.18$), pressure fluctuations lead to an increased heat release rate, and $(\partial \dot{h}/\partial p)|_0 > 0$. In the post-flame region ($x/L \gtrsim 0.19$), the opposite is observed, i.e., $(\partial \dot{h}/\partial p)|_0 < 0$. In the low Mach number approximation, the flame only sees a spatially constant, time varying acoustic pressure. Hence, one can compute $\int_x (\partial \dot{h}/\partial p)|_0 \, dx$ to predict the gain and phase of the heat release as $\omega \to \infty$. These theoretical values are represented by

green crosses in Fig. 4.12 and are in excellent agreement with the simulation results. As $(\partial \dot{h}/\partial p)|_0$ takes negative values for a large fraction of the domain, its spatial integral is overall negative. This explains why $\theta_{\dot{Q}} \to -\pi$ as $\omega \to \infty$ for the low Mach number simulations in Fig. 4.12d. For the fully compressible simulations, the acoustic pressure varies sinusoidally in space as $(p - p_0) \propto \sin(\omega t - kx)$. Under these conditions, Eq. 4.19 is nothing more than the Fourier transform of $(\partial \dot{h}/\partial p)|_0$. Hence, the shape of this function ultimately controls the high frequency behavior of the flame. Since $(\partial \dot{h}/\partial p)|_0$ is continuous and compactly supported, its Fourier modes decay to zero as the frequency goes to infinity. This implies that the heat release gain $G_{\dot{Q}} \to 0$ as $\omega \to \infty$. The flame essentially sees the average pressure field and behaves as if there was no acoustic perturbation. This is indeed the trend that can be observed in Fig. 4.12 for all the fully compressible simulations.

From Fig. 4.14, it can also be seen that the length for which the heat release is sensitive to pressure fluctuations is much larger than the flame thickness, i.e., $0 \lesssim (x - x_F)/l_F \lesssim 10$. Hence, the acoustic wavelength for which a significant difference is expected between integrating $(\partial \dot{h}/\partial p)|_0$ against a spatially-constant pressure (low Mach number approach) and against a sinusoidal pressure field (fully compressible approach) is expected to be much larger than the flame thickness. This might explain why the departure between the low Mach number and fully compressible frameworks happens for $\lambda_b \gg l_{F,0}$, as seen in Fig. 4.12.
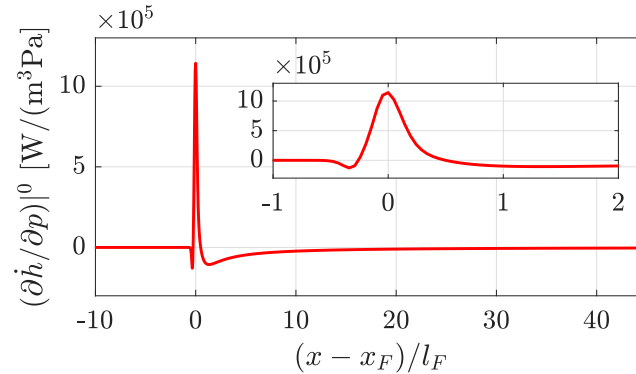
Figure 4.14: Sensitivity of the local heat release $\dot{h}$ to isentropic pressure changes for Case 6.

Finally, to highlight the need for detailed chemistry, Fig. 4.15 shows the reactions contributing the most to the gain when $\omega \to \infty$ for the simulations using the low Mach number approximation. For Case 6, the phase $\theta_{\dot{Q}} \to -\pi$ (see Fig. 4.12d) because endothermic reactions contribute the most to the fluctuating heat release response, causing it to be out of phase with pressure. On the other hand, exothermic

reactions dominate for Case 5, which explains why $\theta_{\dot{Q}}|_{\omega\to\infty} \to 0$ in Fig. 4.12h. In both case, the high-frequency behavior is controlled by the combination of multiple elementary reactions, hence stressing the need for detailed chemistry when investigating the response of these complex chemical systems.

(a) Case 5 - Hydrogen

(b) Case 6 - n-Heptane
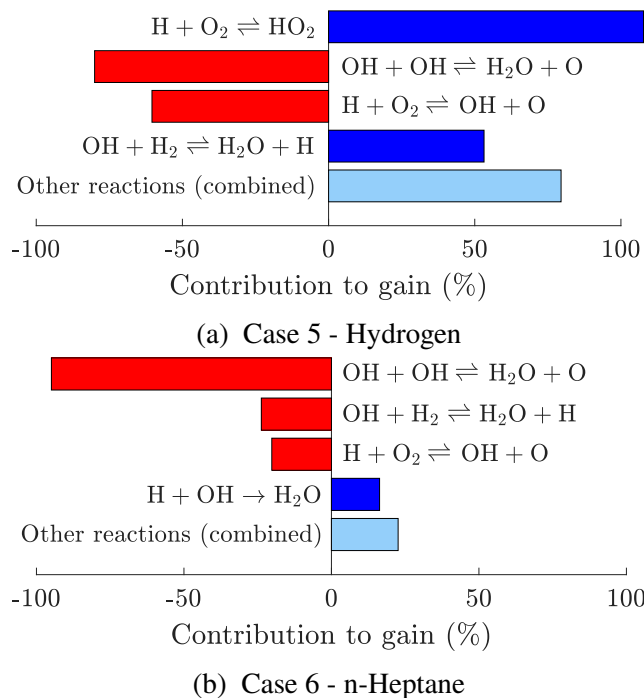
Figure 4.15: Main reactions contributing to the fluctuating heat release response when $\omega \to \infty$ for the low Mach number approximation. The sum of all reactions adds up to -100% for *n*-heptane (out of phase), and 100% for hydrogen (in phase).

4.4 Summary

In this chapter, we investigated the direct pressure effects on the dynamics of laminar premixed flames, i.e., the response of flames subjected to the thermodynamic fluctuations that accompany an acoustic wave. First, we described the numerical methodology for both the low Mach number and compressible simulations. Under the low Mach number approximation, we extracted the gain and phase of the heat release. For all fuels, we observed a local peak for $\omega\tau_F \sim 10^0 - 10^2$, corresponding to a phase angle $\theta_{\dot{Q}} \approx 0$, therefore being unstable according to the Rayleigh criterion. We also showed that the flame behavior in the high frequency limit can be predicted from the steady state solution. Then, we used a fully compressible formulation to investigate the direct pressure effects under engine-relevant conditions. The differences between results obtained with the fully compressible framework and the low Mach number approximation were thoroughly investigated. The low Mach number

approximation and the fully compressible framework are in good agreement at low frequencies, as expected. At higher frequencies, i.e., for $\lambda_b/l_F, 0 \lesssim 10^2$, the two frameworks differ. In the high frequency limit, the gain reaches a plateau using the low Mach number approximation, while it goes to zero using the fully compressible framework. This is related to the spatial variations in the acoustic pressure field, which are not captured by the low Mach number approximation. However, the low Mach number framework is found to yield accurate results for practically-relevant acoustic frequencies.

C h a p t e r   5

PHYSICS-BASED FORCING FOR COMPRESSIBLE FLOWS

When performing simulations of turbulence using simplified geometries such as a triply-periodic box, one has to append a forcing term to the momentum equation to sustain turbulence, since there is no large-scale turbulence generation mechanism. As reviewed in Sec. 1.3.4, various forcing schemes have been proposed and employed in the literature. The aim of most of these schemes is simply to maintain turbulence at a desired level, and are not necessarily representative of the turbulence injection from the missing large scales. For incompressible flows, Dhandapani *et al.*[38] and Rah *et al.*[35] derived a physics-based forcing scheme for a shear layer and the centerline of a jet, respectively. They considered the governing equations for the small scales of the flow, following the decomposition of the velocity field into large and small scales. The proper forcing terms then arise naturally. In this chapter, we seek to extend this approach to compressible flows, where special care must be taken regarding the energy equation. In Sec. 5.1, we explain the general framework, which we apply to the centerline of a jet in Sec. 5.2. We then explore an issue that has plagued previous simulations of forced compressible turbulence using periodic boundary conditions: large coherent oscillations of the dilatational component of the velocity field [27, 28]. In Sec. 5.3, we investigate the mechanisms that cause this behavior. In Sec. 5.4, we apply a modification to the forcing scheme to reduce its highly oscillatory nature. Finally, we summarize the findings in Sec. 5.5.

5.1   Methodology

5.1.1   Velocity decomposition

We consider the fully compressible Navier-Stokes equations i.e., Eqs. (2.1)–(2.3), closed with the ideal gas law (Eq. (2.11)). We derive the forcing scheme for a single fluid, but results can easily be extended to mixtures of different fluids.

The idea is to simulate a small portion of a flow, e.g., the vicinity of the centerline of a turbulent jet, as illustrated by the schematics shown in Fig. 5.1. Following the same notation as Dhandapani [106], we split the velocity field into two components:

$$u_i = u_i^r + u_i^i, \tag{5.1}$$

where u_i^r is the resolved (small-scale) part of the velocity field, and u_i^i is the imposed
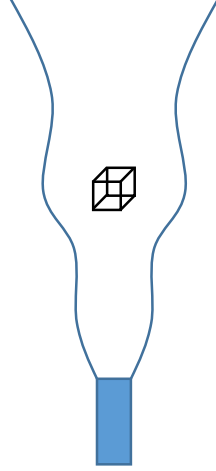
Figure 5.1: Schematics of a typical target domain for our simulations (box, in black), which is a small portion of a full flow (jet, in blue).

(large-scale) component. The latter is assumed to be known beforehand, e.g., from experiments, theory, or results obtained from lower-fidelity simulation frameworks such as Large Eddy Simulations (LES) or Reynolds-Averaged Navier-Stokes simulations (RANS). Following the decomposition given by Eq. (5.1), Eqs. (2.1)–(2.3) become

$$\frac{\partial \rho}{\partial t} + (\rho u_i^r)_{,i} = -u_i^i \rho_{,i} - \rho u_{i,i}^i \,, \tag{5.2}$$

$$\frac{\partial \rho u_i^r}{\partial t} + (\rho u_j^r u_i^r)_{,j} + p_{,i} - \tau_{ij,j}^r = -u_j^i (\rho u_i^r)_{,j}$$
$$- \rho u_i^r u_{j,j}^i - \rho u_j^r u_{i,j}^i + \tau_{ij,j}^i - \rho \frac{\partial u_i^i}{\partial t} - \rho u_j^i u_{i,j}^i \,, \tag{5.3}$$

$$\frac{\partial \rho e_t^r}{\partial t} + (\rho u_i^r h_t^r)_{,i} + q_{i,i} - \left(u_j^r \tau_{ij}^r \right)_{,i} = -u_i^i \left(\rho e_t^r \right)_{,i} - \rho h_t^r u_{i,i}^i$$
$$- \rho u_i^r u_j^r u_{i,j}^i + \tau_{ij}^r u_{i,j}^i + \tau_{ij}^i u_{i,j}^i + \left(u_j^r \tau_{ij}^i \right)_{,i} - \rho u_i^r \frac{\partial u_i^i}{\partial t} - \rho u_i^r u_j^i u_{i,j}^i \,, \tag{5.4}$$

where

$$e_t^r = e + u_i^r u_i^r / 2 \,, \tag{5.5}$$

$$h_t^r = h + u_i^r u_i^r / 2 \,, \tag{5.6}$$

and

$$\tau_{ij}^r = \mu(u_{i,j}^r + u_{j,i}^r - (2/3)u_{k,k}^r \delta_{ij}) \,. \tag{5.7}$$

Note that the summation convention only applies to the lower indices. Details about the derivation of Eqs. (5.3) and (5.4) can be found in Appendix E. The Left-Hand Side (LHS) of Eqs. (5.2) to (5.4) is identical to Eqs. (2.1) to (2.3), but we now have several additional source terms showing up on the Right-Hand Side (RHS). Each equation includes advection by the imposed flow, i.e., terms of the form $u_i^i \phi_{,i}$, where ϕ is the transported quantity, and dilatation by the imposed flow, i.e., terms of the form $\phi u_{i,i}^i$. Additional, we have production terms: $\rho u_j^r u_{i,j}^i$ in the momentum equation, and $\rho u_i^r u_j^i u_{i,j}^i$ in the energy equation. They are referred to as production terms because they are responsible for the injection of turbulent kinetic energy due to shear by the imposed flow. We also have $\rho u_j^i u_{i,j}^i$ (momentum), $\rho u_i^r u_j^i u_{i,j}^i$ (energy), and terms involving the time derivative of the imposed flow. They are referred to as acceleration terms since they act like a body force. Finally, we have additional viscous terms. For the rest of the analysis, we will consider a statistically-stationary flow in which u_i^i is constant in time. Hence, the additional terms involving the time derivative of the imposed flow in Eqs. (5.3) and (5.4) drop.

5.1.2 Favre averaging and Helmholtz decomposition

For variable-density flows, it is common to perform a Favre velocity decomposition, i.e., $u_i = u_i'' + \tilde{u}_i$, where $\tilde{u}_i = \langle \rho u_i \rangle / \langle \rho \rangle$ is the Favre average, and $\langle \ \rangle$ denotes the ensemble average. We can further perform a Helmholtz decomposition of the Favre-averaged velocity field, i.e., $\tilde{u}_i = \tilde{u}_i^s + \tilde{u}_i^d$, where $\tilde{u}_i^s$ and $\tilde{u}_i^d$ are the solenoidal and dilatational components, respectively. It is convenient to choose

$$u_i^i = \tilde{u}_i^s, \qquad u_i^r = u_i'' + \tilde{u}_i^d . \tag{5.8}$$

A schematic of this decomposition is shown in Fig. 5.1.2. Following Eq. (5.8), the imposed part of the velocity field being divergence-free, the additional terms involving dilatation by the imposed flow in Eq. (5.2) to (5.4) are identically zero.
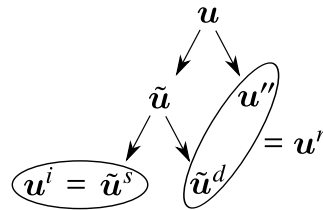
Figure 5.2: Schematic diagram of the velocity decomposition presented in Sec. 5.1.2.

5.1.3 Additional viscous terms involving τ^i

We seek to compare the magnitude of the viscous terms involving the imposed τ^i_{ij} and resolved τ^r_{ij} components of the flow. Since we are dealing with matrices, we estimate the ratio of the ensemble average of the double-dot products of the viscous stress tensors, i.e.,

$$\frac{\langle \tau^i_{ij} \tau^i_{ij} \rangle}{\langle \tau^r_{ij} \tau^r_{ij} \rangle} = \frac{\tau^i_{ij} \tau^i_{ij}}{\langle \tau^r_{ij} \tau^r_{ij} \rangle} \approx \frac{S^i_{ij} S^i_{ij}}{\langle S^r_{ij} S^r_{ij} \rangle} \approx \frac{\epsilon^i}{\epsilon^r}, \tag{5.9}$$

where S_{ij} is the rate-of-strain tensor, ϵ^i is the dissipation rate of the imposed flow, and ϵ^r is the dissipation rate of the resolved flow. The molecular viscosity μ has been taken to be constant in Eq. (5.9) for scaling purposes. For incompressible flows, the scaling $\epsilon^i / \epsilon^r \sim Re_t^{-1}$ is generally accepted [22], and we assume that it remains valid for compressible flows. At sufficiently high turbulent Reynolds numbers Re_t, all the terms involving τ^i_{ij} on the RHS of Eqs. (5.3) and (5.4) are small compared to the terms involving τ^r_{ij}, and they can be safely neglected. We will then simply refer to τ^r_{ij} as τ_{ij}.

By a similar reasoning process, the remaining term on the RHS of Eq. (5.4), i.e., $\tau_{ij} u^i_{i,j}$, is small when compared to $\tau_{ij} u^r_{i,j}$ since $u^i_{i,j} u^i_{i,j} / \langle u^r_{i,j} u^r_{i,j} \rangle \sim Re_t^{-1}$. It can thus be removed. Equations (5.2) to (5.4) reduce to

$$\frac{\partial \rho}{\partial t} + (\rho u^r_i)_{,i} = -u^i_i \rho_{,i} , \tag{5.10}$$

$$\frac{\partial \rho u^r_i}{\partial t} + (\rho u^r_j u^r_i)_{,j} + p_{,i} - \tau_{ij,j} = -u^i_j (\rho u^r_i)_{,j} - \rho u^r_j u^i_{i,j} - \rho u^i_j u^i_{i,j} , \tag{5.11}$$

$$\frac{\partial \rho e^r_t}{\partial t} + \left(\rho u^r_i h^r_t \right)_{,i} + q_{i,i} - \left(u^r_j \tau_{ij} \right)_{,i} = -u^i_i \left(\rho e^r_t \right)_{,i} - \rho u^r_i u^i_j u^i_{i,j} - \rho u^r_i u^i_j u^i_{i,j} . \tag{5.12}$$

5.1.4 Flow homogeneity

We are interested in simulating a stationary (in space) small portion of the full flow. Since the flow described by Eqs. (5.10)–(5.12) is general, it is not necessarily homogeneous, e.g., for a turbulent jet. Technically, we could perform simulations in an inflow/outflow configuration aligned with the mean flow u^i_i. That way, the flow inhomogeneities would be naturally accounted for. However, we would need to provide a turbulent field at the inlet, and generating the proper turbulent inflow is not straightforward. The natural alternative to inflow/outflow boundary conditions are periodic boundary conditions, but these require spatial homogeneity. The goal of the present work is to provide a way to account for the flow inhomogeneities

in a periodic box. To this end, we will perform the appropriate transformations to make the flow homogeneous. Once the transformed flow is homogeneous, the terms involving advection by the mean flow in Eqs. (5.10)–(5.12) become unnecessary, as we are effectively simulating a spatially stationary portion of the flow. Hence, we can safely remove them. In summary, we want to perform a triply-periodic realization of the vicinity of a fixed location in a flow of interest, which will be made possible by performing the appropriate transformations to make the flow homogeneous in the transformed setting. To illustrate the effectiveness of this method, in the next section, we apply this framework to the centerline of a turbulent jet.

5.2 Governing equations for the centerline of a jet

We want to reproduce the turbulence characteristics on the centerline of a compressible round jet in a triply-periodic box. We closely follow the approach by Rah *et al.*[35], who performed it for the incompressible case.

5.2.1 Imposed mean flow

As described in Sec. 5.1.2, we seek a decomposition of the instantaneous velocity field into a resolved and an imposed mean flow. In the self-similar region of an incompressible turbulent jet, the mean flow and the gradient of the mean flow are

$$
\boldsymbol{u}^i = U_c \begin{bmatrix} 1 \\ 0 \\ 0 \end{bmatrix} \qquad \nabla \boldsymbol{u}^i = \frac{U_c}{x_0} \begin{bmatrix} -1 & 0 & 0 \\ 0 & 1/2 & 0 \\ 0 & 0 & 1/2 \end{bmatrix}, \tag{5.13}
$$

where x_0 is the axial distance, and U_c is the centerline velocity at this location. It can easily be verified that $u^i_{i,i} = 0$, so this imposed field is consistent with the decomposition performed in Eq. (5.8). We expect Eq. (5.13) to be a good approximation for subsonic compressible flows. More specifically, we will assume that the solenoidal part of the Favre averaged mean of the compressible velocity field is the same as the mean incompressible velocity field.

5.2.2 Statistical homogeneity for velocity

As hinted in Sec. 5.1.4, the flow is not statistically homogeneous in the axial direction. In other words, the moments of the resolved velocity field (such as the variance) vary in the axial direction. That is why the first step is to perform the adequate rescalings for the velocity fluctuations to be statistically homogeneous. Specifically, in an incompressible turbulent jet, it is well-known that the velocity fluctuations scale as $1/x$. Guided by the normalization performed by Rah *et al.*[35]

for the self-similar region of incompressible turbulent jets, we perform the coordinate transformation

$$u_x^r = \frac{x_0}{x}\exp\left(\frac{x}{x_0} - 1\right)u_x^*, \qquad u_y^r = \frac{x_0}{x}u_y^*, \qquad u_z^r = \frac{x_0}{x}u_z^*. \tag{5.14}$$

Equations (5.10) to (5.12) become

$$\frac{\partial \rho}{\partial t} + (\rho u_i^*)_{,i} = -U_c \rho_{,x}, \tag{5.15}$$

$$\frac{\partial \rho u_i^*}{\partial t} + (\rho u_j^* u_i^*)_{,j} + p_{,i} - \tau_{ij,j} = -U_c(\rho u_i^*)_{,x} + \rho u_j^* B_{ij}$$
$$- \rho \frac{U_0^2}{x_0}\delta_{1i} + \frac{1}{x_0}\rho u_x^* u_y^* \delta_{2i} + \frac{1}{x_0}\rho u_x^* u_z^* \delta_{3i}, \tag{5.16}$$

$$\frac{\partial \rho e_t^*}{\partial t} + \left(\rho u_i^* h_t^*\right)_{,i} + q_{i,i} - \left(u_j^* \tau_{ij}\right)_{,i} = -U_c\left(\rho e_t^*\right)_{,x}$$
$$+ \rho u_i^* u_j^* B_{ij} - \rho u_x^* \frac{U_0^2}{x_0} + \frac{1}{x_0}\rho u_x^*(u_y^* u_y^* + u_z^* u_z^*), \tag{5.17}$$

where we have simplified the equations assuming that we are in the vicinity of x_0, and where

$$B = \frac{U_c}{x_0}\begin{bmatrix} 1 & 0 & 0 \\ 0 & 1/2 & 0 \\ 0 & 0 & 1/2 \end{bmatrix} \tag{5.18}$$

is the so-called forcing matrix, composed of contributions from the production terms due to $u_{i,j}^i$ and new terms introduced by the normalization. The additional viscous terms originating from the normalization are neglected [35]. It is important to emphasize that Eq. (5.13) and the rescaling given by Eq. (5.14) were derived for incompressible flows. We assume that they remain appropriate for compressible flows.

On the centerline of a turbulent jet, $\sqrt{(u_x^*)^2}/U_c \approx 0.25$ [107]. Combined with the fact that u_i^* oscillates with zero mean by definition, we must have $\langle \rho u_x^* u_i^* \rangle \ll U_c \langle \rho u_i^* \rangle$, and $\langle \rho u_x^* u_i^* u_i^* \rangle \ll U_c \langle \rho u_i^* u_i^* \rangle$. Hence, the contribution of the terms $(1/x_0)\rho u_x^* u_y^*$ and $(1/x_0)\rho u_x^* u_z^*$ are small compared to $(U_c/(2x_0))\rho u_y^*$ and $(U_c/(2x_0))\rho u_z^*$ in the y-momentum and z-momentum equations, respectively, and are thus neglected. Similarly, the term $(1/x_0)\rho u_x^*(u_y^* u_y^* + u_z^* u_z^*)$ in Eq. (5.17) is small in comparison to $\rho u_i^* u_j^* A_{ij}$, and is also neglected. Equations (5.16) and (5.17) simplify to

$$\frac{\partial \rho u_i^*}{\partial t} + (\rho u_j^* u_i^*)_{,j} + p_{,i} - \tau_{ij,j} = -\rho \frac{U_0^2}{x_0}\delta_{1i} - U_c(\rho u_i^*)_{,x} + \rho u_j^* B_{ij}, \tag{5.19}$$

$$\frac{\partial \rho e_t^*}{\partial t} + \left(\rho u_i^* h_t^*\right)_{,i} + q_{i,i} - \left(u_j^* \tau_{ij}\right)_{,i} = -U_c \left(\rho e_t^*\right)_{,x} + \rho u_i^* u_j^* B_{ij} - \rho u_x^* \frac{U_0^2}{x_0}. \quad (5.20)$$

5.2.3 Statistical homogeneity for the thermodynamic variables

In addition to velocity, it is important to ensure that all thermodynamic variables are homogeneous. In this work, we focus on the inhomogeneities that prevent the flow from reaching a statistically-stationary state when periodic boundary conditions are applied. It is beyond the scope of this work to develop a framework to make both the mean and the fluctuations of all thermodynamic quantities to be statistically homogeneous. The term $(\rho U_0^2/x_0)\delta_{1i}$ in Eq. (5.19) is constant, and will thus only lead to a mean pressure gradient in the x direction. To make the flow homogeneous, it is thus removed, along with its counterpart in Eq. (5.20). Now, consider the ensemble average of Eq. (5.20). Leveraging the statistical stationarity of the flow, it becomes

$$\left\langle \rho u_i^* h_t^* \right\rangle_{,i} + \left\langle q_i \right\rangle_{,i} - \left\langle u_j^* \tau_{ij} \right\rangle_{,i} = -U_c \left\langle \rho e_t^* \right\rangle_{,x} + \left\langle \rho u_i^* u_j^* \right\rangle B_{ij}. \quad (5.21)$$

If both the velocity and thermodynamic variables were homogeneous, any derivatives of ensemble-averaged quantities would be zero. For Eq. (5.21), this means that the three terms on the LHS and the advection by the mean would be zero, thus leaving only the production term $\langle \rho u_i^* u_j^* \rangle B_{ij}$. This is obviously not correct, since the production term is responsible for the injection of turbulent kinetic energy [35, 38, 108], and is strictly positive. Practically, this production term leads to an increase in $\langle \rho e_t^* \rangle$ along the direction of the imposed flow, and is balanced by the advection by the imposed flow. For flows with large turbulent Mach numbers (not necessarily supersonic) $M_t = \sqrt{\langle u_i^{*2} \rangle}/c_0$, where c_0 is the speed of sound, the production term deposits a large amount of energy. In other words, in a statistically-stationary configuration, this term is balanced by a constant influx of "fresh" gases through advection by the imposed flow. Hence, to be homogeneous, we define

$$(\rho e_t)^\dagger = \rho e_t^* - \frac{1}{U_c} \int_x \langle \rho u_i^* u_j^* \rangle B_{ij} dx, \quad (5.22)$$

such that Eq. (5.20) becomes

$$\frac{\partial \left(\rho e_t\right)^\dagger}{\partial t} + \left(u_i^* (\rho e_t)^\dagger\right)_{,i} + \left(\frac{u_k^*}{U_c} \int_x \langle \rho u_i^* u_j^* \rangle B_{ij} dx\right)_{,k} + \left(\rho u_i^* p^*\right)_{,i}$$
$$+ q_{i,i} - \left(u_j^* \tau_{ij}\right)_{,i} = -U_c \left(\rho e_t\right)_{,x}^\dagger + \left(\rho u_i^* u_j^* - \langle \rho u_i^* u_j^* \rangle\right) B_{ij}. \quad (5.23)$$

In Eq. (5.23), the term $\left((u_i^*/U_c)\int_x \langle \rho u_i^* u_j^* \rangle B_{ij} dx\right)_{,i}$ is the divergence of the product of a constant at a given x, i.e., $(1/U_c)\int_x \langle \rho u_i^* u_j^* \rangle B_{ij} dx$, and a quantity that oscillates around zero, i.e., u_i^*. Hence, we choose to neglect it. Equation (5.23) simplifies to

$$\frac{\partial(\rho e_t)^\dagger}{\partial t} + \left(u_i^*(\rho e_t)^\dagger\right)_{,i} + (\rho u_i^* p^*)_{,i} + q_{i,i} - \left(u_j^* \tau_{ij}\right)_{,i}$$
$$= -U_c (\rho e_t)_{,x}^\dagger + \left(\rho u_i^* u_j^* - \langle \rho u_i^* u_j^* \rangle\right) B_{ij} .$$
$$(5.24)$$

Note that if we were to impose periodicity in the direction of the imposed flow without performing the transformation prescribed by Eq. (5.22), $\langle\!\langle \rho e_t \rangle\!\rangle$ would increase over time due to viscous dissipation, and violate the assumption that the flow is statistically stationary. Such an increase in $\langle\!\langle \rho e_t \rangle\!\rangle$ was observed by Kida & Orszag [28], who had not performed such transformation. The operator $\langle\!\langle \ \rangle\!\rangle$ denotes the volume and time averages, which approximates the ensemble average for homogeneous and statistically stationary flows.

Theoretically, any rescaling of one thermodynamic variable requires the rescaling of all thermodynamic variables, since p, ρ, and T are related via the equation of state. Such additional rescalings would introduce new terms in Eq. (5.23). Here, we only perform the minimal necessary rescaling to make the mean thermodynamic fields homogeneous. We. do not propagate the normalization given by Eq. (5.22) to the other thermodynamic variables, which would give rise to second order effects that we choose to neglect.

The term $\langle \rho u_i^* u_j^* \rangle B_{ij}$ in Eq. (5.24) acts as an energy sink. It balances the forcing term $\rho u_i^* u_j^* B_{ij}$, and enables a statistically-stationary state to be reached. Indeed, taking the volume average of Eq. (5.24) assuming periodicity, we have

$$\frac{d\langle (\rho e_t)^\dagger \rangle}{dt} = 0 .$$
$$(5.25)$$

Hence, the transformation given by Eq. (5.22) is sufficient to achieve a statistically-stationary thermodynamic state.

5.2.4 Summary

In Sec. 5.2.2, the velocity field was made homogeneous by performing the coordinate transformation given by Eq. (5.14). In Sec. 5.2.3, we removed the mean production term in the energy equation to account for the heat deposition due to viscous dissipation. Our main assumption is that the modifications performed in Secs. 5.2.2 and 5.2.3 are sufficient to yield a set of governing equations whose solution is a

homogeneous field describing the turbulent flow on the centerline of a compressible jet at a fixed location. Now that the flow has been made homogeneous, the terms involving advection by the imposed flow U_c are superfluous and can be removed, as explained in Sec. 5.1.4. Dropping the superscripts $(\ )^*$ and $(\ )^\dagger$, Eqs. (5.15), (5.19) and (5.24) then become

$$\frac{\partial \rho}{\partial t} + (\rho u_i)_{,i} = 0\,, \tag{5.26}$$

$$\frac{\partial \rho u_i}{\partial t} + (\rho u_j u_i)_{,j} + p_{,i} - \tau_{ij,j} = \rho u_j B_{ij}\,, \tag{5.27}$$

$$\frac{\partial \rho e_t}{\partial t} + (\rho u_i h_t)_{,i} + q_{i,i} - \left(u_j \tau_{ij}\right)_{,i} = \left(\rho u_i u_j - \langle \rho u_i u_j \rangle\right) B_{ij}\,, \tag{5.28}$$

with B given by Eq. (5.18). From Eqs. (5.27) and (5.28), one can derive the kinetic energy

$$\frac{\partial \rho u_i u_i/2}{\partial t} + (\rho u_j u_i u_i/2)_{,j} + u_i p_{,i} - u_i \tau_{ij,j} = \rho u_i u_j B_{ij}\,, \tag{5.29}$$

and internal energy

$$\frac{\partial \rho e}{\partial t} + (\rho u_i h)_{,i} + q_{i,i} - u_i p_{,i} = u_{j,i} \tau_{ij} - \langle \rho u_i u_j \rangle B_{ij}\,, \tag{5.30}$$

transport equations. For a statistically-stationary homogeneous flow, we obtain from Eq. (5.29) that

$$\langle u_{j,i} \tau_{ij} \rangle = \langle \rho u_i u_j \rangle B_{ij}\,, \tag{5.31}$$

where the contribution of the pressure-dilatation term is neglected, since it fluctuates around zero [28]. Using Eq. (5.30), we also obtain Eq. (5.31). Hence, in both the kinetic energy and internal energy transport equations, the production term $\rho u_i u_j B_{ij}$ is on average balanced by the viscous dissipation term $u_{j,i} \tau_{ij}$.

5.2.5   Link to previous studies that used linear forcing

Petersen & Livescu [27] studied forced turbulence using the so-called linear forcing method. The set of governing equations they solved for is

$$\frac{\partial \rho}{\partial t} + (\rho u_i)_{,i} = 0\,, \tag{5.32}$$

$$\frac{\partial \rho u_i}{\partial t} + (\rho u_j u_i)_{,j} + p_{,i} - \tau_{ij,j} = \rho A u_i\,, \tag{5.33}$$

$$\frac{\partial \rho e_t}{\partial t} + (\rho u_i h_t)_{,i} + q_{i,i} - (u_j \tau_{ij})_{,i} = 0, \tag{5.34}$$

where A is a constant, corresponding to the forcing matrix being the identity matrix. The set of equations Eqs. (5.32) to (5.34) is strikingly similar to the ones previously developed for the centerline of a turbulent jet. Both sets of equations have a production term linear in velocity, with a forcing matrix composed of diagonal entries only. There are only two differences: the magnitude of the entries of the forcing matrices, and the additional term in the energy equation. In Eq. (5.28), the ensemble mean of $\rho u_i u_j B_{ij}$ is removed to enable a statistically stationary state, while in Eq. (5.34), the additional source term in the energy equation has simply been set to zero [27]. For simplicity, and for consistency with previous studies using linear forcing [27, 40, 46, 51], we will present in this thesis results for isotropic turbulence, i.e., we will use a forcing matrix corresponding to the identity matrix. In other words, we will use $\rho A u_i$ instead of $\rho B_{ij} u_j$ as the forcing term for all simulations.

5.3 Acoustic modes and periodic boundary conditions

For the analysis presented in this section, we set c_p, μ and λ to be constants, with unity Prandtl number. For a single fluid with constant c_p, the equation for temperature (Eq. (3.34)) simplifies to

$$T = (\gamma - 1) \frac{W}{R} \left(e_t - \frac{1}{2}|\boldsymbol{u}|^2 \right). \tag{5.35}$$

5.3.1 Problem statement

One can always perform a Helmholtz decomposition of the velocity field and obtain the dilatational u_i^d and solenoidal components u_i^s, with $\nabla \cdot \boldsymbol{u}^s = 0$ and $\nabla \times \boldsymbol{u}^d = 0$. Equation (5.27) prescribes to use the full velocity field in the production term $\rho u_i A_{ij}$, i.e., $u_i = u_i^d + u_i^s$. However, Petersen & Livescu [27] reported observing the unbounded growth of the ratio of the dilatational kinetic energy $\tilde{k}^d = \widetilde{u_i^d u_i^d}/2$ to the solenoidal kinetic energy $\tilde{k}^s = \widetilde{u_i^s u_i^s}/2$, when the full velocity field is used in the production term. To remedy the situation, they proposed to force the solenoidal and dilatational components of the velocity field separately in Eq. (5.27), replacing the original production term by

$$\left(\frac{\epsilon_{\text{target}}^s}{2\tilde{k}^s} \right) \rho u_i^s + \left(\frac{\epsilon_{\text{target}}^d + \langle u_i p_{,i} \rangle}{2\tilde{k}^d} \right) \rho u_i^d, \tag{5.36}$$

where $\epsilon_{\text{target}}^s$ and $\epsilon_{\text{target}}^d$ are the user-specified target solenoidal and dilatational dissipation rates, respectively. This enabled them to control the ratio $\epsilon_{\text{target}}^s / \epsilon_{\text{target}}^d$. This approach can be seen as an extension to compressible flows of the method proposed by Carroll [108] to reduce the oscillatory nature of the forcing term, which is summarized in Sec. 5.4. However, prescribing the partition of u_i into its dilatational and solenoidal components does not come from the governing equations, and thus requires more attention. In the following subsections, we will show that

1) periodic boundary conditions promote the growth of standing acoustic waves, which allow $\tilde{k}^d$ to reach unphysical values,

2) the ratio $\tilde{k}^d / \tilde{k}^s$ does not grow unboundedly as previously claimed [27].

5.3.2 Toy problem: forced one-dimensional "turbulence"

Here, we study a toy problem: forced one-dimensional "turbulence". Equations (5.26) to (5.28) become

$$\frac{\partial \rho}{\partial t} + (\rho u_x)_{,x} = 0 \tag{5.37}$$

$$\frac{\partial \rho u_x}{\partial t} + (\rho u_x u_x)_{,x} + p_{,x} - \frac{4}{3}\mu u_{x,xx} = A\rho u_x , \tag{5.38}$$

$$\frac{\partial \rho e_t}{\partial t} + (\rho u_x h_t)_{,x} - \lambda T_{,xx} - \frac{4}{3}\mu (u_x u_{x,x})_{,x} = A \left(\rho u_x u_x - \langle \rho u_x u_x \rangle \right) , \tag{5.39}$$

Although this configuration might not correspond to a practical flow, it will be shown that it captures the instabilities previously observed [27] and thus provides a simple numerical platform to characterize them.

5.3.2.1 Linear stability analysis

To get theoretical insight into the behavior of Eqs. (5.37) to (5.39), we perform a linear stability analysis. For all thermodynamic variables, we consider $\phi = \phi_0 (1 + \phi'/\phi_0)$, with $\phi' \ll \phi_0$. We further assume that there is no mean flow, i.e., $\tilde{u} = 0$, and that $u'' \ll c_0$, where c_0 is the sound speed. Equations (5.37) to (5.39) become

$$\frac{\partial \rho'}{\partial t} + \rho_0 u'_{,x} = 0 \tag{5.40}$$

$$\frac{\partial u'}{\partial t} + \frac{p_0}{\rho_0^2}\rho'_{,x} + \frac{R}{W}T'_{,x} - \frac{4}{3}\nu u'_{,xx} = Bu' , \tag{5.41}$$

$$\frac{\partial T'}{\partial t'} + (\gamma - 1)T_0 u'_{,x} - \gamma\alpha T'_{,xx} = 0, \tag{5.42}$$

where the equation of state for the fluctuating quantities

$$\frac{p'}{p_0} = \frac{\rho'}{\rho_0} + \frac{T'}{T_0} \tag{5.43}$$

has been used to replace p' in Eq. (5.38). Note that the production term in the energy equation, i.e., the term on the RHS of Eq. (5.39), is not present in Eq. (5.42), as a result of the linearization. Imposing periodic boundary conditions on $x = (0, L)$, all quantities have a solution of the type

$$\phi(x, t) = \sum_{\kappa \to -\infty}^{\infty} \hat{\phi}_\kappa(t) \exp(i\kappa x) , \tag{5.44}$$

where κ is the wavenumber. We now proceed to normalize all variables, i.e., we set $\rho^* = \rho'/\rho_0$, $T^* = T'/T_0$, $u^* = u'/c_0$, $x^* = \kappa x$, and $t^* = c_0 \kappa t$. Performing the Fourier transform of Eqs. (5.40) to (5.42), they can be rewritten as

$$\frac{d}{dt^*}\begin{bmatrix}\hat{\rho}^* \\ \hat{u}^* \\ \hat{T}^*\end{bmatrix} = \underbrace{\begin{bmatrix} 0 & -i & 0 \\ -i/\gamma & (B - (4/3)\nu\kappa^2)/(\kappa c_0) & -i/\gamma \\ 0 & -i(\gamma - 1) & -\alpha\gamma\kappa/c_0 \end{bmatrix}}_{:=\boldsymbol{\Omega}}\begin{bmatrix}\hat{\rho}^* \\ \hat{u}^* \\ \hat{T}^*\end{bmatrix} . \tag{5.45}$$

To the leading order when $c_0 \to \infty$ (zeroth order for the imaginary part and first order for the real part), the eigenvalues of $\boldsymbol{\Omega}$ are

$$\begin{bmatrix}\lambda_1 \\ \lambda_2 \\ \lambda_3\end{bmatrix} = \begin{bmatrix} -\alpha\kappa^2 \\ \kappa c_0 i + \dfrac{B - \kappa^2\left(\nu(4/3) + \alpha(\gamma - 1)\right)}{2} \\ -\kappa c_0 i + \dfrac{B - \kappa^2\left(\nu(4/3) + \alpha(\gamma - 1)\right)}{2} \end{bmatrix} . \tag{5.46}$$

The first eigenvalue λ_1 is associated with the decay of entropic waves. The second and third eigenvalues λ_2 and λ_3 are associated with acoustic waves. The normalized growth rate σ of the acoustic dilatational modes is given by the real part of the latter eigenvalues, i.e.,

$$\sigma = \frac{\mathrm{Re}(\lambda_2)}{B} = \frac{\mathrm{Re}(\lambda_3)}{B} = \frac{B - \kappa^2\left(\nu(4/3) + \alpha(\gamma - 1)\right)}{2B} . \tag{5.47}$$

We define

$$\kappa_c = \sqrt{\frac{B}{\nu(4/3) + \alpha(\gamma - 1)}} . \tag{5.48}$$

For $\kappa < \kappa_c$, $\mathrm{Re}(\lambda_2) = \mathrm{Re}(\lambda_3) > 0$ such the amplitude of the wave will grow exponentially in time. The results of this linear stability analysis are verified numerically in the next section.

5.3.2.2 Numerical simulations of one-dimensional "turbulence"

We want to verify the results obtained in Sec. 5.3.2.1 using numerical simulations. To this end, we initialize a flow field with small-amplitude standing acoustic modes

$$
\begin{aligned}
u(x) &= \sum_{\kappa^*=1}^{K} A_u \sin\left(\frac{2\pi\kappa^* x}{L}\right) \\
p(x) &= p_0 \\
\rho(x) &= \rho_0
\end{aligned}
\tag{5.49}
$$

with $K = 8$, $A_u/c_0 = 10^{-6}$, and $\kappa_c^* \equiv \kappa_c L/(2\pi) = 3.4$. We run the simulation for a short time and extract σ by fitting an exponential to the envelope of each of the Fourier modes, as shown in Fig. 5.3 for the first mode, i.e., $\kappa^* = 1$. In Fig. 5.4, we compare the theoretical growth rate given by Eq. (5.47) with σ extracted from the simulations. The agreement is excellent.
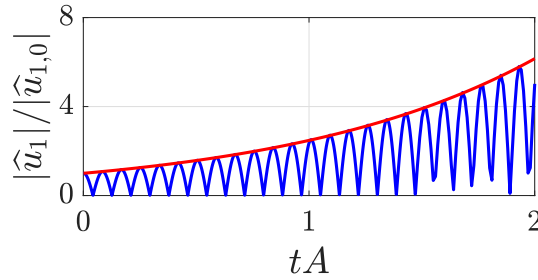
Figure 5.3: Time evolution of the norm of the first velocity Fourier mode $|\hat{u}_1|$ (blue), along with the exponential curve fitted to extract the growth rate σ (red).
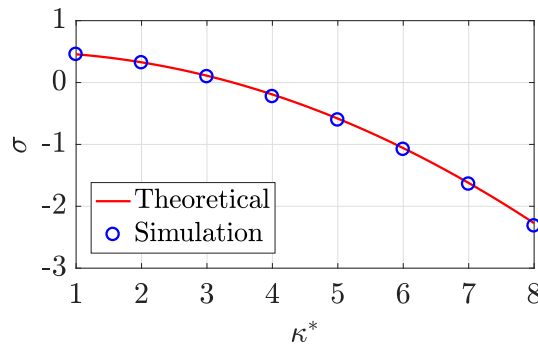
Figure 5.4: Growth rate of the first 8 modes, from theory (Eq. (5.47), red line) and from simulations (blue dots).

Figure 5.5 shows the time evolution of the kinetic energy, normalized with the mean kinetic energy at statistical stationarity $\langle \tilde{k} \rangle$. Note that the linearly unstable modes do not grow unboundedly. Eventually, non-linear effects cause a one-dimensional

"turbulent" energy cascade. The flow reaches a statistically-stationary state where the energy input from the large scales is balanced by viscous dissipation at the small scales. On Fig. 5.5b, one can clearly see that the kinetic energy undergoes large oscillations on a timescale determined by the domain size and the sound speed, typical of large-scale standing acoustic waves. Next, we consider the energy spectrum, which for a one-dimensional homogeneous flow can be simply computed as

$$E_k(\kappa) = |\hat{u}(\kappa)|^2 \,, \tag{5.50}$$

where $\hat{u}$ is the Fourier transform of u. Figure 5.6 shows E_k once the flow has reached a statistically-stationary state, normalized by the kinetic energy $\tilde{k}$. The inertial sub-range has a slope of κ^{*-2}, as observed for various Mach numbers in previous simulations of one-dimensional "turbulence" using large-scale forcing [109]. For this flow, the Mach number at statistical stationary is $M_t = 5 \cdot 10^{-2}$.
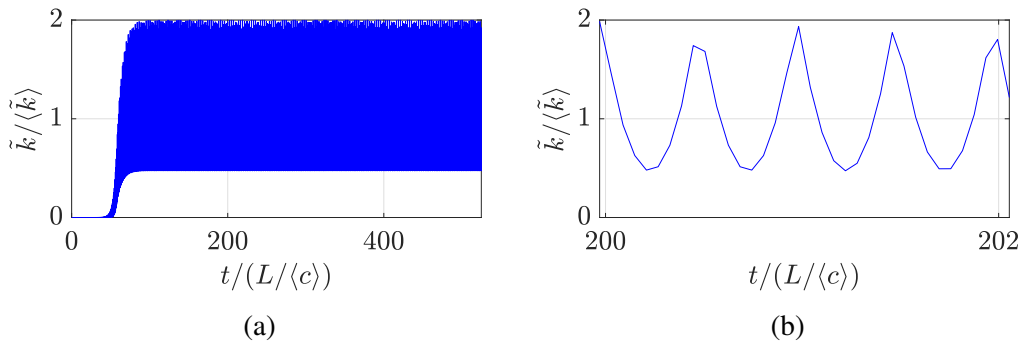
Figure 5.5: Time evolution of the kinetic energy for one-dimensional "turbulence" problem: full time evolution (left), and zoom (right).
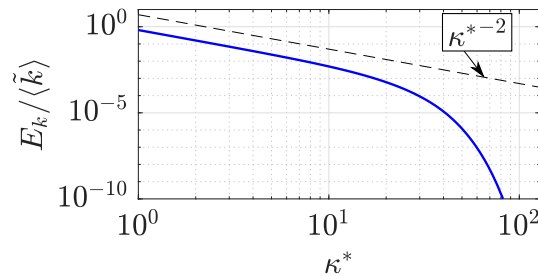
Figure 5.6: Normalized energy spectrum of the one-dimensional "turbulence" simulations.

5.3.2.3 Discussion about periodic boundary conditions for forced compressible flows

In a unconfined flow configuration, e.g., a turbulent jet in an anechoic chamber, acoustic dilatational modes "radiate to infinity", i.e., they escape the turbulent part of the flow [110, 111]. In Sec. 5.1, we developed a framework to make a general flow homogeneous, and we applied it to the centerline of a turbulent jet in Sec. 5.2. For homogeneous flows, periodic boundary conditions are convenient. However, regarding the acoustic modes, periodic boundary conditions "trap" acoustic waves that would otherwise radiate to infinity. As it was found in Sec. 5.3.2.1, some of these waves are linearly unstable. Hence, it is problematic to impose periodic boundary conditions when the dilatational component of the velocity field is forced. One way to prevent the growth of these acoustic modes is to force the solenoidal velocity field u^s only, which is equivalent to keeping only the first of the two terms in the expression proposed by Petersen & Livescu [27] (Eq. (5.36)). Equations (5.27) and (5.28) then become

$$\frac{\partial \rho u_i}{\partial t} + (\rho u_j u_i)_{,j} + p_{,i} - \tau_{ij,j} = A \rho u_i^s \,, \tag{5.51}$$

$$\frac{\partial \rho e_t}{\partial t} + (\rho u_i h_t)_{,i} + q_{i,i} - \left(u_j \tau_{ij}\right)_{,i} = \left(\rho u_i u_i^s - \langle \rho u_i u_i^s \rangle\right) A \,, \tag{5.52}$$

where the isotropic forcing matrix A has been used instead of the anisotropic forcing matrix B derived in Sec. 5.2. Note that a possible avenue would be to also use the stable dilatational modes in the forcing term, i.e., force the full solenoidal velocity as well as the dilatational wavenumbers that satisfy $\kappa > \kappa_c$. However, this would require performing a Fourier transform of the full velocity field at each timestep, which is computationally expensive. Another avenue would be to modify the periodic boundary conditions to filter out the acoustic waves, using a similar philosophy as the NSCBC. However, this is beyond the scope of the present work.

In summary, from first principles, we found that the forcing term should be linear in velocity, using the full velocity field. However, when using periodic boundary conditions, this promotes the growth of unstable dilatational modes. Hence, inspired by the work of Petersen & Livescu [27], it was decided to only use the solenoidal velocity field in the forcing term.

5.4 Modification to the forcing term to reduce its oscillatory nature

First, let's examine what are some of the expected steady-state quantities obtained using this forcing scheme for a homogeneous flow. Consider the volume-averaged kinetic energy equation, obtained from Eq. (5.51), i.e.,

$$\frac{d\bar{\rho}\tilde{k}}{dt} = \langle u_i \tau_{ij,j}\rangle + 2A\langle \rho u_i u_i^s\rangle - \langle u_i p_{,i}\rangle , \tag{5.53}$$

where $\tilde{k} = \langle \rho k\rangle/\langle \rho\rangle$ is the Favre-averaged kinetic energy, The pressure-dilatation term $\langle u_i p_{,i}\rangle$ leads to oscillations on a fast time scale, but has been found to have a negligle impact on the evolution of the turbulent kinetic energy [112]. It is thus discarded from the present analysis. For moderate turbulent Mach numbers $M_t \lesssim 0.6$, the kinetic energy of the flow is mostly contained in the solenoidal mode [26, 29]. Hence, we rewrite $\langle \rho u_i u_i^s\rangle \approx 2\langle \rho\rangle\tilde{k}$. For low Mach numbers, we also have $\langle \tilde{k}\rangle \approx \langle\langle k\rangle\rangle$. Leveraging the homogeneity of the flow, assuming μ to be constant, and assuming that a statistically-stationary state if obtained, Eq. (5.53) can be rewritten as

$$\langle\langle \epsilon\rangle\rangle = 2A\langle\langle k\rangle\rangle , \tag{5.54}$$

where the definition for the viscous dissipation rate ϵ (Eq. (1.11)) has been used. Using the definition for the integral length scale (Eq. (1.10)), we obtain

$$u' = 3Al , \tag{5.55}$$

$$Re_t = \frac{u'l}{\nu} = \frac{3Al^2}{\nu} , \tag{5.56}$$

$$\langle\langle k\rangle\rangle \equiv k_0 = \frac{3}{2}u'^2 = \frac{27}{2}A^2l^2 , \tag{5.57}$$

and

$$\langle\langle \epsilon\rangle\rangle \equiv \epsilon_0 = 27A^3l^2 . \tag{5.58}$$

Equations Eq. (5.55)–(5.58) were obtained for incompressible flows by Carroll & Blanquart [108]. For compressible flows at low turbulent Mach numbers, the present analysis shows that they remain valid.

The forcing term in Eq. (5.51) produces flows that exhibit large fluctuations in turbulent statistics, a feature that becomes more prominent as Re_t is increased [36, 37, 108]. To reduce the oscillatory nature of this forcing scheme, Carroll &

Blanquart [108] proposed to slightly modify the forcing term by multiplying it by $k_0/\langle k\rangle$. Here, we follow a similar procedure, by multiplying the forcing term by $k_0/\tilde{k}$. The final set of equations used in the following chapter are

$$\frac{\partial\rho}{\partial t} + (\rho u_i)_{,i} = 0 \,, \tag{5.59}$$

$$\frac{\partial\rho u_i}{\partial t} + (\rho u_j u_i)_{,j} + p_{,i} - \tau_{ij,j} = f_i \,, \tag{5.60}$$

$$\frac{\partial\rho e_t}{\partial t} + (\rho u_i h_t)_{,i} + q_{i,i} - \left(u_j\tau_{ij}\right)_{,i} = f_i u_i - \langle f_i u_i\rangle \,, \tag{5.61}$$

where

$$f_i = A\frac{k_0}{\tilde{k}}\rho u_i^s \tag{5.62}$$

is the forcing term. Dotting Eq. (5.60), and using the relation $u_i^s u_i \approx u_i u_i$ for flows at low Mach numbers, one obtains that the mean forcing term in the kinetic energy transport equation is

$$\langle f_i u_i\rangle = 2A\langle\rho\rangle k_0 \,. \tag{5.63}$$

Hence, the effect of the modification to the forcing term applied in this section is to inject a constant amount of kinetic energy, i.e., it yields a constant production term.

5.5 Summary

In this chapter, we derived how compressible turbulent flows should be forced when simplified geometries such as a periodic box are used, i.e., when the flow lacks a natural turbulence generation mechanism due to the large scale shear. In Sec. 5.1, we introduced the general framework, which relies on a simple decomposition of the velocity field into large-scale (imposed) and small-scale (resolved) components. Then, in Sec. 5.2, we applied this framework to the centerline of a jet. The methodology to make the velocity and thermodynamic fields homogeneous was presented. In Sec. 5.3, we investigated the unphysical growth of dilatational kinetic energy when forced turbulence is simulated with periodic boundary conditions. It was found that standing acoustic modes were responsible for this unphysical behavior, and it was decided to force the solenoidal component of the velocity field only to remedy the situation, similarly to what was proposed by Petersen & Livescu [27]. Finally, in Sec. 5.4, we applied a modification to the forcing scheme to reduce its oscillatory nature, following the work of Carroll & Blanquart [108].

Chapter 6

NUMERICAL SIMULATIONS OF COMPRESSIBLE HOMOGENEOUS TURBULENCE

In this chapter, we investigate compressible homogeneous isotropic turbulence using DNS. In the past, such flows have mostly been investigated using ad-hoc turbulence forcing schemes, such as stochastic forcing at the largest scales [28, 29, 113, 114]. To the author's knowledge, the only studies of compressible turbulence using linear forcing are the ones by Rosales & Meneveau [37], and Petersen & Livescu [27]. These two studies focused primarily on comparing the linear forcing technique with the large-scale forcing in Fourier space. The goal of this chapter is to provide insight into homogeneous isotropic subsonic compressible turbulence, using the linear forcing technique presented in Chapter 5. In Sec. 6.1, we review some of the theory regarding the decomposition of the flow field into solenoidal and dilatational components, as well as how these fields are related to the different terms in the low Mach number expansion. In Sec. 6.2, we present simulation results. We first fix the Reynolds number and vary the turbulent Mach number. We are specifically interested in how key quantities, such as solenoidal and dilatational kinetic energies, scale with the Mach number. Second, we evaluate how these quantities change with the Reynolds number, fixing the turbulent Mach number. The findings are summarized in Sec. 6.3.

6.1 Theoretical considerations

As mentioned previously, the flow field can be decomposed in two separate ways, either into solenoidal and dilatational components (Helmholtz decomposition), or via the low Mach number expansion. In this section, we review the theoretical links between the two.

6.1.1 Solenoidal and dilatational fields

As introduced in Sec. 1.3.2, the velocity field can be split into its solenoidal u_s and dilatational u_d components by performing a Helmholtz decomposition. For homogeneous non-reacting turbulence, the low Mach number approximation is nothing more than the incompressible limit (see Sec.2.1.2.2), and the velocity field is purely solenoidal. Hence, for compressible homogeneous non-reacting turbulence,

we expect $\langle \tilde{k}^d \rangle / \langle \tilde{k}^s \rangle \to 0$ when $M_t \to 0$, where

$$\langle \tilde{k}^s \rangle = \frac{1}{2} \frac{\langle\!\langle \rho \boldsymbol{u}^s \cdot \boldsymbol{u}^s \rangle\!\rangle}{\langle\!\langle \rho \rangle\!\rangle}, \tag{6.1}$$

and

$$\langle \tilde{k}^d \rangle = \frac{1}{2} \frac{\langle\!\langle \rho \boldsymbol{u}^d \cdot \boldsymbol{u}^d \rangle\!\rangle}{\langle\!\langle \rho \rangle\!\rangle}, \tag{6.2}$$

are the Favre-averaged solenoidal and dilatational kinetic energies, respectively. The turbulent Mach number is defined as $M_t \equiv \sqrt{2\langle\!\langle k \rangle\!\rangle}/\langle\!\langle c \rangle\!\rangle$ (Eq. (1.18)).

Sarkar et al.[115] proposed a decomposition of the mean viscous dissipation rate $\langle\!\langle \epsilon \rangle\!\rangle$ into a solenoidal component

$$\langle\!\langle \epsilon^s \rangle\!\rangle = \frac{\langle\!\langle \mu \boldsymbol{\omega} \cdot \boldsymbol{\omega} \rangle\!\rangle}{\langle\!\langle \rho \rangle\!\rangle}, \tag{6.3}$$

where $\boldsymbol{\omega} \equiv \nabla \times \boldsymbol{u}$ is the vorticity vector, and dilatational component

$$\langle\!\langle \epsilon^d \rangle\!\rangle = \frac{4}{3} \frac{\langle\!\langle \mu (\nabla \cdot \boldsymbol{u})^2 \rangle\!\rangle}{\langle\!\langle \rho \rangle\!\rangle}. \tag{6.4}$$

This decomposition is exact, i.e., $\langle\!\langle \epsilon^s \rangle\!\rangle + \langle\!\langle \epsilon^d \rangle\!\rangle = \langle\!\langle \epsilon \rangle\!\rangle$, for homogeneous flows, since

$$
\begin{aligned}
\langle\!\langle \rho \rangle\!\rangle \langle\!\langle \epsilon \rangle\!\rangle &= \langle\!\langle \mu \tau_{ij} u_{i,j} \rangle\!\rangle = \langle\!\langle \mu \left(u_{i,j} + u_{j,i} - (2/3) u_{k,k} \delta_{ij} \right) u_{i,j} \rangle\!\rangle \\
&= \langle\!\langle \mu \left(2 w_{ij} w_{ij} + 2 u_{i,j} u_{j,i} - (2/3) u_{i,i}^2 \right) \rangle\!\rangle \\
&= \langle\!\langle \mu \left(2 w_{ij} w_{ij} + 2((u_i u_{j,i} - u_{i,i} u_j)_{,j} + (4/3) u_{i,i}^2 \right) \rangle\!\rangle \\
&= \langle\!\langle \mu \left(2 w_{ij} w_{ij} + (4/3) u_{i,i}^2 \right) \rangle\!\rangle \\
&= \langle\!\langle \mu \left(\boldsymbol{\omega} \cdot \boldsymbol{\omega} + (4/3)(\nabla \cdot \boldsymbol{u})^2 \right) \rangle\!\rangle = \langle\!\langle \rho \rangle\!\rangle (\langle\!\langle \epsilon^s \rangle\!\rangle + \langle\!\langle \epsilon^d \rangle\!\rangle),
\end{aligned}
\tag{6.5}
$$

where $w_{ij} = (1/2)(u_{i,j} - u_{j,i})$ is the vorticity tensor. Equation (6.3) is the so-called solenoidal dissipation rate, since only the divergence-free component of velocity $\boldsymbol{u}^s$ is used ($\nabla \times \boldsymbol{u}^d = 0$). Equation (6.4) is the so-called dilatational dissipation rate, since only the curl-free component of velocity $\boldsymbol{u}^d$ is employed ($\nabla \cdot \boldsymbol{u}^s = 0$). Similarly to the ratio of dilatational to solenoidal kinetic energies, we expect $\langle\!\langle \epsilon^d \rangle\!\rangle / \langle\!\langle \epsilon^s \rangle\!\rangle \to 0$ as $M_t \to 0$, since $u' \to u^s$.

The fluctuating pressure field $p' = p - \langle\!\langle p \rangle\!\rangle$ can be split into dilatational p_d and solenoidal p_s components, with $p' = p_d + p_s$. The solenoidal pressure field is

defined by the Poisson equation found for pressure in the incompressible case [26], i.e.,

$$\nabla^2 p^s = -\langle\!\langle\rho\rangle\!\rangle \frac{\partial u_i^s}{\partial x_j}\frac{\partial u_j^s}{\partial x_i},\tag{6.6}$$

which is obtained by taking the divergence of the momentum equation (Eq. (2.2)), considering a purely solenoidal velocity field and constant density, and using the incompressibility constraint $\nabla \cdot \boldsymbol{u}^s = 0$ to eliminate the time-derivative and viscous terms. The solenoidal pressure p^s, extracted during post-processing, is thus the pressure that satisfies the "incompressible" part of the Navier-Stokes equations. Hence, we expect $p' \rightarrow p^s$ as $M_t \rightarrow 0$.

6.1.2 Low Mach number expansion - Review and interpretation

In this chapter, we solve the equations for forced turbulence developed in Chapter 5, i.e., Eqs. (5.59)–(5.61). In Sec. 2.1.2, we reviewed the low Mach number approximation, focusing on the zeroth order continuity, momentum, and energy equations. Since the incompressible limit (see Sec.2.1.2.2) is recovered for the zeroth order governing equations in homogeneous non-reacting turbulence, this set of equations reduces to the well-known incompressible Navier-Stokes equations, i.e.,

$$\nabla \cdot \boldsymbol{u}_0 = 0\,,\tag{6.7}$$

$$\frac{\partial \boldsymbol{u}_0}{\partial t} + \boldsymbol{u}_0 \cdot \nabla \boldsymbol{u}_0 + \frac{\nabla p_1}{\rho_0} = \frac{\nabla \cdot \boldsymbol{\tau}_0}{\rho_0} + \frac{\boldsymbol{f}_0}{\rho_0}\,,\tag{6.8}$$

with the addition of a forcing term in the momentum equation, and where the notation introduced in Sec. 2.1.2 is employed, i.e., the subscript $(\ )_0$ refers to the ϵ^0 term in the expansion, the subscript $(\ )_1$ refers to the ϵ^1 term in the expansion, and so on, where $\epsilon = \gamma M^2$. In addition, p_0, ρ_0, and T_0 are constant in time and in space in the incompressible limit, i.e., $p_0 = \langle\!\langle p\rangle\!\rangle$, $T_0 = \langle\!\langle T\rangle\!\rangle$, and $\rho_0 = \langle\!\langle\rho\rangle\!\rangle$. Here, we consider the first order equations to gain insight into flows at small, but non-zero, Mach numbers. The first order equations for homogeneous non-reacting turbulence are

$$\frac{D\rho_1}{Dt} + \rho_0\nabla \cdot \boldsymbol{u}_1 = 0\,,\tag{6.9}$$

$$\rho_0\frac{D\boldsymbol{u}_1}{Dt} + \nabla p_2 = \nabla \cdot \boldsymbol{\tau}_1 - \rho_1\frac{D\boldsymbol{u}_0}{Dt} - \rho_0\boldsymbol{u}_1 \cdot \nabla \boldsymbol{u}_0 + \boldsymbol{f}_1\,,\tag{6.10}$$

$$\rho_0 c_p\frac{DT_1}{Dt} = \frac{Dp_1}{Dt} - \nabla \cdot \boldsymbol{q}_1 + \boldsymbol{\tau}_0 : \nabla \boldsymbol{u}_0 - \langle\boldsymbol{f}_0 \cdot \boldsymbol{u}_0\rangle\,,\tag{6.11}$$

where $D(\ )/Dt = \partial(\ )/\partial t + u_0 \cdot \nabla(\ )$. The system of equations (6.9)–(6.11) is closed with the first-order equation of state

$$p_1 = \frac{\rho_0 R T_1}{W} + \frac{\rho_1 R T_0}{W}. \tag{6.12}$$

Note that ρ_0, u_0, p_1, and τ_0 are inputs to the first order set of governing equations, since the zeroth order set of equations is closed. Several key theoretical results can be drawn from this low Mach number expansion.

First, in the absence of viscosity and conductivity, Eq. (6.11) reduces to

$$\frac{1}{T_0}\frac{DT_1}{Dt} = \frac{\gamma-1}{\gamma}\frac{1}{p_0}\frac{Dp_1}{Dt}. \tag{6.13}$$

Equation (6.13) yields the linearized isentropic relation

$$\frac{T_1}{T_0} = \frac{\gamma-1}{\gamma}\frac{p_1}{p_0}, \tag{6.14}$$

which would be satisfied everywhere in the limit of large Reynolds and low Mach numbers. In a actual flow, the conduction and viscous dissipation terms in Eq. (6.11) will alter this behavior. Hence, the flow is not expected to be perfectly isentropic, even at very low Mach numbers.

Second, it is evident from Eq. (6.9) that u_1 is not divergence-free. In other words, the leading order contribution to the dilatational velocity field comes from u_1. This goes in pair with the prior observation that the leading order contribution to the solenoidal velocity field was u_0. Hence, we expect $\langle \tilde{k}^d \rangle / \langle \tilde{k}^s \rangle \sim \epsilon^2 \sim M_t^4$, at low Mach numbers.

Third, since p^s is defined as the pressure that satisfies the Poisson equation obtained from Eqs. (6.7)–(6.8), p^s is identically ϵp_1. As a result, the dilatational pressure must come from the higher order pressure terms, i.e., $p^d = \epsilon^2 p_2 + O(\epsilon^3)$. We thus expect $p^s/p_0 \sim M_t^2$, and $p^d/p_0 \sim M_t^4$, at low Mach numbers. Figure 6.1 shows a schematic summarizing how the solenoidal and dilatational fields are related to the different terms in the low Mach number expansion. The solid black arrows denote a theoretically-known relation, e.g., u_1 has a dilatational component. The gray dashed arrows denote possible relations, e.g., in addition to having a dilatational component, u_1 could also have a solenoidal component.

$$u^s \longrightarrow u_0 \qquad\qquad p^s \longrightarrow p_1$$

$$u^d \longrightarrow u_1 \qquad\qquad p^d \longrightarrow p_2$$

$$u_2 \qquad\qquad\qquad p_3$$

$$\vdots \qquad\qquad\qquad \vdots$$
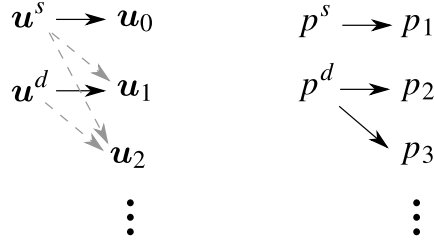
Figure 6.1: Schematic of the relation between the solenoidal and dilatational fields with the different terms in the low Mach number expansion.

6.1.3 Link to other theoretical analyses

Theoretical predictions available in the literature regarding the behavior of the compressible components of the flow at low Mach numbers appear not to be in agreement with each other. On one hand, the weak acoustic equilibrium hypothesis [115]

$$\frac{\gamma^2 M_t^2 \chi \langle\!\langle p \rangle\!\rangle^2}{(p_{rms}^d)^2} = F_w \,, \tag{6.15}$$

where F_w a non-dimensional parameter and $\chi = \langle \tilde{k}^d \rangle / \langle \tilde{k}^s \rangle$, stipulates that F_w should be close to unity in homogeneous, compressible turbulence at low Mach numbers. Sarkar *et al.* found that F_w was reaching values close to unity for decaying turbulence. This is inconsistent with the results obtained from the low Mach number expansion, which predict that $F_w \sim M_t^{-2}$ at low Mach numbers. It should be noted that decaying turbulence can be very sensitive to the initial conditions. By performing simulations of statistically-stationary turbulence, we aim to remove any transient effect due to the initial conditions.

On the other hand, the improved Fauchet-Bertoglio model [26, 116], based on an asymptotic analysis using Eddy-Damped Quasi-Normal Markovian (EDQNM) theory, predicts that $\langle \tilde{k}^s \rangle / \langle \tilde{k}^d \rangle \sim M_t^4$, $\langle\!\langle \epsilon^d \rangle\!\rangle / \langle\!\langle \epsilon^s \rangle\!\rangle \sim M_t^4$, and $p_{rms}^d / p_{rms}^s \sim M_t^4$, in agreement with the scalings obtained from the low Mach number expansion.

6.2 Numerical results

6.2.1 Simulation framework

We use the solver presented in Chapter 3. The mesh is uniform, and the domain is triply-periodic, with $\kappa_{max}\eta > 1.5$, where κ_{max} is the maximum wavenumber resolved. All simulations are initialized with a field with very low turbulence intensity, i.e., $\tilde{k}/k_0 \approx 10^{-6}$. We then apply the linear forcing technique detailed in Chapter 5, but without the modification introduced in Sec. 5.4, i.e., without appending $k_0/\tilde{k}$ to the forcing term. Using this modification with such a small

initial Reynolds number would lead to a very large deposition of kinetic energy in a very short time, since $k_0/\tilde{k} \gg 1$ at $t = 0$. The modification is only applied once the ratio $k_0/\tilde{k}$ becomes close to unity.

Figure 6.2 shows the time evolution of normalized kinetic energy (Fig. 6.2a), the ratio of solenoidal to dilatational kinetic energies (Fig. 6.2b), the ratio of dilatational to solenoidal dissipation rates (Fig. 6.2c), and the ratio of dilatational to solenoidal pressures (Fig. 6.2d), for $Re_\lambda = 31$ and $M_t = 0.32$. All ratios are very small during the initial transient, up to $t/\tau \approx 20$, when the statistically-stationary state is reached. Two key observations are made. First, it can be seen that the compressible quantities (Figs. 6.2b–6.2d) oscillate on a timescale much faster than the solenoidal quantities (Fig. 6.2a). In Fig. 6.3, we show $\langle \tilde{k}^s \rangle / \langle \tilde{k}^d \rangle$, using the acoustic time scale associated with the large scales to normalize time, i.e., $t^* = t/(L/\langle\!\langle c \rangle\!\rangle)$, where L is the length of the computational domain. The oscillations in $\tilde{k}^d/\tilde{k}^s$ appear to have a timescale close to $L/\langle\!\langle c \rangle\!\rangle$. Second, the compressible quantities display large oscillations on a time scale much larger than the eddy turnover time. Hence, this implies that we need to run simulations for very long times to obtain converged statistics for the compressible quantities. The simulation results shown in Fig. 6.2 were performed for 500 eddy turnover times.

6.2.2 Effect of Mach number

In this section, we perform a series of simulations at $Re_t = 63$, with varying turbulent Mach numbers $0.02 \le M_t \le 0.65$. This low Reynolds number is chosen as it enables for an extensive Mach number sweep at an affordable computational cost. Here, we are specifically interested in the partition between dilatational and kinetic energies, dissipation rates, and pressure fluctuations. We compare our results against the ones of Jagannathan & Donzis [29], who used a turbulent Reynolds number based on the Taylor microscale λ, i.e.,

$$Re_\lambda \equiv \frac{\langle\!\langle \mu \rangle\!\rangle \langle\!\langle (2/3)k \rangle\!\rangle^{1/2} \lambda}{\langle\!\langle \rho \rangle\!\rangle}, \tag{6.16}$$

where

$$\lambda \equiv \frac{\langle\!\langle u^2 \rangle\!\rangle}{\langle\!\langle \partial u/\partial x \rangle\!\rangle^{1/2}}. \tag{6.17}$$

For incompressible flows, Re_t and Re_λ are related through [108]

$$Re_\lambda \equiv \sqrt{15 Re_t}. \tag{6.18}$$
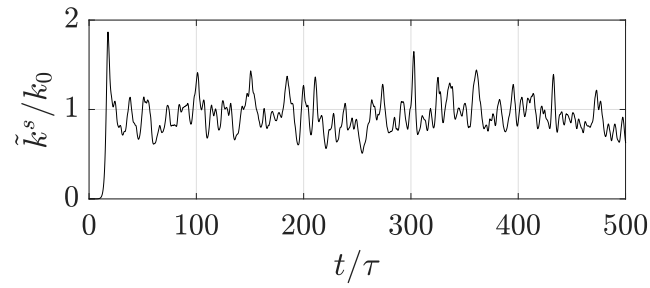
(a) Normalized solenoidal kinetic energy.
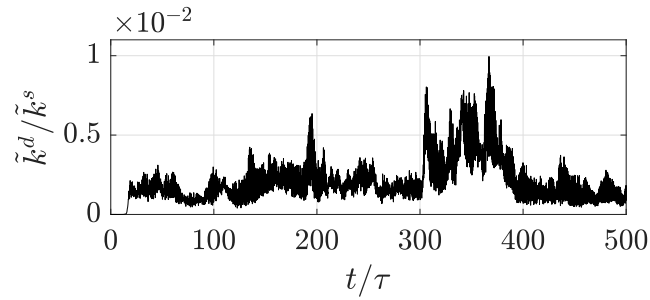
(b) Ratio of dilatational to solenoidal kinetic energies.
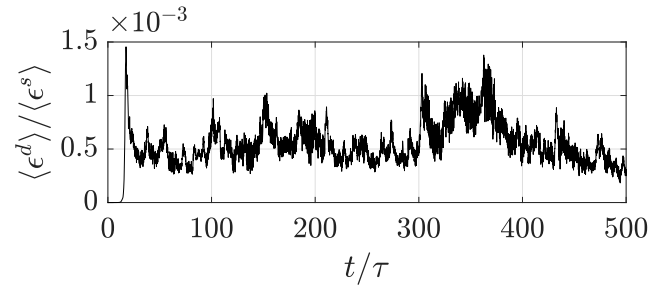
(c) Ratio of dilatational to solenoidal dissipation rates.
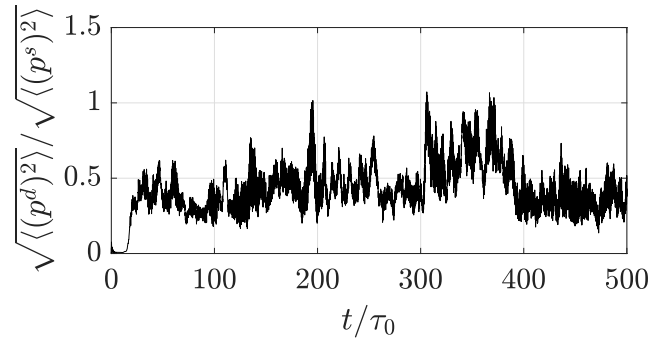
(d) Ratio of dilatational to solenoidal pressures.

Figure 6.2: Time evolution of different key quantities for $M_t = 0.32$ and $Re_\lambda = 31$.
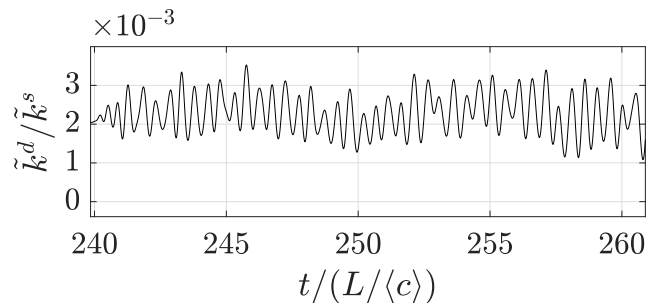
Figure 6.3: Ratio of the dilatational to solenoidal kinetic energies for $M_t = 0.32$ and $Re_\lambda = 31$, normalized with the large scale acoustic timescale.

Given that the flows considered here are at low Mach numbers, we will use Eq. (6.18) to relate Re_λ and Re_t. From Eq. (6.18), we obtain that $Re_\lambda = 31$ for the simulations considered in this section. In the following sections, all quantities are averaged over more than 400 eddy turnover times, once any transient behavior has passed, to obtain converged statistics.

6.2.2.1 Solenoidal and dilatational kinetic energy

Figure 6.4 shows the ratio $\langle \tilde{k}^d \rangle / \langle \tilde{k}^s \rangle$ for different Mach numbers. Our results are in good agreement with the results of Jagannathan & Donzis [29] at $Re_\lambda = 38$. At low Mach numbers, it can be seen that $\langle \tilde{k}^d \rangle / \langle \tilde{k}^s \rangle \sim M_t^4$, in agreement with the scaling obtained from the low Mach number expansion.

Figure 6.4 also shows the dilatational to solenoidal kinetic energy ratio for simulation results obtained forcing the full velocity field, i.e, with a forcing term $A(k_0/\langle k \rangle)\rho \boldsymbol{u}$ instead of $A(k_0/\langle k \rangle)\rho \boldsymbol{u}^s$ in the momentum equation. These results are shown by blue squares. It can be seen that $\langle \tilde{k}^d \rangle / \langle \tilde{k}^s \rangle$ increases as the Mach number is decreased, which is undoubtedly unphysical. However, it does not grow unboundedly as previously claimed [27], and is consistent with our analysis of one-dimensional dilatational "turbulence" presented in Sec. 5.3. Forcing the dilatational mode when using periodic boundary conditions is linearly unstable, but non-linear effects limit the growth of the dilatational mode, and a finite $\langle \tilde{k}^d \rangle / \langle \tilde{k}^s \rangle$ ratio is obtained.

6.2.2.2 Solenoidal and dilatational dissipation rate

Figure 6.5 shows the ratio $\langle\!\langle \epsilon^d \rangle\!\rangle / \langle\!\langle \epsilon^s \rangle\!\rangle$ for various Mach numbers, compared to the results of Jagannathan & Donzis at $Re_\lambda = 38$. The agreement is satisfactory, except at $M_t = 0.1$, where the two sets of results differ by more than one order of magnitude. The results of Jagannathan & Donzis [29] show an increase in $\langle\!\langle \epsilon^d \rangle\!\rangle / \langle\!\langle \epsilon^s \rangle\!\rangle$ as the
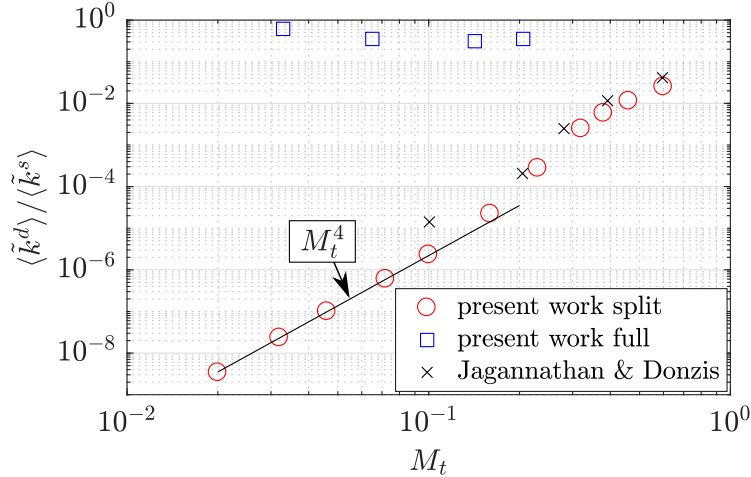
Figure 6.4: Ratio of the dilatational to solenoidal kinetic energies, obtained by forcing the solenoidal velocity field only (red circles), and by forcing the full velocity field (blue squares), compared with the results of Jagannathan & Donzis [29] at $Re_\lambda = 38$ (black crosses).

Mach number is decreased. On the other hand, our results follow $\langle\!\langle \epsilon^d \rangle\!\rangle / \langle\!\langle \epsilon^s \rangle\!\rangle \sim M_t^4$ at low Mach numbers, in agreement with the results obtained by considering the low Mach number expansion.

In Fig. 6.6, we use Eq. (1.10) to compute the ratio of the integral length scale to the domain length, i.e., l/L. The black dashed line represents the integral length scale extracted from an incompressible simulation at the same Reynolds number. It can be seen that $l/L \approx 0.18$ for all Mach numbers, which is also the integral length scale for the incompressible case. This suggests that the solenoidal velocity field in the compressible simulations is similar to the full velocity field in the incompressible case.

6.2.2.3 Thermodynamic fluctuations

For compressible turbulence at low Mach numbers, it is often assumed that the thermodynamic fluctuations are isentropic [117, 118], i.e., that density, temperature, and pressure are related through

$$\frac{T}{\langle\!\langle T \rangle\!\rangle} = \left(\frac{p}{\langle\!\langle p \rangle\!\rangle} \right)^{(\gamma-1)/\gamma} , \tag{6.19}$$

$$\frac{\rho}{\langle\!\langle \rho \rangle\!\rangle} = \left(\frac{p}{\langle\!\langle p \rangle\!\rangle} \right)^{1/\gamma} . \tag{6.20}$$
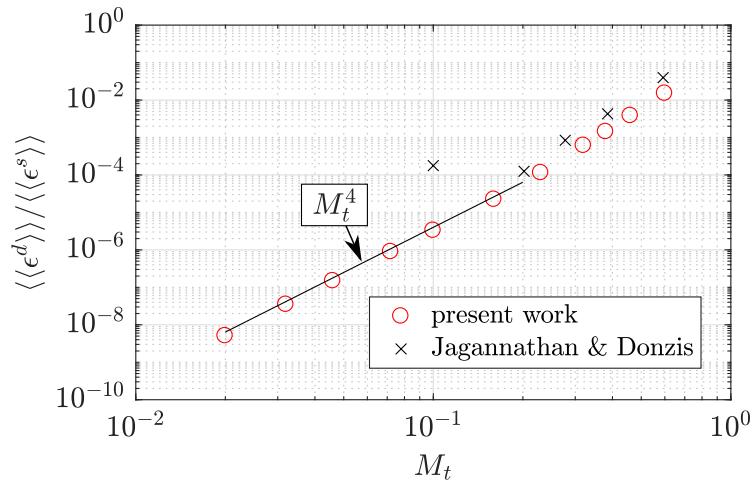
Figure 6.5: Ratio of the dilatational to solenoidal viscous dissipation rates (red circles), compared with the results of Jagannathan & Donzis [29] for $Re_\lambda = 38$ (black crosses).
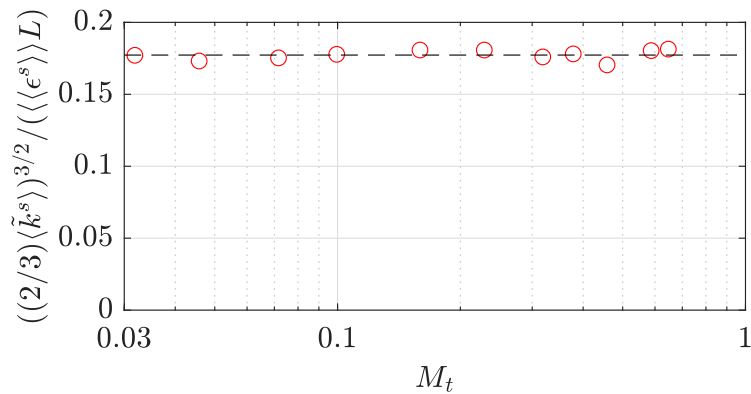
Figure 6.6: Evaluation of the integral length scale associated with the solenoidal velocity field.

For small fluctuations, it follows from Eqs. (6.19)–(6.20) that

$$\frac{T_{rms}}{\langle\!\langle T \rangle\!\rangle} \approx \left(\frac{\gamma - 1}{\gamma}\right) \frac{p_{rms}}{\langle\!\langle p \rangle\!\rangle}, \tag{6.21}$$

$$\frac{\rho_{rms}}{\langle\!\langle \rho \rangle\!\rangle} \approx \frac{1}{\gamma} \frac{p_{rms}}{\langle\!\langle p \rangle\!\rangle}. \tag{6.22}$$

However, as presented in Sec. 6.1.2, a perfectly isentropic behavior is not expected even at very low Mach numbers. This non-isentropic behavior was verified numerically by Donzis & Jagannathan [119]. To quantify the deviation from the isentropic behavior, they suggested to use Eq. (6.22) to compute a polytropic exponent γ_t for

the thermodynamic fluctuations, i.e.,

$$\gamma_t \equiv \frac{p_{rms}}{\langle\!\langle p \rangle\!\rangle} \frac{\langle\!\langle \rho \rangle\!\rangle}{\rho_{rms}}. \tag{6.23}$$

A value of $\gamma_t = \gamma$ corresponds to an isentropic process, while $\gamma_t = 1$ corresponds to an isothermal process. In Fig. 6.7, we present γ_t extracted from the simulation results. Our values are in reasonable agreement with the results of Donzis & Jagannathan [119]. Interestingly, γ_t appears to reach an asymptote $\gamma_t \approx 1.23$ at low Mach numbers. In Fig. 6.8, the normalized density fluctuations $\langle \rho'^2 \rangle^{1/2}/\rho_0$ as a function of time for $M_t = 2 \cdot 10^{-2}$ are shown in black. The dashed red line shows the density fluctuations predicted using

$$\frac{\langle \rho'^2 \rangle^{1/2}_{predicted}}{\langle\!\langle \rho \rangle\!\rangle} = \frac{1}{\gamma_t} \frac{\langle p'^2 \rangle^{1/2}}{\langle\!\langle p \rangle\!\rangle}, \tag{6.24}$$

with γ_t computed using Eq. (6.23). Equation (6.24) accurately captures the density fluctuations at any given time.

To further characterize the thermodynamic fluctuations, we show in Fig. 6.9 the joint probability density functions of temperature/density with pressure at a low Mach number ($M_t = 0.1$). The dashed green line corresponds to a locally isentropic behavior, and the red dashed line in Fig. 6.9b corresponds to the polytropic behavior using γ_t. On the temperature joint pdf, it can be seen that the fluctuations are aligned with the isentropic behavior, but that there is a considerable spread. This is consistent with the results presented in Sec. 6.1.2, since the conduction and viscous dissipation terms in Eq. (6.11) act as diffusion terms, and induce the spread in the joint pdfs shown in Fig. 6.9.

6.2.2.4 Solenoidal and dilatational pressure

Figure 6.10 shows the solenoidal pressure fluctuations normalized by the mean pressure. Our results are in very good agreement with those of Jagannathan & Donzis [29]. For the full range of Mach numbers investigated, $p^s_{rms}/\langle\!\langle p \rangle\!\rangle \sim M_t^2$. Note that this Mach number dependence is not a compressibility effect. Figure 6.11 shows the root mean square of the solenoidal pressure fluctuations, normalized with the solenoidal velocity field. The black dashed line shows $p_{rms}/(\rho u_{rms}^2)$ obtained from an incompressible simulation at the same Reynolds number. It can be seen that $p^s_{rms}/(\langle\!\langle \rho \rangle\!\rangle (u^s_{rms})^2)$ is mostly constant and in agreement with the incompressible value up to $M_t \lesssim 0.3$, after which it drops significantly. By relating pressure to
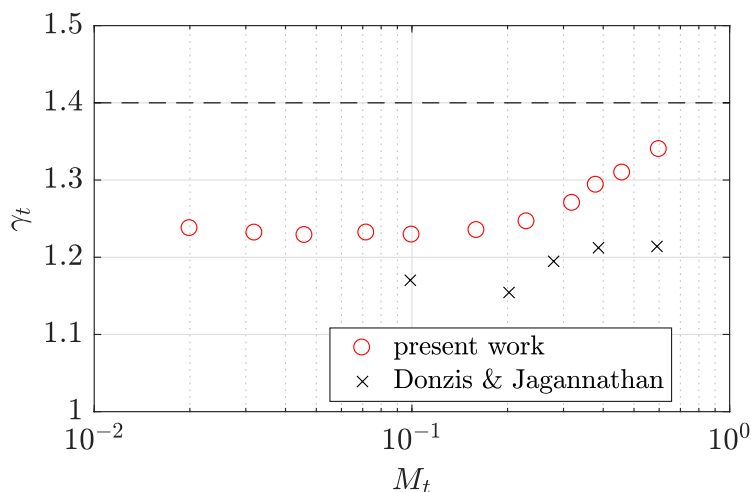
Figure 6.7: Effective exponent γ_t (red circles), compared with the results of Donzis & Jagannathan [119] at $Re_\lambda = 38$ (black crosses).
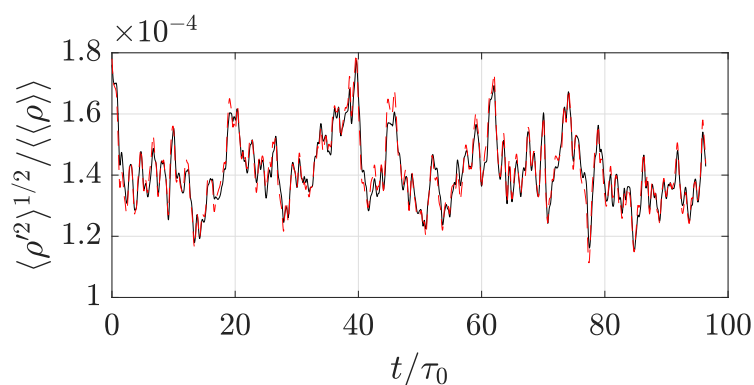
Figure 6.8: Root mean square of the density fluctuations (solid black line), along with the predictions from the pressure fluctuations using the polytropic exponent $\gamma_t = 1.23$ (dashed red line) for $M_t = 2 \cdot 10^{-2}$.

(a)

(b)
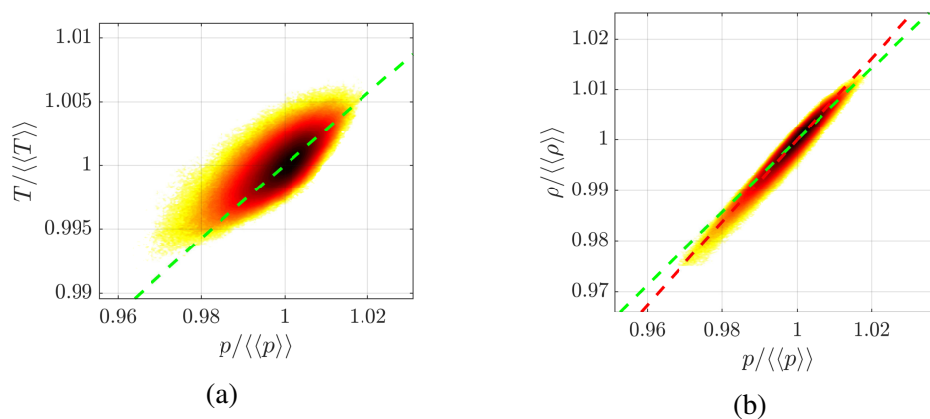
Figure 6.9: Joint pdf of temperature and pressure (a) and density and pressure (b), for $Re_\lambda = 31$ and $M_t = 0.1$. The green dashed lines correspond to the isentropic relations, while the red dashed line is obtained using γ_t.

the fourth moment of the velocity fluctuations, and assuming a very large Reynolds number, Batchelor [120] showed that the pressure rms scales with the square of the velocity rms, and predicted that the proportionality constant should be 0.58, i.e., $p_{rms}/(\rho u_{rms}^2) = 0.58$. While the scaling is recovered here, the predicted factor is significantly lower than the present results. By performing simulations of forced incompressible turbulence, Donzis *et al.*[121] computed $p_{rms}/(\rho u_{rms}^2) = 1.0$ at $Re_\lambda = 38$, which is in reasonable agreement with our results. In light of these results, i.e., $p_{rms}^s \approx \langle\!\langle \rho \rangle\!\rangle (u_{rms}^s)^2$, the M_t^2 scaling observed in Fig. 6.10 is not surprising, since we can write

$$\frac{p_{rms}^s}{\langle\!\langle p \rangle\!\rangle} \sim \frac{p_{rms}^s}{\langle\!\langle \rho \rangle\!\rangle \langle\!\langle c \rangle\!\rangle^2} \sim \frac{(u_{rms}^s)^2}{\langle\!\langle c \rangle\!\rangle^2} \sim M_t^2 . \tag{6.25}$$

Note that this result is also simply predicted by the low Mach number expansion.

Figure 6.12 shows the ratio of the dilatational pressure fluctuations to the mean pressure. Our results are in reasonable agreement with the ones of Jagannathan & Donzis, except at $M_t = 0.1$, where they differ by more than one order of magnitude. At low Mach numbers, our results follow $p_{rms}^d/\langle\!\langle p \rangle\!\rangle \sim M_t^4$, which is again in agreement with the low Mach number expansion. Figure 6.13 shows the ratio of the dilatational to solenoidal pressures. At Mach numbers $M_t \gtrsim 0.3$, the ratio is close to one. At low Mach numbers, it follows $p_{rms}^d/p_{rms}^s \sim M_t^2$, as expected from Figs. 6.10 and 6.12.
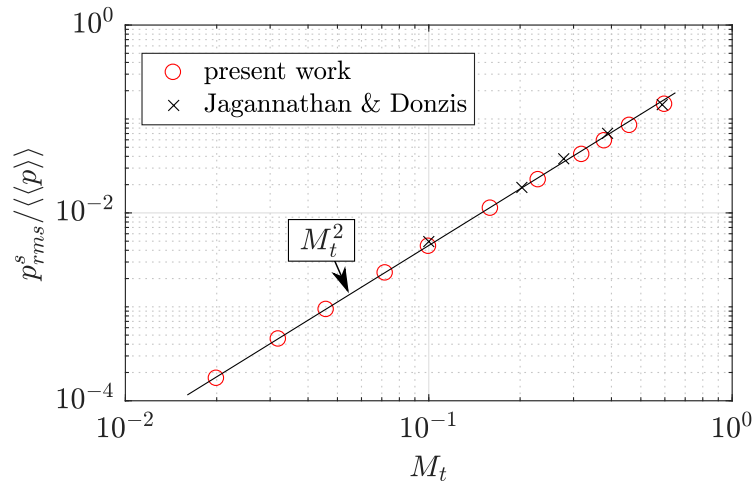
Figure 6.10: Ratio of the solenoidal pressure fluctuations and the mean pressure (red circles), compared with the results of Jagannathan & Donzis [29] at $Re_\lambda = 38$ (black crosses).
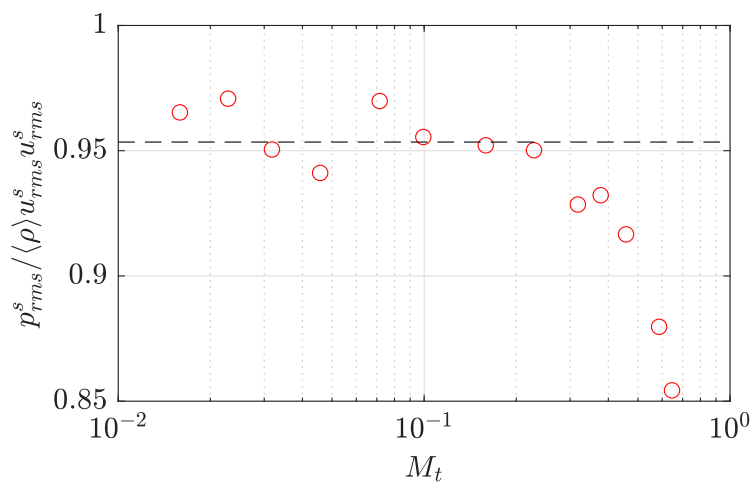
Figure 6.11: Scaling of the solenoidal pressure fluctuations as a function of the turbulent Mach number.
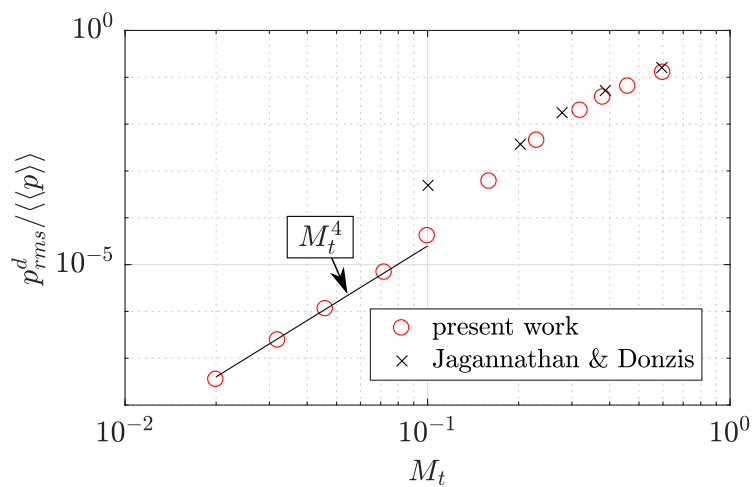
Figure 6.12: Ratio of the dilatational pressure fluctuations and the mean pressure (red circles), compared with the results of Jagannathan & Donzis [29] at $Re_\lambda = 38$ (black crosses).
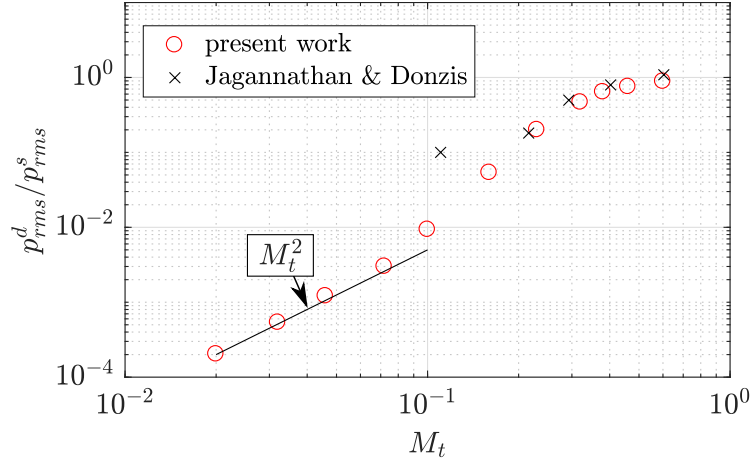
Figure 6.13: Ratio of the dilatational and solenoidal pressure fluctuations (red circles), compared with the results of Jagannathan & Donzis [29] at $Re_\lambda = 38$ (black crosses).

Table 6.1: Summary of the scalings computed from the compressible homogeneous turbulence simulation results.

Quantity	Scaling	Valid up to
$\langle \tilde{k}^d \rangle / \langle \tilde{k}^s \rangle$	$0.02M_t^4$	$M_t = 0.1$
$\langle\!\langle \epsilon^d \rangle\!\rangle / \langle\!\langle \epsilon^s \rangle\!\rangle$	$0.04M_t^4$	$M_t = 0.2$
$p_{rms}^s / \langle\!\langle p \rangle\!\rangle$	$0.5M_t^2$	at least up to $M_t = 0.6$
$p_{rms}^d / \langle\!\langle p \rangle\!\rangle$	$0.3M_t^4$	$M_t = 0.08$
p_{rms}^d / p_{rms}^s	$0.6M_t^2$	$M_t = 0.08$

6.2.2.5 Summary of the Mach number scaling results

Table 6.1 summarizes the scalings obtained at low Mach numbers. All the scaling results are in agreement with the low Mach number expansion reviewed in Sec. 6.1.2. The scalings involving the compressible components of the field are valid up to $M_t \approx 0.1$. The scaling $p_{rms}^s / \langle\!\langle p \rangle\!\rangle \approx 0.5M_t^2$ is valid for the full range of Mach numbers considered. Once again, this particular scaling is not due to compressibility effects. Obtaining these scalings required performing simulations at Mach numbers much smaller than the ones considered by Jagannathan & Donzis [29], and averaging quantities over more than 400 eddy turnover times to obtain converged statistics.

6.2.3 Effect of Reynolds number

So far, we considered a single Reynolds number, i.e., $Re_\lambda = 31$. We observed a strong Mach number dependence on all quantities of interest. We now want to determine if the results obtained in Sec. 6.2.2 are sensitive to the Reynolds number.

Table 6.2: Parameters of the homogeneous compressible turbulence performed to assess the impact of the Reynolds number.

Re_λ	Re_t	M_t	N^3	$\kappa_{max}\eta$	Statistics averaged over
31	63		64^3	1.6	400τ
50	165		128^3	1.6	100τ
80	420	0.40	264^3	1.6	90τ
125	1050		512^3	1.6	40τ
200	2640		1024^3	1.6	6τ

In this section, we perform additional simulations at a fixed $M_t = 0.40$, but at different Re_λ. The simulation parameters are shown in Table 6.2. Figure 6.14d shows instantaneous isocontours of the local Mach number $M = |\boldsymbol{u}|/c$ for for $M_t = 0.4$, at various Reynolds numbers. The local Mach number reaches values up to $M = 1.2$ locally.

(a) $Re_\lambda = 50$

(b) $Re_\lambda = 80$

(c) $Re_\lambda = 125$

(d) $Re_\lambda = 200$
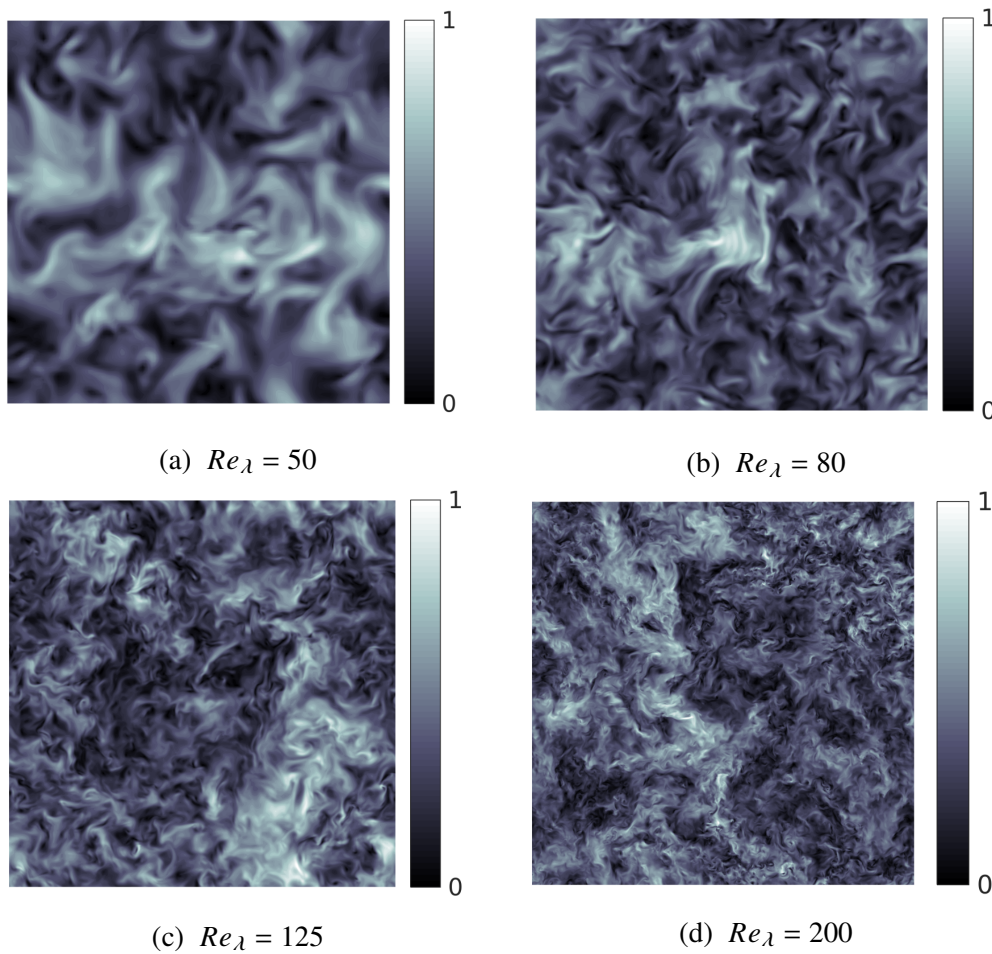
Figure 6.14: Instantaneous isocontours of the local Mach number at $M_t = 0.4$.

Figure 6.15 shows the ratio of the dilatational to solenoidal viscous dissipation rates, kinetic energies, and pressure fluctuations for the five Reynolds numbers considered. The non-monotonicity of the results prevents us from reaching definitive conclusions regarding the Reynolds number dependence of these ratios. The largest difference is obtained for the ratio of dilatational to solenoidal pressure fluctuations. We obtain $p_{rms}^{d}/p_{rms}^{s} = 0.5$ at $Re_{\lambda} = 50$, and $p_{rms}^{d}/p_{rms}^{s} = 1.1$ at $Re_{\lambda} = 200$. Although the Reynolds number is increased by a factor of four, p_{rms}^{d}/p_{rms}^{s} only changes by a factor of two. Hence, if there is any dependence of these ratios on the Reynolds numbers, it must be small. Note that we only considered one turbulent Mach number. The Reynolds number dependence of these ratios could also change with M_{t}. However, it is beyond the scope of this thesis to consider all combinations of Reynolds numbers and Mach numbers.

6.3 Summary

In this chapter, we explored compressibility effects in subsonic homogeneous turbulence, using the forcing technique presented in Chapter 5. We first described how velocity, dissipation rate, and pressure fluctuations can be decomposed into solenoidal and dilatational components. We also reviewed the low Mach number expansion to get insight into how these quantities are expected to scale with M_{t} at low Mach numbers. We then presented simulation results, first fixing the Reynolds number and varying the turbulent Mach number. The Mach number scaling of the ratios of dilatational to solenoidal kinetic energies, dissipation rates, and pressure fluctuations were found to be consistent with the scalings obtained by considering the low Mach number expansion, and in agreement with the improved Fauchet-Bertoglio model [26, 116]. The thermodynamic fluctuations were found to be almost isentropic, in agreement with previous studies [119, 122]. Finally, there does not appear to be a strong Reynolds number influence on the ratios of solenoidal to dilatational kinetic energies, dissipation rates, and pressure fluctuations.
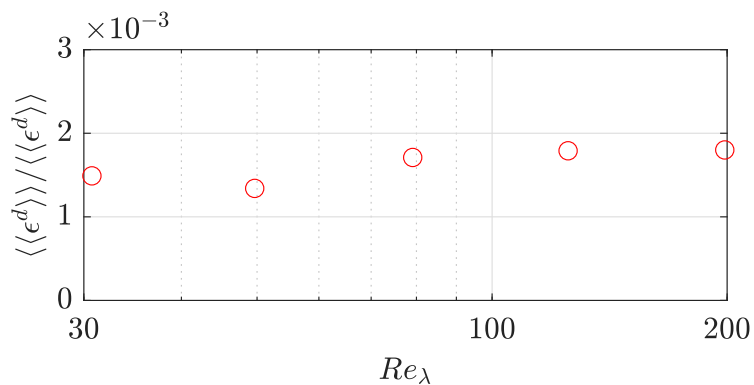
(a) Ratio of the dilatational to solenoidal viscous dissipation rates.
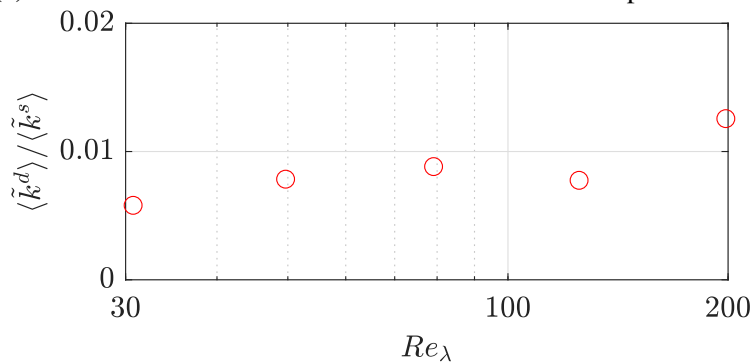
(b) Ratio of the dilatational to solenoidal kinetic energies.
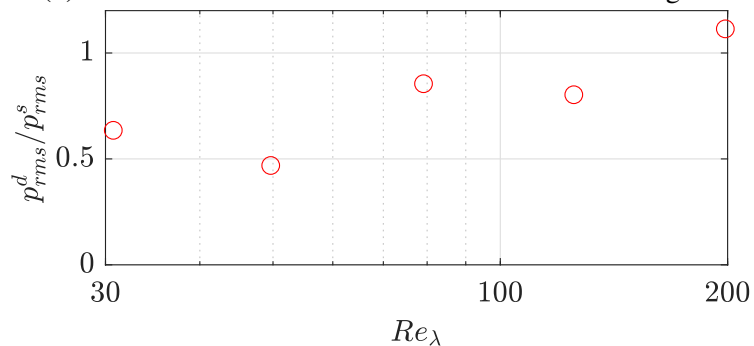
(c) Ratio of the dilatational to solenoidal root mean square of the pressure fluctuations.

Figure 6.15: Effect of the turbulent Reynolds number. All simulations are performed at $M_t = 0.40$.

Chapter 7

COMPRESSIBILITY EFFECTS IN TURBULENT FLAMES

In Chapter 6, we considered the effect of compressibility in non-reacting flows. The goal of the present chapter is to investigate compressibility effects in premixed turbulent deflagration fronts using an inflow/outflow configuration, as depicted in Fig. 7.1. There has been previous work simulating fully compressible turbulent flames with an inflow/outflow configuration [52, 123, 124]. The following approach was used:

1. A statistically-stationary incompressible turbulent state is achieved by means of large-scale forcing with periodic boundary conditions on all sides;

2. A laminar flame solution is superimposed on the turbulent field, and the non-homogeneous boundary conditions are switched to zero-order extrapolation, i.e., Neumann boundary conditions;

3. Flame statistics are gathered.

This procedure presents several issues. First, as seen in Sec. 3.4.2, Neumann boundary conditions are perfectly reflecting, such that any pressure waves generated by the interaction of the flame with the turbulence would be reflected at the boundary instead of leaving the domain. Second, a turbulent flame field differs from the superimposition of a non-reacting turbulent field and a laminar flame solution, which might yield to an unphysical and long transient behavior. Third, the turbulence forcing technique used in [52, 123, 124] is decorrelated from the velocity field, whereas we showed in Chapter 5 that forcing should be linear with the velocity field. Fourth, their forcing technique causes gradual heating of the fuel due to viscous dissipation. Hence, they cannot reach a statistically-stationary state. Lastly, a one-step chemical mechanism was used, which fails to capture the complex turbulence-flame [46, 51] and acoustics-flame [2, 3] interactions.

We seek to improve this procedure by

1. Using the NSCBC at the inlet/outlet to allow acoustic waves generated by the flame and turbulence to exit the domain freely;
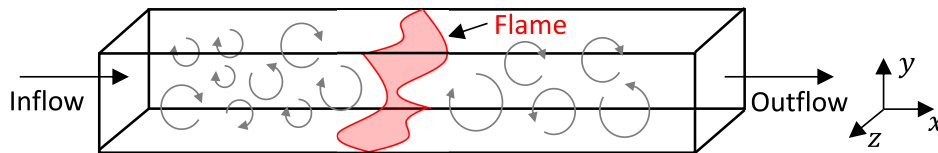
Figure 7.1: Schematic of the turbulent flame configuration.

2. Using a detailed chemical mechanism to capture the complex flame-turbulence and flame-acoustics interactions;

3. Leveraging the fact that the low Mach number solution should be close to the compressible solution to initialize the fully compressible simulations.

The flame configurations investigated are detailed in Sec. 7.1. We then propose a numerical framework to obtain a desired compressible turbulent field in an out-flow/outflow configuration, that allows us to use the NSCBC at the inlet/outlet. This is detailed in Sec. 7.2. In Sec. 7.3, we present simulation results obtained with both the low Mach number approximation and the compressible framework. We separately investigate the impact of turbulence intensity on the flame (Karlovitz number effects), and the impact of compressibility on the flame (Mach number effects).

7.1 Flame configurations

We examine three n-heptane/air premixed flame configurations similar to the ones that Lapointe et $al.$[40] investigated under the low Mach number approximation. The temperature in the unburnt region is $T_{0,u} = 800$ K, the pressure is $p_{0,u} = 1$ atm, and the equivalence ratio is $\phi = 0.9$. This elevated unburnt temperature is chosen for two reasons. First, practical combustion devices usually operate at elevated unburnt temperatures. Second, for a same turbulent Mach number in the unburnt region $M_{t,u} = \sqrt{2k}/c_u$, where c_u is the sound speed in the unburnt region, compressibility effects on the flame are expected to be more pronounced for a higher unburnt temperature, which is precisely what we want to explore in this chapter. This is because the ratio of the sound speed in the unburnt region to the one at the reaction zone $c_u/c_\delta < 1$ will be larger for a higher unburnt temperature. Kinetic energy being constant throughout the flame with the forcing technique employed, the turbulent Mach number at the reaction zone $M_{t,\delta} = \sqrt{2k}/c_\delta = M_{t,u}c_u/c_\delta$ will be larger for a higher unburnt temperature.

The flow parameters for the three flame configurations investigated are given in Table 7.1. The Karlovitz number in the unburnt region Ka_u is obtained from Eq. (1.32)

with ν_u, the kinematic viscosity evaluated in the unburnt region. We consider Cases C* and D*, performing both simulations under the low Mach number approximation and the fully compressible framework. These flames are at slightly higher Karlovitz numbers than Cases C and D in Lapointe *et al.*[40], hence why we refer to them as Cases C* and D*. We also consider Case E, which is at a even higher Karlovitz number than Flame D*. This flame is only simulated using the low Mach number approximation, for reasons that will be made clear after we explain the procedure to initialize the compressible fields in Sec. 7.2.4. For all cases, the domain is periodic in the y and z directions, and is eleven times larger in the x direction, i.e., $L_x = 11L_y$, with $L_y = L_z$. The laminar flame thickness $l_F = 2.5 \cdot 10^{-4}$ m, and the laminar flame speed $S_L = 2.3$ m/s, are extracted from a 1D simulation at the same flow conditions. For both cases, we have $\Delta x < 2\eta_u$, and $\Delta x < (l_F/20)$, which are necessary to properly resolve both the turbulence and the flame structure [22, 40]. We use constant non-unity Lewis numbers, using the approach detailed in Sec. 3.3.2. The Lewis numbers used for the present simulations are included in Appendix F.

For Cases C* and D*, we keep l/l_F and S_L/c_u constant. The impact of l/l_F has been previously investigated; no impact on the local chemistry [78] and the flow field [59] were observed. Since l/l_F and S_L/c_u are the same for the two cases, we obtain $M_t \sim Ka^{2/3}$ from Eq. (1.37). Hence, by changing the Mach number, we also change the Karlovitz number. That is why, in Sec. 7.3, we first investigate the impact of turbulence on the flame (Karlovitz number effects) using the low Mach number approximation, considering the three cases listed in Table 7.1. Then, we investigate the impact of compressibility (Mach number effects) by comparing results obtained using the low Mach number approximation and the compressible framework for Cases C* and D*. This procedure allows us to investigate the effects of these two parameters separately.

Table 7.1: Parameters of the turbulent flame configurations. The subscript ( )$_u$ refers to quantities evaluated in the (forced) unburnt region. Cases C* and D* are simulated using both the low Mach number approximation and the fully compressible framework, while Case E is simulated with the low Mach number approximation only.

Case	$Re_{t,u}$	$M_{t,u}$	u'/S_L	Ka_u	Ka_δ	Δx [m]	η_u [m]	Grid
C*	172	0.17	24	303	117	$1.1 \cdot 10^{-5}$	$5.4 \cdot 10^{-6}$	$11 \cdot 144^3$
D*	385	0.39	53	1010	366	$5.8 \cdot 10^{-6}$	$2.9 \cdot 10^{-6}$	$11 \cdot 264^3$
E	708	-	98	2530	860	$3.7 \cdot 10^{-6}$	$1.9 \cdot 10^{-6}$	$11 \cdot 416^3$

Table 7.2: Notation for the different quantities discussed in Sec. 7.2.

Desired flow conditions in the unburnt forced region	$T_{0,u}, p_{0,u}, \rho_{0,u}, u_{0,u}, k_{0,max}, Y_{s,0,u}$
Boundary conditions for the low Mach number simulations	$u_{in,LM}, T_{in,LM}, \rho_{in,LM}$
Boundary conditions for the compressible simulations	$u_{in,C}, T_{in,C}, \rho_{in,C}, p_{out,C}$
Modified planar-averages for the compressible simulations	$\langle u \rangle_C, \langle T \rangle_C, \langle p \rangle_C, \langle \rho \rangle_C$

7.2 Numerical setup

Table 7.2 summarizes the notation used for the different quantities discussed in this section.

7.2.1 Governing equations

As shown in Fig. 7.1, a turbulent flame with cold reactants on the left and hot products on the right is located in a flow field with a mean velocity $u_{0,u} = \overline{S}_T$, where S_T is the instantaneous turbulent flame speed, such that the flame is statistically-stationary. The goal is to obtain a compressible turbulent flow at a desired turbulence intensity $k_{0,max}$ and mean thermodynamic variables in the unburnt region $\rho_{0,u}$, $p_{0,u}$, and $T_{0,u}$, using the linear forcing technique detailed in Chapter 5.

We want to use the Navier-Stokes Characteristics Boundary Conditions (NSCBCs) at the inlet/outlet to allow acoustic waves generated by the turbulent reacting flow to exit the domain freely. The NSCBC require $u > 0$ locally at the inlet/outlet for the amplitudes of the characteristic waves to be computed correctly, as detailed in Sec. 3.4.2. For the Karlovitz numbers considered, the local fluctuations in velocity are much greater than the mean flow speed, i.e., $|u'| \gg u_{0,u} = \overline{S}_T$. Hence, such a turbulent flow at the inlet/outlet is incompatible with the use of the NSCBC. Thus, our strategy is to force turbulence away from the boundaries only. The target kinetic energy profile is shown in Fig. 7.2. It is designed such that $u \approx \overline{u} > 0$ at the boundaries. In Fig. 7.2, the different sections correspond to: 1) the unburnt unforced region, 2) the unburnt forced region, 3) the turbulent flame brush, 4) the burnt forced region, and 5) the burnt unforced region.

Extending the derivation presented in Chapter 5 from a periodic box to an in-
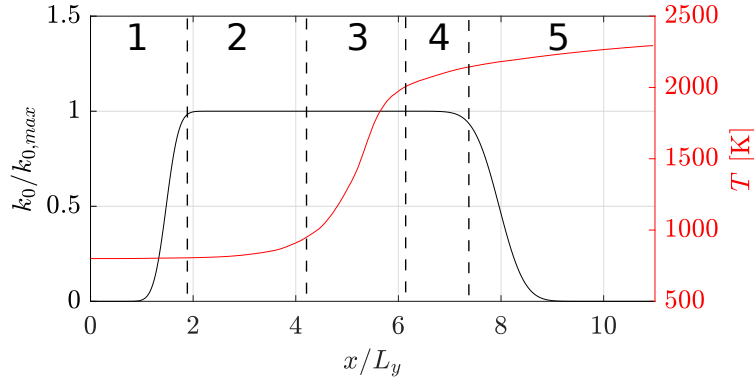
Figure 7.2: Theoretical (desired) kinetic energy profile for the inflow/outflow configuration (black). The planar-averaged temperature profile for Case D* is shown in red to illustrate where the flame is located. The different sections denote (1 to 5) the flow regions (see text).

flow/outflow configuration, we solve the following momentum equation

$$\frac{\partial \rho \boldsymbol{u}}{\partial t} + \nabla \cdot (\rho \boldsymbol{u} \otimes \boldsymbol{u}) = -\nabla p + \nabla \cdot \boldsymbol{\tau} + \rho A \frac{k_0}{\tilde{k}} (\boldsymbol{u}_s - \langle \boldsymbol{u}_s \rangle) , \qquad (7.1)$$

where the operators $\langle \ \rangle$ and $\tilde{k}$ now denote planar averages (in the y-z directions). Note that we only force the solenoidal velocity field $\boldsymbol{u}_s$, to avoid the instabilities investigated in Sec. 5.3. Also, the modification proposed by Carroll & Blanquart [108], detailed in Sec 5.4, is employed. We solve the following energy equation

$$\frac{\partial \rho e_t}{\partial t} + \nabla \cdot (\boldsymbol{u} (\rho e_t + p)) = -\nabla \cdot \boldsymbol{q} + \nabla \cdot (\boldsymbol{\tau} \cdot \boldsymbol{u})$$
$$+ \rho A \frac{k_0}{\tilde{k}} (\boldsymbol{u}_s - \langle \boldsymbol{u}_s \rangle) \cdot \boldsymbol{u} - \langle \rho A \frac{k_0}{\tilde{k}} (\boldsymbol{u}_s - \langle \boldsymbol{u}_s \rangle) \cdot \boldsymbol{u} \rangle , \qquad (7.2)$$

which is obtained by adding the kinetic energy equation obtained from Eq. 7.1 and the internal energy equation, and removing the planar average of the forcing term to achieve statistical stationarity, as detailed in Sec. 5.2.3.

We want to leverage the fact that the low Mach number solution should be a good approximation to the fully compressible one, i.e., we want to use low Mach number fields at the desired turbulent conditions to initialize the compressible simulations. For the simulations using the low Mach number approximation, the boundary conditions are trivial. We simply set $T_{in,LM} = T_{0,u} = 800$ K, $u_{in,LM} = u_{0,u} = \overline{S}_T$, and set the constant background pressure to be $p_0 = p_{0,u} = 1$ atm. However, as it will be seen shortly, the boundary values need to be modified for the compressible simulations to account for the fact that, unlike in the low Mach number case, the

thermodynamic state of the flow in the fully compressible framework depends on its turbulent state.

7.2.2 Planar-averaged equations

We consider the planar averages (in y and z) of Eqs. (2.1), (7.1), and (7.2). Neglecting the viscous/diffusive terms, the planar-averaged continuity, x-momentum, and total energy equations are given by

$$\frac{\partial \langle \rho \rangle}{\partial t} + \frac{\partial \langle \rho u \rangle}{\partial x} = 0 \,, \tag{7.3}$$

$$\frac{\partial \langle \rho u \rangle}{\partial t} + \frac{\partial \langle \rho u^2 \rangle}{\partial x} + \frac{\partial \langle p \rangle}{\partial x} = 0 \,, \tag{7.4}$$

$$\frac{\partial \langle \rho e_t \rangle}{\partial t} + \frac{\partial \langle u \rho h_t \rangle}{\partial x} = 0 \,. \tag{7.5}$$

Assuming that we reach a statistically-stationary state, we obtain the following relations:

$$\langle \rho u \rangle = C_1 \,, \tag{7.6}$$

$$\langle p + \rho u^2 \rangle = C_2 \,, \tag{7.7}$$

$$\langle u \rho h_t \rangle = C_3 \,, \tag{7.8}$$

where C_1, C_2, and C_3 are constant throughout the domain that depend on the thermodynamic and turbulent state of the flow.

We perform a Reynolds decomposition in terms of the planar-averaged mean and fluctuations, i.e., $p = \langle p \rangle + p'$, $\rho = \langle \rho \rangle + \rho'$, and $u = \langle u \rangle + u'$, $T = \langle T \rangle + T'$, and insert it into Eqs. (7.6)-(7.8). For continuity (Eq. (7.6)), we get

$$\langle \rho u \rangle = \langle \rho' u' \rangle + \langle \rho \rangle \langle u \rangle = C_1 \,. \tag{7.9}$$

The x-momentum equation yields

$$\langle p + \rho u^2 \rangle = \langle p \rangle + \langle \rho \rangle \langle u \rangle^2 + \langle \rho' u' u' \rangle + \langle \rho \rangle \langle u' u' \rangle + 2 \langle u \rangle \langle \rho' u' \rangle = C_2 \,. \tag{7.10}$$

Using homogeneous turbulence results, it was found that the terms $\langle \rho' u' \rangle$ and $\langle \rho' u' u' \rangle$ can be neglected, and a good approximation of Eqs. (7.9)-(7.10) is given by

$$\langle \rho \rangle \langle u \rangle = C_1 \,, \tag{7.11}$$

$$\langle p \rangle + \langle \rho \rangle \langle u \rangle^2 + \langle \rho \rangle \langle u'^2 \rangle = C_2 \,. \tag{7.12}$$

For the energy equation, we have

$$\langle u\rho h_t \rangle = \left\langle u \left(\rho \sum_{s=1}^{n_s} \left(Y_s \left(h_{s,ref} + \int_{T'=T_{ref}}^{T} c_{p,s}(T')dT' \right) \right) + \rho|\boldsymbol{u}|^2/2 \right) \right\rangle = C_3 .$$

(7.13)

Similarly to what was done for continuity and the x-momentum equations, Eq. (7.13) is approximated as

$$\langle u \rangle \left[\langle \rho \rangle \sum_{s=1}^{n_s} \left(\langle Y_s \rangle \left(h_{s,ref} + \int_{T'=T_{ref}}^{\langle T \rangle} c_{p,s}(T')dT' \right) \right) \right.$$

$$\left. + \langle \rho \rangle \frac{\langle u \rangle^2}{2} + \langle \rho \rangle \langle u'^2 \rangle + \langle \rho \rangle \langle k \rangle \right] = C_3 .$$

(7.14)

Note that, in Eqs. (7.12) and (7.14), $\langle u'^2 \rangle$ is the variance of the velocity in the x direction only, and $\langle k \rangle = \langle u'^2 + v'^2 + w'^2 \rangle / 2$.

Equations (7.11), (7.12), and (7.14) should be valid on average anywhere in the computational domain. This includes the unforced unburnt region, from $x/L_y = 0$ to $x/L_y = 2$, and the forced unburnt region, from $x/L = 2$ to about $x/L = 4$. As a direct consequence of the target kinetic energy amplitude changing with x, as shown in Fig. 7.2, the mean pressure $\langle p \rangle$ also changes (see Eq. (7.12)). The goal is to obtain the desired flow conditions $\langle u \rangle = u_{0,u} = \bar{S}_T$, $\langle p \rangle = p_{0,u} = 1$ atm, $\langle T \rangle = T_{0,u} = 800$ K, and $\langle k \rangle = k_{0,max}$ in the unburnt forced region. To do so, we must specify the correct boundary conditions at the inlet. The procedure is then to evaluate C_1, C_2, C_3 in the unburnt forced region, where the desired flow conditions are known, and use them to evaluate the correct inlet temperature $T_{in,C}$, and velocity $u_{in,C}$. In other words, C_1, C_2, C_3 are determined from Eqs. (7.11), (7.12), and (7.14) by using the known flow conditions in the unburnt forced region, i.e.,

$$C_1 \equiv \rho_{0,u} u_{0,u} ,$$

(7.15)

$$C_2 \equiv p_{0,u} + \rho_{0,u} u_{0,u}^2 + \frac{2}{3}\rho_{0,u} k_{0,max} ,$$

(7.16)

$$C_3 \equiv u_{0,u} \left[\rho_{0,u} \sum_{s=1}^{n_s} \left(Y_{s,0,u} \left(h_{s,ref} + \int_{T'=T_{ref}}^{T_{0,u}} c_{p,s}(T')dT' \right) \right) \right.$$

$$\left. + \rho_{0,u} \frac{u_{0,u}^2}{2} + \frac{5}{3}\rho_{0,u} k_{0,max} \right] ,$$

(7.17)

where we have used the isotropic relation $\langle u'^2 \rangle = (2/3)\langle k \rangle$ in Eqs. (7.16) and (7.17).

7.2.3 Boundary conditions

At the inlet, there is no turbulence, and Eqs. (7.11), (7.12), and (7.14) become

$$\rho_{in,C} u_{in,C} = C_1, \tag{7.18}$$

$$p_{in,C} + \rho_{in,C} u_{in,C}^2 = C_2, \tag{7.19}$$

$$u_{in,C} \left[\rho_{in,C} \sum_{s=1}^{n_s} \left(Y_{s,in,C} \left(h_{s,ref} + \int_{T'=T_{ref}}^{T_{in,C}} c_{p,s}(T') dT' \right) \right) + \rho_{in,C} \frac{u_{in,C}^2}{2} \right] = C_3. \tag{7.20}$$

We now want to solve Eqs. (7.18)–(7.20) to get the inlet boundary conditions that should be applied, i.e., we want to extract $u_{in,C}$, and $T_{in,C}$. Equations (7.18)–(7.20) contains $n_s + 4$ unknowns, where n_s is the number of species transported: $p_{in,C}, \rho_{in,C}, T_{in,C}, u_{in,C}$, and n_s $Y_{s,in,C}$. We set $Y_{s,in,C} = Y_{s,0,u}$, and add the planar-averaged equation of state

$$p_{in,C} = \frac{\rho_{in,C} R T_{in,C}}{W_{in}}, \tag{7.21}$$

with W_{in} computed using Eq. (2.9). We now have a system of 4 equations and 4 unknowns, that we can solve to obtain the inlet quantities.

The NSCBC framework also requires the desired pressure at the outlet p_{out}, which we compute as

$$p_{out,C} = C_2 - \rho_b u_b^2, \tag{7.22}$$

where ρ_b and u_b are the density and x velocity in the burnt region, extracted from the low Mach number simulations. In Table 7.3, we provide the boundary values for the two flame configurations considered, obtained by solving Eqs. (7.18)–(7.20) to obtain $u_{in,C}$, $p_{in,C}$, $\rho_{in,C}$, and $T_{in,C}$, and Eq. (7.22) to get $p_{out,C}$. It can be seen that $p_{in,C}$ and $p_{out,C}$ are very similar, and larger than $p_{0,u} = 101$ kPa. Note that $p_{in,C}$ and $\rho_{in,C}$ are not imposed, and are provided for reference only. The required inlet temperature $T_{in,C}$ is also larger than $T_{0,u} = 800$ K. For the low Mach number simulations, p_{in} and p_{out} are not provided, since in this framework the thermodynamic pressure is constant and imposed.

It is important to note that the computed boundary conditions differ significantly from the target quantities. This stresses the importance of this procedure. If one were to naively set $T_{in,C} = T_{0,u} = 800$ K, $p_{out,C} = p_{0,u} = 101$ kPa, and $u_{in,C} = u_{0,u} = \overline{S}_T$, then $\langle T \rangle$ would differ significantly from $T_{0,u}$ in the unburnt forced region (and likewise for the other flow quantities) when statistical stationarity is reached. Table

Table 7.3: Boundary conditions for the turbulent flame simulations.

compressible			low Mach # approximation		
Case	C*	D*	Case	C*	D*
$T_{in,C}$ [K]	806	829	$T_{in,LM}$ [K]	800	800
$u_{in,C}$ [m/s]	8.75	10.7	$u_{in,LM}$ [m/s]	8.80	11.0
$\rho_{in,C}$ [kg/m^3]	0.460	0.470	$\rho_{in,LM}$ [kg/m^3]	0.455	0.455
$p_{in,C}$ [Pa]	102,630	107,850			
$p_{out,C}$ [Pa]	102,560	107,770			

7.4 shows the expected planar-averaged quantities in the unburnt forced region if the "naive" boundary conditions were to be used.

Table 7.4: Expected mean flow quantities in the unburnt forced region if "naive" boundary conditions were used.

Case	C*	D*
$\langle T \rangle$ [K]	794	771
$\langle u \rangle$ [m/s]	8.85	11.3
$\langle p \rangle$ [Pa]	100,000	94,980
$\langle \rho \rangle$ [kg/m^3]	0.455	0.445

7.2.4   Initial conditions

Poludnenko *et al.*[52, 123, 124] initialized their compressible turbulent flame simulations by superimposing a turbulent non-reacting flow with a laminar flame solution. However, it is well known that turbulence impacts the flame structure and area [39]. Hence, this initialization technique is likely to cause a long transient, since it initially assumes that there are no turbulence-flame interactions. In the present work, we seek to use statistically-stationary turbulent flame solutions obtained using the low Mach number approximation to initialize the compressible simulations. Hence, the initial compressible field will already capture the complex turbulence-flame interactions, and only the compressibility effects will be missing. One could simply use the low Mach number field to initialize the fully compressible simulation, use the proper boundary conditions for the fully compressible configuration, and run the simulation for long enough for the flow to be statistically stationary.

In Sec. 7.2.3, we showed that the correct boundary conditions for the fully compressible simulations differ significantly from the ones for the low Mach number approximation, when the inflow/outflow configuration with non-uniform forcing is employed. As a result, a simulation with this initialization procedure would take

on the order of one flow through time, which poses a challenge in that it is often prohibitively computationally expensive to run simulations of turbulent flames with detailed chemistry for so long. Hence, to reduce the transient time, we propose to modify the initial compressible field. Specifically, we know that the statistically-stationary compressible flow field in the unforced region close to the inlet differs from the one obtained using the low Mach number approximation, since we have different boundary conditions. Hence, we seek to modify this flow region, corresponding to Region 1 in Fig. 7.2, to match the boundary conditions. For each plane in this section of the flow, we compute modified planar averages for all flow quantities by solving

$$\langle \rho \rangle_C \langle u \rangle_C = C_1 \,, \tag{7.23}$$

$$\langle p \rangle_C + \langle \rho \rangle_C \langle u \rangle_C^2 + \frac{2}{3} \langle \rho \rangle_C k_0 = C_2 \,, \tag{7.24}$$

$$\langle u \rangle_C \left[\langle \rho \rangle_C \sum_{s=1}^{n_s} \left(\langle Y_s \rangle_C \left(h_{s,ref} + \int_{T'=T_{ref}}^{\langle T \rangle_C} c_{p,s}(T')dT' \right) \right) \right. $$
$$\left. + \langle \rho \rangle_C \frac{\langle u \rangle_C^2}{2} + \frac{5}{3} \langle \rho \rangle_C k_0 \right] = C_3 \,, \tag{7.25}$$

where we set $\langle Y_s \rangle_C = \langle Y_s \rangle_{LM}$, completed with

$$\langle p \rangle_C = \frac{\langle \rho \rangle_C R \langle T \rangle_C}{W} \,, \tag{7.26}$$

with C_1, C_2, C_3 computed from Eqs. 7.15–(7.17), similarly to what was done to derive the correct boundary conditions. The subscript $\langle \ \rangle_{LM}$ refers to planar-averaged quantities from the low Mach number simulations, while the subscript $\langle \ \rangle_C$ denotes the new planar-averaged quantities for the compressible simulations. The flow quantities are then updated by computing

$$\psi_C(x, y, z) = \psi_{LM}(x, y, z) - \langle \psi \rangle_{LM}(x) + \langle \psi \rangle_C(x) \,, \tag{7.27}$$

where ψ represents u, p, and ρ, for $0 \leq x/L_y \leq 2$. This procedure should help in achieving a statistically-stationary flow faster, since the flow quantities in the unforced unburnt region are now compatible with the boundary conditions. Note that our approach, i.e., using a low Mach number field to initialize a fully compressible simulation, is likely to introduce some inconsistencies in the initial compressible field. However, the initial compressible field obtained using the proposed method should be closer to the solution for a compressible turbulent flame than if we were

to use the procedure employed by Poludnenko *et al.*, i.e., superimpose a turbulent non-reacting field with a laminar flame solution [52, 123, 124].

There are some limitations with the proposed framework. In a low Mach number field, pressure fluctuations are unbounded. In a compressible field, pressure fluctuations are bounded, i.e., $p' > -p$. Hence, if the pressure fluctuations in the low Mach number field are too large, i.e., $p' < -p$, then there is no straightforward way to convert the low Mach number field in a fully compressible one. For the cases considered here, $p'_{min} \approx -20$ kPa and $p'_{min} \approx -90$ kPa for Case C* and D*, respectively. This approach is not suited for Case E, since $p' < -101$ kPa for this configuration.

7.3   Results

Since it was chosen to vary the turbulent Mach number by changing the Karlovitz number (Cases C* and D*), we first examine the impact of the Karlovitz number on the flame characteristics, using simulation results obtained with the low Mach number approximation.

7.3.1   Karlovitz number effects

Figure 7.3 shows instantaneous slices of the temperature field for the three cases considered. The white temperature isolines, at $T = 1000$ K and $T = 1900$ K, delimit the extent of the flame brush. It can be seen that the flame brush thickens as the Karlovitz number is increased, and is much larger than the laminar flame thickness. Smaller turbulent structures can also be seen at high Karlovitz numbers, pointing to increased turbulent mixing.

Next, we look at the turbulent flame speed, given by Eq. (1.31). Figure 7.4 shows the mean turbulent flame speed as a function of the reaction zone Karlovitz number. The dashed black line is a power law fit of the form $\overline{S}_T/S_L = 1 + aKa_\delta^b$ [46]. Increasing the Karlovitz number leads to an increase in the mean turbulent flame speed. To understand this evolution, it is insightful to write the instantaneous turbulent flame speed as

$$\frac{S_T}{S_L} = \frac{A_T}{A_c} I_0 \,, \tag{7.28}$$

where A_T is the instantaneous turbulent flame area, A_c is the cross-sectional area, and I_0 is the burning efficiency factor [125, 126]. The approximate relation

$$I_0 \approx \frac{\langle \dot{\omega}_F/|\nabla T| \mid T_{\text{peak}} \rangle}{\dot{\omega}_{F,\text{lam}}/|\nabla T_{\text{lam}}|} \,, \tag{7.29}$$

(a) Case C*

(b) Case D*

(c) Case E
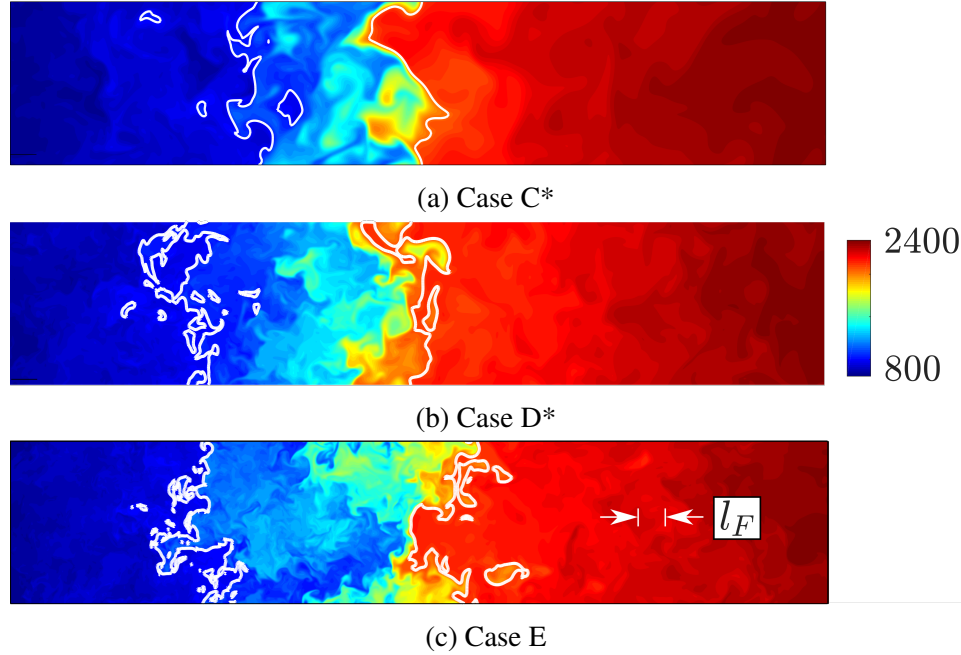
Figure 7.3: Instantaneous isocontours of the temperature field for flames at different Karlovitz numbers. The white isolines denote $T = 1000$ K and $T = 1900$ K.

was derived by Lapointe & Blanquart [46], where T_{peak} is the temperature at which fuel consumption is maximum. Equation (7.29) shows that the burning efficiency factor is related to the fuel consumption rate.

In Fig. 7.5, we show $\langle \dot{\omega}_F \mid T \rangle$ for the three cases considered, in addition to the profiles for the non-unity and unity Lewis number laminar flames. It can be seen that, as Ka_δ increases, the peak fuel consumption rate increases, and the temperature at which the fuel consumption rate is maximum also increases. To explore this further, we compute

$$\Delta T_{\text{norm}} = \frac{T_{\text{peak,turb}} - T_{\text{peak,lam},Le\neq1}}{T_{\text{peak,lam},Le=1} - T_{\text{peak,lam},Le\neq1}}, \tag{7.30}$$

where $T_{\text{peak,turb}}$, $T_{\text{peak,lam},Le\neq1}$, and $T_{\text{peak,lam},Le=1}$ are the temperatures at which the fuel consumption rate is maximum for the turbulent flame, one-dimensional flame with non-unity Lewis numbers, and one-dimensional flame with unity Lewis numbers, respectively. Figure 7.6 shows ΔT_{norm} for the three cases considered, along with the results of Lapointe & Blanquart [46]. The change in the temperature of peak fuel consumption rate is linked to a change in the effective Lewis number due to

enhanced turbulent mixing. The semi-empirical model of Savard & Blanquart [127]

$$Le_{s,\text{eff}} = \frac{1 + a_1 Ka_\delta}{\left(\dfrac{1}{Le_s} + a_1 Ka_\delta\right)}, \tag{7.31}$$

where a_1 is a proportionality coefficient, aims to explain the changes in ΔT_{norm} by changes in the effective Lewis numbers $Le_{s,\text{eff}}$, due to increased turbulent mixing. For $Ka_\delta \to 0$, Eq. (7.31) yields $Le_{s,\text{eff}} \to Le_s$, and $\Delta T_{norm} \to 0$, i.e., the flame behaves as a laminar flame. For $Ka_\delta \to \infty$, Eq. (7.31) gives $Le_{s,\text{eff}} \to 1$, and $\Delta T_{norm} \to 1$, i.e., turbulent mixing suppresses all differential diffusion effects. Multiple laminar one-dimensional flame simulations are performed using the effective Lewis numbers computed using Eq. (7.31), and the temperature of peak fuel consumption rate is extracted. The coefficient a_1 is adjusted to best fit the data in Fig. 7.6 ($a_1 = 0.01$) [40]. It can be seen in Fig. 7.6 that the model is in very good agreement with the turbulent flame results. Finally, Figure 7.7 shows the conditional average of the normalized fuel consumption rate at the temperature of peak fuel consumption rate, i.e, the peak values in Fig. 7.5, which are seen to increase monotonically with Ka_δ.
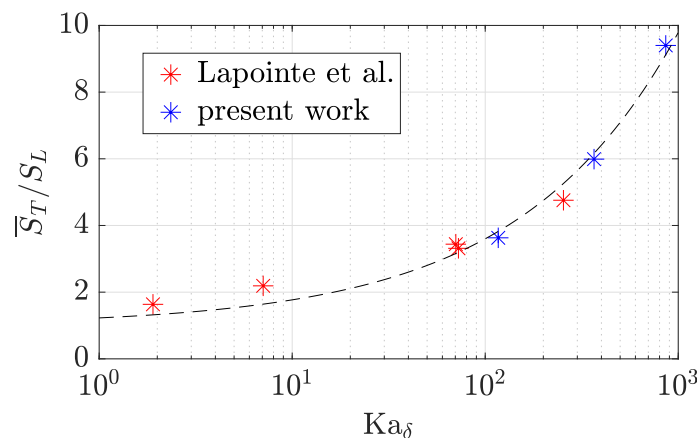
Figure 7.4: Normalized mean turbulent flame speed as a function of the reaction zone Karlovitz number Ka_δ. The red stars are simulations results from Lapointe & Blanquart [46]. The dashed black line is a power law fit.

7.3.2 Compressibility effects

The purpose of this section is to assess whether compressibility effects impact the flame behavior for Cases C* ($M_{t,u} = 0.17$) and D* ($M_{t,u} = 0.39$). The initial compressible fields are obtained following the procedure presented in Sec. 7.2.
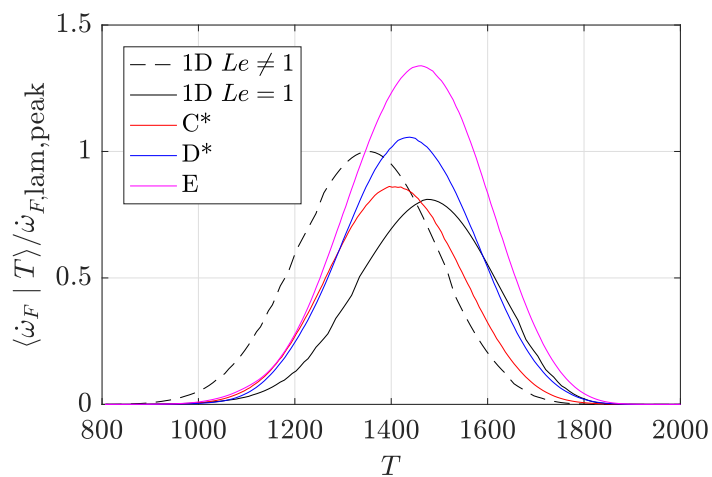
Figure 7.5: Normalized fuel consumption rate on temperature. The one-dimensional profile obtained with non-unity Lewis numbers is shown by a black dashed line, and the one obtained with unity Lewis numbers is shown by a solid black line.
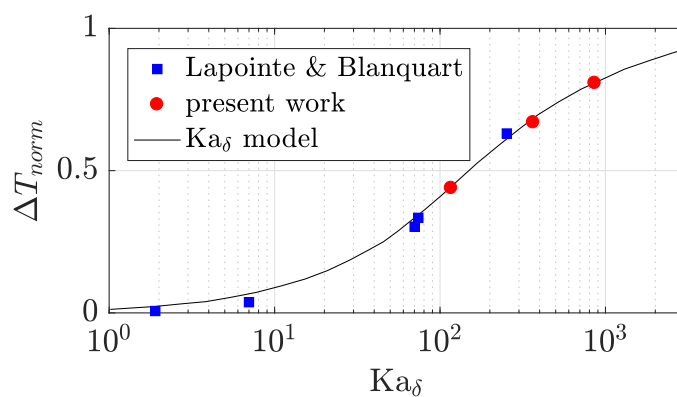
Figure 7.6: Temperature at which the peak burning rate is observed in the turbulent flames, normalized with the temperatures at which the peak burning rate is observed in the unity and non-unity Lewis number one-dimensional flames. The solid black line shows the fit obtained using the semi-empirical model of Savard & Blanquart [127].
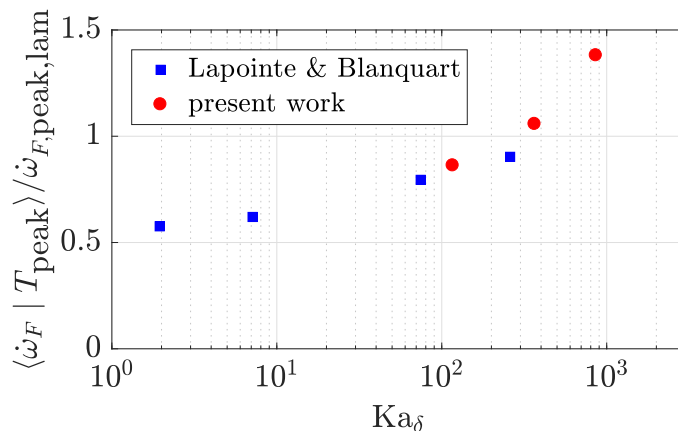
Figure 7.7: Conditional average of the normalized fuel consumption rate at the temperature of peak fuel consumption rate.

Figure 7.8 shows instantaneous isocontours of the local Mach number $M = |\mathbf{u}|/c$. It can be seen that the local Mach number reaches values up to $M = 0.5$ for Case C*, and $M = 1$ for Case D*.

(a) Case C*

(b) Case D*
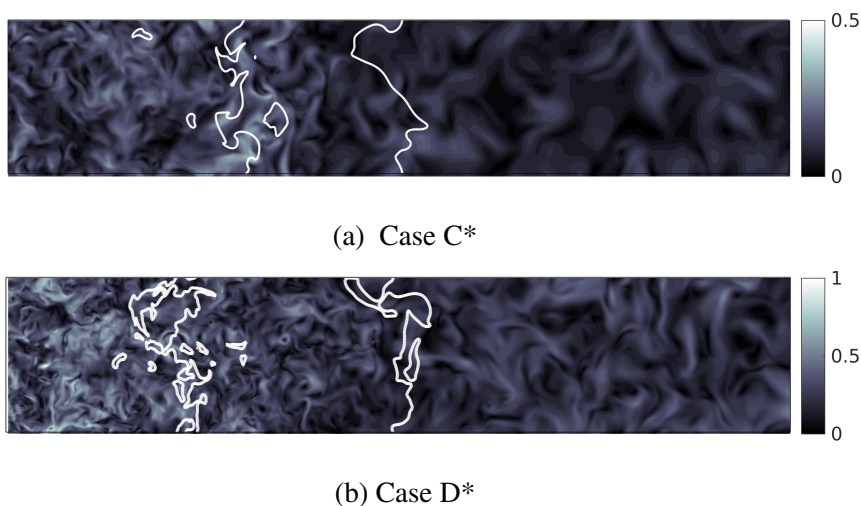
Figure 7.8: Instantaneous isocontours of the local Mach number. The white isolines denote $T = 1000$ K and $T = 1900$ K.

7.3.2.1 Compressibility effects on turbulence

Figure 7.9 shows the planar Favre-averaged turbulent kinetic energy (TKE) for the simulation results obtained with the low Mach number solver and the fully compressible solver, against the target TKE profile (see Fig. 7.2). The obtained TKE profiles follow the desired behavior. When the forcing is stopped ($x/L_y = 8$),

the TKE decays rapidly. The predicted "lag" between the theoretical TKE profile and the computed ones can be estimated as

$$\Delta x_{decay} = u_b \tau , \tag{7.32}$$

where u_b is the mean velocity in the burnt region, and τ is the eddy turnover time. For Flame C*, Eq. (7.32) yields $\Delta x_{decay}/L_y = 0.13$. For Flame D*, we obtain $\Delta x_{decay}/L_y = 0.07$. This is what we observe in Fig. 7.9, i.e., $\Delta x_{decay} \ll L_y$.

(a) Case C*
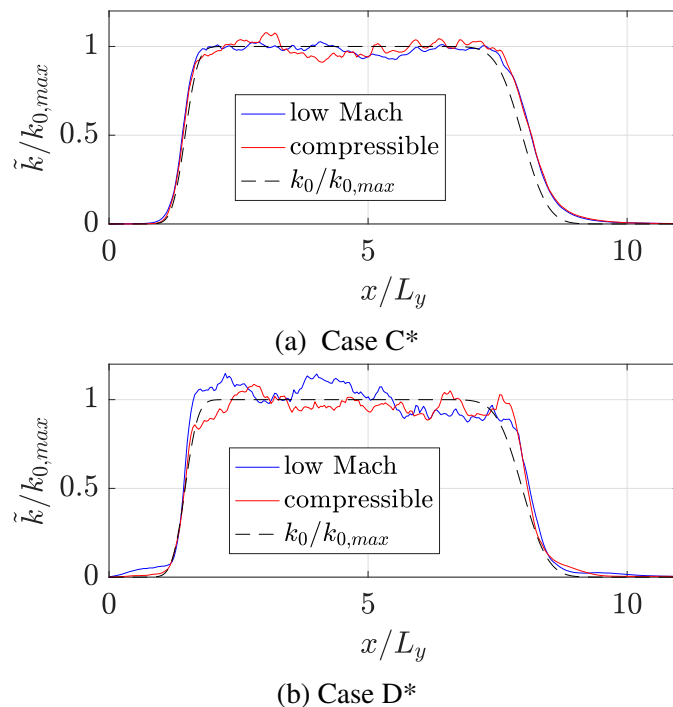
(b) Case D*

Figure 7.9: Planar-averaged turbulent kinetic energy.

Figure 7.10 shows the planar-averaged density for Case D*. The planar-averaged density is similar for the low Mach number and compressible simulations. The exception is the unburnt unforced region close to the inlet, where for the compressible simulation density is larger than for the low Mach number simulation, in line with the values $\rho_{in,C} = 0.470$ kg/m^3 and $\rho_{in,LM} = 0.455$ kg/m^3 given in Table 7.3.

Figure 7.11 shows the planar-averaged pressure fields for Case D*. The target pressure in the unburnt forced region $p_{0,u}$ is shown by a dashed line. The low Mach number hydrodynamic pressure field being defined up to a constant, we adjust the constant such that the pressure in the unburnt forced region is $p_{0,u}$, for visualization purposes. The low Mach number and compressible planar-averaged pressure fields are in very good agreement. This is because they have similar density and kinetic
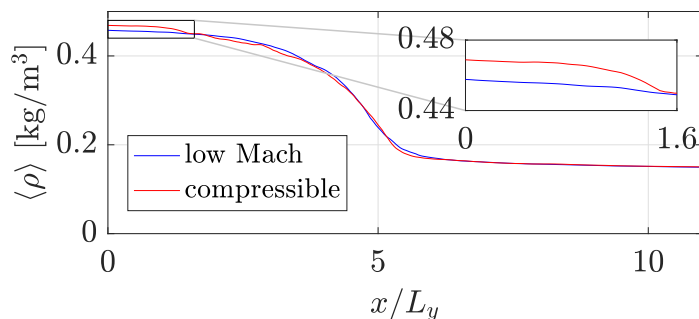
Figure 7.10: Planar-averaged density for Case D*.

energy profiles, as shown in Figs. 7.9b and 7.10, and Eq. (7.7) applies in both cases, i.e., $\langle p + \rho u^2 \rangle = C_2$, since the momentum equation is identical in the low Mach and compressible formulations. In Fig. 7.12, we show $\langle p + \rho u^2 \rangle$ for both frameworks. It can be seen that $\langle p + \rho u^2 \rangle$ is indeed constant throughout the domain.
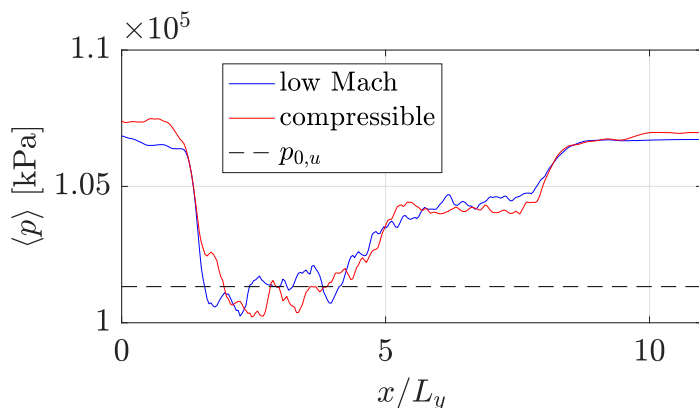
Figure 7.11: Planar-averaged pressure for Case D*.
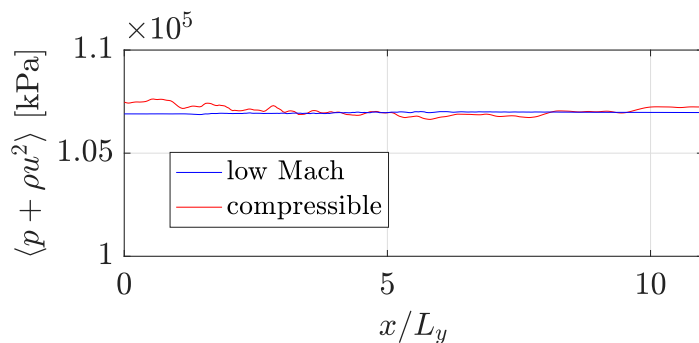
Figure 7.12: Planar average of $p + \rho u^2$ for Case D*.

In Fig. 7.13, the red line shows the time evolution of ρ_{rms} in the forced region ahead of the flame for Case D*, i.e., for $2 \leq x/L_y \leq 3$. The black dashed line show the density fluctuations predicted from the fluctuating pressure field, assuming an

isentropic behavior, following Eq. (6.20). Initially, the density fluctuations are much smaller in magnitude than the isentropic predictions. This is because the initial compressible field is initialized with a low Mach number field, which doesn't have any density fluctuations directly caused by turbulence. The small initial density fluctuations ($\rho_{rms}/\langle\!\langle\rho\rangle\!\rangle \approx 0.01$) are hence entirely due to turbulent mixing ahead of the flame. As it can be seen in Fig. 7.13, the density fluctuations quickly reach a statistically-stationary value (in less than one eddy turnover time τ), which is close to the isentropic behavior. However, we don't expect a perfect collapse between the two curves for two reasons: 1) the isentropic behavior was not exactly recovered in homogeneous non-reacting turbulence (see Sec. 6.2.2.3), and 2) there is some turbulent mixing between colder and warmer reactants, as evidenced by the fact that $\rho_{rms} > 0$ at $t = 0$.
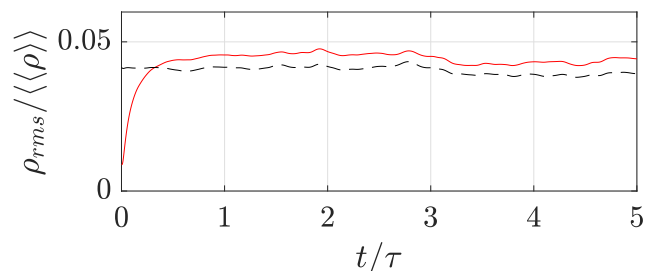
Figure 7.13: Time evolution of the root mean square of the density fluctuations in the forced region ahead of the flame for Case D*.

Figure 7.14 shows the planar-averaged root mean square of the pressure fluctuations once statistical stationarity for the thermodynamic variables is achieved, i.e., for $t/\tau > 1$. It can be seen that for both Cases C* and D*, the amplitude of the pressure fluctuations are similar for the simulations performed with the low Mach number approximation and the compressible formulation. The black dashed line shows the pressure fluctuations predicted from the density and velocity fields, following the relation $p_{rms} \approx 0.91\langle\rho k\rangle/3$, obtained from simulations of homogeneous incompressible turbulence [121], similarly to what was found in Sec. 6.2.2.4. Hence, the amplitude of the pressure fluctuations in both the compressible and the low Mach turbulent flame simulations are controlled by the "incompressible" pressure field induced by turbulence. In other words, with regards to the low Mach number expansion, the pressure fluctuations in the compressible simulations are mostly hydrodynamic, i.e., $p' \approx \epsilon p'_1$.

Figure 7.15 shows the planar-averaged root mean square of the density fluctuations.
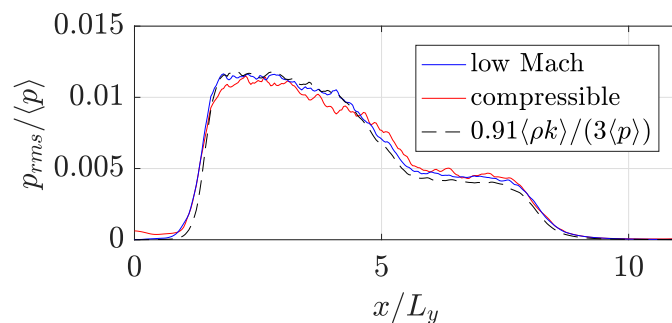
(a) Case C*
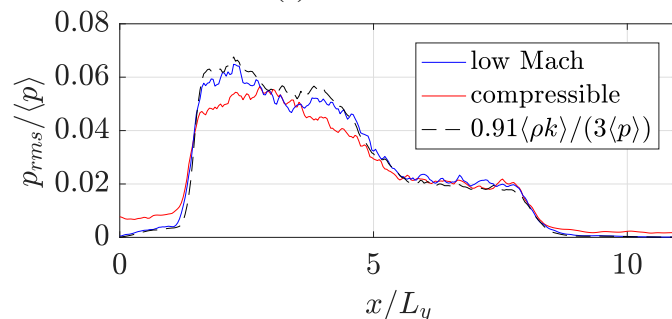
(b) Case D*

Figure 7.14: Planar-averaged pressure fluctuations. The black dashed line is the rms of the pressure fluctuations predicted from the velocity and density fields.

For Case D*, the density fluctuations in the unburnt forced region are much larger for the compressible simulations than for the low Mach number ones. The dashed black line shows the amplitude of the density fluctuations predicted from the pressure fluctuations, assuming an isentropic behavior, i.e., using Eq. (6.20) with the planar-averaged specific heat ratio $\langle \gamma \rangle$. The predicted density fluctuations match the rms extracted from the compressible simulations very well, away from the flame. In the turbulent flame brush, which appears as a peak in Figs. 7.15a and 7.15b, the density fluctuations for both the low Mach number and compressible simulations agree very well. For the compressible cases, this implies that, in the flame, density fluctuations due to the turbulent mixing of cold reactants with hot products dominates over the density fluctuations induced by turbulence. With regards to the low Mach number expansion, in the forced regions away from the flame, the density fluctuations for Case D* are dominated by the contribution of the first order density, i.e., $\rho' \approx \epsilon \rho_1' \gg \rho_0'$. In the turbulent flame brush, the main contribution to the density fluctuations comes from the zeroth order term, i.e., $\rho' \approx \rho_0' \gg \epsilon \rho_1'$. This is in contrast with the results obtained for homogeneous non-reacting turbulence, where ρ_0 is constant, and the leading contribution to the fluctuating density comes from ρ_1.

(a) Case C*

(b) Case D*
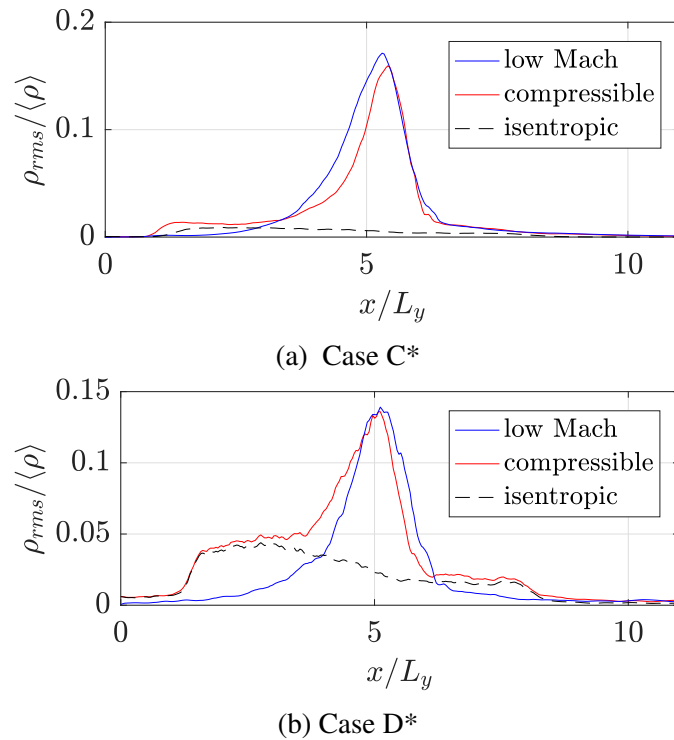
Figure 7.15: Planar-averaged density fluctuations. The black dashed line is the amplitude of the density fluctuations predicted from the pressure fluctuations, assuming an isentropic behavior.

7.3.2.2 Compressibility effects on chemistry

We first assess the impact of compressibility on the turbulent flame speed. Figure 7.16 shows the evolution of the turbulent flame speed for Case C*. The black circle denotes where we performed the low Mach number to compressible conversion, and started the compressible simulation. It can be seen that the two simulations yield the same flame speed for $\sim 5\tau$, after which they start to deviate. This is not surprising since turbulence is stochastic, and the flame speed is partially controlled by the large scale turbulent structures [46].

For Flame C*, we obtain $\overline{S}_T/S_L = 3.8 \pm 0.1$ for the low Mach number simulation, and $\overline{S}_T/S_L = 3.6 \pm 0.2$ for the compressible one. For Flame D*, we obtain $\overline{S}_T/S_L = 6.0 \pm 0.3$ for the low Mach number simulation, and $\overline{S}_T/S_L = 5.7 \pm 0.7$ for the compressible one. The error bounds are computed by averaging the first and second halves of the data separately, which only gives a qualitative picture of the accuracy of the average. The turbulent flame speed fluctuates greatly in time, and obtaining precise estimates of $\overline{S}_T/S_L$ would require the simulations to be run for times much longer than what was performed in the present work. In contrast to the large impact

of the Karlovitz number, as shown in Fig. 7.4, the differences between the average turbulent flame speeds for the low Mach number and compressible results are small. Hence, there doesn't appear to be a significant impact of compressibility on the turbulent flame speed for the cases considered.
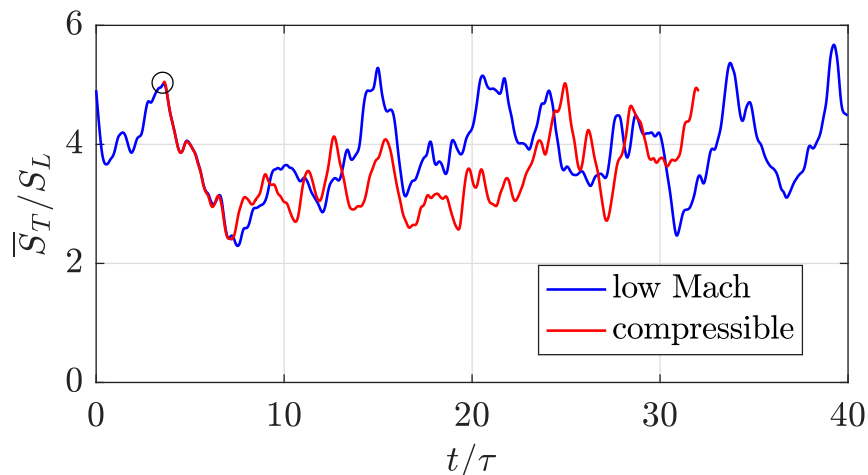
Figure 7.16: Normalized flame speed as a function of time for Flame C*. The black circle denotes when the compressible simulation was initialized.

Next, we look at the impact of compressibility on the local chemistry. Figure 7.17 shows the conditional average of the fuel consumption rate in temperature space for the two cases. Once again, there is a good agreement between the low Mach number and compressible results for both cases, especially when contrasted with the large impact of the Karlovitz number, as shown in Fig. 7.5. Hence, compressibility effects appear to have a limited impact on the local chemistry. In summary, for the Mach numbers considered, although compressibility effects significantly impact the turbulence characteristics, the flame behavior appears to remain relatively unchanged.

7.4 Summary

In this chapter, we performed simulations of n-heptane/air turbulent flames with detailed chemistry in an inflow/outflow configuration, using both the low Mach number approximation and the compressible framework. We proposed a procedure to initialize the compressible simulations with a statistically-stationary turbulent flame solution obtained using the low Mach number approximation. To use the NSCBC framework, it was necessary to force turbulence away from the boundaries only. It was found that special care must be taken with the boundary values for the compressible simulations when a spatially-varying forcing scheme is employed.
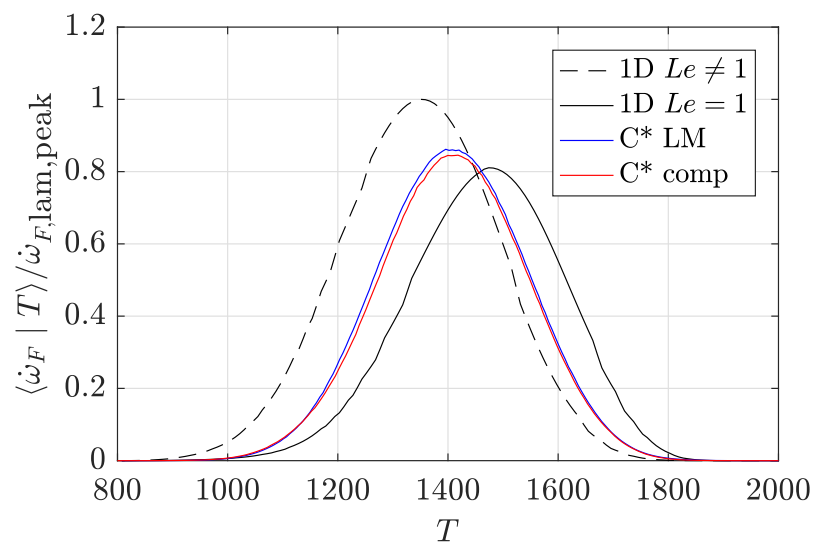
(a) Case C*
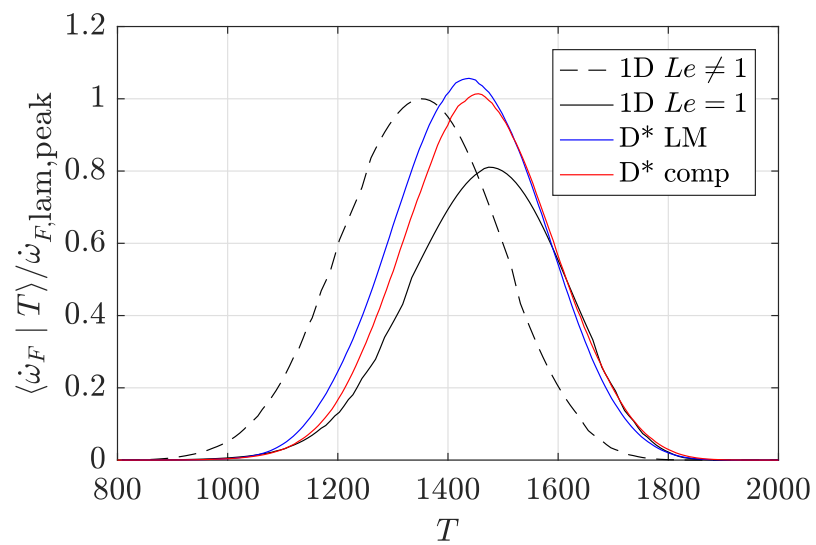
(b) Case D*

Figure 7.17: Normalized fuel consumption rate conditioned on temperature.

Then, we presented simulation results, and investigated Karlovitz number and Mach number effects separately. Karlovitz number were found to have a strong impact on the flame characteristics, consistent with previous results. On the other hand, compressibility effects were found to have a limited impact on the local chemistry, up to at least $M_t = 0.4$. The thermodynamic fluctuations in the compressible cases were explained by considering isentropic fluctuations, which were investigated in Chapter 6, in addition to the effect of the flame, the latter being captured by the low Mach number approximation. In other words, similarly to what was found in homogeneous non-reacting turbulence, the low Mach number expansion (zeroth and first order governing equations) captures all effects observed in the compressible simulations.

Chapter 8

CONCLUSIONS

In this thesis, compressibility effects in subsonic reacting and non-reacting flows were systematically isolated by performing numerical simulations using both the low Mach number approximation and the fully compressible framework. We were specifically interested in the interactions between turbulence, flames, and acoustics. To this end, we investigated flame-acoustics interactions, compressible homogeneous non-reacting turbulence, and turbulence-flame interactions.

8.1 Numerical methodology

In Chapter 3, we presented the fully compressible numerical methodology, which is based on the low Mach number solver NGA [76]. In compressible reacting flows using detailed chemistry, the maximum explicit stable time step is usually limited by the chemical processes at play. The maximum explicit stable time step for chemistry can be orders of magnitude more stringent than the one for acoustics, which is impractical to simulate turbulent compressible reacting flows. To remedy the situation, we presented a novel time integration scheme that blends the semi-implicit midpoint method for the species transport and the RK4 scheme for the transport of the other flow variables. This approach was tested by considering a freely-propagating laminar flame, an acoustic wave impinging on a flame, and a turbulent flame. The time integration scheme was found to perform well, since the semi-implicit correction is especially good at capturing the small chemical time scales, which are responsible for the stiffness of the system. With this approach, the time step was found to be limited by the acoustic CFL only, regardless of the chemical mechanism employed. It also yields fourth-order accurate transport of acoustic waves away from mixing/chemistry. It was also shown that the use of a staggered grid was ideally suited for the transport of acoustic waves. Using a second-order spatial discretization stencil, the numerical dispersion was found to be less severe than if a fourth-order stencil on a collocated grid was used. Finally, we reviewed the NSCBC framework, and presented various test cases to verify its implementation.

8.2 Flame-acoustics interactions

In Chapter 4, we investigated the impact of the thermodynamic fluctuations that accompany an acoustic wave on the response of laminar premixed flames, referred to as the direct pressure effects. In Sec. 4.1, we presented the different flow configurations considered, and described the numerical methodology employed for the low Mach number and compressible simulations. For the low Mach number simulations, a sinusoidal thermodynamic (background) pressure was imposed. For the compressible simulations, an outlet wave modulation technique was employed to generate the acoustic waves. Our numerical implementation was validated against the results of Jimenez *et al.*[14].

In Sec. 4.2, we presented results obtained under the low Mach number approximation for a wide range of fuels, including two large hydrocarbon fuels, *n*-heptane and *n*-dodecane. For a broad spectrum of acoustic frequencies, we extracted the gain and phase of the heat release fluctuations, which determine the stability of the system through the Rayleigh criterion. For all fuels, we observed a local peak in $G_{\dot{Q}}$ for $\omega\tau_F \sim 10^0 - 10^2$. The frequency at which this local peak occurs was seen to roughly coincide with the frequency for which $\theta_{\dot{Q}} = 0$, indicating that the flame-acoustics system is thermo-acoustically unstable. For higher frequencies, we observed and then showed that the gains of the different species mass fractions decrease with the inverse of the acoustic frequency (i.e., $G_{Y_i} \sim \omega^{-1}$). In the limit $\omega \to \infty$, this leads to chemistry being "frozen" (i.e., $G_{Y_i}|_{\omega\to\infty} = 0$). This result allowed us to predict $G_{\dot{Q}}|_{\omega\to\infty}$ and $\theta_{\dot{Q}}|_{\omega\to\infty}$ directly from the steady-state solution.

In Sec. 4.3, we investigated direct pressure effects under engine-relevant conditions, i.e., at elevated temperature and pressure, using the fully compressible formulation. We focused on the combustion of hydrogen and a large hydrocarbon fuel, *n*-heptane. The differences between results obtained with the fully compressible Navier-Stokes equations and the low Mach number approximation were thoroughly investigated. The two simulation frameworks agree very well for acoustic wavelengths much larger than the flame thickness. At high frequencies, the low Mach number approximation erroneously predicts a plateau in the heat release gain. Instead, using the fully compressible framework, the gain decreases at high frequency and tends towards zero. The differences between the two frameworks at high frequency are due to the spatial variations in the acoustic pressure, which are not captured by the low Mach number approximation. In the compressible framework, when the acoustic wavelength becomes of the same order of magnitude as the flame thickness, the

alternating regions of positive and negative acoustic pressure impact the local flame response in opposite ways. When integrated over the whole domain, the heat release gain thus averages out to zero.

The acoustic wavelength for which the low Mach number and fully compressible frameworks yield different results was found to be much larger than the flame thickness, i.e., for $\lambda_b/l_{F,0} \lesssim 10^2$. This was linked to the large region for which the heat release is sensitive to pressure fluctuations, compared to the flame thickness. This acoustic wavelength corresponds to $f \gtrsim 10^4$ Hz for the cases at standard thermodynamic conditions, and $f \gtrsim 10^6$ Hz for the ones at elevated pressure and temperature. In practical combustors, typical frequencies at which thermo-acoustic instabilities occur in are $f \sim 10^3 - 10^4$ Hz [105]. Hence, we conclude that the low Mach number framework is adequate to investigate direct pressure effects for this practically-relevant range of frequencies.

8.3   Physics-based forcing for compressible flows

In Chapter 5, we considered how compressible turbulent flows should be simulated when simplified geometries are used, i.e., in the absence of a natural turbulence generating mechanism due to the large scale shear. The general framework relies on a simple decomposition of the velocity field into large-scale (imposed) and small-scale (resolved) components. We applied this framework to the centerline of a jet, and found that the forcing term should be linear with velocity, similarly to what was found in previous work [35, 38]. It was found that special care must be taken regarding the energy equation when a statistically-stationary state is desired, since the conversion of kinetic energy into internal energy heats up the flow over time. By defining a modified total energy, it was shown that statistical stationarity can be achieved by removing the volume average of the forcing term in the total energy equation.

Forcing the full velocity field while employing periodic boundary conditions was found to promote the unphysical growth of standing acoustic waves, which plagued previous simulations of compressible homogeneous turbulence [28]. These standing modes initially grow exponentially, and eventually saturate due to non-linear effects. To remedy the situation, it was decided to force the solenoidal velocity field only, in line with the decomposition proposed by Petersen & Livescu [27].

8.4 Compressible homogeneous turbulence

In Chapter 6, we explored compressibility effects in subsonic homogeneous non-reacting turbulence. Since we performed simulations in triply-periodic domains, the forcing methodology developed in Chapter 5 was employed to obtain a statistically-stationary state. We first reviewed how velocity, dissipation rate, and pressure fluctuations can be decomposed into solenoidal and dilatational components. We also reviewed the low Mach number expansion to get insight into how these quantities should scale with the turbulent Mach number M_t, at low Mach numbers. We then presented simulation results, first fixing the Reynolds number and varying the turbulent Mach number. The ratio of dilatational to solenoidal kinetic energies was found to scale like $\langle \tilde{k}^d \rangle / \langle \tilde{k}^s \rangle \sim M_t^4$ at low Mach numbers, consistent with the scalings obtained by considering the low Mach number expansion, and in agreement with the theoretical predictions of Fauchet & Bertoglio [116]. The ratio of solenoidal to dilatational dissipation rate was also found to scale like $\langle\!\langle \epsilon^d \rangle\!\rangle / \langle\!\langle \epsilon^s \rangle\!\rangle \sim M_t^4$. In compressible turbulence, pressure fluctuations induce density and temperature fluctuations, unlike in incompressible turbulence. These fluctuations were found to be almost isentropic, in agreement with previous studies [119, 122]. A polytropic exponent was extracted for the density fluctuations to quantify the deviation from the isentropic behavior, which was found to be comparable with the values computed in previous studies [119, 122]. The non-isentropic behavior was explained by considering the first order energy equation of the low Mach number expansion, which simplifies to the isentropic relation only if there is no conduction or viscous dissipation.

Next, the solenoidal and dilatational pressure fields were extracted by solving the Poisson equation for incompressible flows. At low Mach numbers, the ratio of the dilatational to solenoidal pressure fluctuations was found to scale like $p_{rms}^d / p_{rms}^s \sim M_t^2$, in line with the predictions obtained by considering the low Mach number expansion. Finally, we assessed the impact of the Reynolds number, for a fixed $M_t = 0.40$. Although simulations would need to be run for longer to reach definitive conclusions, there does not appear to be a strong Reynolds number influence on the ratio of solenoidal to dilatational kinetic energy, dissipation rate, and pressure fluctuations. In summary, by performing simulations across a wide range of Mach numbers, and averaging statistics over long times, we obtained Mach number scalings that enabled us to verify theoretical predictions obtained from the low Mach number expansion.

8.5 Turbulence-flame interactions

In Chapter 7, we performed simulations of premixed *n*-heptane/air turbulent flames with detailed chemistry in an inflow/outflow configuration, using both the low Mach number approximation and the compressible framework. We aimed to improve upon previous initialization procedures for the compressible simulations [52, 123, 124] by leveraging the fact that a statistically-stationary turbulent flame solution obtained with the low Mach number approximation should be close to the compressible one. To employ the NSCBC framework, it was required to force turbulence away from the boundaries only. However, it was found that special care must be taken regarding the boundary values when a spatially-varying forcing scheme is employed. The correct boundary values were derived by considering the planar-averaged governing equations, and were found to be significantly different from the ones used for the low Mach number simulations. To reduce the transient time, we proposed to modify the unforced unburnt region close to the inlet to match the boundary values.

Since it was decided to vary the turbulent Mach number by changing the Karlovitz number, we first investigated the impact of the Karlovitz number using simulation results obtained with the low Mach number approximation. This was achieved by considering a set of turbulent flames at different turbulence intensities. We extracted the turbulent flame speed, and computed the conditional average of the fuel consumption rate. The turbulent flame speed and the maximum fuel consumption rate were found to increase with the Karlovitz number, in agreement with previous studies. The temperature at which the peak fuel consumption rate occurs was found to be well captured by the semi-empirical model of Savard & Blanquart [127].

We then investigated compressibility effects by performing additional simulations using the compressible framework, at turbulent Mach numbers $M_{t,u} = 0.17$ and $M_{t,u} = 0.39$. By comparing simulation results obtained using both the low Mach number approximation and the compressible framework, we were able to isolate the compressibility effects on the flame. Compressibility effects were identified through increased density fluctuations in the turbulent regions away from the flame. These density fluctuations were found to be related to the pressure fluctuations by assuming an isentropic behavior. However, inside the turbulent flame brush, the density fluctuations due to compressibility were found to remain small compared to the large fluctuations induced by the turbulent mixing of cold reactants and hot products. The pressure fluctuations were not found to be significantly impacted by compressibility. Finally, to investigate the compressibility effects on chemistry, we

extracted the turbulent flame speed, and computed the conditional average of the fuel consumption rate. The impact of compressibility on these two quantities was found to be limited for the range of Mach numbers investigated, especially when contrasted with the large impact of the Karlovitz number. The low Mach number approximation thus remains a valid framework at least up to $M_t = 0.4$, when the primary goal is to characterize the impact of turbulence on the chemical processes at play.

8.6 Limitations and future directions

In parallel to developing the time integration scheme presented in Chapter 3, the author also worked on a semi-implicit correction for the acoustics, presented in Appendix G. This implicit correction is similar in essence to the so-called barely implicit correction algorithm for low Mach number flows developed by Patnaik *et al.*[128]. The methodology showed promising results, but incorporating the NSCBC boundary conditions proved to be challenging. It would be interesting to continue in this direction, since lifting the acoustic CFL condition would yield substantial savings in computational cost.

Concerning the flame-acoustics interactions explored in Chapter 4, the simulations were on purpose one-dimensional to isolate the direct pressure effects. It would be interesting to explore flame-acoustics interactions in two-dimensional and three-dimensional configurations, to see if the phase and gain of the release are impacted by potential multidimensional effects, such as Rayleigh-Taylor instabilities.

Regarding turbulence-flame interactions, the present study only considered flames at moderate turbulent Mach numbers $M_t < 0.4$. This is due to the current numerical procedure in which we convert a low Mach number field at the desired turbulent conditions into the initial compressible field. This procedure has the advantage of providing a reasonable initial compressible field, but is limited in that at higher Mach numbers, the pressure fluctuations in the low Mach number fields are greater than the mean, i.e., $p' < -p_0$. Then, the conversion from a low Mach number field to a compressible one is not straightforward. One possible avenue to perform simulations of compressible turbulent flames at higher Mach numbers would be to initialize the compressible simulation with a low Mach number simulation at a low turbulence intensity, and ramp up the turbulence during the compressible simulation. To do so, the forcing term in the energy equation would need to be modified. With the current formulation, i.e., removing the average of the forcing term in the

total energy equation, changing the turbulence intensity will lead to an artificial conversion of internal energy into kinetic energy. Instead, removing the average viscous dissipation rate in the total energy equation should leave the internal energy field (and thus temperature) intact as the turbulence level is increased. It would be interesting to implement this alternative forcing scheme to simulate turbulent flames at higher Mach numbers.

BIBLIOGRAPHY

[1] Beardsell, G. and Blanquart, G., "A cost-effective semi-implicit method for the time integration of fully compressible reacting flows with stiff chemistry," *Journal of Computational Physics*, 2020. DOI: https://doi.org/10.1016/j.jcp.2020.109479,

[2] Beardsell, G. and Blanquart, G., "Fully compressible simulations of the impact of acoustic waves on the dynamics of laminar premixed flames for engine-relevant conditions," *Proceedings of the Combustion Institute*, 2020. DOI: https://doi.org/10.1016/j.proci.2020.06.003,

[3] Beardsell, G. and Blanquart, G., "Impact of pressure fluctuations on the dynamics of laminar premixed flames," *Proceedings of the Combustion Institute*, vol. 37, no. 2, pp. 1895–1902, 2019. DOI: https://doi.org/10.1016/j.proci.2018.07.125,

[4] *U.S. Energy Information Administration: Annual Energy Outlook, available at http://www.eia.gov/outlooks/aeo/*, 2020.

[5] Pitsch, H., "FlameMaster v3. 1: a C++ computer program for 0D combustion and 1D laminar flame calculations," 1998.

[6] Bisetti, F., Blanquart, G., Mueller, M. E., and Pitsch, H., "On the formation and early evolution of soot in turbulent nonpremixed flames," *Combust. Flame*, vol. 159, no. 1, pp. 317–335, 2012. DOI: 10.1016/j.combustflame.2011.05.021.

[7] Bird, R. B., Stewart, W. E., and Lightfoot, E. N., *Transport phenomena*. John Wiley & Sons, 2007.

[8] Rayleigh, J. W. S. B., "The Explanation of Certain Acoustical Phenomena," *Nature*, vol. 18, no. 455, pp. 319–321, 1878. DOI: 10.1038/018319a0.

[9] Lieuwen, T. C., "Modeling Premixed Combustion - Acoustic Wave Interactions: A Review," *Journal of Propulsion and Power*, vol. 19, no. 5, pp. 765–781, 2003. DOI: 10.2514/2.6193.

[10] Candel, S. M., "Combustion instabilities coupled by pressure waves and their active control," *Symposium (International) on Combustion*, vol. 24, no. 1, pp. 1277–1296, 1992. DOI: http://dx.doi.org/10.1016/S0082-0784(06)80150-5.

[11] Oefelein, J. C. and Yang, V., "Comprehensive Review of Liquid-Propellant Combustion Instabilities in F-l Engines," *Journal of Propulsion and Power*, vol. 9, no. 5, pp. 657–677, 1993.

[12]   Schmidt, H. and Jiménez, C., "Numerical study of the direct pressure effect of acoustic waves in planar premixed flames," *Combustion and Flame*, vol. 157, no. 8, pp. 1610–1619, 2010. DOI: `10.1016/j.combustflame.2010.03.010`.

[13]   Lieuwen, T. C., *Unsteady combustor physics*. Cambridge University Press, 2012.

[14]   Jiménez, C., Quinard, J., Graña-Otero, J., Schmidt, H., and Searby, G., "Unsteady response of hydrogen and methane flames to pressure waves," *Combustion and Flame*, vol. 159, no. 5, pp. 1894–1908, 2012. DOI: `http://dx.doi.org/10.1016/j.combustflame.2012.01.017`.

[15]   McIntosh, A. C., "Pressure disturbances of Different Length Scales Interacting with Conventional Flames," *Combustion Science and Technology*, vol. 75, no. 4-6, pp. 287–309, 1991. DOI: `10.1080/00102209108924093`.

[16]   Ledder, G. and Kapha, A. K., "The Response of Premixed Flames to Pressure Perturbations," *Combustion Science and Technology*, vol. 76, no. 1-3, pp. 21–44, 1991. DOI: `10.1080/00102209108951701`.

[17]   McIntosh, A. C., "The Linearised Response of the Mass Burning Rate of a Premixed Flame to Rapid Pressure Changes," *Combustion Science and Technology*, vol. 91, no. 4-6, pp. 329–346, 1993. DOI: `10.1080/00102209308907652`.

[18]   McIntosh, A. C., "Deflagration fronts and compressibility," *Philosophical Transactions of the Royal Society of London A: Mathematical, Physical and Engineering Sciences*, vol. 357, no. 1764, pp. 3523–3538, 1999. DOI: `10.1098/rsta.1999.0507`.

[19]   Clavin, P., Pelcé, P., and He, L., "One-dimensional vibratory instability of planar flames propagating in tubes," *Journal of Fluid Mechanics*, vol. 216, pp. 299–322, 1990. DOI: `10.1017/S0022112090000441`.

[20]   Clavin, P. and Searby, G., "Unsteady response of chain-branching premixed-flames to pressure waves," *Combustion Theory and Modelling*, vol. 12, no. 3, pp. 545–567, 2008. DOI: `10.1080/13647830701848972`.

[21]   Wangher, A., Searby, G., and Quinard, J., "Experimental investigation of the unsteady response of premixed flame fronts to acoustic pressure waves," *Combustion and flame*, vol. 154, no. 1, pp. 310–318, 2008.

[22]   Pope, S. B., *Turbulent Flows*. Cambridge University Press, 2000. DOI: `10.1017/CBO9780511840531`.

[23]   Richardson, L. F., *Weather prediction by numerical process*. Cambridge university press, 1922.

[24]   Kolmogorov, A., "The Local Structure of Turbulence in Incompressible Viscous Fluid for Very Large Reynolds' Numbers," *Akademiia Nauk SSSR Doklady*, vol. 30, pp. 301–305, 1941.

[25] Kolmogorov, A. N., "The local structure of turbulence in incompressible viscous fluid for very large Reynolds numbers," *Proceedings of the Royal Society of London. Series A: Mathematical and Physical Sciences*, vol. 434, no. 1890, pp. 9–13, 1991.

[26] Sagaut, P. and Cambon, C., *Homogeneous Turbulence Dynamics*. Cambridge University Press, 2008. DOI: 10.1017/CBO9780511546099.

[27] Petersen, M. R. and Livescu, D., "Forcing for statistically stationary compressible isotropic turbulence," *Physics of Fluids*, vol. 22, no. 11, p. 116 101, 2010. DOI: 10.1063/1.3488793.

[28] Kida, S. and Orszag, S. A., "Energy and spectral dynamics in forced compressible turbulence," *Journal of Scientific Computing*, vol. 5, no. 2, pp. 85–125, 1990. DOI: 10.1007/BF01065580.

[29] Jagannathan, S. and Donzis, D. A., "Reynolds and Mach number scaling in solenoidally-forced compressible turbulence using high-resolution direct numerical simulations," *Journal of Fluid Mechanics*, vol. 789, pp. 669–707, 2016. DOI: 10.1017/jfm.2015.754.

[30] Kida, S. and Orszag, S. A., "Energy and spectral dynamics in decaying compressible turbulence," *Journal of Scientific Computing*, vol. 7, no. 1, pp. 1–34, 1992. DOI: 10.1007/BF01060209.

[31] Moin, P. and and Krishnan Mahesh, "DIRECT NUMERICAL SIMULATION: A Tool in Turbulence Research," *Annual Review of Fluid Mechanics*, vol. 30, no. 1, pp. 539–578, 1998. DOI: 10.1146/annurev.fluid.30.1.539.

[32] Gatski, T. B. and Bonnet, J. P., *Compressibility, Turbulence and High Speed Flow*. Elsevier Science, 2009.

[33] Samtaney, R., Pullin, D., and Kosovic, B., "Direct numerical simulation of decaying compressible turbulence and shocklet statistics," *Physics of Fluids*, vol. 13, pp. 1415–1430, 2001.

[34] Lee, M. and Moser, R. D., "Direct numerical simulation of turbulent channel flow up to Re_τ\approx 5200," *Journal of Fluid Mechanics*, vol. 774, pp. 395–415, 2015. DOI: 10.1017/jfm.2015.268.

[35] Rah, K. J., Dhandapani, C., and Blanquart, G., "Derivation of a realistic forcing term to reproduce the turbulent characteristics of round jets on the centerline," *Physical Review Fluids*, vol. 3, no. 8, p. 84 606, 2018. DOI: 10.1103/PhysRevFluids.3.084606.

[36] Lundgren, T. S., "Linearly forced isotropic turbulence," *Annual Research Briefs*, no. 2, pp. 461–473, 2003.

[37] Rosales, C. and Meneveau, C., "Linear forcing in numerical simulations of isotropic turbulence: Physical space Implementations and convergence properties," *Phys. Fluids*, vol. 17, no. 9, pp. 1–8, 2005. DOI: 10.1063/1.2047568.

[38] Dhandapani, C., Rah, K. J., and Blanquart, G., "Effective forcing for direct numerical simulations of the shear layer of turbulent free shear flows," *Phys. Rev. Fluids*, vol. 4, no. 8, p. 84 606, 2019. DOI: 10.1103/PhysRevFluids.4.084606.

[39] Peters, N., *Turbulent Combustion*. Cambridge: Cambridge University Press, 2000. DOI: 10.1017/CBO9780511612701.

[40] Lapointe, S., Savard, B., and Blanquart, G., "Differential diffusion effects, distributed burning, and local extinctions in high Karlovitz premixed flames," *Combustion and Flame*, vol. 162, no. 9, pp. 3341–3355, 2015. DOI: 10.1016/j.combustflame.2015.06.001.

[41] Peters, N., "The turbulent burning velocity for large-scale and small-scale turbulence," *Journal of Fluid Mechanics*, vol. 384, no. May 2017, pp. 107–132, 1999. DOI: 10.1017/S0022112098004212.

[42] Borghi, R., "On the Structure and Morphology of Turbulent Premixed Flames," in *Recent Advances in the Aerospace Sciences: In Honor of Luigi Crocco on His Seventy-fifth Birthday*, C. Casci and C. Bruno, Eds., Boston, MA: Springer US, 1985, pp. 117–138. DOI: 10.1007/978-1-4684-4298-4_7.

[43] Smolke, J., Lapointe, S., Paxton, L., Blanquart, G., Carbone, F., Fincham, A. M., and Egolfopoulos, F. N., "Experimental and numerical studies of fuel and hydrodynamic effects on piloted turbulent premixed jet flames," *Proceedings of the Combustion Institute*, vol. 36, no. 2, pp. 1877–1884, 2017. DOI: https://doi.org/10.1016/j.proci.2016.07.127.

[44] Savard, B., "Characterization and modeling of premixed turbulent n-heptane flames in the thin reaction zone regime," PhD thesis, California Institute of Technology, 2015.

[45] ASPDEN, A. J., DAY, M. S., and BELL, J. B., "Turbulence–flame interactions in lean premixed hydrogen: transition to the distributed burning regime," *Journal of Fluid Mechanics*, vol. 680, pp. 287–320, 2011. DOI: 10.1017/jfm.2011.164.

[46] Lapointe, S. and Blanquart, G., "Fuel and chemistry effects in high Karlovitz premixed turbulent flames," *Combustion and Flame*, vol. 167, pp. 294–307, 2016. DOI: 10.1016/j.combustflame.2016.01.035.

[47] Sankaran, R., Hawkes, E. R., Chen, J. H., Lu, T., and Law, C. K., "Structure of a spatially developing turbulent lean methane–air Bunsen flame," *Proceedings of the Combustion Institute*, vol. 31, no. 1, pp. 1291–1298, 2007. DOI: https://doi.org/10.1016/j.proci.2006.08.025.

[48] Hawkes, E. R., Chatakonda, O., Kolla, H., Kerstein, A. R., and Chen, J. H., "A petascale direct numerical simulation study of the modelling of flame wrinkling for large-eddy simulations in intense turbulence," *Combustion and Flame*, vol. 159, no. 8, pp. 2690–2703, 2012. DOI: https://doi.org/10.1016/j.combustflame.2011.11.020.

[49] Wang, H., Luo, K., and Fan, J., "Direct Numerical Simulation and Conditional Statistics of Hydrogen/Air Turbulent Premixed Flames," *Energy & Fuels*, vol. 27, no. 1, pp. 549–560, 2013. DOI: 10.1021/ef301699a.

[50] Savard, B., Bobbitt, B., and Blanquart, G., "Structure of a high Karlovitz n-C7H16 premixed turbulent flame," *Proc. Combust. Inst.*, vol. 35, no. 2, pp. 1377–1384, 2015. DOI: http://dx.doi.org/10.1016/j.proci.2014.06.133.

[51] Savard, B. and Blanquart, G., "Broken reaction zone and differential diffusion effects in high Karlovitz n-C7H16 premixed turbulent flames," *Combustion and Flame*, vol. 162, no. 5, pp. 2020–2033, 2015. DOI: 10.1016/j.combustflame.2014.12.020.

[52] Poludnenko, A. Y., Gardiner, T. A., and Oran, E. S., "Spontaneous Transition of Turbulent Flames to Detonations in Unconfined Media," *Phys. Rev. Lett.*, vol. 107, no. 5, p. 54 501, 2011. DOI: 10.1103/PhysRevLett.107.054501.

[53] Dunn, M. J., Masri, A. R., and Bilger, R. W., "A new piloted premixed jet burner to study strong finite-rate chemistry effects," *Combustion and Flame*, vol. 151, no. 1, pp. 46–60, 2007. DOI: https://doi.org/10.1016/j.combustflame.2007.05.010.

[54] Billet, G., Giovangigli, V., and Gassowski, G. de, "Impact of volume viscosity on a shock-hydrogen-bubble interaction," *Combustion Theory and Modelling*, vol. 12, no. 2, pp. 221–248, 2008. DOI: 10.1080/13647830701545875.

[55] Giovangigli, V., "Multicomponent flow modeling," *Science China Mathematics*, vol. 55, no. 2, pp. 285–308, 2012. DOI: 10.1007/s11425-011-4346-y.

[56] Day, M. S. and Bell, J. B., "Numerical simulation of laminar reacting flows with complex chemistry," *Combustion Theory and Modelling*, vol. 4, no. 4, pp. 535–556, 2000. DOI: 10.1088/1364-7830/4/4/309.

[57] Laverdant, A. and Thévenin, D., "Interaction of a Gaussian acoustic wave with a turbulent premixed flame," *Combustion and Flame*, vol. 134, no. 1-2, pp. 11–19, 2003. DOI: 10.1016/S0010-2180(03)00065-8.

[58] Pierce, C. D., "Progress-variable approach for large eddy simulation of turbulent combustion," PhD thesis, 2001.

[59] Bobbitt, B., Lapointe, S., and Blanquart, G., "Vorticity transformation in high Karlovitz number premixed flames," *Phys. Fluids*, vol. 28, no. 1, 2016. DOI: `http://dx.doi.org/10.1063/1.4937947`.

[60] Bobbitt, B. and Blanquart, G., "Vorticity isotropy in high Karlovitz number premixed flames," *Phys. Fluids*, vol. 28, no. 10, 2016. DOI: `10.1063/1.4962305`.

[61] Mahesh, K., Constantinescu, G., Apte, S., Iaccarino, G., Ham, F., and Moin, P., "Large-eddy simulation of reacting turbulent flows in complex geometries," *Journal of Applied Mechanics*, vol. 73, no. 3, p. 374, 2006. DOI: `10.1115/1.2179098`.

[62] Nonaka, A., Day, M. S., and Bell, J. B., "A conservative, thermodynamically consistent numerical approach for low Mach number combustion. Part I: Single-level integration," *Combustion Theory and Modelling*, vol. 22, no. 1, pp. 156–184, 2018. DOI: `10.1080/13647830.2017.1390610`.

[63] Pitsch, H. and Duchamp de Lageneste, L., "Large-eddy simulation of premixed turbulent combustion using a level-set approach," *Proceedings of the Combustion Institute*, vol. 29, no. 2, pp. 2001–2008, 2002. DOI: `10.1016/S1540-7489(02)80244-9`.

[64] Abdelsamie, A., Fru, G., Oster, T., Dietzsch, F., Janiga, G., and Thévenin, D., "Towards direct numerical simulations of low-Mach number turbulent reacting and two-phase flows using immersed boundaries," *Computers & Fluids*, vol. 131, pp. 123–141, 2016. DOI: `https://doi.org/10.1016/j.compfluid.2016.03.017`.

[65] Majda, A. and Sethian, J., "The Derivation and Numerical Solution of the Equations for Zero Mach Number Combustion," *Combustion Science and Technology*, vol. 42, no. 3-4, pp. 185–205, 1985. DOI: `10.1080/00102208508960376`.

[66] Zank, G. P. and Matthaeus, W. H., "The equations of nearly incompressible fluids. I. Hydrodynamics, turbulence, and waves," *Physics of Fluids A: Fluid Dynamics*, vol. 3, no. 1, pp. 69–82, 1991. DOI: `10.1063/1.857865`.

[67] Nicoud, F., "Conservative High-Order Finite-Difference Schemes for Low-Mach Number Flows," *Journal of Computational Physics*, vol. 158, no. 1, pp. 71–97, 2000. DOI: `https://doi.org/10.1006/jcph.1999.6408`.

[68] Bell, J. B., Day, M. S., Almgren, A. S., Lijewski, M. J., and Rendleman, C. A., "A parallel adaptive projection method for low Mach number flows," *International Journal for Numerical Methods in Fluids*, vol. 40, no. 1-2, pp. 209–216, 2002. DOI: `10.1002/fld.310`.

[69] Filippova, O. and Hänel, D., "A Novel Lattice BGK Approach for Low Mach Number Combustion," *Journal of Computational Physics*, vol. 158, no. 2, pp. 139–160, 2000. DOI: `https://doi.org/10.1006/jcph.1999.6405`.

[70] Charentenay, J. de, Thévenin, D., and Zamuner, B., "Comparison of direct numerical simulations of turbulent flames using compressible or low-Mach number formulations," *International Journal for Numerical Methods in Fluids*, vol. 39, no. 6, pp. 497–515, 2002. DOI: `10.1002/fld.341`.

[71] Fröhlich, J. and Peyret, R., "Direct spectral methods for the low Mach number equations," *International Journal of Numerical Methods for Heat \& Fluid Flow*, 1992.

[72] Nicoud, F. and Wieczorek, K., "About the Zero Mach Number Assumption in the Calculation of Thermoacoustic Instabilities," *International Journal of Spray and Combustion Dynamics*, vol. 1, no. 1, pp. 67–111, 2009. DOI: `10.1260/175682709788083335`.

[73] Lu, X. and Pantano, C., "On mass conservation and solvability of the discretized variable-density zero-Mach Navier-Stokes equations," *Journal of Computational Physics*, vol. 404, p. 109 132, 2020. DOI: `https://doi.org/10.1016/j.jcp.2019.109132`.

[74] Laidler, K. J., "A glossary of terms used in chemical kinetics, including reaction dynamics (IUPAC Recommendations 1996)," *Pure and Applied Chemistry*, vol. 68, no. 1, pp. 149–192, 1996. DOI: `https://doi.org/10.1351/pac199668010149`.

[75] Boeck, L., Lapointe, S., Melguizo-Gavilanes, J., and Ciccarelli, G., "Flame propagation across an obstacle: OH-PLIF and 2-D simulations with detailed chemistry," *Proc. Combust. Inst.*, vol. 000, no. 2, pp. 1–8, 2016. DOI: `10.1016/j.proci.2016.06.097`.

[76] Desjardins, O., Blanquart, G., Balarac, G., and Pitsch, H., "High order conservative finite difference scheme for variable density low Mach number turbulent flows," *J. Comput. Phys.*, vol. 227, no. 15, pp. 7125–7159, 2008.

[77] Savard, B., Xuan, Y., Bobbitt, B., and Blanquart, G., "A computationally-efficient, semi-implicit, iterative method for the time-integration of reacting flows with stiff chemistry," *Journal of Computational Physics*, vol. 295, pp. 740–769, 2015. DOI: `http://dx.doi.org/10.1016/j.jcp.2015.04.018`.

[78] Lapointe, S., "Simulation of Premixed Hydrocarbon Flames at High Turbulence Intensities," PhD thesis, California Institute of Technology, 2016.

[79] Schlup, J., "Numerical Investigations of Transport and Chemistry Modeling for Lean Premixed Hydrogen Combustion," PhD thesis, 2018.

[80] MacArt, J. F. and Mueller, M. E., "Semi-implicit iterative methods for low Mach number turbulent reacting flows: Operator splitting versus approximate factorization," *Journal of Computational Physics*, vol. 326, pp. 569–595, 2016. DOI: `https://doi.org/10.1016/j.jcp.2016.09.016`.

[81] Herrmann, M., Blanquart, G., and Raman, V., "Flux corrected finite volume scheme for preserving scalar boundedness in reacting large-eddy simulations," *AIAA journal*, vol. 44, no. 12, pp. 2879–2886, 2006.

[82] Mathur, S., Tondon, P. K., and Saxena, S. C., "Thermal conductivity of binary, ternary and quaternary mixtures of rare gases," *Molecular physics*, vol. 12, no. 6, pp. 569–579, 1967.

[83] Ferziger, J. H. and Kaper, H. G., "Mathematical theory of transport processes in gases," *American Journal of Physics*, vol. 41, no. 4, pp. 601–603, 1973.

[84] Bird, R. B., Hirschfelder, J. O., and Curtiss, C. F., *Molecular theory of gases and liquids*. John Wiley, 1954.

[85] Fillo, A. J., Schlup, J., Beardsell, G., Blanquart, G., and Niemeyer, K. E., "A fast, low-memory, and stable algorithm for implementing multicomponent transport in direct numerical simulations," *Journal of Computational Physics*, vol. 406, p. 109 185, 2020. DOI: `https://doi.org/10.1016/j.jcp.2019.109185`,

[86] Burali, N., Lapointe, S., Bobbitt, B., Blanquart, G., and Xuan, Y., "Assessment of the constant non-unity Lewis number assumption in chemically-reacting flows," *Combustion Theory and Modelling*, vol. 20, no. 4, pp. 632–657, 2016. DOI: `10.1080/13647830.2016.1164344`.

[87] Smith, G. P., Golden, D. M., Frenklach, M., Moriarty, N. W., Eiteneer, B., Goldenberg, M., Bowman, C. T., Hanson, R. K., Song, S., Gardiner, W. C., Lissianski, V. V., and Qin, Z., *GRI-Mech 3.0 (http://www.me.berkeley.edu/gri_mech/)*.

[88] Hong, Z., Davidson, D. F., and Hanson, R. K., "An improved H2/O2 mechanism based on recent shock tube/laser absorption measurements," *Combustion and Flame*, vol. 158, no. 4, pp. 633–644, 2011. DOI: `https://doi.org/10.1016/j.combustflame.2010.10.002`.

[89] Lam, K.-Y., Davidson, D. F., and Hanson, R. K., "A shock tube study of H2+ OH $$ H2O+ H using OH laser absorption," *International Journal of Chemical Kinetics*, vol. 45, no. 6, pp. 363–373, 2013.

[90] Hong, Z., Lam, K.-Y., Sur, R., Wang, S., Davidson, D. F., and Hanson, R. K., "On the rate constants of OH+HO2 and HO2+HO2: A comprehensive study of H2O2 thermal decomposition using multi-species laser absorption," *Proceedings of the Combustion Institute*, vol. 34, no. 1, pp. 565–571, 2013. DOI: `https://doi.org/10.1016/j.proci.2012.06.108`.

[91] Blanquart, G., *CaltechMech, v. 2.4, 2018, (to appear on http://theforce.caltech.edu/CaltechMech/)*.

[92] Wang, H., Dames, E., Sirjean, B., Sheen, D. A., Tango, R., Violi, A., Lai, J. Y. W., Egolfopoulos, F. N., Davidson, D. F., Hanson, R. K., Bowman, C. T., Law, C. K., Tsang, W., Cernansky, N. P., Miller, D. L., and Lindstedt, R. P., *JetSurF version 2.0: A high-temperature chemical kinetic model of n-alkane (up to n-dodecane), cyclohexane, and methyl-, ethyl-, n-propyl and n-butyl-cyclohexane oxidation at high temperatures*, 2010.

[93] Goldsmith, C. F., Magoon, G. R., and Green, W. H., "Database of Small Molecule Thermochemistry for Combustion," *The Journal of Physical Chemistry A*, vol. 116, no. 36, pp. 9033–9057, 2012. DOI: `10.1021/jp303819e`.

[94] Poinsot, T. J. and Lelef, S. K., "Boundary conditions for direct simulations of compressible viscous flows," *Journal of Computational Physics*, vol. 101, no. 1, pp. 104–129, 1992. DOI: `http://dx.doi.org/10.1016/0021-9991(92)90046-2`.

[95] Thompson, K. W., "Time dependent boundary conditions for hyperbolic systems," *Journal of Computational Physics*, vol. 68, no. 1, pp. 1–24, 1987. DOI: `https://doi.org/10.1016/0021-9991(87)90041-6`.

[96] Sutherland, J. C. and Kennedy, C. A., "Improved boundary conditions for viscous, reacting, compressible flows," *Journal of Computational Physics*, vol. 191, no. 2, pp. 502–524, 2003. DOI: `http://dx.doi.org/10.1016/S0021-9991(03)00328-0`.

[97] Yoo, C. S., Wang, Y., Trouvé, A., and Im, H. G., "Characteristic boundary conditions for direct simulations of turbulent counterflow flames," *Combustion Theory and Modelling*, vol. 9, no. 4, pp. 617–646, 2005. DOI: `10.1080/13647830500307378`.

[98] Rudy, D. H. and Strikwerda, J. C., "A nonreflecting outflow boundary condition for subsonic navier-stokes calculations," *Journal of Computational Physics*, vol. 36, no. 1, pp. 55–70, 1980. DOI: `https://doi.org/10.1016/0021-9991(80)90174-6`.

[99] Leonard, B. P., "A stable and accurate convective modelling procedure based on quadratic upstream interpolation," *Computer Methods in Applied Mechanics and Engineering*, vol. 19, no. 1, pp. 59–98, 1979. DOI: `https://doi.org/10.1016/0045-7825(79)90034-3`.

[100] Jiang, G.-S. and Peng, D., "Weighted ENO Schemes for Hamilton–Jacobi Equations," *SIAM Journal on Scientific Computing*, vol. 21, no. 6, pp. 2126–2143, 2000. DOI: `10.1137/S106482759732455X`.

[101] Verma, S., Xuan, Y., and Blanquart, G., "An improved bounded semi-Lagrangian scheme for the turbulent transport of passive scalars," *Journal of Computational Physics*, vol. 272, pp. 1–22, 2014. DOI: `https://doi.org/10.1016/j.jcp.2014.03.062`.

[102] Yoo, C. S. and Im, H. G., "Characteristic boundary conditions for simulations of compressible reacting flows with multi-dimensional, viscous and reaction effects," *Combustion Theory and Modelling*, vol. 11, no. 2, pp. 259–286, 2007. DOI: 10.1080/13647830600898995.

[103] Müller, B., *Low Mach Number Asymptotics of the Navier-Stokes Equations and Numerical Implications*, 1999.

[104] Kaufmann, A., Nicoud, F., and Poinsot, T., "Flow forcing techniques for numerical simulation of combustion instabilities," *Combustion and Flame*, vol. 131, no. 4, pp. 371–385, 2002. DOI: http://dx.doi.org/10.1016/S0010-2180(02)00419-4.

[105] Yu, Y., Sisco, J. C., Rosen, S., Madhav, A., and Anderson, W. E., "Spontaneous Longitudinal Combustion Instability in a Continuously-Variable Resonance Combustor," *Journal of Propulsion and Power*, vol. 28, no. 5, pp. 876–887, 2012. DOI: 10.2514/1.B34308.

[106] Dhandapani, C., "Using the force: Applications and implications of turbulence forcing terms in direct numerical simulations," PhD thesis, California Institute of Technology, 2019.

[107] Panchapakesan, N. R. and Lumley, J. L., "Turbulence measurements in axisymmetric jets of air and helium. Part 1. Air jet," *Journal of Fluid Mechanics*, vol. 246, pp. 197–223, 1993. DOI: 10.1017/S0022112093000096.

[108] Carroll, P. L. and Blanquart, G., "A proposed modification to Lundgren's physical space velocity forcing method for isotropic turbulence," *Phys. Fluids*, vol. 25, no. 10, p. 105 114, 2013. DOI: 10.1063/1.4826315.

[109] Ni, Q., Shi, Y., and Chen, S., "Statistics of one-dimensional compressible turbulence with random large-scale force," *Physics of Fluids*, vol. 25, no. 7, p. 75 106, 2013. DOI: 10.1063/1.4816294.

[110] Boersma, B. J. and Lele, S. K., "Large eddy simulation of a mach 0.9 turbulent jet," in *5th AIAA/CEAS Aeroacoustics Conference and Exhibit*, Stanford Univ. Stanford, CA, 1999, p. 221.

[111] Cavalieri, A. V. G., Daviller, G., Comte, P., Jordan, P., Tadmor, G., and Gervais, Y., "Using large eddy simulation to explore sound-source mechanisms in jets," *Journal of Sound and Vibration*, vol. 330, no. 17, pp. 4098–4113, 2011. DOI: https://doi.org/10.1016/j.jsv.2011.04.018.

[112] Sarkar, S., "The pressure–dilatation correlation in compressible flows," *Physics of Fluids A: Fluid Dynamics*, vol. 4, no. 12, pp. 2674–2682, 1992. DOI: 10.1063/1.858454.

[113] Wang, J., Wang, L.-P., Xiao, Z., Shi, Y., and Chen, S., "A hybrid numerical simulation of isotropic compressible turbulence," *Journal of Computational Physics*, vol. 229, no. 13, pp. 5257–5279, 2010. DOI: https://doi.org/10.1016/j.jcp.2010.03.042.

[114] Miura, H. and Kida, S., "Acoustic energy exchange in compressible turbulence," *Physics of Fluids*, vol. 7, no. 7, pp. 1732–1742, 1995. DOI: `10.1063/1.868488`.

[115] Sarkar, S., Erlebacher, G., Hussaini, M. Y., and Kreiss, H. O., "The analysis and modelling of dilatational terms in compressible turbulence," *Journal of Fluid Mechanics*, vol. 227, pp. 473–493, 1991. DOI: `10.1017/S0022112091000204`.

[116] Fauchet, G. and Bertoglio, J. P., "An Analytical Expression for the Spectrum of Compressible Turbulence in the Low Mach Number Limit," in *Advances in Turbulence VII*, U. Frisch, Ed., Dordrecht: Springer Netherlands, 1998, pp. 317–320.

[117] Chandrasekhar, S., "The fluctuations of density in isotropic turbulence," *Proceedings of the Royal Society of London. Series A. Mathematical and Physical Sciences*, vol. 210, no. 1100, pp. 18–25, 1951. DOI: `10.1098/rspa.1951.0227`.

[118] Erlebacher, G., Hussaini, M. Y., Kreiss, H. O., and Sarkar, S., "The analysis and simulation of compressible turbulence," *Theoretical and Computational Fluid Dynamics*, vol. 2, no. 2, pp. 73–95, 1990. DOI: `10.1007/BF00272136`.

[119] Donzis, D. A. and Jagannathan, S., "Fluctuations of thermodynamic variables in stationary compressible turbulence," *Journal of Fluid Mechanics*, vol. 733, pp. 221–244, 2013. DOI: `10.1017/jfm.2013.445`.

[120] Batchelor, G. K., "Pressure fluctuations in isotropic turbulence," *Proc. Cambr. Phil. Soc.*, vol. 47, no. July, pp. 359–374, 1951.

[121] Donzis, D. A., Sreenivasan, K. R., and Yeung, P. K., "Some results on the Reynolds number scaling of pressure statistics in isotropic turbulence," *Physica D: Nonlinear Phenomena*, vol. 241, no. 3, pp. 164–168, 2012. DOI: `https://doi.org/10.1016/j.physd.2011.04.015`.

[122] Blaisdell, G. A., Mansour, N. N., and Reynolds, W. C., "Compressibility effects on the growth and structure of homogeneous turbulent shear flow," *Journal of Fluid Mechanics*, vol. 256, pp. 443–485, 1993. DOI: `10.1017/S0022112093002848`.

[123] Poludnenko, A. Y. and Oran, E. S., "The interaction of high-speed turbulence with flames: Turbulent flame speed," *Combustion and Flame*, vol. 158, no. 2, pp. 301–326, 2011. DOI: `https://doi.org/10.1016/j.combustflame.2010.09.002`.

[124] Poludnenko, A. Y., "Pulsating instability and self-acceleration of fast turbulent flames," *Phys. Fluids*, vol. 27, no. 1, pp. 1–21, 2015. DOI: `10.1063/1.4905298`.

[125] Bray, K. N. C., "Studies of the turbulent burning velocity," *Proceedings of the Royal Society of London. Series A: Mathematical and Physical Sciences*, vol. 431, no. 1882, pp. 315–335, 1990.

[126] Candel, S. M. and Poinsot, T. J., "Flame Stretch and the Balance Equation for the Flame Area," *Combustion Science and Technology*, vol. 70, no. 1-3, pp. 1–15, 1990. DOI: `10.1080/00102209008951608`.

[127] Savard, B. and Blanquart, G., "An a priori model for the effective species Lewis numbers in premixed turbulent flames," *Combustion and Flame*, vol. 161, no. 6, pp. 1547–1557, 2014. DOI: `https://doi.org/10.1016/j.combustflame.2013.12.014`.

[128] Patnaik, G., Guirguis, R. H., Boris, J. P., and Oran, E. S., "A barely implicit correction for flux-corrected transport," *Journal of Computational Physics*, vol. 71, no. 1, pp. 1–20, 1987. DOI: `https://doi.org/10.1016/0021-9991(87)90016-7`.

A p p e n d i x   A

DIFFERENT CHOICES FOR THE REFERENCE PRESSURE USED TO NON-DIMENSIONALIZE THE NAVIER-STOKES EQUATIONS

In Chapter 2, we inherently assumed that the reference p_r was representative of the thermodynamic state of the flow, i.e., $p^* = O(1)$. Zank & Matthaeus [66] investigated the implications of choosing a different reference pressure. Specifically, they considered

$$p_1^* = \frac{p}{p_0} \qquad p_2^* = \frac{p}{\rho_r u_r^2} \qquad p_3^* = \frac{p}{\mu_r u_r / L_r}, \tag{A.1}$$

where ρ_r and u_r are chosen such that $\rho^*, u^* = O(1)$. Note that p_1^* is the non-dimensional pressure used in Chapter 2.

Zank & Matthaeus [66] provided the momentum equations for each of the three normalizations, but did not provide the complete set of governing equations. Here, we briefly consider the implications of using p_2^* to non-dimensionalize the equations, and taking the limit when $M_r \to 0$. We also need to perform a similar normalization for temperature, i.e., we define

$$T_2^* = \frac{T}{u_r^2 W / R}, \tag{A.2}$$

where W is the molecular weight of the mixture, and R is the universal gas constant. Equations (2.1)–(2.3) become

$$\frac{\partial \rho^*}{\partial t^*} + \nabla^* \cdot (\rho^* u^*) = 0, \tag{A.3}$$

$$\frac{\partial \rho^* u^*}{\partial t^*} + \nabla^* \cdot (\rho^* u^* \otimes u^*) = -\nabla^* p_2^* + \frac{1}{Re_r} \nabla^* \cdot \tau^*, \tag{A.4}$$

$$\frac{\partial \rho^* e_t^*}{\partial t^*} + \nabla^* \cdot \left(u^* \left(\rho^* e_t^* + p_2^* \right) \right)$$
$$= -\frac{\gamma}{\gamma - 1} \frac{1}{Re_r Pr_r} \nabla^* \cdot q^* + \frac{1}{Re_r} \nabla^* \cdot (\tau^* \cdot u^*) . \tag{A.5}$$

The non-dimensional equation of state is

$$p_2^* = \rho^* T_2^* .$$

(A.6)

In Eqs. (A.3)–(A.5), there is no dependence in Mach number, which is to be con-trasted with Eqs. (2.16)–(2.18), where p_1^* was used. Hence, taking the limit when $M_r \to 0$ yields the "regular" Navier-Stokes equations. However, the limit $M_r \to 0$ yields issues regarding the initial conditions. For an initial pressure $p_i = p_0$, we have

$$p_{2,i}^* = \frac{p_i}{\rho_r u_r^2} = \frac{1}{\gamma M_r^2} ,$$

(A.7)

which implies that $p_{2,i}^* \to \infty$ as $M_r \to 0$. Similarly,

$$p_{3,i}^* = \frac{p_i}{\mu_r u_r / L_r} = \frac{Re_r}{\gamma M_r^2} ,$$

(A.8)

which also implies that $p_{3,i}^* \to \infty$ as $M_r \to 0$, for a finite Reynolds number. The same goes for T_2^*. Hence, while $\rho_r u_r^2$ and $\mu_r u_r / L_r$ can be used as reference pressures to non-dimensionalize the Navier-Stokes equations, using them to probe the limit $M_r \to 0$ is not insightful. Since we are interested in this limit, we choose to use p_1^* in Chapter 2.

A p p e n d i x   B

SPATIAL DISCRETIZATION OF THE SPECIES TRANSPORT AND ENERGY EQUATIONS

The semi-discrete species transport equation is given by

$$\frac{\partial (\rho Y)_s}{\partial t} + \sum_{i=1}^{3} \frac{\delta F_{Y_s,i}}{\delta x_i} =$$
$$\sum_{i=1}^{3} \frac{\delta}{\delta x_i} \left(\overline{\rho D_s}^{x_i} \frac{\delta Y_s}{\delta x_i} + \overline{\left(\frac{\rho D_s}{W}\right)}^{x_i} \overline{Y_s}^{x_i} \frac{\delta W}{\delta x_i} + \overline{Y_s}^{x_i} j_{c,i} \right) + \rho \dot{\omega}_s, \quad s = 1, ..., n_s, \tag{B.1}$$

where $F_{Y_s,i}$ is usually computed with the BQUICK scheme, i.e.,

$$\sum_{i=1}^{3} \frac{\delta F_{Y_s,i}}{\delta x_i} = \sum_{i=1}^{3} \frac{\delta}{\delta x_i} \left(g_i \overline{\overline{Y_s}}^{x_i} \right), \tag{B.2}$$

where $\overline{\overline{(\,)}}^{x_i}$ is the BQUICK interpolation operator. It is possible to use a centered scheme for the convective term, i.e., we set

$$\sum_{i=1}^{3} \frac{\delta F_{Y_s,i}}{\delta x_i} = \sum_{i=1}^{3} \frac{\delta}{\delta x_i} \left(g_i \overline{Y_s}^{x_i} \right). \tag{B.3}$$

However, due to the oscillatory character of a centered scheme, this can lead to unphysical for Y_s. The correction flux $j_{c,i}$ is given by

$$j_{c,i} = -\sum_{s=1}^{n_s} \left(\overline{\rho D_s}^{x_i} \frac{\delta Y_s}{\delta x_i} + \overline{\left(\frac{\rho D_s}{W}\right)}^{x_i} \overline{Y_s}^{x_i} \frac{\delta W}{\delta x_i} \right). \tag{B.4}$$

The semi-discrete energy equation is written as

$$\frac{\partial (\rho e_t)}{\partial t} + \sum_{i=1}^{3} \frac{\delta \left(u_i \overline{(\rho e_t) + p}^{x_i} \right)}{\delta x_i} = \sum_{i=1}^{3} \frac{\delta}{\delta x_i} \left(\overline{\lambda}^{x_i} \frac{\delta T}{\delta x_i} \right) + EF + VT, \tag{B.5}$$

where the enthalpy flux term EF is computed as

$$EF = \sum_{i=1}^{3} \frac{\delta}{\delta x_i} \left(\overline{\rho D_s h_s}^{x_i} \frac{\delta Y_s}{\delta x_i} + \overline{\left(\frac{\rho D_s}{W}\right)}^{x_i} \overline{h_s Y_s}^{x_i} \frac{\delta W}{\delta x_i} + \overline{h_s Y_s}^{x_i} j_{c,i} \right), \tag{B.6}$$

where $j_{c,i}$ is computed using Eq. (B.4). The viscous term VT is given by Eq. (3.31).

LINEAR STABILITY ANALYSIS FOR THE RK4 AND ITERATIVE EXPLICIT MIDPOINT SCHEMES

C.1 RK4 scheme

C.1.1 Stability region

Assuming $\boldsymbol{f}(\boldsymbol{Q}^n) = \lambda \boldsymbol{Q}^n$, where λ can be complex, we have

$$
\begin{aligned}
\boldsymbol{k}_1 &= \lambda \boldsymbol{Q}^n \,, \\
\boldsymbol{k}_2 &= \lambda \left(1 + \lambda \Delta t/2\right) \boldsymbol{Q}^n \,, \\
\boldsymbol{k}_3 &= \lambda \left(1 + \lambda \Delta t/2 + (\lambda \Delta t)^2/4\right) \boldsymbol{Q}^n \,, \\
\boldsymbol{k}_4 &= \lambda \left(1 + \lambda \Delta t + (\lambda \Delta t)^2/2 + (\lambda \Delta t)^3/4\right) \boldsymbol{Q}^n \,, \\
\boldsymbol{Q}^{n+1} &= \boldsymbol{Q}^n + \Delta t \left(\boldsymbol{k}_1/6 + \boldsymbol{k}_2/3 + \boldsymbol{k}_3/3 + \boldsymbol{k}_4/6\right) \\
&= \left(\lambda \Delta t + (\lambda \Delta t)^2/2 + (\lambda \Delta t)^3/6 + (\lambda \Delta t)^4/24\right) \boldsymbol{Q}^n \,.
\end{aligned}
\tag{C.1}
$$

Figure C.1 shows the stability contour for Eq. (C.1), i.e, the values of $\lambda \Delta t$ for which $\boldsymbol{Q}^{n+1} = \boldsymbol{Q}^n$.

Figure C.1: Stability region for the classical 4$^{\text{th}}$ order Runge-Kutta scheme.

C.1.2 Convective/Acoustic CFL

We look at the advection equation

$$\frac{\partial \phi}{\partial t} = f(\phi) = -a \frac{\partial \phi}{\partial x}, \tag{C.2}$$

with

$$\phi(x) = A \exp(ikx). \tag{C.3}$$

Using a centered scheme in space, we have

$$\frac{\partial \phi}{\partial x} \approx \frac{\delta \phi}{\delta x} = A_k \frac{\exp(ik(x+\Delta x)) - \exp(ik(x-\Delta x))}{2\Delta x} = i\phi \frac{\sin(k\Delta x)}{\Delta x}, \tag{C.4}$$

which implies that

$$f(\phi) = -ia\phi \frac{\sin(k\Delta x)}{\Delta x} = \lambda \phi. \tag{C.5}$$

Hence, λ is purely imaginary. Fig. C.2 shows the amplification factor $\sigma \equiv Q^{n+1}/Q^n$

Figure C.2: Amplification factor σ when λ is imaginary for the RK4 scheme (in blue), corresponding to the imaginary axis on Fig. C.1. The ideal behavior $\sigma = \exp(\lambda \Delta t)$ is shown by a dashed black line.

when λ is purely imaginary, i.e., corresponding to the imaginary axis in Fig. C.1. In order to be stable, we must thus have

$$|\lambda|\Delta t = \left| ia \frac{\sin(k\Delta x)}{\Delta x} \right| \Delta t < a \frac{\Delta t}{\Delta x} < 2.83. \tag{C.6}$$

We get the following criterion for the convective/acoustic CFL

$$\Delta t < \frac{2.83\Delta x}{a}, \tag{C.7}$$

where $a = |u|$ for convection, and $a = |u| + c$ for the acoustics. The dashed line in Fig. C.2 shows the ideal behavior $\sigma = 1$. Significant deviations between the RK4 scheme and the ideal behavior are observed for $|\lambda \Delta t| > 1$. In order to be stable and accurate, we restrict Δt to

$$\Delta t < \frac{\Delta x}{a}. \tag{C.8}$$

C.1.3 Viscous/Diffusive CFL

We consider the diffusion equation

$$\frac{\partial \phi}{\partial t} = f(\phi) = v \frac{\partial^2 \phi}{\partial x^2}, \tag{C.9}$$

with ϕ given by Eq. (C.3). Using a centered scheme in space, we have

$$\frac{\partial^2 \phi}{\partial x^2} \approx \frac{\delta^2 \phi}{\delta x^2} = A \frac{\exp(ik(x + \Delta x)) - 2\exp(ikx) + \exp(ik(x - \Delta x))}{\Delta x^2}$$

$$= 2\phi \frac{\cos(k\Delta x) - 1}{\Delta x^2}. \tag{C.10}$$

Plugging Eq. (C.10) in Eq. (C.9), we have

$$f(\phi) = 2v \frac{\cos(k\Delta x) - 1}{\Delta x^2} \phi = \lambda \phi. \tag{C.11}$$

Hence, λ is purely real. Fig. C.3 shows the amplification factor for λ purely real,

Figure C.3: Amplification factor σ when λ is real for the RK4 scheme (in blue), corresponding to the real axis on Fig. C.1. The ideal behavior $\sigma = \exp(\lambda \Delta t)$ is shown by a dashed black line.

i.e., corresponding to the real axis on Fig. C.1. Hence, to be stable, we must have

$$|\lambda|\Delta t = \left| 2v \frac{\cos(k\Delta x) - 1}{\Delta x^2} \right| \Delta t < \frac{4v\Delta t}{\Delta x^2} < 2.79, \tag{C.12}$$

which implies that

$$\Delta t < \frac{2.79\Delta x^2}{4v}. \tag{C.13}$$

In 2D, we have

$$\frac{\partial \phi}{\partial t} = f(\phi) = v \left(\frac{\partial^2 \phi}{\partial x^2} + \frac{\partial^2 \phi}{\partial y^2} \right). \tag{C.14}$$

Using

$$\phi(x) = A \exp(i \left(k_x x + k_y y\right)) \tag{C.15}$$

with a second-order centered stencil, we obtain

$$\frac{\partial^2 \phi}{\partial x^2} + \frac{\partial^2 \phi}{\partial y^2} = 2\phi \left(\frac{\cos(k_x \Delta x) - 1}{\Delta x^2} + \frac{\cos(k_y \Delta y) - 1}{\Delta y^2} \right), \tag{C.16}$$

which yields

$$\Delta t < \frac{2.79 \Delta x^2}{8\nu}. \tag{C.17}$$

Similarly, in 3D, we obtain

$$\Delta t < \frac{2.79 \Delta x^2}{12\nu}. \tag{C.18}$$

In Fig. C.3, the ideal behavior $\sigma = \exp(\lambda \Delta t)$ is shown by a black dashed line. Significant deviations between the RK4 scheme and the ideal behavior can be observed for $(\lambda \Delta t) < 1$. In order to be not only stable but also accurate, we thus set

$$\Delta t < \frac{\Delta x^2}{12\nu} \tag{C.19}$$

for 3D flows.

C.2 Iterative explicit midpoint scheme with four sub-iterations
C.2.1 Stability region
Assuming $\boldsymbol{f}(\boldsymbol{Y}^n) = \lambda \boldsymbol{Y}^n$, we have

$$
\begin{aligned}
\boldsymbol{Y}_1^* &= \boldsymbol{Y}^n + (\Delta t/2)\, \boldsymbol{f}(\boldsymbol{Y}^n) = (1 + \lambda \Delta t/2)\, \boldsymbol{Y}^n \\
\boldsymbol{Y}_2^* &= \boldsymbol{Y}^n + (\Delta t/2)\, \boldsymbol{f}(\boldsymbol{Y}_1^*) = \left(1 + \lambda \Delta t/2 + (\lambda \Delta t)^2/4\right) \boldsymbol{Y}^n \\
\boldsymbol{Y}_3^* &= \boldsymbol{Y}^n + (\Delta t/2)\, \boldsymbol{f}(\boldsymbol{Y}_2^*) = \left(1 + \lambda \Delta t/2 + (\lambda \Delta t)^2/4 + (\lambda \Delta t)^3/8\right) \boldsymbol{Y}^n \\
\boldsymbol{Y}_4^{n+1} &= \boldsymbol{Y}^n + \Delta t\, \boldsymbol{f}(\boldsymbol{Y}_3^*) = \left(1 + \lambda \Delta t + (\lambda \Delta t)^2/2 + (\lambda \Delta t)^3/4 + (\lambda \Delta t)^4/8\right) \boldsymbol{Y}^n.
\end{aligned}
\tag{C.20}
$$

Figure C.4 shows the stability contour for Eq. (C.20) i.e, the values of $\lambda \Delta t$ for which $\boldsymbol{Y}^{n+1} = \boldsymbol{Y}^n$.

C.2.2 Convective/Acoustic CFL
Following a similar procedure as in Sec. C.1.2, we have from Eq. (C.5) that λ is purely imaginary. Figure C.5 shows the amplification factor for λ purely imaginary.

Figure C.4: Stability region for the iterative explicit midpoint method with four sub-iterations.

To be stable, the condition on Δt is thus

$$\Delta t < \frac{2\Delta x}{a}, \tag{C.21}$$

where $a = |u|$ for convection, and $a = |u| + c$ for the acoustics. In Fig. C.5, the ideal behavior $\sigma = 1$ is shown by a dashed black line. Hence, to be not only stable but accurate, one can set

$$\Delta t < \frac{\Delta x}{a}. \tag{C.22}$$

Figure C.5: Amplification factor $|Y^{n+1}/Y^n|$ for λ purely (in blue), corresponding to the imaginary axis on Fig. C.4. The ideal behavior is shown by a dashed black line.

C.2.3   Viscous/Diffusive CFL

We follow the same procedure as in Sec. C.1.3. In Fig. C.6, the amplification factor for the iterative explicit midpoint method is shown in blue. In 1D, a necessary

condition to be stable is thus

$$\Delta t < \frac{2\Delta x^2}{4\nu}.$$ (C.23)

In 3D, it is

$$\Delta t < \frac{2\Delta x^2}{12\nu}.$$ (C.24)

In Fig. C.6, the ideal behavior $\sigma = \exp(\lambda\Delta t)$ is shown by a dashed black line. To be not only stable but also accurate, we set the following condition for a 3D flow

$$\Delta t < \frac{\Delta x^2}{12\nu}.$$ (C.25)

Figure C.6: Amplification factor σ when λ is real for the iterative explicit midpoint scheme with four sub-iterations (in blue), corresponding to the real axis on Fig. C.4. The ideal behavior $\sigma = \exp(\lambda\Delta t)$ is shown by a dashed black line.

ADDITIONAL FIGURES FOR FLAME-ACOUSTICS INTERACTIONS

(a) Gain for Case 3a

(b) Phase for Case 3a

(c) Gain for Case 3b

(d) Phase for Case 3b

(e) Gain for Case 3c

(f) Phase for Case 3c

Figure D.1: Gain (left) and phase (right) of heat release (black circles) and different intermediate species: hydroxyl radical [red crosses], formyl radical [black circles], and methyl radical [blue squares]. The phases and gains of some intermediate species are not shown for certain frequencies, as their evaluation becomes difficult due to the small amplitude of the fluctuating response at high frequency.

Figure D.2: Gain (left) and phase (right) of heat release (black circles) and different intermediate species: hydroxyl radical [red crosses], formyl radical [black circles], and methyl radical [blue squares]. The phases and gains of some intermediate species are not shown for certain frequencies, as their evaluation becomes difficult due to the small amplitude of the fluctuating response at high frequency.

A p p e n d i x   E

DERIVATION OF THE SPLIT IMPOSED/RESOLVED VELOCITY FIELD GOVERNING EQUATIONS

The momentum equation (5.3) is obtained by plugging the velocity decomposition given by Eq. (5.1) into Eq. (2.2)

$$
\frac{\partial \rho u_i^r}{\partial t} + (\rho u_j^r u_i^r)_{,j} + p_{,i} - \tau_{ij,j}^r = -u_i^r \underbrace{\left(\frac{\partial \rho}{\partial t} + (\rho u_j^r)_{,j} + (\rho u_j^i)_{,j} \right)}_{=0}
$$

$$
- (\rho u_i^r u_j^i)_{,j} - \rho u_j^r u_{i,j}^i - \rho u_j^i u_{i,j}^i - \rho \frac{\partial u_i^i}{\partial t} + \tau_{ij,j}^i \,,
$$

(E.1)

and observing that the 1$^{\text{st}}$ term on the RHS drops because of Eq. (5.2). The energy equation (5.4) is obtained by plugging the velocity decomposition into (2.3)

$$
\frac{\partial \rho e_t^r}{\partial t} + \left(\rho u_i^r h_t^r \right)_{,i} + q_{i,i} - \left(u_j^r \tau_{ij}^r \right)_{,i} = -\frac{u_j^i u_j^i}{2} \underbrace{\left(\frac{\partial \rho}{\partial t} + (\rho u_i^r)_{,i} + (\rho u_i^i)_{,i} \right)}_{=0}
$$

$$
- u_j^i \underbrace{\left(\frac{\partial \rho u_j^r}{\partial t} + \left(\rho u_i^r u_j^r \right)_{,i} + p_{,j} - \tau_{ij,i}^r - \tau_{ij,i}^i + \rho \frac{\partial u_j^i}{\partial t} + \rho u_i^i u_{j,i}^i + \rho u_i^r u_{j,i}^r + \left(\rho u_i^i u_j^r \right)_{,i} \right)}_{=0}
$$

$$
- u_i^i \left(\rho e_t^r \right)_{,i} - \rho h_t^r u_{i,i}^i - \rho u_i^r u_j^r u_{i,j}^i + \tau_{ij}^r u_{i,j}^i + \tau_{ij}^i u_{i,j}
$$

$$
+ \left(u_j^r \tau_{ij}^i \right)_{,i} - \rho u_i^r \frac{\partial u_i^i}{\partial t} - \rho u_i^r u_j^i u_{i,j}^i \,,
$$

(E.2)

and noting that the 1$^{\text{st}}$ term on the RHS drops because of Eq. (5.2), and the 2$^{\text{nd}}$ term drops because of Eq. (5.3).

A p p e n d i x   F

CONSTANT NON-UNITY LEWIS NUMBERS FOR THE TURBULENT FLAME SIMULATIONS

Species	Lewis number
N_2	1.12977
$1 - CH_2$	1.00485
$3 - CH_2$	1.00539
O	0.739306
H_2	0.304862
H	0.190084
OH	0.74653
H_2O	0.797255
O_2	1.07456
HO_2	1.07066
CH	0.690885
CO	1.15128
HCO	1.28976
CH_2O	1.24701
CH_3	0.98631
CO_2	1.37679
CH_4	0.977049
C_2H_3	1.3421
C_2H_4	1.26399
C_2H_5	1.33718
C_2H	1.34147
HCCO	0.910152
C_2H_2	1.32775
C_3H_3	1.75669
$A - C_4H_5$	1.84654
$n - C_3H_7$	1.74015
C_2H_6	1.35465
$P - C_3H_4$	1.7434
$A - C_3H_4$	1.74653
C_3H_6	1.77385
$1 - C_4H_8$	1.93526
$1 - C_5H_{10}$	2.22559
$1 - C_5H_{11}$	1.97632
$2 - C_7H_{15}$	2.6707
$n - C_7H_{16}$	2.64491

A p p e n d i x   G

SEMI-IMPLICIT CORRECTION FOR THE ACOUSTICS

We want to use the Crank-Nicholson time integration scheme, similarly to what is done in the low Mach version of NGA [76]. We first write the continuity, momentum, and total energy equations in residual form. For continuity, we have

$$\rho_{k+1}^{n+1} - \rho_k^{n+1} = -(\rho_k^n - \rho^n + \Delta t \boldsymbol{D}[(\rho\boldsymbol{u})_k^{n+1} + (\rho\boldsymbol{u})^n]),\tag{G.1}$$

which we rewrite as

$$\delta\rho = -\theta_\rho,\tag{G.2}$$

where

$$\delta\rho = \rho_{k+1}^{n=1} - \rho_k^{n+1},\tag{G.3}$$

and

$$\theta_\rho = \rho_k^n - \rho^n + \Delta t \boldsymbol{D}[(\rho\boldsymbol{u})_k^{n+1} + (\rho\boldsymbol{u})^n].\tag{G.4}$$

Similarly, we write momentum as $\delta(\rho\boldsymbol{u}) = -\theta_{\rho u}$, energy as $\delta(\rho e_t) = -\theta_{\rho e_t}$, and species transport as $\delta(\rho Y_s) = -\theta_{\rho Y_s}$.

G.1   Linearized Euler equations

The linearized Euler equations with no mean flow are

$$\frac{\partial\rho'}{\partial t} + \rho_0\nabla \cdot \boldsymbol{u}' = 0,\tag{G.5}$$

$$\rho_0\frac{\partial\boldsymbol{u}'}{\partial t} + \nabla p = 0,\tag{G.6}$$

$$\rho_0\frac{\partial(\rho e)'}{\partial t} + h_0\nabla \cdot \boldsymbol{u}' = 0.\tag{G.7}$$

Since the linearized Euler equations describe the transport of acoustic waves, the idea is to perform an implicit correction in the full Navier-Stokes equations on the terms that have an equivalent in the linearized Euler equations.

G.2 Algorithm

G.2.1 Implicit correction for the viscous/diffusion terms

We **first** perform an implicit correction for the **viscous/diffusive** terms, i.e., we write

$$\delta\rho^\dagger = 0 \tag{G.8}$$

$$\delta(\rho\boldsymbol{u})^\dagger = \rho_k^{n+1}\delta\boldsymbol{u}^\dagger = -\boldsymbol{\theta}_{\rho u} + \frac{\Delta t}{2}\boldsymbol{D}\left[\mu_k^*\boldsymbol{G}\left[\delta\boldsymbol{u}^\dagger\right]\right] \tag{G.9}$$

$$\left(\rho_k^{n+1}\boldsymbol{I} - \frac{\Delta t}{2}\boldsymbol{D}\left[\mu_k^*\boldsymbol{G}\left[\,\cdot\,\right]\right]\right)\delta\boldsymbol{u}^\dagger = -\boldsymbol{\theta}_{\rho u} \tag{G.10}$$

$$\delta(\rho Y_i)^\dagger = \rho_k^{n+1}\delta Y_i^\dagger = -\theta_{\rho Y_i} + \frac{\Delta t}{2}\boldsymbol{D}\left[\rho_k^* D_{i_k}^* \boldsymbol{G}\left[\delta Y_i^\dagger\right]\right] \tag{G.11}$$

$$\left(\rho_k^{n+1}\boldsymbol{I} - \frac{\Delta t}{2}\boldsymbol{D}\left[\rho_k^* D_{i_k}^* \boldsymbol{G}\left[\,\cdot\,\right]\right]\right)\delta Y_i^\dagger = -\theta_{\rho Y_i} \tag{G.12}$$

$$\delta(\rho e_t)^\dagger = \rho_k^{n+1}\delta e_t^\dagger = -\theta_{\rho e_t} + \frac{\Delta t}{2}\boldsymbol{D}\left[\lambda_k^*\boldsymbol{G}\left[\delta T^\dagger\right]\right]$$
$$= -\theta_{\rho e_t} + \frac{\Delta t}{2}\boldsymbol{D}\left[\lambda_k^*\boldsymbol{G}\left[\frac{\delta e_t^\dagger}{(c_v)_k^{n+1}}\right]\right] \tag{G.13}$$

$$\left(\rho_k^{n+1}\boldsymbol{I} - \frac{\Delta t}{2}\boldsymbol{D}\left[\lambda_k^*\boldsymbol{G}\left[\frac{(\,\cdot\,)}{(c_v)_k^{n+1}}\right]\right]\right)\delta e_t^\dagger = -\theta_{\rho e_t} \tag{G.14}$$

We solve for $\delta(\rho\boldsymbol{u})^\dagger$, $\delta(\rho Y_i)^\dagger$, and $\delta(\rho e_t)^\dagger$, and proceed to the next step, which is to perform the implicit correction for the acoustics.

G.2.2 Implicit correction for the acoustics

Inspired by the linearized Euler equations, as presented in Sec. G.1, we write

$$\delta(\rho\boldsymbol{u}) = \delta(\rho\boldsymbol{u})^\dagger - \frac{\Delta t}{2}\boldsymbol{G}\left[\delta p\right]\,, \tag{G.15}$$

$$\delta\rho = -\theta_\rho - \frac{\Delta t}{2}\boldsymbol{D}\left[\delta(\rho\boldsymbol{u})\right] = -\theta_\rho - \frac{\Delta t}{2}\boldsymbol{D}\left[\delta(\rho\boldsymbol{u})^\dagger\right] + \frac{\Delta t^2}{4}\boldsymbol{L}\left[\delta p\right]\,, \tag{G.16}$$

$$\delta(\rho e_t) = \delta(\rho e_t)^\dagger - \frac{\Delta t}{2}\boldsymbol{D}\left[\frac{((\rho e_t)_k^* + p_k^*)}{\rho_k^{n+1}}\left[\delta(\rho\boldsymbol{u}) - \boldsymbol{u}_k^{n+1}\delta\rho\right]\right]\,. \tag{G.17}$$

We now combine Eq. (G.15)–(G.17). We neglect the gradient terms corresponding to convective transport in the implicit correction for $\delta(\rho e_t)$, i.e., we write

$$
\begin{aligned}
\delta(\rho e_t) &= \delta(\rho e_t)^\dagger - \frac{\Delta t}{2} \frac{((\rho e_t)_k^* + p_k^*)}{\rho_k^{n+1}} \left(\boldsymbol{D} \left[[\delta(\rho \boldsymbol{u})] - \delta\rho \boldsymbol{D} \left[\boldsymbol{u}_k^{n+1} \right] \right] \right) \\
&= \delta(\rho e_t)^\dagger - \frac{\Delta t}{2} \frac{((\rho e_t)_k^* + p_k^*)}{\rho_k^{n+1}} \left(\boldsymbol{D} \left[\boldsymbol{u}_k^{n+1} \right] \theta_\rho \right. \\
&\quad \left. - \left(\boldsymbol{I} + \frac{\Delta t}{2} \boldsymbol{D} \left[\boldsymbol{u}_k^{n+1} \right] \right) \left(\frac{\Delta t}{2} \boldsymbol{L} \left[\delta p \right] - \boldsymbol{D} \left[\delta(\rho \boldsymbol{u})^\dagger \right] \right) \right).
\end{aligned}
\tag{G.18}
$$

We now use the definition of total energy to relate $\delta(\rho e_t)$ and δp, i.e.,

$$
\begin{aligned}
\delta(\rho e_t) &= \delta(\rho h) + \delta(\rho |\boldsymbol{u}|^2/2) - \delta p \\
&\approx \rho_k^{n+1} \delta h + h_k^{n+1} \delta\rho - \delta p \\
&= \rho_k^{n+1} c_{p,k}^{n+1} \delta T + h_k^{n+1} \delta\rho - \delta p \,.
\end{aligned}
\tag{G.19}
$$

Using the linearized equation of state

$$
\frac{\delta p}{p_k^{n+1}} = \frac{\delta\rho}{\rho_k^{n+1}} + \frac{\delta T}{T_k^{n+1}} ,
\tag{G.20}
$$

Eq. (G.19) becomes

$$
\begin{aligned}
\delta(\rho e_t) &\approx \left(h_k^{n+1} - c_{p,k}^{n+1} T_k^{n+1} \right) \delta\rho + \frac{\delta p}{\gamma_k^{n+1} - 1} \\
&= (h - c_p T)_k^{n+1} \left(-\theta_\rho - \frac{\Delta t}{2} \boldsymbol{D} \left[\delta(\rho \boldsymbol{u})^\dagger \right] + \frac{\Delta t^2}{4} \boldsymbol{L} \left[\delta p \right] \right) + \frac{\delta p}{\gamma_k^{n+1} - 1} \,.
\end{aligned}
\tag{G.21}
$$

Combining Eqs. (G.18) and (G.21), we obtain the following elliptic system for δp

$$
\begin{aligned}
&- (\gamma_k^{n+1} - 1) (c_p T - h)_k^{n+1} \frac{\Delta t^2}{4} \boldsymbol{L} \left[\delta p \right] - \frac{\tilde{c}_k^2 \Delta t^2}{4} \left(\boldsymbol{I} + \frac{\Delta t}{2} \boldsymbol{D} \left[\boldsymbol{u}_k^{n+1} \right] \right) \boldsymbol{L} \left[\delta p \right] + \delta p \\
&= -(\gamma_k^{n+1} - 1)\theta_{\rho e_t} - \frac{\Delta t}{2} \tilde{c}_k^2 \left(\boldsymbol{D} \left[\boldsymbol{u}_k^{n+1} \right] \theta_\rho + \left(\boldsymbol{I} + \frac{\Delta t}{2} \boldsymbol{D} \left[\boldsymbol{u}_k^{n+1} \right] \right) \boldsymbol{D} \left[\delta(\rho \boldsymbol{u})^\dagger \right] \right) \\
&\quad - (\gamma_k^{n+1} - 1) (c_p T - h)_k^{n+1} \left(\theta_\rho + \frac{\Delta t}{2} \boldsymbol{D} \left[\delta(\rho \boldsymbol{u})^\dagger \right] \right),
\end{aligned}
\tag{G.22}
$$

where

$$\tilde{c}_k^2 = (\gamma_k^{n+1} - 1)\frac{((\rho e_t)_k^* + p_k^*)}{\rho_k^{n+1}} .$$ (G.23)

We solve Eq. (G.22), and obtain δp. We then use it to obtain $\delta(\rho \boldsymbol{u})$, $\delta\rho$, and $\delta(\rho e_t)$ following Eqs. (G.15)–(G.17).

G.2.3 Implicit correction for chemistry

Finally, we consider the species transport equation. The intermediate change in species mass fractions for the acoustics correction $\delta(\rho Y_s)^{\dagger\dagger}$ is computed as

$$\delta(\rho Y_s)^{\dagger\dagger} = \delta(\rho Y_s)^\dagger - \frac{\Delta t}{2}Y_s^* \boldsymbol{D}\left[\delta(\rho \boldsymbol{u})\right] .$$ (G.24)

We perform the **third** and last step, which is to perform an implicit correction on **chemistry**, i.e., we solve

$$\delta(\rho Y_s) = \delta(\rho Y_s)^{\dagger\dagger} - \frac{\Delta t}{2}\frac{\dot{\omega}_{s,k}^{-*}}{(\rho Y_s)_k^*}\delta(\rho Y_s)$$ (G.25)

for $\delta(\rho Y_s)$, which only amounts to inverting a diagonal matrix.

G.3 Test cases

All the test cases considered use periodic boundary conditions. The extension of this method to more complex boundary conditions, such as the NSCBC, should be pursued in future work.

G.3.1 Isochoric ignition

We simulate a "hot spot", i.e., we initialize a periodic one-dimensional field with a mirrored laminar flame solution, using n-heptane/air mixture at $\phi = 0.9, T_u = 298$ K, and $p_0 = 1$ atm, using the 35 species reduced detailed mechanism of Bisetti *et al.*[6]. The timestep is $\Delta t = 5 \cdot 10^{-7}$ s, which corresponds to an acoustic CFL of 25, and a viscous CFL of 3. Figure G.1 shows the comparison between the compressible results and the ones obtained using the low Mach number approximation. The low Mach number results are obtained with the same timestep as the compressible ones. The agreement is excellent. Figure G.2 shows the time evolution of the mean pressure (compressible), and the thermodynamic pressure (low Mach number approximation). Again, the agreement is very good.

(a) $t = 0$

(b) $t = 10^{-3}$ s

(c) $t = 2 \cdot 10^{-3}$ s

(d) $t = 3 \cdot 10^{-3}$ s
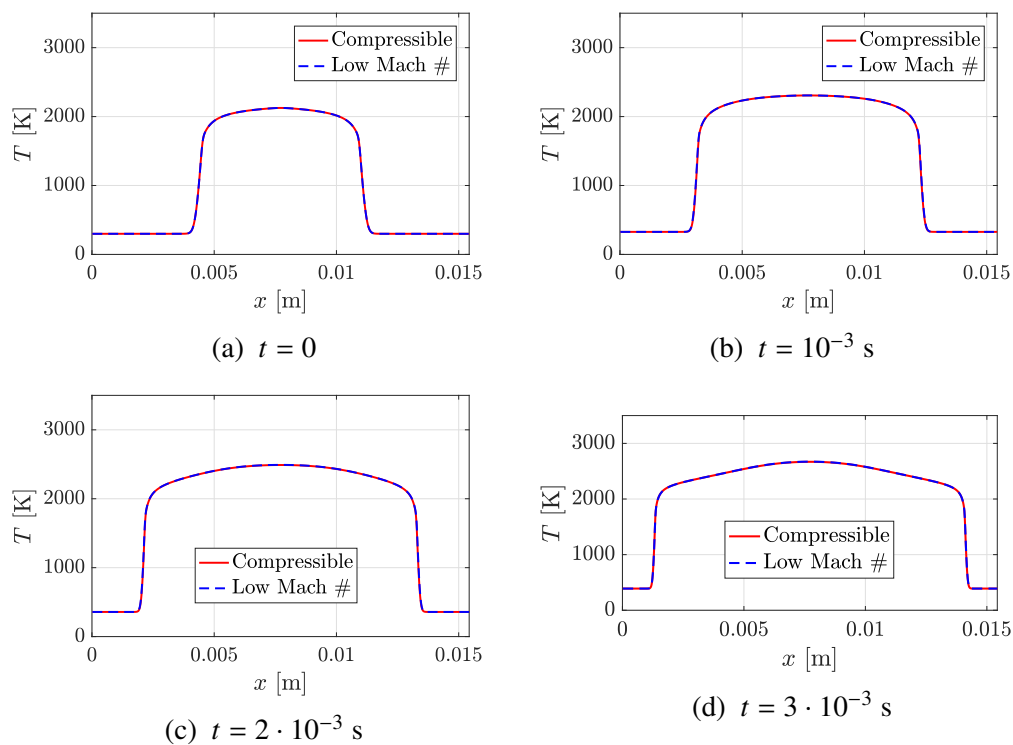
Figure G.1: Temperature profiles for the isochoric ignition case.
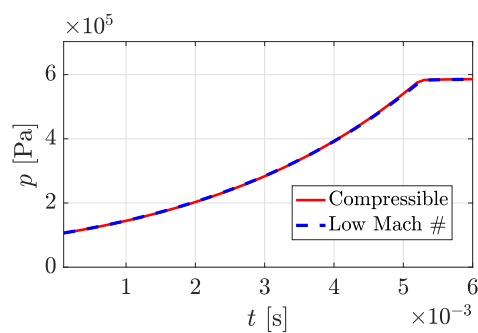
Figure G.2: Evolution of mean pressure (compressible) and thermodynamic pressure (low Mach # solver) as a function of time for the isochoric ignition case.

G.3.2 Vortex advection (inviscid)

Here, we test the implicit correction for the acoustics in multiple dimensions. We perform simulations of an inviscid two-dimensional vortex advected by a mean background velocity u_0, using a timestep of $\Delta t = 10^{-2}$ s corresponds to an acoustic CFL of 10, and a convective CFL of 0.9. Figure G.3 shows the vorticity isocontours initially ($t^* = t/(L/u_0) = 0$) and after one flow-through time ($t^* = 1$). There agreement between the two profiles is excellent. To explore this further, we plot in Fig. G.4 the vorticity profile at $x/L = 0.5$ after one flow-through time ($t^* = 1$) for the simulation using the midpoint method using the implicit correction for acoustics with $\Delta t = 10^{-2}$ s, and a reference simulation using the RK4 scheme with $\Delta t = 5 \cdot 10^{-4}$ s (corresponding to an acoustic CFL of 0.5). The agreement is excellent.

(a) $t^* = 0$ (b) $t^* = 1$
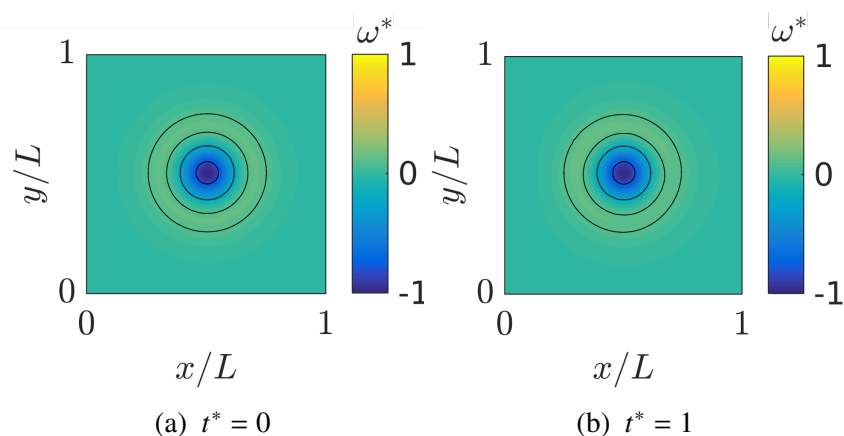
Figure G.3: Vorticity isocontours for the inviscid vortex advection case, using the compressible formulation with $\Delta t = 10^{-2}$ s.
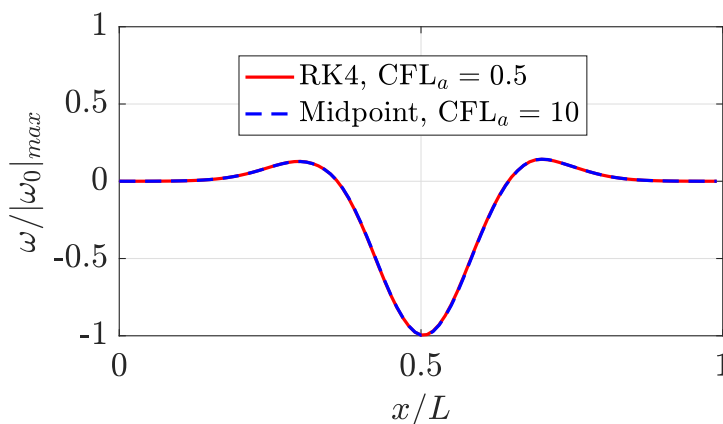
Figure G.4: Vorticity profile at $x/L = 0.5$, after one flow-through time ($t^* = 1$).

G.4 Travelling acoustic wave with density change

Here, we consider an acoustic wave in an non-homogeneous mixture of N_2 and H_2. The base flow is H_2 (blue in Fig. G.5a), and there is small circular region of N_2 (yellow in Fig. G.5a). The reference density ρ_0 is the density of H_2. The initial pressure profile is shown in Fig. G.5b, which shows where the acoustic wave is. Figure G.6 shows the normalized density and pressure profiles after the wave has impinged on the large-density region. We are not so much interested in the physics at play, but on how well the acoustic wave is captured as a function of the time step. Figure G.7 shows the density and pressure profiles corresponding to $x/L = 0.5$ in Fig. G.6, obtained by using three different time steps corresponding to different acoustic CFLs. In Fig. G.7b, the solution with $CFL_a = 8$ is in good agreement with the one with $CFL_a = 0.8$. However, the solution with $CFL_a = 80$ is very different from the other two. As a matter Hence, while performing an implicit correction for the acoustics yields a stable solution for the three CFLs considered, significant dispersion errors are introduced when very large time steps are used. This is important if the acoustic field is of interest.

(a) ρ/ρ_0

(b) $(p - p_0)/p_0$
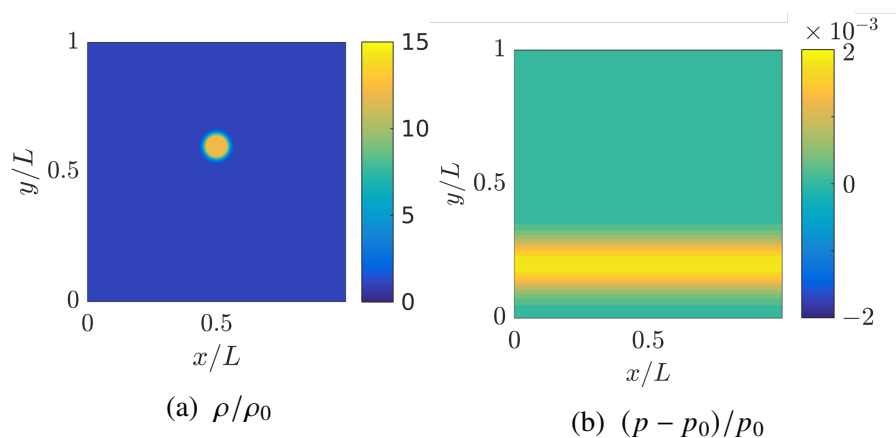
Figure G.5: Normalized initial density and pressure isocontours for the acoustic wave with density change.

(a) ρ/ρ_0

(b) $(p - p_0)/p_0$
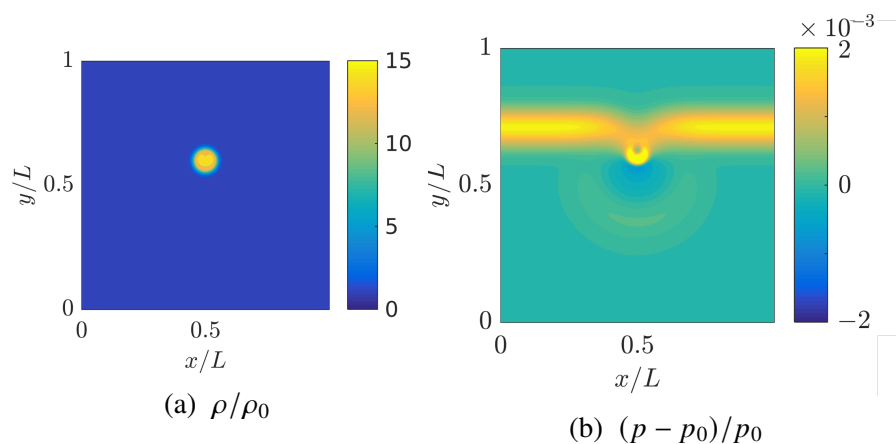
Figure G.6: Normalized density and pressure isocontours for the acoustic wave with density change, after the acoustic wave has impinged on the large-density region.

(a) ρ/ρ_0

(b) $(p - p_0)/p_0$
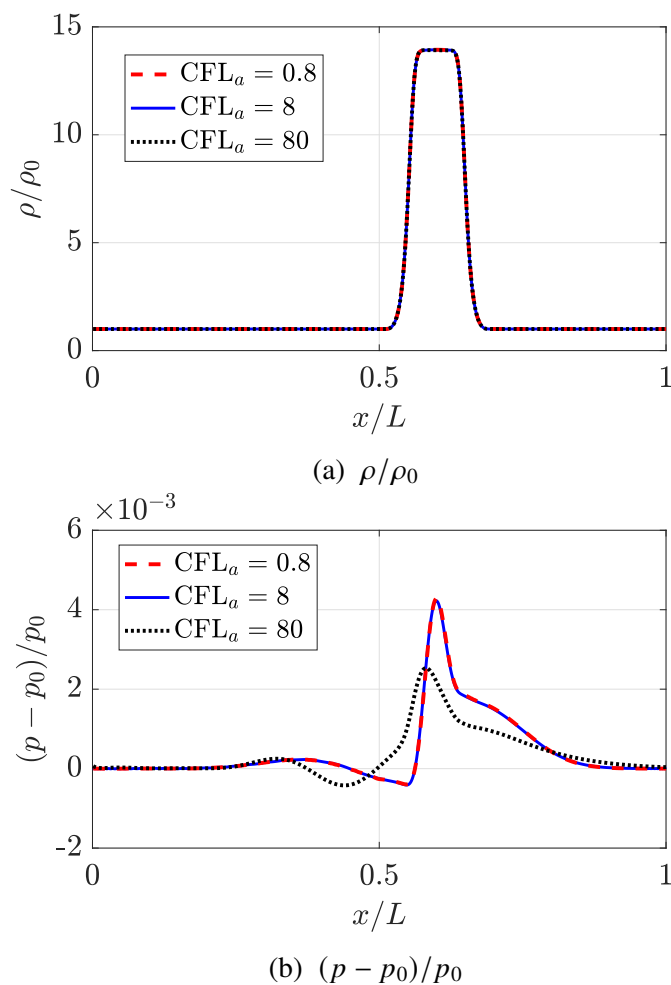
Figure G.7: Normalized density and pressure profile at $x/L = 0.5$ for the acoustic wave with density change, after the acoustic wave has impinged on the large-density region.